DESIGN AND DEVELOPMENT OF BILAYER SENSOR SYSTEMS FOR BIOMEDICAL AND AUTOMOTIVE APPLICATIONS

A Thesis Submitted to the University of Wales Cardiff in Candidature for the Degree of

Doctor of Philosophy

by

George S. Katranas
M.Eng. (Hons)

Cardiff School of Engineering
University of Wales Cardiff

September 2006

ProQuest LLC
789 East Eisenhower Parkway
P.O. Box 1346
Ann Arbor, MI 48106-1346

Summary

This investigation concerned the design and development of a novel measurement system that incorporates bilayer sensors for monitoring applications in the biomedical and automotive industry. The bilayer sensors are made primarily from a configuration of soft magnetic material on a non magnetic substrate that is used to enhance the changes in the relative permeability of the material, caused by tensile or compressive stresses.

Three modulation techniques were examined as a method for convening the sensor signal information; this is the first use of the phase (*PM*) and frequency (*FM*) modulation methods in conjunction with bilayer sensors. The measurement system incorporated, in software code, a range of mathematical concepts used for extracting and processing the sensor information signal. The use of simulated and acquired modulation signals allowed the comparison of the modulation techniques. Optimisation of the bilayer sensor was considered by studying the effects of the bilayer sensor physical dimensions and parameters on its performance. Also the thermal stability of the bilayer sensor and *FM* system was examined.

Physiological measurements for the detection and monitoring of cardio-respiratory activities were conducted. A bilayer sensor measurement system was used for the first time not only to detect but also to map the normal heartbeat rate through the hemo-dynamics of the carotid artery. The system was used to monitor a range of respiratory activities such as normal respiration, deep inhalation/exhalation and apnoea. The application of the sensor is a non-invasive and a non-disturbing method for monitoring biomedical activities related to skin curvature changes.

The bilayer sensor measurement system was used for monitoring of airflow in turbulent conditions. Measurements were conducted for a variety of airflows and at a range of distances from the centre of the tube, were the flow is at maximum. Furthermore the effect of substrate thickness and material choice was investigated on the performance of the sensor.

This investigation led to the design and construction of a novel measurement system than can successfully detect and quantify displacements in the micron range. The application of this system to biomedical and automotive applications showed the universality and adaptability of the bilayer sensors and its measurement method.

Acknowledgements

This investigation was carried out at the Wolfson Centre for Magnetics, School of Engineering, University of Wales, Cardiff.

I wish to take this opportunity to express my sincere thanks to my supervisors Dr. T. Meydan and Prof. D. C. Jiles, for their interest, encouragement and assistance throughout the period of this investigation.

I would also like to thank Dr. T. A. Ovari and Dr. F. Borza for kindly providing with the sensor material.

My sincere thanks also go to the staff at Wolfson, in particularly Dr. P. Williams and Mr. P. Bartlett for the regular discussions on the topic, industry insight and patience.

Last but certainly not least, I wish to thank my family and my friends for their endless support. Without their help and encouragement I would have never had this opportunity to learn and enhance my knowledge.

To: My family and friends

Table of Contents

Glossary

Roman letters

	Description	Units
A	Area	m^2
a	Acceleration	m/s^2
B	Magnetic Flux Density	T
c	Curvature	rad/m
C	Capacitance	F
d	Centroidal Distance from the Neutral Axis	m
dm	Diameter	m
E	Young's Modulus	Pa
e	Thermal Expansion Coefficient	K^{-1}
E_d	Young's Modulus (Demagnetised State)	Pa
E_s	Young's Modulus (Saturated State)	Pa
F	Force	N
f	Frequency	Hz
h	Height	m
H	Magnetic Field	A/m
I	Electric Current	A
In	Area Moment of Inertia	m^4
L	Inductance	H
ℓ	Length	m
m	Mass	kg
M	Bending Moment	N·m
M'	Magnetisation	A/m
m_{AM}	Modulation Depth for Amplitude Modulation	-
m_{FM}	Modulation Depth for Frequency Modulation	-
m_m	Magnetic Moments	$A \cdot m^2$
m_{PM}	Modulation Depth for Phase Modulation	-
N	Number of Coil Turns	-
P	Pressure	Pa
P_s	Static Pressure	Pa
q	Dynamic Pressure	Pa
R	Resistance	Ω
r	Radius	m
r_c	Radius of Curvature	m/rad
R_e	Reynolds Number	-
sc	Square Correlation Coefficient	-
t	Time	s
T	Temperature	°C
T_c	Curie Temperature	°C
th	Thickness	m
u	Velocity	m/s
U'	Stored Energy Per Unit Volume	J/m^3

V	Voltage Waveform Amplitude (Peak)	V
v	Electric Voltage	V
w	Width	m
W	Work	J
W_i	Magnetisation Energy	J/m^3
W_K	Anisotropic Energy	J/m^3
W_λ	Magnetostriction Energy	J/m^3
X	Reactance	Ω

Greek Letters

	Description	**Units**
γ	Shear Strain	-
δ	Elongation	m
ε	Strain	-
ζ	Deflection	m
θ	Angle of Rotation	rad
λ	Magnetostriction	-
μ	Permeability	H/m
μ_0	Permeability of Free Space	H/m
μ_r	Relative Permeability	-
ν_d	Dynamic Viscosity	Pa·s
ξ	Centroidal Distance Between Two Layers	m
ρ	Density	kg/m^3
σ	Stress	Pa
τ	Shear Stress	Pa
Φ	Magnetic Flux	Wb
φ	Phase	Degrees
χ'	Magnetic Susceptibility	-
ω	Angular Frequency	rad/s

Acronyms

.html	Hyper Text Mark-up Language
.xls	Microsoft Excel® File Format
AC	Alternating Current
Al	Aluminium
AlMg	Aluminium-Magnesium Alloy
AM	Amplitude Modulation
B	Boron
Be	Beryllium
C	Carbon
Co	Cobalt
Cu	Copper
CuBe	Copper Beryllium Alloy

DC	Direct Current
e.m.f.	Electro-Motive Force
ECG	Electrocardiogram
EEG	Electroencephalography
EMG	Electromyography
Fe	Iron
FEM	Finite Element Modelling
FM	Frequency Modulation
HAVAR	High-Strength Non-magnetic Alloy
LSF	Lower Side Frequency
Mg	Magnesium
Mo	Molybdenum
NI	National Instruments
Ni	Nickel
Op-amp	Operational Amplifier
PC	Personal Computer
PCB	Printed Circuit Board
PCI	Peripheral Component Interconnect
PM	Phase Modulation
PSD	Phase-Sensitive Detector
PSG	Polysomnography
REM	Rapid Eye Movement
Si	Silicon
SNR	Signal-to-Noise Ratio
USF	Upper Side Frequency
VCC	Voltage-to-Current Converter

Chapter 1 General Introduction

1.1 Preface

The highly sophisticated systems and instruments that surround us in our every day life need information from the outside world via the use of sensors (transducers). Thus, sensors aid these devices to comprehend and interpid the surrounding environment by transforming physical phenomena that are associated with the laws of nature into electrical signals (Figure 1.1).

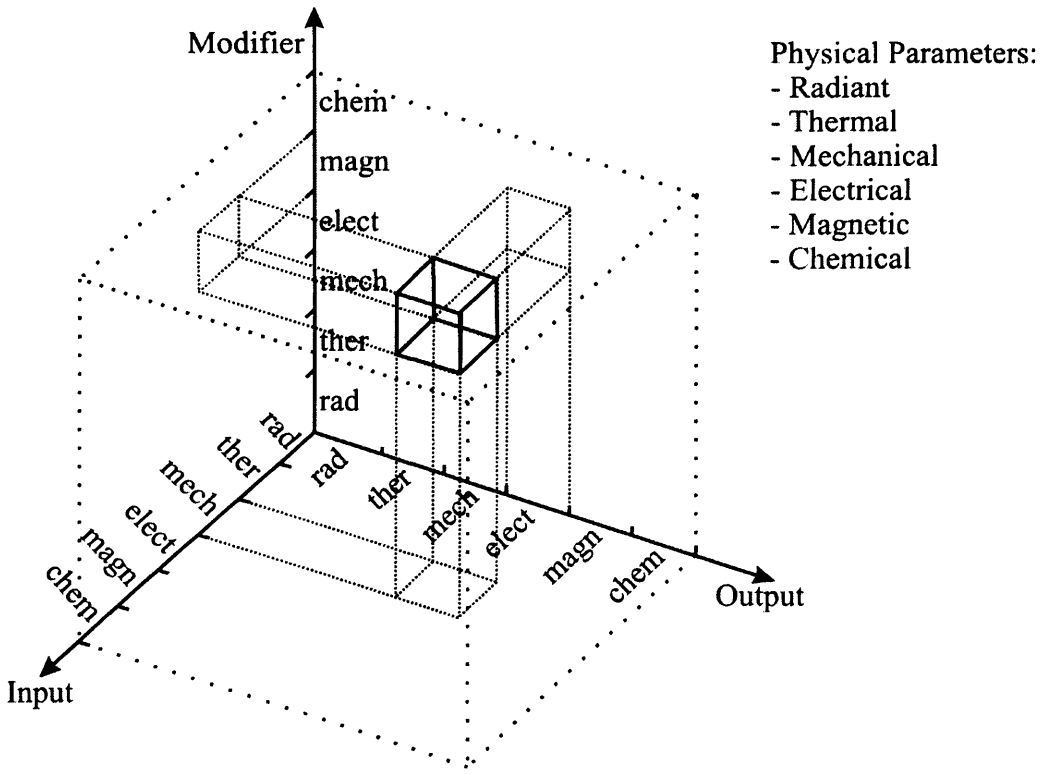

Figure 1.1: Example diagram of a bilayer magnetic sensor indirectly converting a mechanical stimulus to an electrical signal using the magnetic principle of permeability as the modifier[1].

Currently sensors are able to convert a variety of physical parameters, directly or indirectly into electrical signals. These parameters may be but not limited to[1]:

G. S. Katranas, "Design and Development of Bilayer Sensor Systems for Biomedical and Automotive Applications", Ph.D. Thesis, Cardiff University.

- *Radiant*: Light intensity, polarisation, reflectance, transmittance, wavelength.
- *Mechanical*: Acceleration, amplitude, force, inclination, position, pressure, stress, torsion, velocity, vibration.
- *Magnetic*: Magnetic field strength, magnetic flux density, permeability.
- *Electrical*: Capacitance, current, frequency, inductance, resistance, voltage.
- *Thermal*: Entropy, temperature, thermal flux.
- *Chemical*: Composition, concentration, toxicity.

1.2 Magnetic Sensors

Magnetic sensors follow the same principle as all sensors, i.e. they are devices that receive a signal or stimulus and can respond with an electrical output signal. The difference between the other types of sensors is that magnetic sensors utilize laws of electromagnetism and effects in electromagnetic fields in order to achieve their goal.

The magnetic sensors have two main groups of application[1]:

i. *Direct*: When the sensor is placed in the presence of a magnetic field, it converts the stimulus to an electrical signal.
ii. *Indirect*: There is a strong interaction in magnetic materials between their magnetic and mechanical properties. Any change in the sensor's mechanical properties will result in a change in its magnetic behaviour. Hence, this change can be converted into an electrical signal[2].

Traditionally magnetic sensors can be used for the detection of a variety of physical phenomena such as mechanical, thermal and of course magnetic. The most common types of magnetic sensors are[2]:

- *Magnetic gradiometer*: A pair of identical and aligned field sensors that are used for the detection of the change in magnitude and direction i.e. gradient of small fields.

G. S. Katranas, "Design and Development of Bilayer Sensor Systems for Biomedical and Automotive Applications", Ph.D. Thesis, Cardiff University.

- *Magnetic field*: An induction coil arrangement with a ferromagnetic core used for the detection of magnetic field generated by alternating currents. Part of this category is the SQUID (Superconductive Quantum Interface Device) sensor that is able to achieve magnetic field resolution in the order of fT (10^{-15} T).
- *Magnetoresistive*: These sensors exploit of the effect of magnetic field on the resistivity of a material.
- *Magnetostrictive*: Sensors that use magnetic materials that changes in dimensions under the application of a magnetic field. Inverse magnetostrictive sensors utilise the effect where the change of a magnetic materials dimensions, due to applied stress, creates a magnetic field.

One way to classify the various magnetic sensors is by their sensing range. Table 1.1 lists, as an example, the various sensor technologies used for the magnetic field sensing and their respective ranges[3].

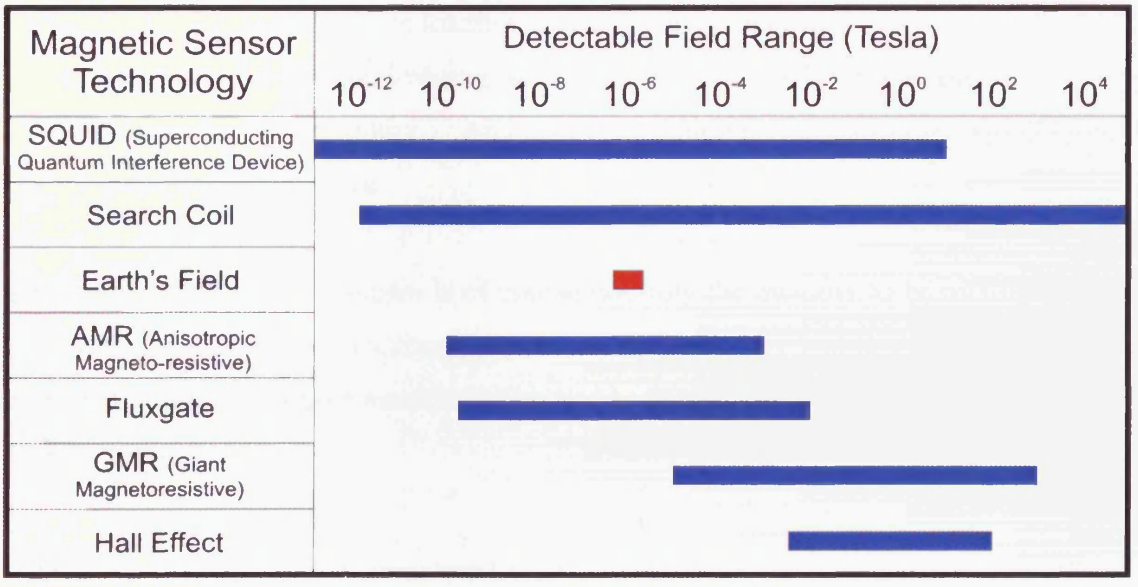

Table 1.1: Example of magnetic sensor technology field ranges.

The application area of magnetic sensors can encompass a very broad field in engineering. Even sensors that work under the same principle can be used in completely different environments such as displacement sensors used in the

G. S. Katranas, "Design and Development of Bilayer Sensor Systems for Biomedical and Automotive Applications", Ph.D. Thesis, Cardiff University.

automotive industry, for monitoring airflow, and biomedical systems, for monitoring cardio-respiratory activity. Some of the applications areas of magnetic sensors are [2, 4]:

- Aerospace
- Automotive
- Biomedical
- Consumer/domestic
- Industrial (Construction, Electrical, Mechanical)
- Scientific research
- Surveying

For those areas the magnetic sensors may have some of the following applications[4]:

- Fluid flow: Blood flow, engine air or water flow monitoring and control.
- Vibration and acceleration: Earthquake detection.
- Displacement and position: Cardio-respiratory activities,
- Stress and torque: Force loading, steering wheel torsion.
- Magnetic field: Brain imaging, security systems, vehicle navigation.
- Magnetic permeability: Archaeology, mineral exploration/exploitation, unexploded ordnance.

The factor for choosing a sensor is of course not only the quantity to be measured but also attributes such as the accuracy, performance, range, size and last but not least the cost involved in the sensor manufacturing and in the realisation and production of the measurement system.

1.3 Bilayer Sensors, Applications and Requirements

Bilayer sensors use as their operating principle the inverse magnetostrictive effect. They comprise of a bilayer strip and a coil wound around one end. The bilayer strip comprises a magnetostrictive layer and a substrate which is non-magnetic in most cases. It's bending yields single-sign stress in the magnetic layer; the corresponding

G. S. Katranas, "Design and Development of Bilayer Sensor Systems for Biomedical and Automotive Applications", Ph.D. Thesis, Cardiff University.

relative permeability change can be detectable with simple electronics. The performance and behaviour of the bending-sensitive material can be influenced significantly by layer thickness and the modulus of elasticity. The bilayer composition takes advantage from existing types of materials such as *Fe*-based amorphous ribbons. In addition, new alloys can be manufactured by means such as *RF* sputtering. The adhesion of layers may be performed by agglutination or deposition of the magnetic material on the substrate.

This project aims at this new category of bilayer materials as a basic standard element for multi-functional sensor families which may replace the variety of sensor principles utilised in systems for monitoring and control. The work involves a variety of specific technologies for the development of the sensor system (e.g. modulation methods, signal processing etc.) and disciplines (electronics, magnetism, material science, mechanics, physiology, software programming). The main objective is to use novel bilayer strips, as (i) robust but low-force activated, (ii) compact and low mass (up to 1 g), and (iii) very cheap standard components in a universal family of new sensors. A part of the project aims was the development of a hardware and/or software measurement system that will aid to the establishment of the sensor signals and help exploit the bilayer configuration capabilities.

One focus of this project was to examine the application of these sensors and the system for monitoring multi-parametric physiological quantities. Here special attractiveness results from low-force activation and low mass. To illustrate the versatility: Sleep laboratory sensors[5] could include skin sensors for respiration, blood pressure, extremity or Rapid Eye Movements (REM), foetal movements, heartbeat rate; miniaturised catheter sensors could measure oesophageal pressure, blood pressure and blood velocity. At present, no sensor principle is available which can be applied in a comparably universal way. Another area of focus is the possible use of the sensors and the measurement system in the automotive industry. An application to combine both focal points (automotive and biomedical) can probably arise from the physiological monitoring of the driver status for increased safety. The bilayers offer sensor applications for bending, displacement[5], force, flow, vibration, acceleration[6] and temperature[7] with a similar basic design[8].

Other sensor principles that are successfully in use today to measure parameters such as force and displacement are most commonly capacitive, piezoelectric, ultrasound and optical based systems. The application of these principles, compared to the bilayer sensors, present certain limitations:

- Capacitive – Moisture, dust and humidity will have an effect on the sensor performance[9]
- Piezoelectric – Unable to measure a static force over a long period of time due to leakage currents and susceptible to ageing[10].
- Ultrasound – Target surface reflectivity can affect the accuracy of the measurements[11].
- Optical – Ambient light will interfere with the measurement[12].

Regarding airflow measurements the two most common types of sensors used today in the automotive industry are the vane and the hot wire[13] anemometers. These technologies are not able to measure airflow directly, require the presence of laminar flow (non-turbulence) and are composed of moving parts, subjected to wear and tear.

These principles are used for specific applications i.e. optical sensors can be used for measuring displacement but not airflow. There is a need in industry for a sensor principle that can be used for many different applications[14]. The new types of bending-sensitive materials is expected to yield a variety of sensors all based on a common procedure for the measurement of very different parameters. Modern systems and devices require many sensors for monitor and control purposes. Each of these sensors might have its own operation principle and a corresponding measurement system. This leads to a cost and size discrepancy. The universality of the bilayer sensor and the adaptability of its measurement system may help to reduce costs for all types of applications that it is intended. It can be produced by industrial mass production with a high degree of automation. This offers a multiple impact:

- Reduction of expensive work as resulting from incompatible sensors and components.
- Cost reduction due to application-independent signal establishment methods, highly integrated systems and due to favored servicing.

- Improvement of safety levels with respect to novel driver monitoring and alarm systems.
- New market sectors in diagnostics and supervision (e.g. driver status monitoring, sleep laboratories or intensive care). Patient comfort increases with the new sensors in ambulatory as well as providing undisturbed clinical sleep monitoring

1.4 Thesis Outline

There has been a detailed attempt to include a comprehensive literature review in the form of references. These references are found throughout the thesis to directly link previous work related not only to bilayer sensors but to the techniques used for the implementation of the measurement system. This practice is hoped to enable the reader to embrace and understand the steps taken to design this multi-disciplinary project.

In Chapter 2 a brief introduction to the principles of mechanical engineering is given, servicing as a framework for many of the subsequent topics. It is this examination of the sensor's mechanical behaviour which aids in the understanding its operation and its evaluation. Since the bilayer sensor acts as a cantilever beam, the conditions of deflection, bending and curvature change are examined along with a brief look on the development of the internal stresses in the material under the application of an external force. Due to the nature of bilayer strips, special interest is given to the effect of layered structures on the analysis of cantilever principles. Finally for the application of the bilayer sensor on airflow measurements the mechanics of fluids are briefly investigated.

Chapter 3 focuses on the working principles of magnetism behind the operation of the bilayer sensors. Attempts to explain how the mechanical stimulation on the sensor can be exploited and converted to inductance changes, are performed by examining the properties of magnetic materials and phenomena such as inverse magnetostriction.

The desired magnetic and mechanical properties of materials, for bilayer sensor applications, are looked upon along with their fabrication methods.

The brief study of the existing modulation method used as the process of exploiting the inductance changes of the bilayer sensors is described in Chapter 4 along with its circuitry. Here the introduction of two alternative techniques is explained along with the principle of operation and the hardware that is necessary to realise them. The concepts used for extracting the sensor information signal are examined with emphasis to their mathematical aspect. This aided their later conversion into software code that was implemented for the signal acquisition, demodulation and processing of the modulated waveforms.

The details of the measurement system design are presented in Chapter 5. The software algorithm that is responsible for the signal processing of each modulation technique is presented. A controlled displacement setup, using an actuator, was designed in order to aid to the direct comparison of the performance of the three modulation methods. These results were also assessed against data obtained via a laser Doppler Vibrometer (*LDV*). The *LDV* was used to examine the linearity, mechanical hysteresis and quality of the measurement system. An examination on the optimisation of the bilayer sensor was considered by studying the effects of the bilayer sensor physical dimensions and parameters on its performance. Also the thermal stability is briefly examined to evaluate the bilayer sensor and the measuring system performance.

Finally, in Chapter 6, two applications of the bilayer sensor measurement system are considered for use in the field of the biomedical and automotive industry. Here the application of the measurement system is described, using bilayer sensors originally used for the detection of bending, in order to measure with minimum disturbance the physiological activities that involve the dynamic deformations of the curvature of the skin. Internal physiological activities are mirrored on the human body in the form of active variations of the skin curvature. Depending on the body region these signals can display cardiac activity, lung ventilation and body movements. Another application that was examined for the bilayer sensor measurement system is the monitoring of airflow. Results were obtained for a variety of airflows and at a range

of distances from the centre of the tube, where the flow is at maximum. Also the effect of substrate thickness and choice of material was investigated on the performance of the sensor.

References

[1] C. Roumenin, "Solid state magnetic sensors", New York: Elsevier, 1994, Vol. 2, Ch. 1, pp. 9-10.
[2] R. Boll et al, "Sensors: a comprehensive survey", VCH: Weinheim, 1989, Vol. 5, Ch. 4, pp. 98-147.
[3] J. E Lenz, "A review of magnetic sensors", IEEE Proceedings, 1990, Vol. 78, pp. 973-989.
[4] T. Meydan, "Amorphous materials in sensor applications", IEE Colloquium on Magnetic Materials for Sensors and Actuators, 1994, Vol. 183, pp. 1-3.
[5] E. Kaniusas et al, "Magnetoelastic skin curvature sensor for biomedical applications", Proceedings of IEEE Sensors, 2004, Vol. 3, pp. 1484-1487.
[6] E. Kaniusas et al, "A magnetostrictive acceleration sensor for registration of chest wall displacements", Journal of Magnetism and Magnetic Materials, Vol. 215-216, 2000, pp. 776-778
[7] E. Kaniusas et al, "Optimisation of sensitivity and time constant of thermal sensors based on magnetoelastic amorphous bilayers", Journal of Alloys and Compounds, Vol. 369, 2004, pp. 198-201.
[8] L. Mehnen et al, "Magnetostrictive bilayer sensors – a survey", Journal of Alloys and Compounds, Vol. 369, 2004, pp. 202-204.
[9] W. N. Alerich et al, "Electricity 4: AC/DC Motors, Controls and Maintenance", Delmar: New York, 2001, Ch. 18, pp.207-228.
[10] G. H. Gautschi, "Piezoelectric Sensorics: Force, Strain, Pressure, Acceleration and Acoustic Emission Sensors, Materials and Amplifiers", Springer: Berlin, 2002, Ch. 1, pp. 1-12.
[11] D. Irwin, "The Industrial Electronics Handbook", CRC Press: Boca Raton, 1997, Ch. 53, pp.738-744.
[12] A. Mandelis et al, "Physics, Chemistry and Technology of Solid State Gas Sensor Devices", Wiley: London, Ch. 5, pp. 163-178
[13] HFM5 Air mass meter, Operating Principle, Bosch GmbH, Germany, 2006.
[14] A. M. Merlo, Private communication, Centro Ricerche Fiat, Torino, Italy, 2004.

Chapter 2 Mechanical Analysis

One of the parameters that influence the sensitivity and performance of the bilayer sensors is the stress which is induced due to bending. These devices employ bilayer strips that consist of a magnetic layer and a non-magnetic counter layer that is used to enhance the changes in the relative permeability of the material caused by tensile or compressive stresses during bending. Depending on the manufacturing procedure (*RF* sputtering or agglutination) there may be an additional agglutination layer (trilayer strip). Since the sensitivity depends on specific parameters such as Young's modulus (modulus of elasticity) and dimensions it is necessary to briefly examine the principles of the mechanics involved. Also sensor applications such as airflow measurements, depend on the understanding of the fluid dynamics and the environment where the sensor is applied.

2.1 Stress, Strain and Shear Force

Both magnetostriction and the Villari effect are properties of magnetic materials that involve mechanical principles for their characterisation. The most essential concepts in mechanical engineering are stress and strain. The explanation of these concepts can be performed by considering a straight structural member, initially of constant cross sectional area throughout its length, been subjected to an axial force (Figure 2.1)[1].

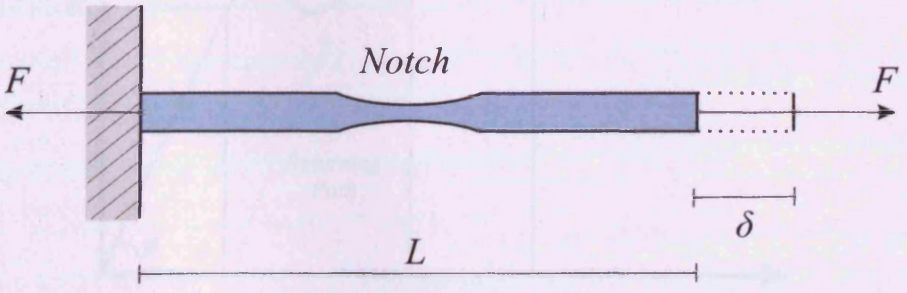

Figure 2.1: Member subjected to a tensile force with a notch forming during elongation[1].

[1] G. S. Katranas, "Design and Development of Bilayer Sensor Systems for Biomedical and Automotive Applications", Ph.D. Thesis, Cardiff University.

Disregarding the own weight of the bar, an assumption is made that the only force acting on it is the axial force, F (N). This force is resisted by internal forces which are called stresses which do not allow the bar to move in the direction of the force. Stress is force per unit area and it is symbolised as σ (Pa). The external force F is in equilibrium with the forces that are acting inside the member. The summation of internal stresses is equal to σ times A, where A is the cross-sectional area (m^2) of the member. For equilibrium[1]:

$$\sigma \cdot \mathrm{A} = F \Rightarrow \sigma = \frac{F}{A} \qquad 2\text{-}1$$

When a member is subjected to stress a deformation (in this case a notch) will take place causing the member to change in length. The elongation, δ (m), is the cumulative result of stretching all elements of the bar. The elongation per unit length, ℓ, is the strain, ε and can be written as[1]:

$$\varepsilon = \frac{\delta}{\ell} \qquad 2\text{-}2$$

By drawing a diagram of stress versus strain various conclusions can be made regarding the behaviour of material under an applied load (Figure 2.2)[1].

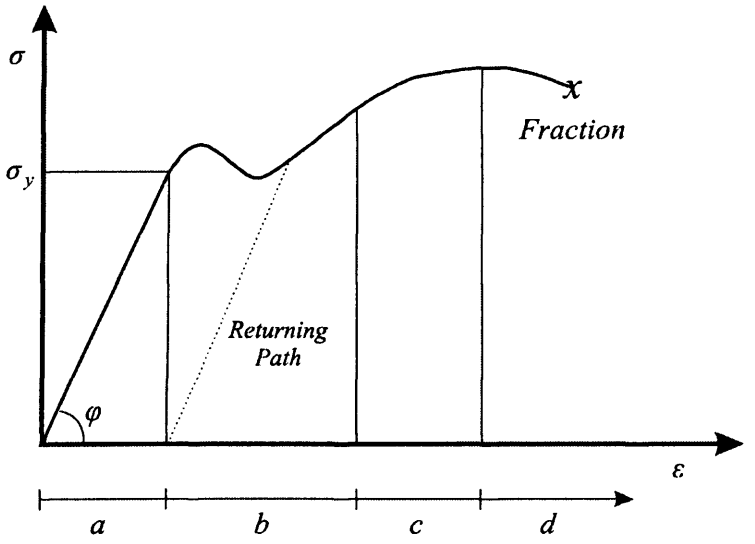

Figure 2.2: Stress-strain diagram[1].

G. S. Katranas, "Design and Development of Bilayer Sensor Systems for Biomedical and Automotive Applications", Ph.D. Thesis, Cardiff University.

a. Elastic region: In this region the relationship between stress and strain is expressed by a constant. This constant is the modulus of elasticity, E (Pa), (Young's modulus) and it is defined via Hooke's law[1]:

$$\frac{\sigma}{\varepsilon} = E = \tan\varphi \qquad 2\text{-}3$$

b. Plastic region: When the stress increases beyond σ_y (yield stress) the material enters in to the second region which is called plastic region. Here small increments in σ, i.e. F, produce large increments in ε.

c. Strain hardening region: In this region greater increase in σ is needed to produce greater amount of ε.

d. Fracture region: The last region is where the material eventually breaks and has a parabolic line. This parabolic line is due to the fact that the denominator in Eq. 2-1 is theoretically kept constant through out the application of the external force F, when in fact the area A decreases creating a notch.

If the force was to be removed the following would be observed:

i. Elastic region: The member will return to its original condition.

ii. All the other regions: The member is permanently deformed (in this case elongated) and the returning path will be parallel to the path of the elastic region, with zero strains. By re-applying the member with a new force, it will follow the returning path. Thus, the σ_y increases but the material becomes more brittle and much less ductile.

Stresses that act tangential to the surface of the material are called shear stresses (as seen in Figure 2.3)[2]. Assuming that a force F is acting on the surface of the bar and that F' and F'' are in equilibrium ($F' = F''$), then the force F will "try" shear apart the bar. Therefore the bar at plane aa' suffers in shear, hence developing shear stresses which must balance the shear force F. Thus, if the shear area is A and the shear force is F then the shear stress, τ (Pa), is expressed as[2]:

G. S. Katranas, "Design and Development of Bilayer Sensor Systems for Biomedical and Automotive Applications", Ph.D. Thesis, Cardiff University.

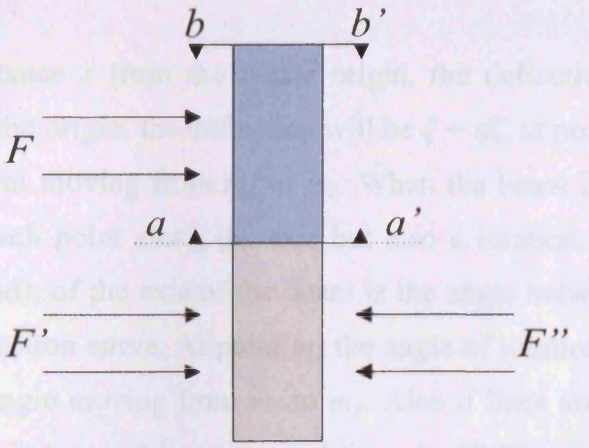

Figure 2.3: Shear stress on a member[2].

$$\tau = \frac{F}{A} \qquad 2\text{-}4$$

2.2 Deflection and Stress in Cantilever Beams

When a concentrated load is acting upward at the free end of a cantilever beam, its axis will deform into a curve (Figure 2.4). The resulting stresses in the beam are related to the curvature of the deflection curve. If the loads acts on the *x*-*y* plane of symmetry of the beam then the deflection, ζ, is the displacement of the beam, in the direction where the load is applied (*y* direction in this case).

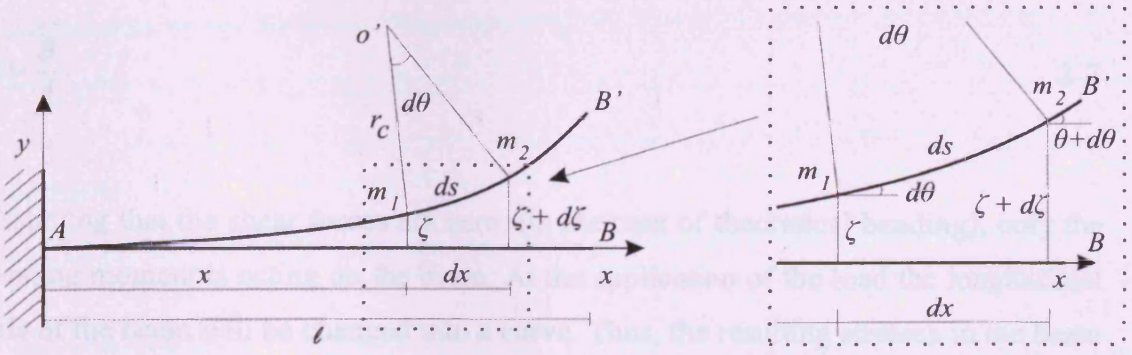

Figure 2.4: Deflection of a cantilever beam under the application of a concentrated load at the free end[2, 3].

At point m_1, at a distance x from the x-axis origin, the deflection will be ζ. In a distance $x + dx$, from the origin, the deflection will be $\zeta + d\zeta$, at point m_2, where $d\zeta$ is the deflection increment moving from m_1 to m_2. When the beam is bent there is not only a deflection at each point along the axis but also a rotation. For point m_1, the angle of rotation, θ (rad), of the axis of the beam is the angle between the x-axis and the tangent to the deflection curve. At point m_2 the angle of rotation is $\theta + d\theta$, where $d\theta$ is the increase in angle moving from m_1 to m_2. Also if lines are drawn normal to the tangents, the angle between the two normal lines, is $d\theta$. The point of intersection of those two lines is the centre of curvature o' and the distance from o' to the curve is the radius of curvature, r_c (m/rad). These are related as:

$$r_c \cdot d\theta = ds \qquad 2\text{-}5$$

where the ds (m) is the distance along the deflection curve between points m_1 and m_2. This leads to the definition of curvature[3], c (rad/m):

$$c = \frac{1}{r_c} = \frac{d\theta}{ds} \qquad 2\text{-}6$$

In the case of a cantilever beam with a constraint at one end and a force applied at the free end (as in Figure 2.4) Equation 2-6 can be written as:

$$c = \frac{\theta}{\ell} \qquad 2\text{-}7$$

Assuming that the shear forces are zero, (in the case of theoretical bending), only the bending moment is acting on the beam. At the application of the load the longitudinal axis of the beam will be changed into a curve. Thus, the resulting stresses in the beam are directly related to the curvature of the deflection curve. During the deflection of the beam the elements on the convex side of the beam lengthen as a result of a tensile

longitudinal force and the elements on the concave side shorten due to a compressive longitudinal force (Figure 2.5)[3].

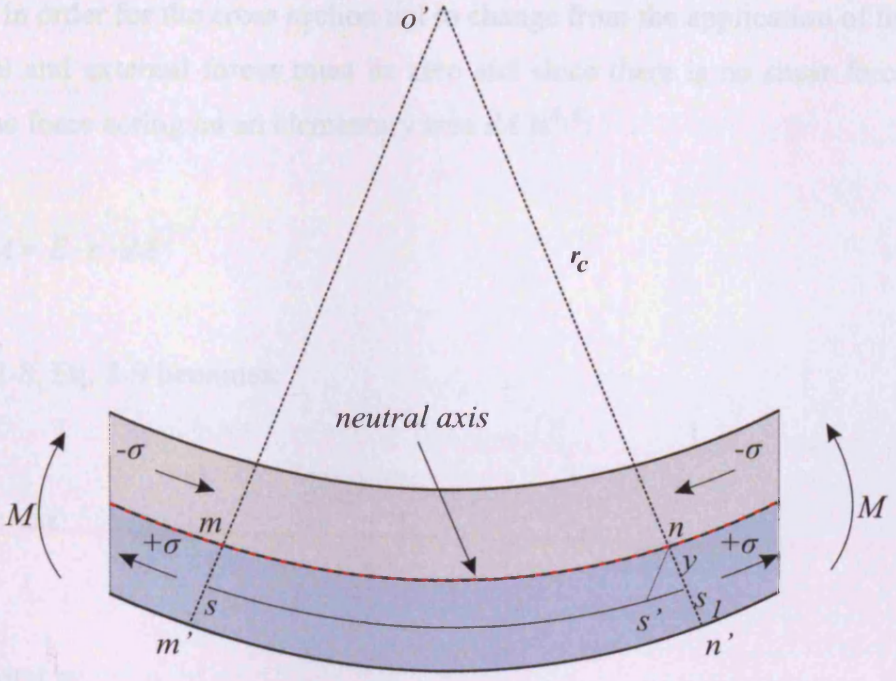

Figure 2.5: Stresses in beams[4].

Through the beam cross section there is a neutral axis where elements are neither longer nor shorter and hence there is no stress and strain present. The stresses and strains in the beam are proportional to the distance from the neutral axis. Thus, the maximum stresses and strains arise at the greatest distance in the cross section from the neutral axis. By considering the deformation of the beam over the cross section, the distribution of the internal forces can be calculated. If the beam has a rectangular cross section and two adjacent vertical lines *mm'* and *nn'* are drawn on its sides (see Figure 2.5), it can be found that during bending these lines will remain straight and will rotate so as to be perpendicular to the longitudinal axis of the beam. By using the theorem in geometry of the similarity of triangles ns_1s' and $o'nm$ the following can be written[4]:

$$\varepsilon = \frac{\delta}{\lambda} = \frac{s's_1}{ss'} = \frac{s's_1}{mn} = \frac{ns_1}{o'n} = \frac{y}{r_c} \qquad 2\text{-}8$$

G. S. Katranas, "Design and Development of Bilayer Sensor Systems for Biomedical and Automotive Applications", Ph.D. Thesis, Cardiff University.

It can be seen that the longitudinal strains are proportional to the distance, y (m), from the neutral axis or the neutral surface and inversely proportional to the radius of curvature. In order for the cross section not to change from the application of the force the internal and external forces must be zero and since there is no shear forces then $\Sigma F = 0$. The force acting on an elementary area dA is[4, 5]:

$$dF = \sigma \cdot dA = E \cdot \varepsilon \cdot dA \qquad 2\text{-}9$$

From Eq. 2-8, Eq. 2-9 becomes:

$$dF = \frac{E}{r_c} \cdot y \cdot dA \qquad 2\text{-}10$$

Thus, the total is:

$$F = \int \frac{E}{r_c} \cdot y \cdot dA \Rightarrow F = \frac{E}{r_c} \int y \cdot dA = 0 \qquad 2\text{-}11$$

For Eq. 2-11 to be equal to zero either:

$$\frac{E}{r_c} = 0 \qquad 2\text{-}12$$

or

$$\int y \cdot dA = 0 \qquad 2\text{-}13$$

Of course $E/r_c \neq 0$, hence in this case the x-axis (the centroidal axis) is the axis where Eq. 2-13 is equal to zero and therefore the neutral axis passes through the centroid of

the cross section. The stresses on the beam have a resulting internal moment, M_{int} (N·m):

$$dM_{\text{int}} = \sigma \cdot dA \cdot y \qquad 2\text{-}14$$

From Eq. 2-3 and Eq. 2-8:

$$\sigma = E \cdot \frac{y}{r_c} \qquad 2\text{-}15$$

So Equation 2-14 becomes:

$$dM_{\text{int}} = \frac{E}{r_c} \cdot y \cdot y \cdot dA = \frac{E}{r_c} \cdot y^2 \cdot dA \Rightarrow M_{\text{int}} = \frac{E}{r_c} \int y^2 \cdot dA \qquad 2\text{-}16$$

The internally applied moment, M_{int}, must be equal to its producer, which is the externally applied bending moment, M. The integral in Eq. 2-16 is defined as the area moment of inertia, In (m^4). The area moment of inertia is a tool, a mathematical expression rather than a physical representation which was introduced by Euler in the early 19th century. It is defined as the product of the area times the square of the distance of the area from the reference axis. For the area in Figure 2.6 the moment of inertia around a reference $\acute{y}$-axis parallel to the y-axis will be[5]:

$$dIn_{y'} = (d + x)^2 \cdot dA = d^2 \cdot dA + x^2 \cdot dA + 2 \cdot x \cdot d \cdot dA \Rightarrow$$

$$In_y = d^2 \int dA + \int x^2 \cdot dA + 2 \cdot d \cdot \int x \cdot dA = d^2 \cdot A + In_y + In_c \qquad 2\text{-}17$$

where In_y and In_c are the moment of inertia and the first moment of area respectively about the y-axis. If the *y-axis* is passing through the centroid of the area then In_c and In_y become equal to zero.

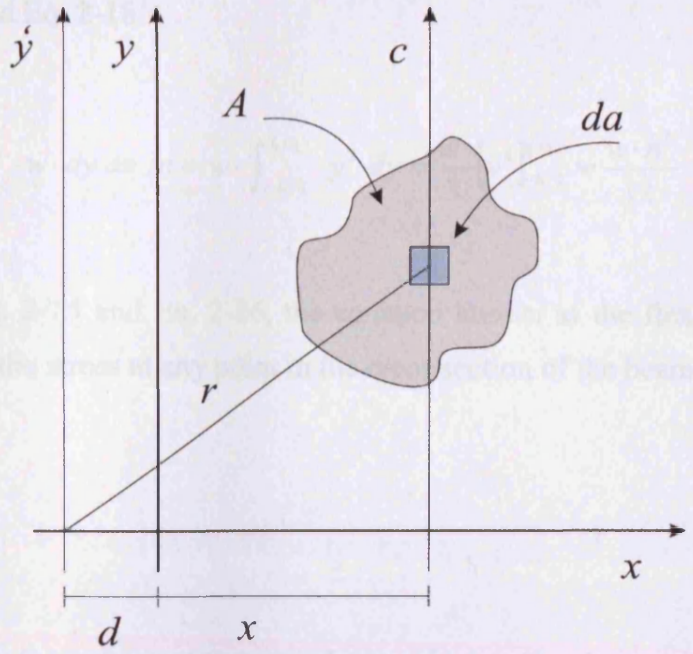

Figure 2.6: Calculation of inertia[5].

Thus, for a rectangular parallelogram, (of width w (m) and height h (m)), with regard to the x-axis and y-axis passing through the centroid (Figure 2.7)[6]:

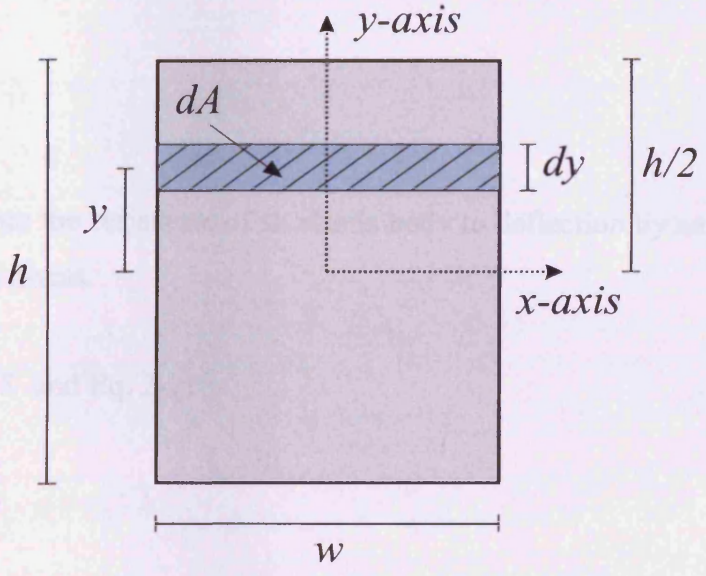

Figure 2.7: Calculation of area moment of inertia for a rectangular parallelogram[6].

$$dA = w \cdot dy \qquad 2\text{-}18$$

From Eq. 2-17 and Eq. 2-18[7]:

$$dIn = y^2 \cdot dA = y^2 \cdot w \cdot dy \Rightarrow In = w \cdot \int_{-h/2}^{h/2} y^2 \, dy = \frac{w}{3}\left[y^3\right]_{-h/2}^{h/2} = \frac{w \cdot h^3}{12} \qquad 2\text{-}19$$

By combining Eq. 2-15 and Eq. 2-16, the equation known as the flexure formula, is found that shows the stress at any point in the cross section of the beam:

$$\sigma = \frac{M \cdot y}{In} \qquad 2\text{-}20$$

From this equation it can be seen that in order to calculate the stresses in the beam, the parameters under consideration are the geometry of the cross section, the distance along the cross section from the neutral axis and the externally applied moment.

Thus, Equation 2-16 can be written as[8]:

$$\frac{1}{r_c} = \frac{M}{E \cdot In} \qquad 2\text{-}21$$

The $E \cdot In$ term states the resistance of an elastic body to deflection by an applied force and it is termed stiffness.

Combining Eq. 2-5 and Eq. 2-21:

$$d\theta = \frac{M}{E \cdot In} \cdot ds \qquad 2\text{-}22$$

Since the two adjacent cross sections m_1 and m_2, (in Figure 2.4), are very close, and $d\theta$ is very small then $ds \approx dx$. Hence:

G. S. Katranas, "Design and Development of Bilayer Sensor Systems for Biomedical and Automotive Applications", Ph.D. Thesis, Cardiff University.

$$d\theta = \frac{M}{E \cdot In} \cdot dx \Rightarrow \Theta = \int_A^B \frac{1}{E \cdot In} \cdot M \cdot dx = \frac{1}{E \cdot In} \int_0^\ell F \cdot (\ell - x) \cdot dx = \frac{F \cdot \ell^2}{2 \cdot E \cdot In} \qquad 2\text{-}23$$

The deflection, ζ, is measured along BB' (Figure 2.4) and is equal to:

$$d\zeta = (x + dx) \cdot d\theta = x \cdot d\theta + \underbrace{dx \cdot d\theta}_{\approx 0} = x \cdot \frac{M}{E \cdot In} dx \qquad 2\text{-}24$$

This can be written as[9]:

$$\zeta = \int_A^B x \cdot \frac{M}{E \cdot In} dx = \frac{1}{E \cdot In} \int_0^\ell x \cdot F \cdot (\ell - x) \cdot dx = \frac{F \cdot \ell^3}{3 \cdot E \cdot In} \qquad 2\text{-}25$$

2.3 Elastic Strain Energy

When a load (tensile, compressive or bending) is applied on a piece of material, within its elastic region, it is deformed; the work done is stored as energy. After the removal of the loading, the material will return to its initial state as a result of the releasing of the stored energy. This energy is called elastic strain energy (J) and it is stated as[10, 11]:

$$Work\ done = W = \frac{1}{2} F \cdot \delta \qquad 2\text{-}26$$

The stored energy per unit volume is:

$$U' = \frac{Work\ done}{Volume} = \frac{1}{2} \cdot \frac{F \cdot \delta}{A \cdot \ell} \qquad 2\text{-}27$$

From Eq. 2-3 and Eq. 2-8, Eq. 2-27 becomes an equation that shows the relationship between the energy stored and the stress applied to the member[10, 11]:

$$U' = \frac{1}{2} \cdot \sigma \cdot \varepsilon = \frac{1}{2} \cdot \frac{\sigma^2}{E} = \frac{1}{2} \cdot E \cdot \varepsilon^2 \qquad 2\text{-}28$$

2.4 Cantilever n[th]-layer Beams

The moment-curvature relationship (Eq. 2-21) for a composite beam of n^{th} layers can be determined from the condition that the moment resultant of the bending stresses is equal to the bending moment acting at the cross section[12, 13].

$$M = M_1 + M_2 + \cdots + M_n = \frac{E_1 \cdot In_1}{r_c} + \frac{E_2 \cdot In_2}{r_c} + \cdots + \frac{E_n \cdot In_n}{r_c} =$$

$$= \frac{E_1 \cdot In_1 + E_2 \cdot In_2 + \cdots + E_n \cdot In_n}{r_c} \qquad 2\text{-}29$$

In order to calculate the moment of inertia of each layer, the distance, d, between the neutral axis and the centroid of each layer needs to be determined (Appendix A). The general formula that defines the distance d is[14]:

$$d_n = \frac{\sum_n (\xi_n \cdot \Delta A_n)}{\sum_n \Delta A_n} \qquad 2\text{-}30$$

where ξ_n is the distance from the centroid of the layer in question to the centroid of reference layer n and A_n is the cross sectional area of layer n.

The bending stress (Eq. 2-15) in the composite beam will be the sum of the stresses of each material:

$$\sigma_t = \sigma_1 + \sigma_2 + \cdots + \sigma_n = \frac{E_1 \cdot y}{r_c} + \frac{E_2 \cdot y}{r_c} + \cdots + \frac{E_n \cdot y}{r_c} \qquad 2\text{-}31$$

From equations 2-29 and 2-31 the bending stress equation for a composite beam can be found[15]:

$$\sigma_t = M \cdot y \cdot \left(\frac{E_1 + E_2 + \cdots + E_n}{E_1 \cdot In_1 + E_2 \cdot In_2 + E_n \cdot In_n} \right) \qquad 2\text{-}32$$

In the case of the deformation of composite or multi-layer beams the stiffness of the structure will change. This can be seen from combining Eq. 2-25 and Eq. 2-29:

$$\zeta = \frac{F \cdot \ell^3}{3 \cdot (E_1 \cdot In_1 + E_1 \cdot In_1 + \cdots + E_n \cdot In_n)} \qquad 2\text{-}33$$

2.5 Brief Principles of Fluid Mechanics

Solid, liquid and gas are the three states of matter. Liquids and gases both share the common properties of fluids; they lack the ability of solids to resist a deforming force. For as long as the force is applied fluids will flow under the action of such forces deforming continuously. Liquids and gases also have many distinctive characteristics of their own. Liquids are usually regarded as incompressible. A set mass of liquid occupies a fixed volume, irrespective of the size of its container and in the case where the volume of the container is greater than that of the liquid, a free surface is formed. Unless restrained by a vessel, a given mass of gas will have no fixed volume and will continuously expand filling any vessel in which it is placed without forming a free surface[16, 17]. In gases the molecules are in constant, random motion colliding frequently with the walls of the containing vessel and each other. During the collisions a change in velocity and therefore a change in the momentum of the molecules take place. The measure of the average linear momentum of the moving molecules is the pressure, P (Pa), of the gas. Although pressure itself is a scalar quantity, it can be defined as the force, with a direction perpendicular to the surface, times the surface area. If a gas is static and not flowing, the measured pressure, static

pressure P_s, is the same in all directions. But if the gas is moving, the measured pressure depends on the direction of motion[18]:

$$P_t = P_s + q = P_s + \frac{\rho \cdot u^2}{2} \qquad 2\text{-}34$$

This is Bernoulli's equation for incompressible flow. The dynamic pressure, q, is a property of a moving flow of gas that depends on the density, ρ, and the velocity, u, of the gas[18].

When a fluid flows over a solid surface the velocity of the part of fluid in contact with that boundary will stick to it, and will, therefore have the same velocity as that boundary. This is the non-slip condition of fluid mechanics. Moving away from the boundary the velocity of the successive layers of fluid will increase, mainly as a result of viscosity. Shear stresses will therefore develop between the layers of fluid moving with different velocities. Mathematically this can be described by Figure 2.8 that represents an element of fluid (*abcd*) in a tube under the application of a force, F[16].

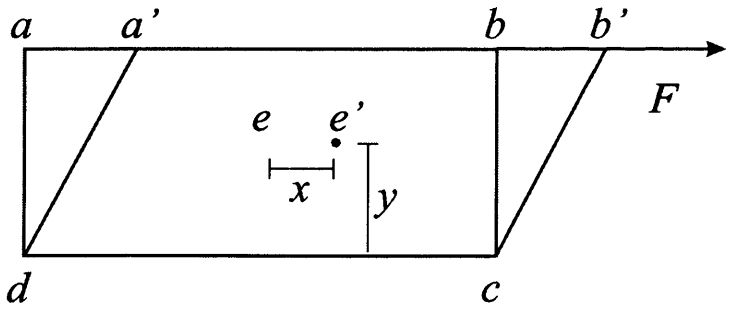

Figure 2.8: Flow of a fluid particle in a tube[16].

The force per unit area is the shear stress, τ, which is proportional to the deformation, γ, (shear strain). Since solids can permanently resist shear stresses, γ, will be a fixed quantity for a given τ. In the case of fluids, γ will continue to increase with time, hence the fluid will flow (*a'b'cd*). If a particle at a radial distance $\acute{r}$ from *dc* (the tube wall) moves a distance x from point *e* to *e'*, then at small angles the shear strain will be $\gamma = x/\acute{r}$. The velocity of the particle will be $u = x/t$, hence the rate of shear strain is

$= x/\dot{r} \cdot t = u/\dot{r}$, which is the change of velocity with $\dot{r}$ and can be re-written as *du/dy*. Assuming that the shear stress is proportional to the shear strain, then[19]:

$$\tau = v_d \cdot \frac{du}{d\dot{r}} \qquad 2\text{-}35$$

The term v_d (Pa·s) is the constant that depends on the fluid under consideration and is known as the dynamic viscosity of the fluid. This equation is Newton's law of viscosity and it shows that the velocity of fluid increases as we move away from the boundary, i.e. the tube wall. The force balance due to pressure difference at $\dot{r}$ over a tube length ℓ is[19]:

$$\pi \cdot \dot{r}^2 \cdot \Delta P = 2 \cdot \pi \cdot \dot{r} \cdot \ell \cdot \tau \qquad 2\text{-}36$$

Combining equations 2-35 and 2-36:

$$\pi \cdot \dot{r}^2 \cdot \Delta P = 2 \cdot \pi \cdot \dot{r} \cdot \ell \cdot v_d \cdot \frac{du}{d\dot{r}} \Rightarrow \frac{du}{d\dot{r}} = \frac{\dot{r} \cdot \Delta P}{2 \cdot \ell \cdot v_d} \qquad 2\text{-}37$$

Solving for u:

$$u = \frac{\Delta P}{2 \cdot v_d \cdot \ell} \cdot \int_{\dot{r}}^{r} \dot{r} \cdot d\dot{r} = \frac{1}{4} \cdot \frac{\Delta P}{v_d \cdot \ell} \cdot (r^2 - \dot{r}^2) = u_{\max}\left(1 - \left(\frac{\dot{r}}{r}\right)^2\right) \qquad 2\text{-}38$$

Where u is the fluid velocity at the radial point $\dot{r}$, r is the radius of the tube, and u_{max} is the maximum velocity, located at the axis of the tube. This equation gives a parabolic profile of u across the tube[19]. From the parabolic profile of fluid velocity in a tube the nature of fluid motion and the interactions between fluid particles can be described. Flow profiles can be separated to categories depending on the velocity of the fluid; laminar when the velocity is low and turbulent when it is high. In the laminar flow, the layers of fluid present smooth flow patterns without any fluid particle mixing (at

the macroscopic level). In the turbulent flow, fluid velocities are higher and particles move at all angles forming unstable patterns. The transition from laminar to turbulent flow in tubes is a function of the fluid velocity, dynamic viscosity and tube diameter, *dm* and is defined as:

$$R_e = \frac{u \cdot dm}{\nu_d} \qquad 2\text{-}39$$

where R_e is the Reynolds number. In a straight tube when the Reynolds number is less than 2100 the flow is considered laminar and when it exceeds 4000 the flow is turbulent. The flow between these two values is referred to as the transition region where motion can be either laminar or turbulent[19, 20].

2.6 Summary

A brief overview of the physics involved was given in this Chapter. This is important as it gives an understanding of how an applied force can deform (deflect) and stress the bilayer strip and also how the size and number of layers affect its mechanical characteristics. The effect of the force on internal stresses of the material is where the universality of the bilayer sensor lies. Applications involving displacement, force, fluid flow or generally curvature change of the bilayer strip due to bending, are related to the creation of internal stresses and hence changes in the structure of the material.

References

[1] P. P. Benham et al et al, "Mechanics of engineering materials", Longman: Harlow, 1996, Ch. 3, pp. 64-68.
[2] S. P. Timoshenko et al, "Mechanics of materials", PWS Publishing: Boston, 1997, Ch. 1, pp. 27-34.
[3] W. H. Bowes et al, "Mechanics of engineering materials", Wiley: New York, 1984, Ch. 3, pp. 151-157.
[4] S. P. Timoshenko et al, "Mechanics of materials", PWS Publishing: Boston, 1997, Ch. 5, pp. 303-317.
[5] S. P. Timoshenko et al, "Mechanics of materials", PWS Publishing: Boston, 1997, Ch. 12, pp. 811-819.
[6] P. P. Benham et al, "Mechanics of engineering materials", Longman: Harlow, 1996, App. A, pp. 598-606.
[7] W. H. Bowes et al, "Mechanics of engineering materials", Wiley: New York, 1984, Ch. 2, pp. 100-104.
[8] R. C. Stephens, "Strength of materials: theory and examples", Edward Arnold: London, 1970, Ch. 5, pp. 81-82.
[9] R. J. Roark, "Formulas for stress and strain", McGraw-Hill: London, 1975, Ch. 7, pp. 89-112.
[10] S. P. Timoshenko et al, "Mechanics of materials", PWS Publishing: Boston, 1997, Ch. 2, pp. 110-116.
[11] P. P. Benham et al, "Mechanics of engineering materials", Longman: Harlow, 1996, Ch. 3, pp. 75-76.
[12] S. P. Timoshenko et al, "Mechanics of materials", PWS Publishing: Boston, 1997, Ch. 6, pp. 391-398.
[13] R. J. Roark, "Formulas for stress and strain", McGraw-Hill: London, 1975, Ch. 7, pp. 112-115.
[14] R. L. Mott, "Applied strength of materials", Prentice-Hall: Englewood Cliffs, 1976, Ch. 8, pp. 179-184.
[15] R. L. Mott, "Applied strength of materials", Prentice-Hall: Englewood Cliffs, 1976, Ch. 4, pp. 71-73.
[16] J. F. Douglas et al, "Fluid Mechanics", Longman: Harlow, 1995, Ch. 1, pp. 3-6.
[17] N. P. Cheremisinoff, "Practical fluid mechanics for engineers and scientists", Technomic Publications Co: Lancaster, 1990, Ch. 1, pp. 21-25.
[18] J. F. Douglas et al, "Fluid Mechanics", Longman: Harlow, 1995, Ch. 5, pp. 134-136.
[19] R. Baker, "An introductory guide to industrial flow", Mechanical Engineering Publication Ltd: London, 1996, Ch. 3, pp. 53-61.
[20] N. P. Cheremisinoff, "Practical fluid mechanics for engineers and scientists", Technomic Publications Co: Lancaster, 1990, Ch. 5, pp. 124-125.

Chapter 3 Magnetostriction and Amorphous Metallic Alloys

3.1 Basic Principles of Magnetics

The generation of a magnetic field, H (A/m), takes place when an electrical charge is in motion due to the flow of an electrical current, I (A), flowing through a conductor. In the case of a infinetly long circular conductor (solenoid) of N turns and ℓ length, the relationship between the magnetic field and the current is given by:

$$H = N\frac{I}{\ell} \qquad 3\text{-}1$$

The intensity of the magnetic field at any point in the magnetic field is a measure of the force exerted on an electrical charge moving through the field. When the current generates the field H in a medium, such as air, then the response of the medium is defined as its flux density, B (T). The relationship between B and H is stated as[1,2]:

$$B = \mu \cdot H \qquad 3\text{-}2$$

where the permeability, μ, denotes the "easiness" of magnetisation of a medium in the presence of a magnetic field. In the case of a ferromagnetic medium Eq. 3-2 becomes[2]:

$$B = \mu_0(H + M') \qquad 3\text{-}3$$

where μ_0 is a constant, referred to as the permeability of free space and it is equal to $\mu_0 = 4\pi \cdot 10^{-7}$ (H/m) and M' (A/m) is the magnetisation of the magnetic material and it is defined as the atomic magnetic moments, m_m, per unit volume, V[1,2]:

$$M' = \frac{m_m}{V} \qquad 3\text{-}4$$

The relationship between the magnetisation and the magnetic field is given by[1, 2]:

$$M' = x' \cdot H \qquad 3\text{-}5$$

where x' is the magnetic susceptibility of the material. By substituting Eq. 3-5 into Eq. 3-3[1, 2]:

$$B = \mu_0 H + \mu_0 x' H = \mu_0 (1 + x') H \qquad 3\text{-}6$$

The term $(1+x') = \mu_r$, where the term μ_r is the permeability of the ferromagnetic medium and termed relative permeability[1, 2]. Comparing Eq. 3-2 with Eq. 3-6 the permeability μ is expressed as[1, 2]:

$$\mu = \mu_0 \cdot \mu_r \qquad 3\text{-}7$$

There is another way of expressing flux density by the number of flux lines, Φ (Wb), passing through a unit area, A,[1, 2]:

$$B = \frac{\Phi}{A} \qquad 3\text{-}8$$

When the magnetic flux, Φ, changes with time ($d\Phi/dt$) it can induce an electro-motive force (*e.m.f.*), which in turn cause a current to flow through a coil of N turns, in a direction that opposes the flux. The induced *e.m.f.* can be expressed in volts by:

$$v = -N \frac{d\Phi}{dt} \qquad 3\text{-}9$$

Combining Eq. 3-8 and Eq 3-9 it can be seen that a time dependant magnetic induction can generate an electric current:

$$v = -NA\frac{dB}{dt} \qquad 3\text{-}10$$

Expanding Eq. 3-2 with Eq. 3-1 and Eq. 3-7:

$$B = \mu \cdot H = \mu_0\mu_r \cdot H = \mu_0\mu_r \cdot \frac{N \cdot I}{\ell} \qquad 3\text{-}11$$

From Eq. 3-11 the rate of change of flux density is:

$$\frac{dB}{dt} = \mu_0\mu_r \cdot \frac{N}{\ell} \cdot \frac{dI}{dt} \qquad 3\text{-}12$$

Substituting Eq. 3-12 into Eq. 3-10:

$$v = -\mu_0\mu_r \cdot \frac{N^2 A}{\ell} \cdot \frac{dI}{dt} \qquad 3\text{-}13$$

The rate of change of current in a coil results in the generation of an *e.m.f.* and the relationship between them is[3]:

$$v = -L\frac{dI}{dt} \qquad 3\text{-}14$$

where L (H) is the inductance of the coil that opposes the change of current. The dependence of inductance on the permeability of the medium, the number of turns and the dimensions of the coil can be seen by merging Eq. 3-13 and Eq. 3-14:

$$-L\frac{dI}{dt} = -\mu_0\mu_r \cdot \frac{N^2 A}{\ell} \cdot \frac{dI}{dt} \Rightarrow L = \mu_0\mu_r \cdot \frac{N^2 A}{\ell} \qquad 3\text{-}15$$

3.2 Magnetostriction

3.2.1 Principles of Magnetostriction

The electron revolution around its self and about the nucleus of the atom is conducted in a clockwise or anticlockwise direction depending on the placement of the electrons in the atom. It is these spin motions of electrons in an atom that are responsible for the magnetic moments and hence magnetisation[4]. A simple illustration of the relationship between magnetostriction and spin-orbit coupling is shown in Figure 3.1.

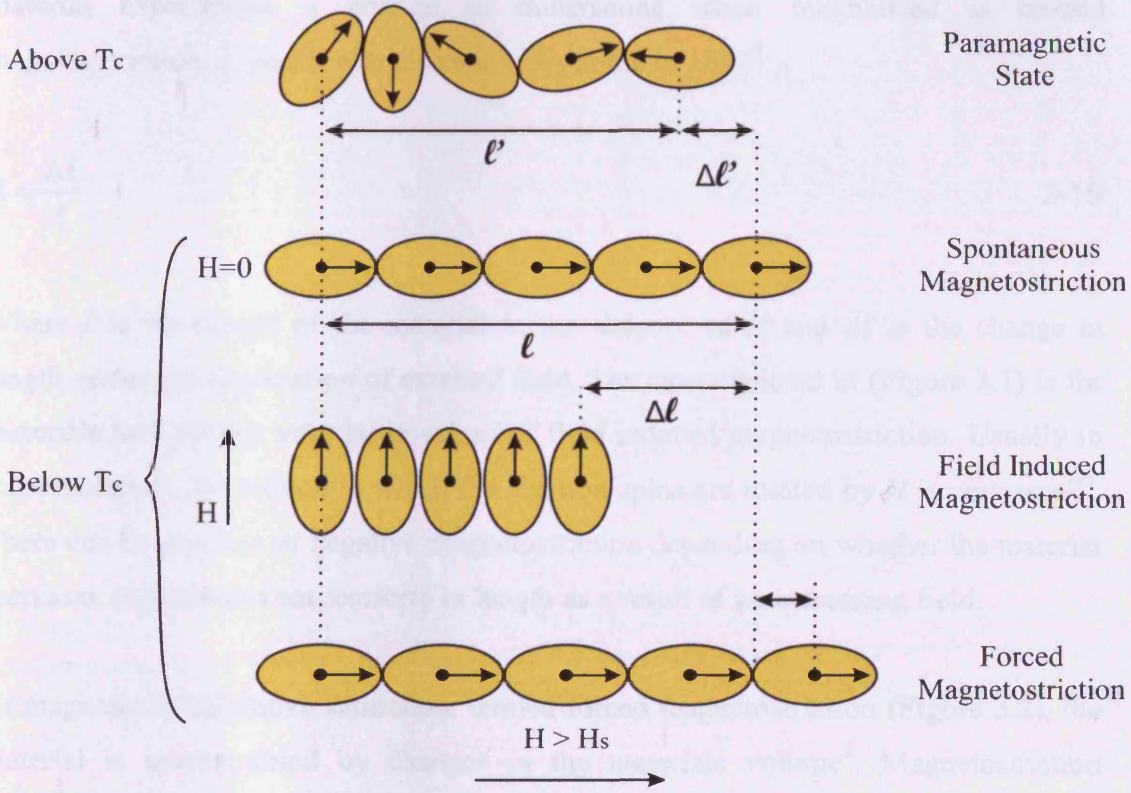

Figure 3.1: Mechanism of magnetostriction[5].

In the diagram the black dots depict the atomic nuclei, the arrows show the net magnetic moment per atom and the oval lines represent the electron cloud of each nucleus, distributed non-spherically around it[5]. The exchange interaction between two neighbouring spins is opposed by the thermal agitation of the atoms caused by the increase in temperature[5]. Thus, when the material is heated above its Curie

G. S. Katranas, "Design and Development of Bilayer Sensor Systems for Biomedical and Automotive Applications", Ph.D. Thesis, Cardiff University.

temperature, T_c, the magnetic moments become randomly oriented (Figure 3.1). The spontaneous magnetisation occurring below T_c, during the cooling of the material, rotates the spins and the electron clouds into an ordered state.

The magnetic alignment of atoms takes place within small volumes or domains of the bulk material. In an un-magnetised sample, the net magnetisation of the specimen within the bulk material is zero[6, 7]. The ordering of the magnetic moments has the effect of increasing the distance between adjacent atomic nuclei. Thus, the original length, ℓ' of the sample will become $\ell'+\Delta\ell' = \ell$. If a strong magnetic field is applied vertically the electron clouds will rotate into the direction of the magnetisation vector, reducing the distance between the atomic nuclei by $\Delta\ell$. The phenomenon were by a material experiences a change in dimensions when magnetised is termed magnetostriction, λ, and it was discovered by Joule in 1842[5]:

$$\lambda = \frac{\Delta\ell}{\ell} \qquad 3\text{-}16$$

Where ℓ is the length of the material in the absence of H and $\Delta\ell$ is the change in length under the application of external field. The case depicted in (Figure 3.1) is for materials that exhibit very large values of field induced magnetostriction. Usually in most materials, the extend to which the electron spins are rotated by H is very small[5]. There can be positive or negative magnetostriction depending on whether the material increases or decreases respectively in length as a result of an increasing field.

At magnetic fields above saturation, termed forced magnetostriction (Figure 3.2), the material is accompanied by changes in the materials volume[5]. Magnetostriction depends greatly on the internal structure of the magnetic material. When the spins inside a domain with a magnetisation are either parallel or anti-parallel to the external field it is said that they are in an easy direction towards the field, [100], and they do not experience any rotational force. If the spins inside the domain make some angle with the field direction (Figure 3.3a), then they start to rotate towards the field direction. The spin rotation will result in an increase in the volume of the domain at the expense of other domains with magnetisation at an angle to the external field.

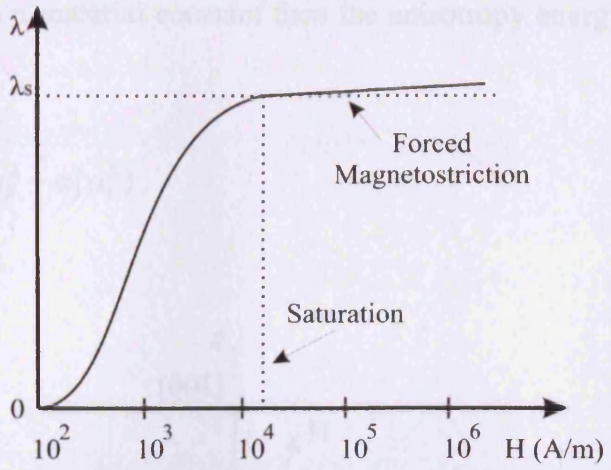

Figure 3.2: Variation of magnetostriction with field strength[7].

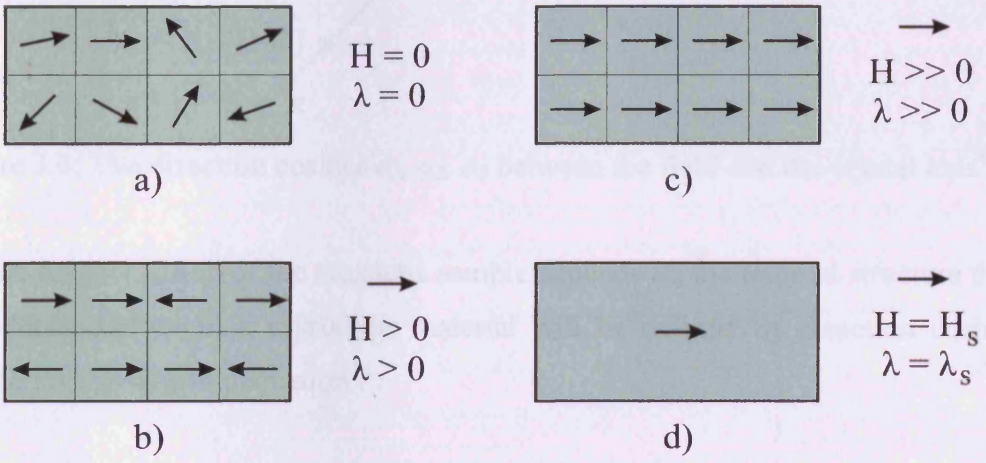

Figure 3.3: The effect of field to the domain magnetisation[8].

As the magnetisation increases the domains with magnetisation at an angle to the external field will start to rotate (Figure 3.3b, c) and finally merge with the domains that are parallel to *H* (Figure 3.3d). When the additional increase in external field results in no further changes in the magnetisation of the material then this is condition is termed saturation magnetisation. Magnetisation in directions at an angle to the easy axis will require larger fields to attain saturation magnetisation, hence requiring larger amounts of energy. This energy is known as magnetic anisotropy energy[9]. If the material in question is a cubic crystal then this energy can be expressed containing the direction cosines between the field and the crystal axis (Figure 3.4). Assuming that the field makes angles *a*, *b*, *c* with the crystal axis, α_1, α_2, α_3 are the cosines of these

G. S. Katranas, "Design and Development of Bilayer Sensor Systems for Biomedical and Automotive Applications", Ph.D. Thesis, Cardiff University.

angles and K_1 (J/m^3) a material constant then the anisotropy energy, W_K (J/m^3), will be[4]:

$$W_K = K_1(\alpha_1^2\alpha_2^2 + \alpha_2^2\alpha_3^2 + \alpha_3^2\alpha_1^2) \qquad 3\text{-}17$$

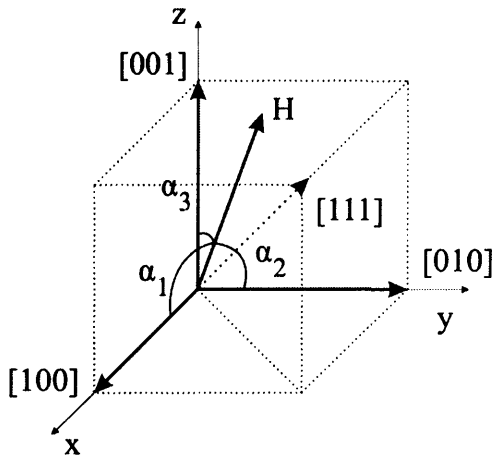

Figure 3.4: The direction cosines α_1, α_2, α_3 between the field and the crystal axis[4].

Since the magnetisation of the magnetic sample depends on the internal structure then the magnetostriction in a crystalline material will be defined by direction cosines using the Becker-Doring equation[5]:

$$\lambda_s = \frac{3}{2}\lambda_{100}\left(\alpha_1^2\beta_1^2 + \alpha_2^2\beta_2^2 + \alpha_3^2\beta_3^2 - \frac{1}{3}\right) +$$

$$+ 3\lambda_{111}(a_1a_2\beta_1\beta_2 + a_2a_3\beta_2\beta_3 + a_3a_1\beta_3\beta_1) + \cdots \qquad 3\text{-}18$$

where λ_{100} and λ_{111} are the saturation magnetostrictions (induced strain) conventionally measured when the crystal is magnetised in directions [100] and [111] respectively and $\beta_1, \beta_2, \beta_3$ are the cosines of the angles between λ_s and the crystal axis. In the case where the strain is in the same direction as the magnetic field Eq. 3-18 will be reduced to[5]:

$$\lambda_s = \lambda_{100} + 3(\lambda_{111} - \lambda_{100})(\alpha_1^2\alpha_2^2 + \alpha_1^2\alpha_2^2 + \alpha_1^2\alpha_2^2) \quad 3\text{-}19$$

In the case of isotropic materials ($\lambda_s=\lambda_{100}=\lambda_{111}$) Eq. 3-18 can be further simplified:

$$\lambda_\theta = \frac{3}{2}\lambda_s\left(\cos^2\theta - \frac{1}{3}\right) \quad 3\text{-}20$$

where λ_θ is the saturation magnetostriction at and angle θ to the direction of the magnetic field.

3.2.2 Inverse Magnetostriction

Villari in 1864 found that when a stress is applied the direction of domain magnetisation changes due to the externally induced magnetostriction; this phenomenon is termed inverse magnetostriction. This in turn affects magnetic properties such as permeability. The elastic elongation of a magnetic material produces a change in permeability in the direction of the applied force. A material with positive λ will show an increase in its permeability under tensile stress where as a negative magnetostriction will display a decrease in its μ[13]. Taking as an example a material with positive magnetostriction it can be seen that when the sample is magnetised with a field H_1 (along [100]) at $\sigma_1 = 0$, it has a magnetostriction value λ_1. If a tensile force is applied (along [100]) at $\sigma_2 > \sigma_1$, the magnetisation of the sample increases to $H_2 > H_1$. For this process to take place the material must posses some magnetisation because no change in H will take place if the material is stressed in a demagnetised state[7].

In the case of inverse magnetostriction the energy, W_i (J/m^3), which governs the direction of magnetisation will be influenced by the material's magnetostriction and anisotropy[7]:

$$W_i = K_1(\alpha_1^2\alpha_2^2 + \alpha_2^2\alpha_3^2 + \alpha_3^2\alpha_1^2) - \frac{3}{2}\lambda_{100}\sigma(\alpha_1^2\alpha_2^2 + \alpha_2^2\alpha_3^2 + \alpha_3^2\alpha_1^2) -$$

$$-3\lambda_{111}\sigma(\alpha_1\alpha_2\gamma_1\gamma_2 + \alpha_3\alpha_2\gamma_3\gamma_2 + \alpha_1\alpha_3\gamma_1\gamma_3)\cdots \qquad 3\text{-}21$$

where the second and third term in the equation are the magnetostriction energy, W_λ (J/m^3), of the cubic crystal that arises under the application of a uniform stress to the material and γ_1, γ_2, γ_3 are the direction cosines between the stress and the crystal axis[10]. If the material is isotropic, the first part of the equation can be omitted and both λ_{100} and λ_{111} will be substituted by λ_s. Eq. 3-21 then is simplified to[5]:

$$W_i = W_\lambda = -\frac{3}{2}\lambda_s \cdot \sigma \cdot \cos^2\theta \qquad 3\text{-}22$$

where θ is the angle between the magnetisation and the applied stress.

3.2.3 Magneto-mechanical Effect

The magneto-mechanical effect is the phenomenon where the mechanical stresses are interconnected with the change in magnetisation. The applied field is producing magnetostriction on the material, elongating or contracting it depending on the sign of λ. This deformation is the result of the rotation of magnetisation inside the material[11]. The change in dimensions is caused by the rotation of the magnetisation or displacement of 90° domain walls. The application of stress has an effect on the magnetisation of the magnetic material. In the case of a positive magnetostrictive material, stress will increase the magnetisation M' and raise μ[8]. Mathematically the stresses, the applied field and magnetostriction are related by[12, 13]:

$$\sigma = \frac{(M_s')^2}{3\mu_0\mu_r\lambda_s} \qquad 3\text{-}23$$

3.3 Amorphous Metallic Alloys

The bilayer sensors use as their operating principle the inverse magnetostrictive effect. Since the demand is that the sensor is sensitive, robust, reliable and compact, the magnetic material that is used should have such qualities as to favourably exploit the operating principle. Amorphous alloys posses a unique set of magnetic and mechanical properties that make them near ideal in stress/displacement sensors. Due to the lack of crystal structure, near isotropic at the macroscopic level, the magnetostriction of amorphous alloys is the same in all directions[13]. Amorphous is derived from the Greek word "morphe", which means "form" or "shape". Thus, the word "a-morphous" means without form or shape. Amorphous are materials that have not got any ordered crystalline structure (at the macroscopic level) (Figure 3.5).

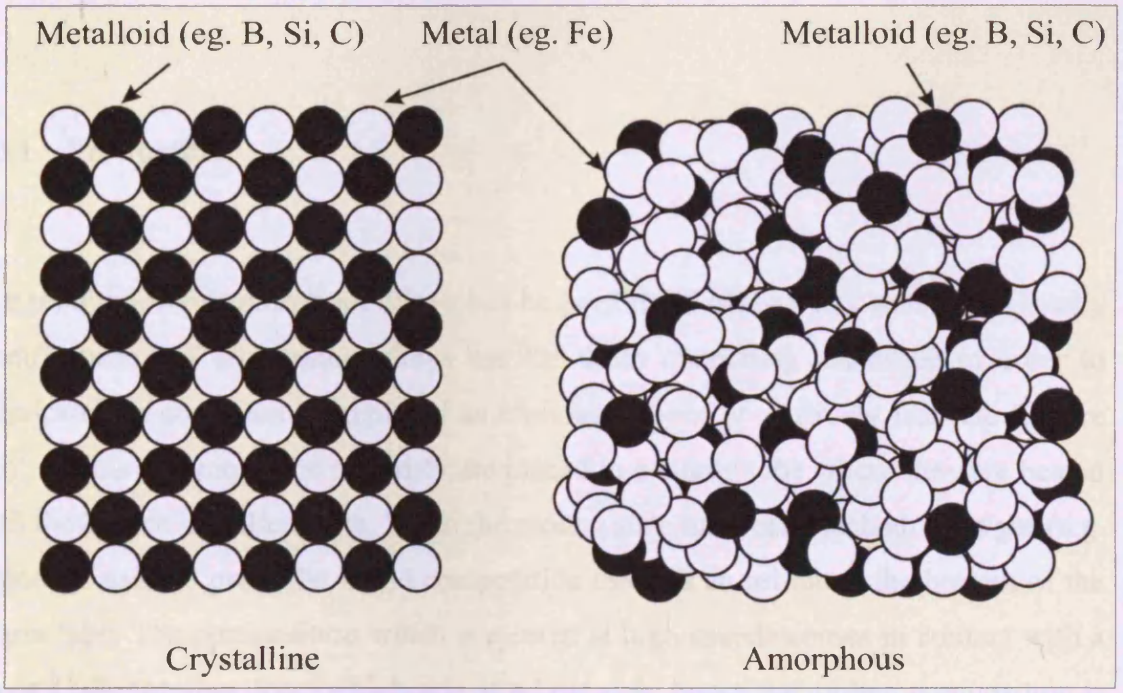

Figure 3.5: The order of individual atoms in the crystalline and amorphous structure[14].

The amorphous state forms mostly by controlling the rate at which the molten alloy composition is cooled. When the material is still in liquid state the atoms and molecules have enough thermal energy to move randomly in any direction. Any temperature decrease is accompanied by a reduction in the mobility of the atoms and hence an increase in the viscosity of the substance[7]. One of the characteristics of the

G. S. Katranas, "Design and Development of Bilayer Sensor Systems for Biomedical and Automotive Applications", Ph.D. Thesis, Cardiff University.

amorphous alloy compositions is the fact that they exhibit large viscosity changes over narrow temperature intervals. It is these large changes in viscosity that causes the alloy to turn into a rigid glass at certain temperature. At this temperature the atoms have their mobility reduced at such extent that they are restrained from forming a crystalline structure. In other words the molten alloy is cooled so rapidly (at least at 10^6 K/s), that its atoms become frozen in their liquid configuration[7].

If the alloy was then heated back to a liquid state and then cooled down at a slower rate then the alloy would form a crystalline structure. Amorphous alloys can be created using a number of possible chemical compositions. The principle composition of ferromagnetic amorphous alloys is M_xS_{100-x} where M represents one or more metals such as *Fe*, *Co* and *Ni*, S represents one or more metalloids (semiconductors) and x is the metallic atomic percentage in the composition ($70\ \% < x < 86\ \%$)[7].

3.3.1 Production

The production of amorphous alloys can be performed using many methods. Usually manufacturers of amorphous alloys use the drum quenching technique in order to mass-produce continuous lengths of amorphous ribbons at relatively fast rate (Figure 3.6)[7]. In this technique the materials are placed in a quartz tube where they are heated until they reach a molten state. When the molten state has been reached, inert gas (e.g. Argon) is used to press the liquid composition through an orifice at the bottom of the quartz tube. The composition which is ejected at high speeds comes in contact with a *Cu* or *CuBe* rotating drum which acts as a heat sink; hence the molten composition is quenched from its liquid phase to an amorphous state. These amorphous ribbons can then be cut to the desirable size and agglutinated (using a Cyanoacrylate adhesive) on a non-magnetic foil in order to create the bilayer strip that is used in the sensors.

These strips have been developed with thickness of the order of tens of micrometers. One of the disadvantages of such bilayers is the production process i.e. the agglutination. The agglutination layer effectively forms a third layer (thickness ~75

G. S. Katranas, "Design and Development of Bilayer Sensor Systems for Biomedical and Automotive Applications", Ph.D. Thesis, Cardiff University.

μm) which can be detriment to the overall performance of the sensor. These problems can be avoided if a different bilayer manufacturing process, as well as the amorphous material production, is used[7].

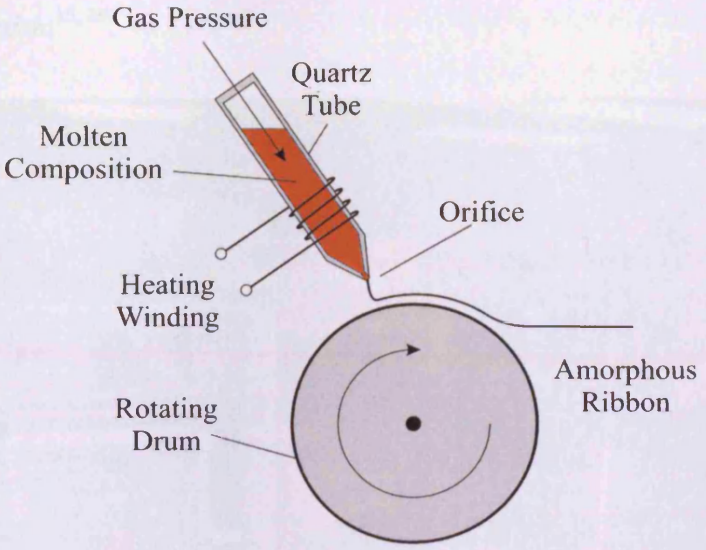

Figure 3.6: Production of amorphous ribbon by drum quenching[7].

The alternative method is the thin film deposition process such as the *RF* sputtering technique[15, 16]. In this process the magnetic films are grown by *RF* magnetron sputter deposition on a 3 inch diameter (76.2 mm) non-magnetic substrate (*AlMg* or *CuBe*)[17]. The target materials used were Metglas® 2605SC and 2705M (Appendix E) as seen in Table 3.1[18, 19].

Material	**Metglas® 2605SC**	**Metglas® 2705M**	
Metglas® Composition	$Fe_{81}B_{13.5}Si_{3.5}C_2$	$Co_{69}B_{12}Si_{12}Fe_4Mo_2Ni_1$	
Metglas® Magnetostriction	($\lambda_s \approx 30 \cdot 10^{-6}$)	($\lambda_s \approx 0$)	
Metglas® Thickness (μm)	2.9	5	2.9
Substrate	*CuBe*	*CuBe*	*AlMg*
Substrate Thickness (μm)	25	25	30
Bilayer Fabrication	*RF*	*RF*	*RF*

Table 3.1: Characteristics of the bilayer strip materials manufactured with the *RF* sputtering technique[18, 19].

The bilayer strips were grown using the thin film magnetron sputtering system at Cardiff University (Figure 3.7). The base pressure of the sputtering chamber was 67

G. S. Katranas, "Design and Development of Bilayer Sensor Systems for Biomedical and Automotive Applications", Ph.D. Thesis, Cardiff University.

μPa (0.5 μTorr), and using a sputtering power of 75 W and a pressure of 0.53 Pa (4 mTorr) of argon which produced a deposition rate of 0.1 nm/sec (Appendix E)[17]. The thickness of each film was measured in situ by a thin film thickness sensor. The disadvantage of this method is that it is a very slow fabrication technique which is not for mass-production[15, 20].

Figure 3.7: The thin film magnetron sputtering system at Cardiff University[17].

3.3.2 Properties

The magnetic properties of amorphous alloys present them as the obvious choice for use in bilayer sensors. Because of the amorphous structure, (near isotropic at the macroscopic level), the magneto-crystalline anisotropy is almost non-existent[7]. Hence no extra energy is required to shift the magnetic moments towards the direction of stress or the magnetic field. However a small uni-axial anisotropy exists along the ribbon axis due to residue stresses during the manufacturing process (drum quenching

G. S. Katranas, "Design and Development of Bilayer Sensor Systems for Biomedical and Automotive Applications", Ph.D. Thesis, Cardiff University.

technique). This can be removed through annealing; heating the material to achieve stress relief at temperatures around 150 °C – 250 °C[7]. Another interesting property of amorphous alloys is that their relative permeability can be much larger than conventional ferromagnetic materials. This means that under the same stress, a material with higher μ_r will induce more H in comparison with a material with lower relative permeability[7]. As far as magnetostriction amorphous materials exhibit a range of λ_s values, from 0 to $40 \cdot 10^{-6}$ (approximately). Since the operating principle of these samples is the magnetostrictive effect, high values of λ_s are desirable, which prompts to the selection of Iron-based amorphous alloys[7, 14].

The bilayer sensors robustness relies mainly on the mechanical properties of the amorphous materials used. The high values of the Young's modulus and the high tensile strength of the amorphous alloys give the material a significantly increased elastic limit. This ensures that amorphous alloys can withstand high stresses and strains without incurring any plastic deformation. Another advantage of using amorphous alloys as the magnetic material in bilayer sensors is because they exhibit large bending fatigue limits. This makes certain that the material will withstand continuous cyclic motion without incurring fatigue as early as crystalline material[7, 21].

3.4 Summary

The amorphous magnetic materials that are used in these sensors tend to exhibit "sensitivity" to applied stress. When a bilayer sensor is physically bent at its free end, tensile stress develops along its length. This results in changes in the magnetisation of the strip and hence influences the relative permeability of the material. These changes are detected by a pick-up coil, wound around one end of the bilayer sensor, which produces the sensor signal as a result of changes in the inductance, ΔL. Thus, the change in ΔL corresponds to the displacement of the free end of the bilayer sensor. These materials also posses good mechanical properties such as high values of the modulus of elasticity and increased elastic limit. Thus, amorphous alloys can withstand high stresses and exhibit large bending fatigue limits.

References

[1] D. C. Jiles, "Introduction to magnetism and magnetic materials", Chapman and Hall: London, 1998, Ch. 1, pp. 3-32.
[2] H. Oduncu, "Development of amorphous magnetostrictive sensors with application to monitoring of fracture healing", Cardiff University, Ph.D. Thesis, 1997, Ch. 1, pp. 1-7.
[3] P. Horowitz, "The art of electronics", Cambridge University Press: Cambridge, 1989, Ch. 1, pp. 28-35.
[4] L. Hon Fai, "Magnetic domains observation in structural steels under stress", Cardiff University, Ph.D. Thesis, 1995, Ch. 1, pp. 1-34.
[5] B. D. Cullity, "Introduction to magnetic materials", London: Addison-Wesley, 1972, Ch. 8, pp. 248-284.
[6] R. Lassow, "Novel shock and vibration transducers using amorphous materials", Cardiff University, Ph.D. Thesis, 1995, Ch. 1, pp. 10-15.
[7] P. Choudhary, "Magnetostrictive accelerometer using amorphous metallic alloy" , Cardiff University, Ph.D. Thesis, 1995, Ch. 2, pp. 35-47.
[8] R. M. Bozorth, "Ferromagnetism", IEEE Press: New Jersey, 1993, Ch. 13, pp. 595-712.
[9] S. Chikazumi, "Physics of magnetism", Krieger: New York 1978, Ch. 6, pp. 113-126.
[10] M. Hardcastle, "Development of a non-contact amorphous magnetostrictive torque sensor", Cardiff University, Ph.D. Thesis, 1995, Ch. 3, pp. 33-40.
[11] S. Chikazumi, "Physics of magnetism", Krieger: New York, 1978, Ch. 19, pp. 431-437.
[12] M. Hardcastle, "Development of a non-contact amorphous magnetostrictive torque sensor", Cardiff University, Ph.D. Thesis, 1995, Ch. 3, pp. 46-50.
[13] R. Boll et al, "Sensors: a comprehensive survey", VCH: Weinheim, 1989, Ch. 4, pp. 98-102.
[14] N. Derebasi, "Effect of tension and surface properties on magnetic domains and power loss in amorphous ribbons", Cardiff University, Ph.D. Thesis, 1994, Ch. 2, pp. 18-27.
[15] D. A. Glocker et al, "Handbook of thin film process technology", Institute of Physics Publications: Philadelphia, 1995, Ch. A3.0, pp. 1-15.
[16] M, Watts et al, "The use of stress for the control of magnetic anisotropy in amorphous FeSiBC thin films: a magneto-optic study", Journal of Magnetism and Magnetic Materials Vol. 190, 1998, pp. 199-204.
[17] Thin film magnetron sputtering system manual, Kurt J. Lesker Inc., Clairton, PA, 2003.
[18] 2605SC Magnetic Alloy Data Sheet, Metglas Inc., Conway, SC, 2004.
[19] 2705M Magnetic Alloy Data Sheet, Metglas Inc., Conway, SC, 2004.
[20] A. Wagendristel et al, "An introduction to physics and technology of thin films", World Scientific Publishing, London, 1994, Ch. 2, pp31-40.
[21] N. Derebasi, "Effect of tension and surface properties on magnetic domains and power loss in amorphous ribbons", Cardiff University, Ph.D. Thesis, 1994, Ch. 2, pp. 18-27.

Chapter 4 Signal Modulation and Processing

4.1 Why Modulate?

The modulation of the information signal in communication engineering is performed in order to convert the message into a form suitable for propagation over the transmitting medium[1]. Signal transmission over appreciable distance always involves a travelling electromagnetic wave, with or without a guiding medium. The efficiency of any particular transmission method also depends upon the frequency (Hz) of the signal being transmitted. By exploiting the frequency translation property of continuous wave modulation, (sinusoidal carrier modulation), the message information can be impressed on a carrier whose frequency has been selected for the desired transmission method. This efficiency can be made apparent by comparing modulated and unmodulated signal transmission. Unmodulated transmission of an audio signal contains frequency components of around 100 Hz (average male human voice frequency)[2], where as in frequency modulation (*FM*) broadcasting transmissions can be around 100 MHz. Taking into consideration that the efficient line-to-sight ratio propagation requires antennas that are at least 1/10 to 1/2 of the signals wavelength and that the wavelength and transmission frequencies are related by[2]:

$$Wavelength = 300 / frequency \text{ (MHz)} \qquad 4\text{-}1$$

then for the unmodulated transmission, a 300 km long antenna is needed in contrast with the *FM* broadcasting where only 1 m antenna can be used[2].

The modulation and demodulation of information signals is a concept borrowed from communication engineering and applied to magnetic sensors technology not to transmit information over a distance, but in order to detect displacement. When a bilayer sensor is physically bent at its free end (Figure 4.1), stresses, σ, develop along its length.

G. S. Katranas, "Design and Development of Bilayer Sensor Systems for Biomedical and Automotive Applications", Ph.D. Thesis, Cardiff University.

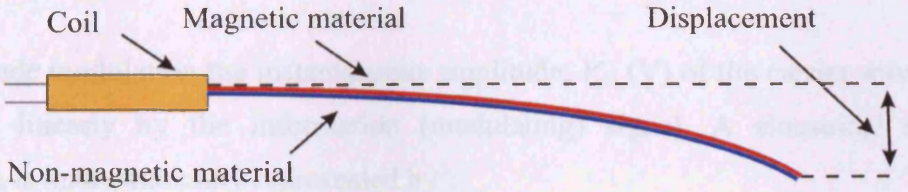

Figure 4.1: Bilayer sensor physically bend at its free end.

This results in changes in the relative permeability, μ_r, of the material. These changes are detected by a pick-up coil, wound around one end of the bilayer sensor, which produces the sensor signal as a result of changes in the inductance (H), ΔL, and hence its reactance X_L [3, 4]. Thus, the change in ΔL corresponds to the displacement of the free end of the bilayer sensor. As part of an electronic circuit the bilayer sensor, acts as an inductor, L. Any changes ΔL may influence the alternating current (AC) that is used to excite the magnetic material, (Chapter 3), hence the properties of the output voltage signal. The main reason why AC is used is that in DC the excitation of L is non existent since the inductance depends on a time varying current. In principle DC excitation can be used to detect magnetisation dependence in stress but the output will be an extremely low-amplitude AC signal superimposed on DC, which would be very difficult to detect especially in the presence of noise.

When the displacement signal is conveyed through changes of the output waveform in amplitude, phase or frequency then the corresponding modulation scheme is amplitude (AM), phase (PM) or frequency (FM) respectively.

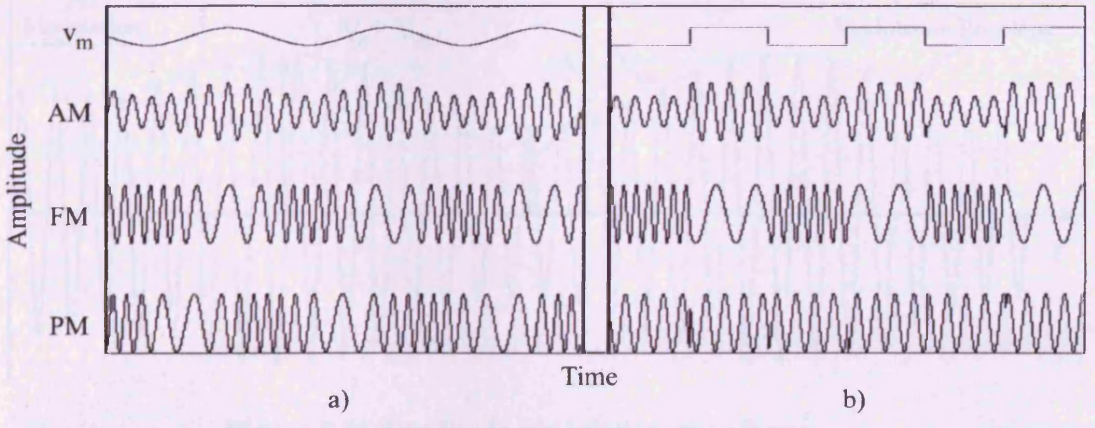

Figure 4.2: Classic AM, FM and PM waveforms under a) sine or b) square v_m.

4.2 Amplitude Modulation

In amplitude modulation the instantaneous amplitude, V_c, (V) of the carrier waveform is varied linearly by the information (modulating) signal. A sinusoidal carrier waveform is mathematically represented by[5]:

$$v_c = V_c \cdot \cos(\omega_c \cdot t + \phi) \xrightarrow{\phi=0} v_c = V_c \cdot \cos(\omega_c \cdot t) \qquad 4\text{-}2$$

where the angular frequency $\omega_c = 2\pi f_c$, f_c is the carrier frequency (Hz) and ϕ is the phase. If the modulating signal has the form of:

$$v_m = V_m \cdot \cos(\omega_m \cdot t + \phi) \xrightarrow{\phi=0} v_m = V_m \cdot \cos(\omega_m \cdot t) \qquad 4\text{-}3$$

where the angular frequency $\omega_m = 2\pi f_m$, f_m is the frequency of the information signal and ϕ is the phase, then the *AM* waveform is[5]:

$$v_{AM} = [V_c + V_m \cdot \cos(\omega_m \cdot t)] \cdot \cos(\omega_c \cdot t) \qquad 4\text{-}4$$

When plotting Eq. 4-4 it can be seen that the amplitude of the modulated carrier varies sinusoidally between the values of $V_c + V_m$ and $V_c - V_m$ (Figure 4.3).

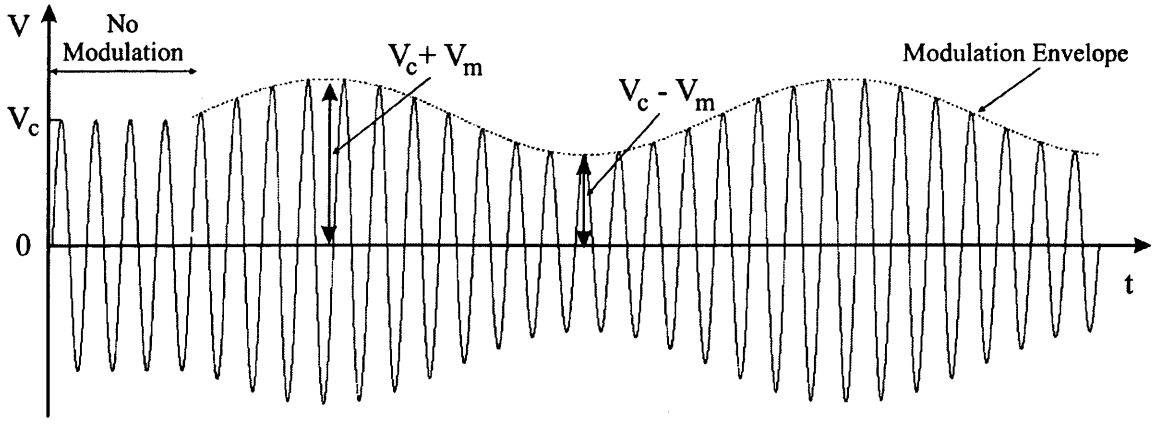

Figure 4.3: Amplitude modulation waveform[5].

G. S. Katranas, "Design and Development of Bilayer Sensor Systems for Biomedical and Automotive Applications", Ph.D. Thesis, Cardiff University.

If

$$\frac{V_m}{V_c} = m_{AM} \qquad 4\text{-}5$$

where m_{AM} is the modulation depth, then the *AM* waveform becomes:

$$v_{AM} = V_c \cdot \cos(\omega_c \cdot t) + m_{AM} \cdot V_c \cdot \cos(\omega_m \cdot t) \cdot \cos(\omega_c \cdot t) \qquad 4\text{-}6$$

From trigonometry:

$$\cos(A) \cdot \cos(B) = \frac{1}{2} \cdot [\cos(A+B) + \cos(A-B)] \qquad 4\text{-}7$$

Hence, from Eq. 4-6, Eq. 4-7 becomes[5]:

$$v_{AM} = V_c \cdot \cos(\omega_c \cdot t) + \frac{m_{AM} \cdot V_c}{2} \cdot \cos[(\omega_m + \omega_c) \cdot t] + \frac{m_{AM} \cdot V_c}{2} \cdot \cos[(\omega_m - \omega_c) \cdot t] \qquad 4\text{-}8$$

Equation 4-8 shows that the *AM* carrier wave contains three frequency components. The first term is the carrier waveform (Eq. 4-2). The second and third terms are the lower side frequency, *LSF*, and the upper side frequency, *USF*, respectively. The side frequencies are above and below the carrier frequency by an amount equal to f_m (Figure 4.4).

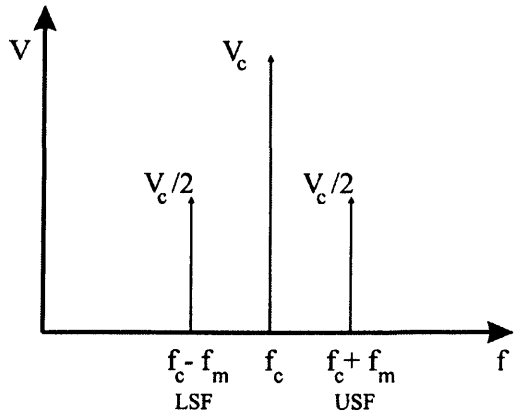

Figure 4.4: The *LSF* and *USF* when the modulation depth is equal to unity[5, 6].

All three terms are waveforms of different frequencies. Eq. 4-8 shows that energy is added to the carrier v_c in the form of the side frequencies. The information is contained in both side frequencies only and not in the carrier. The modulation factor is a measure of the amplitude of the information signal and at $m_{AM} = 1$ the amplitude of each side band becomes half the amplitude of the carrier ($V_c/2$). If the modulation depth is $m_{AM} = 1$, (100 % modulation), the peak to peak amplitude range of the composite waveform will be from $2 \cdot V_c$ to zero. The stronger the information signal is, the higher the modulation depth will be, but it should not exceed unity ($m_{AM} > 1$). This will lead to over modulation which will alter the modulation envelope and introduce a series of harmonics that will distort v_{AM} [5, 6].

4.3 Voltage-to-Current Converter (*VCC*)

Analogue voltage signals are susceptible to many factors, including the impedance of the wire that is used, the quality of the connections and in addition to that, voltage signals, especially small signals, are very susceptible to noise[7]. Converting voltage signals to current signals gets rid of these problems very easily. Once the signal is in current form, the impedance of the wire, the distance and the connection resistance do not change the current value[7]. The simplest way to convert voltage signals to current signals is by connecting a shunt resistor across the voltage source. Although this seems an ideal solution in reality it does not work because the signal source usually has high output impedance so it can not supply a lot of current[7]. In order to overcome the problem of high output impedance, an active circuit utilising an operational amplifier is used. An operational amplifier buffers the output of the signal source so that the current drained from the signal source is negligible. The operational amplifier instead provides the necessary current[7, 8]. An operational amplifier based voltage-to-current (*VCC*) circuit is shown in Figure 4.5.

The currents I_1 and I_2 are:

$$I_1 = \frac{V_1 - V_L}{R_4} \qquad 4\text{-}9$$

$$I_2 = \frac{V_2 - V_L}{R_4} \qquad 4\text{-}10$$

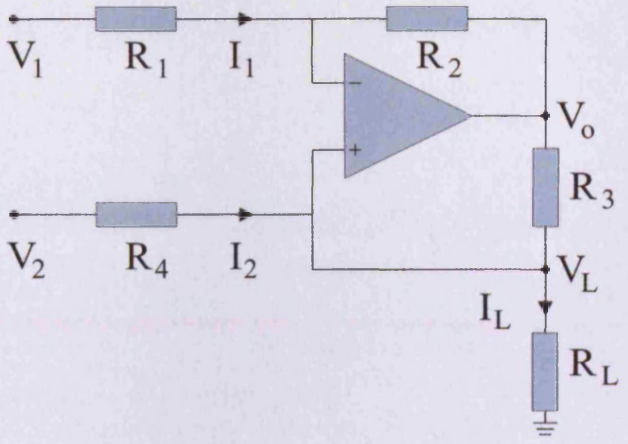

Figure 4.5: Operational amplifier based voltage-to-current converter[9].

The currents through the input leads of an unsaturated operational amplifier can be neglected (due to very high input impedance). For an ideal operational amplifier the inverting amplifier gain is given simply by:

$$\frac{V_1}{V_o} = -\frac{R_2}{R_1} \qquad 4\text{-}11$$

For I_L equations 4-9, 4-10 and 4-11 are combined to[9]:

$$I_L = \frac{V_2}{R_3} - \frac{V_L}{R_3} + \frac{R_1 \cdot V_1}{R_2 \cdot R_4} - \frac{R_1 \cdot V_L}{R_2 \cdot R_4} = \frac{V_2}{R_3} - \frac{R_1 \cdot V_L}{R_2 \cdot R_4} \cdot \frac{R_3}{R_3} + \frac{R_1 \cdot V_L}{R_2 \cdot R_4} - \frac{R_4}{R_4} \cdot \frac{V_L}{R_3} =$$

$$= \frac{1}{R_3} \cdot \left(V_3 - \frac{R_1}{R_2} \cdot \frac{R_3}{R_4} \cdot V_1 \right) + \frac{1}{R_4} \left(\frac{R_1}{R_2} - \frac{R_4}{R_3} \right) \cdot V_L \qquad 4\text{-}12$$

By making $R_1/R_2 = R_4/R_3 = n$, Eq. 4.2-4 can be written as:

$$I_L = \frac{1}{R_3} \cdot (V_2 - V_1) \qquad 4\text{-}13$$

Thus, a signal in current form and proportional to the input voltage difference is created. Obviously, grounding just one of the two voltage inputs makes either an inverting or a non-inverting *VCC*.

By replacing R_L (Ω) with the bilayer sensor in Figure 4.5, the resistive element of the inductor which is its reactance X_L, ($X_L = 2\pi f \cdot L$) will act as the load resistance of the *VCC*. Thus, the bilayer will be magnetised by a magnetic field, H, generated by the sinusoidal current i_L of constant amplitude I_L and frequency f in the pickup coil. As seen from Eq. 3-11, the magnetic field, B, depends on the permeability of the bilayer strip and the current i. The induced voltage, v_L, of the pickup coil is given by Eq. 3-13[10]:

$$v_L = -\mu_0 \mu_r \cdot \frac{N^2 A}{\ell} \cdot \frac{dI}{dt} \qquad 4\text{-}14$$

By displacing the free end of the bilayer strip or changing its curvature, v_L will change accordingly. The displacement information will be carried as changes of voltage amplitude of v_L; hence, amplitude modulation is achieved[10]

4.4 Angle Modulation

Angle modulation is the modulation in which the angle of a sinusoidal carrier is the parameter subject to variation. Considering Eq. 4-2:

$$v_c = V_c \cdot \cos(\theta_{PM}) = V_c \cdot \cos(\omega_i \cdot t + \phi_i) \qquad 4\text{-}15$$

It can be seen that the frequency of the carrier or its phase is also available for carrying information. Although frequency changes and phase changes are

G. S. Katranas, "Design and Development of Bilayer Sensor Systems for Biomedical and Automotive Applications", Ph.D. Thesis, Cardiff University.

synonymous there is a difference between what is known as frequency modulation and phase modulation[11, 12].

Phase modulation is angle modulation in which the phase of a sinusoidal carrier is caused to depart from the carrier phase by an amount proportional to the instantaneous value of the modulating waveform. The instantaneous phase must be linearly related to the amplitude of the modulating signal v_m:

$$\phi_i \cong \phi_c + v_m \qquad 4\text{-}16$$

therefore:

$$\theta_{PM} = \omega_c \cdot t + \phi_c + v_m \qquad 4\text{-}17$$

Substituting Eq. 4-17 to Eq. 4-15[11, 12]:

$$v_{PM} = V_c \cdot \cos\left(\omega_c \cdot t + \phi_c + k_p \cdot V_m \cdot \cos(\omega_m \cdot t)\right) = V_c \cdot \cos\left(\omega_c \cdot t + m_{PM} \cdot \cos(\omega_m \cdot t)\right) \qquad 4\text{-}18$$

where k_p is an arbitrary constant and m_{PM} is the modulation depth.

Frequency modulation is angle modulation in which the instantaneous frequency of a sinusoidal carrier is caused to depart from the carrier frequency by an amount proportional to the instantaneous value of the modulating waveform. The carrier frequency will vary by[12]:

$$f_i = f_c + v_m \qquad 4\text{-}19$$

In the unmodulated carrier the angular velocity moves constantly through a distance $\theta = \omega \cdot t$ in t seconds. When the carrier is frequency modulated the angular velocity is no longer constant. The angle of the carrier waveform will change according to[12]:

$$\theta_{FM} = \int \omega_i \cdot dt = \int 2 \cdot \pi \cdot f_i \cdot dt = \int 2 \cdot \pi \cdot [f_c + v_m] \cdot dt =$$

$$= 2 \cdot \pi \cdot f_c \cdot t + 2 \cdot \pi \cdot \int v_m \cdot dt \qquad 4\text{-}20$$

Combining Eq. 4-15 and Eq 4-20, the expression for the *FM* signal becomes:

$$v_{FM} = V_c \cdot \cos\left[\omega_c \cdot t + 2 \cdot \pi \cdot \int v_m \cdot dt\right]$$

$$= V_c \cdot \cos\left[\omega_c \cdot t + \frac{k_f \cdot V_m}{2 \cdot \pi \cdot f_m} \cdot \sin(\omega_m \cdot t)\right]$$

$$= V_c \cdot \cos[\omega_c \cdot t + m_{FM} \cdot \sin(\omega_m \cdot t)] \qquad 4\text{-}21$$

where m_{FM} is the modulation depth and k_f an arbitrary constant.

The relationship that differentiates *PM* from *FM* is the definition of instantaneous frequency. Instantaneous frequency is the rate of change of time of the angle of a sine wave function the argument of which is a function of time[12]:

$$angular\,frequency = \frac{d}{dt} angle \qquad 4\text{-}22$$

Applying Eq. 4-17 and Eq. 4-20 to Eq. 4-22[12]:

$$\frac{d}{dt}\left[2 \cdot \pi \cdot f_c \cdot t + \int v_m \cdot dt + \phi_c\right] = \omega_c + v_m + \phi_c \qquad 4\text{-}23$$

$$\frac{d}{dt}[2 \cdot \pi \cdot f_c \cdot t + v_m + \phi_c] = \omega_c + \frac{d}{dt} v_m + \phi_c \qquad 4\text{-}24$$

From Eq 4-23 it can be seen that in the *FM*, the deviation of the instantaneous frequency from its unmodulated value is proportional to the magnitude of the

modulating waveform, v_m. Whereas from Eq. 4-24 it is found that in a *PM* system the deviation of the instantaneous frequency from its unmodulated value is proportional to the magnitude of the derivative of the modulating waveform. Although *PM* and *FM* are forms of angle modulation they are not essentially different. In fact, *PM* and *FM* are inseparable in the sense that any variation of the phase of a sinusoidal carrier is accompanied by a frequency variation and similarly, any frequency change necessarily involves a phase change. Thus, the terms *PM* and *FM* merely indicate which parameter is made proportional to the modulating waveform and they represent two cases of the same type of modulation[12].

The *LSF* and *USF* of a *FM* or *PM* waveform can be found by expanding their equivalent expressions. Thus, for the *FM* (and similarly for *PM*)[12-14]:

$$v_{FM} = V_c \cdot \cos[\omega_c \cdot t + m_{FM} \cdot \sin(\omega_m \cdot t)] \qquad 4\text{-}25$$

Expanding Eq. 4-25 yields[12-14]:

$$v_{FM} = V_c \cdot \{ \cos(\omega_c \cdot t) \cdot \cos[m_{FM} \cdot \sin(\omega_m \cdot t)] - \sin(\omega_c \cdot t) \cdot \sin[m_{FM} \cdot \sin(\omega_m \cdot t)] \} \qquad 4\text{-}26$$

From trigonometry:

$$\cos[m_{FM} \sin(\omega_m \cdot t)] = J_0 \cdot m_{FM} + 2 \cdot J_2 \cdot m_{FM} \cos(2\omega_m \cdot t) + \ldots \qquad 4\text{-}27$$

$$\sin[m_{FM} \sin(\omega_m \cdot t)] = 2 \cdot J_1 \cdot m_{FM} \sin(\omega_m \cdot t) + 2 \cdot J_3 \cdot m_{FM} \sin(3\omega_m \cdot t) + \ldots \qquad 4\text{-}28$$

The coefficients $J_n \cdot m$ are called Bessel functions of the first kind and order n and can be written as:

$$J_n m = \left(\frac{m}{2}\right)^2 \left[\frac{1}{n} - \frac{(m/2)^2}{1!(n+1)!} + \frac{(m/2)^4}{2!(n+2)!} - \frac{(m/2)^6}{1!(n+3)!} + \cdots\right] \qquad 4\text{-}29$$

where m is the modulation depth of *PM/FM*. By combining Eq. 4-27 and Eq. 4-28 into Eq. 4-29[13, 14]:

$$v_{FM} = V_c\{J_0 m_{FM} \cdot \cos\omega_c t - J_1 m_{FM}\left[\cos(\omega_c - \omega_m)\cdot t - \cos(\omega_c + \omega_m)\cdot t\right] +$$

$$+ J_2 m_{FM}\left[\cos(\omega_c - 2\cdot\omega_m)\cdot t + \cos(\omega_c + 2\cdot\omega_m)\cdot t\right] + \ldots\} \qquad 4\text{-}30$$

which reveals an infinite set of side frequencies whose amplitudes are determined by the Bessel functions $J_0 m_{FM}$, $J_1 m_{FM}$ etc. When m_{FM} is small there are few side frequencies of large amplitude and when m_{FM} is large there are many side frequencies with smaller amplitudes[14]. The relative amplitude of the carrier $J_0 m_{FM}$ varies with the modulation depth and hence depends on the modulating signal. Thus, in contrast to *AM* the carrier frequency component of the *PM/FM* waveform contains part of the message information. The number of side frequencies having appreciable relative amplitude also depends on m_{FM}. With $m_{FM} << 1$ only J_0 and J_1 are significant, so the spectrum will consist of carrier and two side frequencies but if $m_{FM} >> 1$ there will be many side frequencies[13].

4.5 Oscillators

When the bilayer sensors are placed in an electrical circuit, they act as inductors whose reactance is varied during the displacement/stress of the bilayer strip. The generation of a *FM/PM* waveform can be performed using a device/circuit whose sinusoidal output will undergo a phase or frequency deviation proportional to the change in the sensor reactance. In communication engineering the most common way to generate a *FM/PM* waveform is by varying the reactance of the tuned circuit of an oscillator[15]. Oscillators are circuits that produce specific, periodic waveforms such as square, triangular, saw-tooth and sinusoidal. Operational amplifier (op-amp) oscillators are circuits that are intentionally designed to remain in an unstable or oscillatory state. Oscillators are useful for generating uniform signals that are used as a reference in applications such as audio, function generators and communication

systems. Op-amp sine-wave oscillators operate without an externally applied input signal. Instead a combination of positive and negative feedback is used to drive the op-amp into an unstable state, causing the output to cycle back and forth between the supply rails at a continuous rate. The frequency and amplitude of oscillation are set by the arrangement of passive and active components around the op-amp. The simplest form of a negative feedback system is used to demonstrate the requirements for oscillation to occur. Figure 4.6 shows the block diagram for this system in which V_{in} is the input voltage, V_{out} is the output voltage from the amplifier gain block A, and β is the signal, called the feedback factor, which is fed back to the summoning junction. Er represents the signal error term that is equal to the summation of the feedback factor and the input voltage[16]. The corresponding classical expression for a feedback system is derived as follows:

$$V_{out} = Er \cdot A \qquad 4\text{-}31$$

$$Er = V_{in} \cdot \beta \cdot V_{out} \qquad 4\text{-}32$$

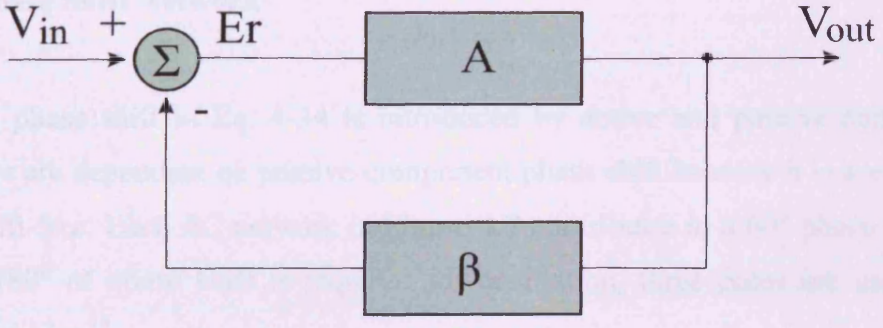

Figure 4.6: Canonical form of a feedback system[16].

By combining Eq. 4-31 and Eq. 4-32 [16]:

$$\frac{V_{out}}{A} = V_{in} - \beta \cdot V_{out} \Rightarrow V_{in} = V_{out} \cdot \left(\frac{1}{A} + \beta\right) \Rightarrow \frac{V_{out}}{V_{in}} = \frac{A}{1 + A \cdot \beta} \qquad 4\text{-}33$$

Oscillation results when the feedback system is not able to find a stable steady-state because its transfer function can not be satisfied. The system goes unstable when the

denominator in Eq. 4-33 becomes zero, i.e., when $1+A\beta = 0$ or $A\beta = -1$. The key to the oscillation is $A\beta = -1$. Satisfying this criterion requires that the magnitude of the loop gain is unity with a corresponding phase shift of 180^0 as indicated by the minus sign[16]:

$$A \cdot \beta = \angle -180^0 \qquad 4\text{-}34$$

As the phase shift approaches 180° and $|A\beta| \rightarrow 1$, the output voltage of the now unstable system tends to infinity but, is limited to finite values by the power supply (rail voltage). When the output voltage approaches either power rail, the active devices in the amplifiers change gain. This causes the value of A to change and forces $A\beta$ away from the singularity; thus the trajectory towards an infinite voltage slows and eventually halts. At this stage the system stays linear and reverses direction, heading for the opposite power rail. This produces a sine waveform at the output[16].

4.5.1 Phase Shift Network

The 180° phase shift in Eq. 4-34 is introduced by active and passive components. Oscillators are dependant on passive-component phase shift because it is accurate and almost drift-free. Each *RC* network in Figure 4.7 contributes to a 60° phase shift, and because 180° of phase shift is required for oscillation, three poles are used in the oscillator design[16].

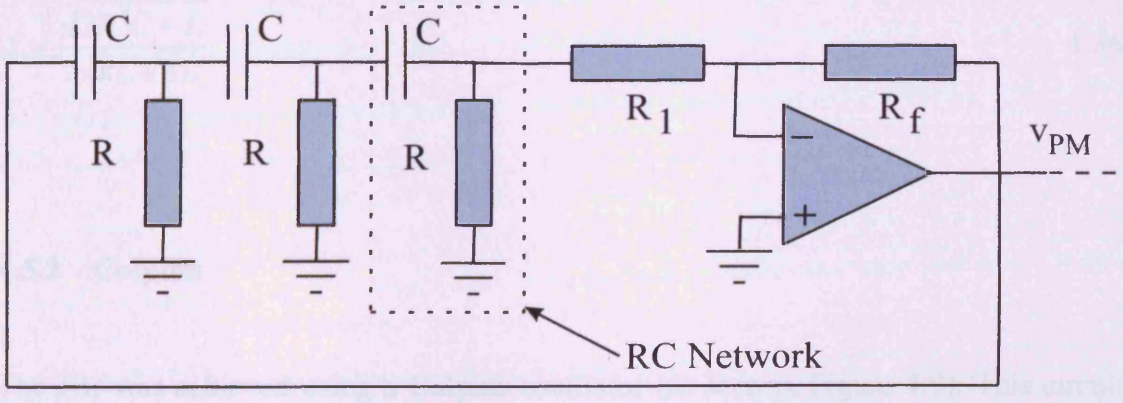

Figure 4.7: Classic phase shift oscillator[17].

G. S. Katranas, "Design and Development of Bilayer Sensor Systems for Biomedical and Automotive Applications", Ph.D. Thesis, Cardiff University.

The frequency of the output waveform can be calculated by (Appendix B):

$$f = \frac{1}{2 \cdot \pi \cdot R \cdot C \cdot \sqrt{6}} \qquad 4\text{-}35$$

Since frequency and phase are interconnected, a change in the value of the passive components of the oscillator will shift the phase of the output waveform. By placing the bilayer sensor in one of the *RC* networks (Figure 4.8), any displacement of the bilayer strip will change the reactance of the sensor coil, hence changing the phase shift contribution of that network; Hence phase modulation is achieved.

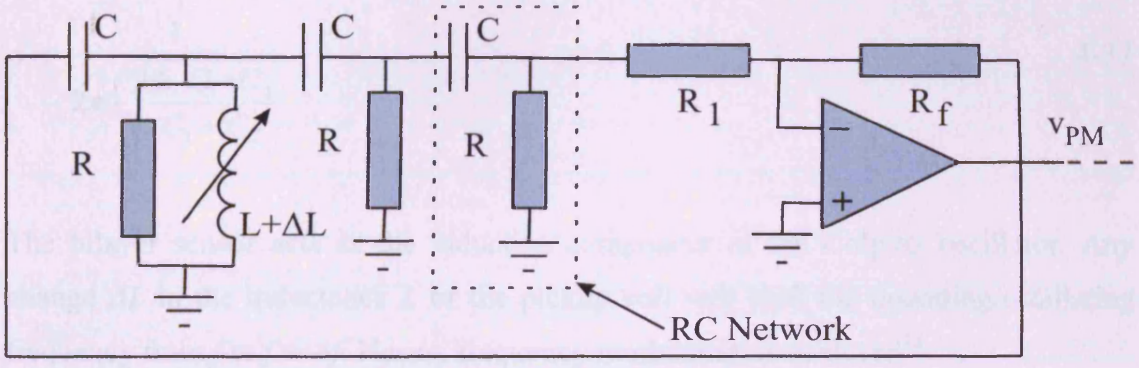

Figure 4.8: Phase modulating circuit.

Using classical network analysis, (Appendix B), the frequency of the output waveform can be calculated by:

$$f = \frac{\sqrt{3R^2C + L}}{2\pi RC\sqrt{6L}} \qquad 4\text{-}36$$

4.5.2 Colpitts

The *FM* was achieved using a Colpitts oscillator (as seen in Figure 4.9). This circuit utilizes an *LC* tank with an inductor connected in parallel to two series capacitors (F).

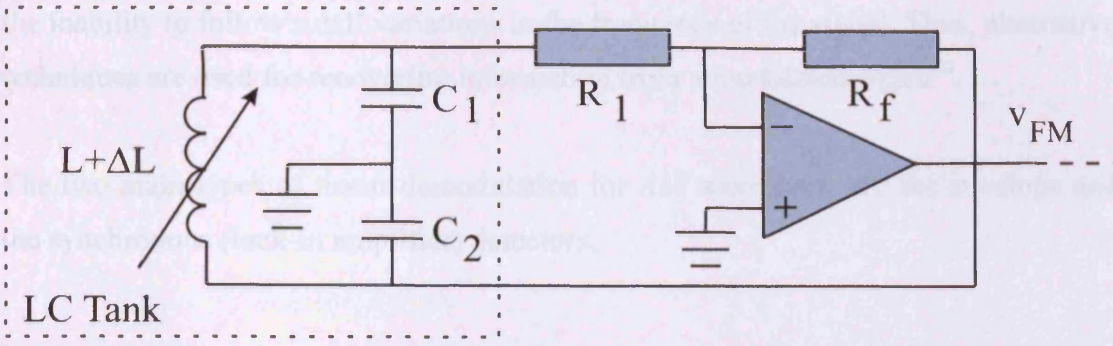

Figure 4.9: Colpitts oscillator[18].

The output is a sine wave at a frequency, f, which is defined by the values of L and C (Appendix B):

$$f = \frac{1}{2\pi \cdot \sqrt{\frac{L \cdot C_1 \cdot C_2}{C_1 + C_2}}} \qquad 4\text{-}37$$

The bilayer sensor acts as the inductive component of the Colpitts oscillator. Any change ΔL in the inductance L of the pickup coil will shift the operating/oscillating frequency from f to $f + \Delta f$. Hence, frequency modulation is achieved[18].

4.6 Signal Demodulation

Extracting or recovering information from a modulated signal is a procedure known as demodulation or detection. Signals with different characteristics such as amplitude or angle modulation require different methods of demodulation. In both cases it is essential to ensure linear demodulation in order to minimise distortion[19].

Techniques such as low-pass or band-pass filtering are not able to demodulate successfully amplitude or angle modulated waveforms. Signals that carry modulation occupy a finite bandwidth which determines the smallest possible filter bandwidth. Also by designing filters with high selectivity (centre frequency/bandwidth) results in

G. S. Katranas, "Design and Development of Bilayer Sensor Systems for Biomedical and Automotive Applications", Ph.D. Thesis, Cardiff University.

a tightly tuned system; hence problems arise in the form of susceptibility to drift and the inability to follow small variations in the frequency of the signal. Thus, alternative techniques are used for recovering information from a modulated signal[20].

The two main types of linear demodulation for *AM* waveforms are the envelope and the synchronous (lock-in amplifier) detectors.

4.6.1 Envelope Detector

The principal operation of the envelope detector is to "follow" the envelope of the *AM* waveform because the shape of v_{AM} is similar to that of the information signal v_m. Thus, the information can be recovered electrically by rectifying the full *AM* signal to produce an output that is linearly proportional to its envelope. The basic circuit of an envelope detector consists of a diode in series with an *RC* tank (Figure 4.10). Even though the diode is a non-linear device, the *V-I* characteristics of it are considered linear at large input signals[19]. The charging and discharging of the capacitor (at time constant = $R \cdot C$) will half-wave rectify the *AM* waveform. The output signal produced will follow the modulation envelope $V_E = V_c + v_m$. The V_c is a *DC* term which can be removed with the series capacitor C_s, at the output.

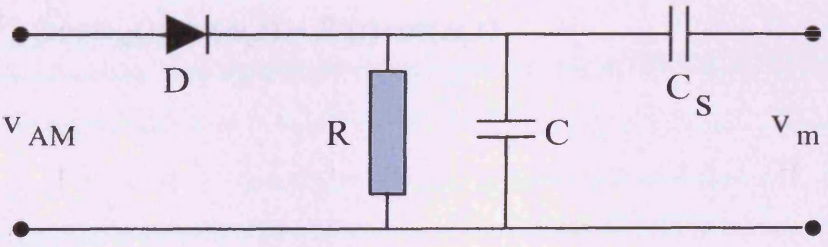

Figure 4.10: Envelope detector

Mathematically, envelope detection is possible through a technique called Hilbert transform[21, 22]. The Hilbert transform of a signal *s(t)* is denoted by $\hat{s}(t)$ and is obtained by shifting all the frequency components of *s(t)* by $\pi/2$ (90°)[23, 24]. A function *s(t)* and its Hilbert transform $\hat{s}(t)$ can form together a complex signal[21-25]:

$$S(t) = s(t) + j \cdot \hat{s}(t) \qquad 4\text{-}38$$

Using Euler's formula:

$$e^{j\omega \cdot t} = \cos(\omega \cdot t) + j \sin(\omega \cdot t) \qquad 4\text{-}39$$

the signal *S(t)* can be represented as:

$$S(t) = E'(t) \cdot e^{j\varphi(t)} \qquad 4\text{-}40$$

where $\varphi(t)$ is the phase of *S(t)* given as:

$$\varphi(t) = \tan^{-1}\left(\frac{\hat{s}(t)}{s(t)}\right) \qquad 4\text{-}41$$

and *E'(t)* is the envelope of *S(t)*:

$$E'(t) = |S(t)| = \sqrt{s^2(t) + \hat{s}^2(t)} \qquad 4\text{-}42$$

For the demodulation of the *AM* waveform via the Hilbert transform:

$$v_{AM} = [V_c + V_m(\cos \omega_m t)]\cos(\omega_c t) = E'(t)\cos(\omega_c t) \qquad 4\text{-}43$$

and

$$\hat{v}_{AM} = E'(t)\sin(\omega_c t) \qquad 4\text{-}44$$

Converting Eq. 4-43 and Eq. 4-44 in a complex signal as in Eq. 4-38:

$$v_{env} = v_{AM} + j \cdot \hat{v}_{AM} = E'(t)\cos(\omega_c t) + j \cdot E'(t)\sin(\omega_c t) \qquad 4\text{-}45$$

From Eq. 4-39, Eq. 4-45 becomes:

$$v_{env} = E'(t) \cdot e^{j\omega_c t} \qquad 4\text{-}46$$

The envelope of v_{AM} can be found from:

$$E'(t) = |v_{env}| = V_c + V_m \cos(\omega_c t) = V_c + v_m \qquad 4\text{-}47$$

The component V_c can then be removed, leaving only the information signal v_m; hence *AM* demodulation is achieved.

Envelope detection is only possible when the signal to noise ratio (*SNR*) is above 1:1. Below the 1:1 threshold the envelope detection deteriorates rapidly and the demodulated output becomes grossly distorted. The *SNR* of the modulated signals that arise from the displacement of bilayer sensors is usually below the 1:1 threshold. Thus, the envelope detection is not the preferred method here for signal demodulation. On the other hand synchronous detectors (lock-in amplifiers) have the ability to measure signals accompanied by relatively high levels of noise and interference[20].

4.6.2 Lock-in Amplifier

A lock-in amplifier has the capability of recovering small *AC* signals (nV) in the presence of overwhelming background noise. This technique achieves this by acting as a very narrow band-pass filter that removes the unwanted noise and allows the desired signal to pass through. The capability of the lock-in amplifier can be seen in the following example[26]:

If the information signal is a 10 nV sine wave at 5 kHz it needs amplification in order to be measured. Taking into consideration a good amplifier with 1000 gain, 1 MHz bandwidth and low input noise of 5 nV/√Hz, then the output will be the information signal amplified to 10 μV (10 nV · 1000 gain) and broadband noise of 5 mV (√1 MHz · 5 nV · 1000 gain). Obviously the signal is buried under the noise; even if the signal

G. S. Katranas, "Design and Development of Bilayer Sensor Systems for Biomedical and Automotive Applications", Ph.D. Thesis, Cardiff University.

is band-passed filtered at a very good filter selectivity of a 5 kHz centre frequency and 3db bandwidth (point of a 50 % drop to the signal power) of 50 Hz, the noise level will be 35 μV (√50 Hz · 5 nV · 1000 gain). Accurate measurement is not possible to take place since the output noise is greater than the information signal. In contrast a standard commercial lock-in amplifier has a 0.125 Hz noise bandwidth and at a time constant of 1 second it will produce a noise level of only 1.7 μV (√0.125 Hz · 5 nV · 1000 gain), thus enabling the measurement of the 10 μV information signal[26].

In essence lock-in amplifiers measure the amplitude, V, of a sinusoidal voltage $v = V \cdot sin(\omega t)$. This is achieved by multiplying the signal in question, v_{in}, with a reference signal, v_{ref}, of the same frequency and phase by using a phase-sensitive detector (*PSD*) which is a composed of a mixer followed by a low pass filter (Figure 4.11). Mathematically the mixer produces a signal that is the sum of two new sinusoids, one having a frequency of $f_{in} + f_{ref}$ and the other a frequency of $f_{in} - f_{ref}$[20, 26, 27]:

$$v_{mixer} = 2 \cdot v_{in} \cdot v_{ref} = 2 \cdot V_{in} \cos(\omega_{in} t) \cdot V_{ref} \cos(\omega_{ref} t) \qquad 4\text{-}48$$

From Eq. 4-7, Eq. 4-48 becomes:

$$v_{mixer} = 2 \cdot V_{in} \cdot V_{ref} \left(\frac{1}{2} \cos(\omega_{in} t + \omega_{ref} t) + \frac{1}{2} \cos(\omega_{in} t - \omega_{ref} t) \right) =$$

$$= V_{in} \cdot V_{ref} \cos(\omega_{in} t + \omega_{ref} t) + V_{in} \cdot V_{ref} \cos(\omega_{in} t - \omega_{ref} t) \qquad 4\text{-}49$$

Therefore a signal that is the sum of two new sinusoids, one having a frequency of $f_{in} + f_{ref}$ and the other a frequency of $f_{in} - f_{ref}$, is generated. When the signal v_{ref} is synchronised in frequency and phase with the v_{in}, $f_{in} = f_{ref}$ then[20, 26, 27]:

$$v_{mixer} = V_{in} \cdot V_{ref} \cos(2\omega_{in}) + V_{in} \cdot V_{ref} \qquad 4\text{-}50$$

In the case when the signal v_{in} is obscured by noise v_n then:

$$v_{in} = V_{in}\cos(\omega_{in}t) + \sum V_{noise}\cos(\omega_{noise}t) \qquad 4\text{-}51$$

Hence Eq. 4-50 will become:

$$v_{mixer} = V_{in}\cdot V_{ref} + V_{in}\cdot V_{ref}\cos(2\omega_{in}) + \sum V_{noise}\cdot V_{ref}\cos(\omega_{noise}t + \omega_{ref}t) +$$

$$+ \sum V_{noise}\cdot V_{ref}\cos(\omega_{noise}t - \omega_{ref}t) \qquad 4\text{-}52$$

When passing the v_{mixer} from a low-pass filter with sufficiently low cut-off frequency the signal $V_{in}\cdot V_{ref}\cdot cos(2\omega_{in}t)$ is eliminated along with most of the noise, including the component of the noise with frequencies near the frequency of the reference signal. The waveform, $V_{in}\cdot V_{ref}$, from the *PSD* may be passed through a low frequency *DC* amplifier to boost the signal. If the signal V_{in} is in the form of an *AM* waveform (Eq. 4-4) then the *DC* output of the lock-in amplifier would be[20, 26, 27]:

$$v_{AM} = \left[V_c + V_m\cdot\cos(\omega_m\cdot t)\right]\cdot V_{ref} \qquad 4\text{-}53$$

If the magnitude V_{ref} is kept constant then the *DC* signal from the lock-in amplifier will be proportional to the magnitude of V_{in}, hence proportional to signal v_m. Thus, the demodulation of the *AM* waveform is achieved[20, 26, 27].

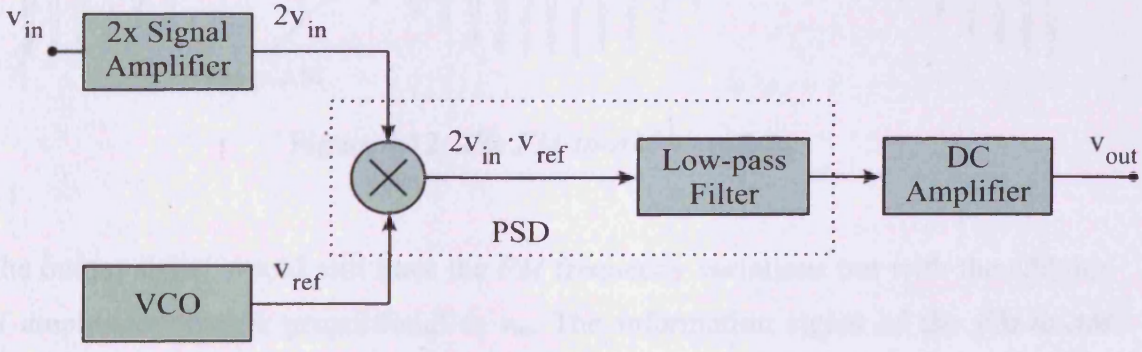

Figure 4.11: Lock-in amplifier block diagram[27].

4.6.3 Discriminator

Extracting the modulation from an *FM* waveform requires converting the changes in frequency to changes in amplitude. In other words the instantaneous amplitude of the *FM* demodulator (discriminator) must be directly proportional to the instantaneous frequency of the *FM* waveform[28, 29]. Since *FM* discriminators are sensitive to amplitude variations the *FM* signal is first passed through a limiter to reduce any random fluctuations. This step removes most of the unwanted noise interference that affects the quality of the amplitude modulation waveforms, without influencing v_m, because in an *FM* signal the information is carried as changes in frequency[30]. The simplest type of discriminator is the slope detector. The output of this system equals to the time derivative of the input waveform (*FM*), hence producing an *FM-to-AM* signal. Electronically the slope detector can be realised in the form of an *LC* tank tuned to a frequency that is slightly higher than $f_c+\Delta f$. The *LC* tank amplitude will vary proportional according to the frequency variations of the *FM* waveform (Figure 4.12).

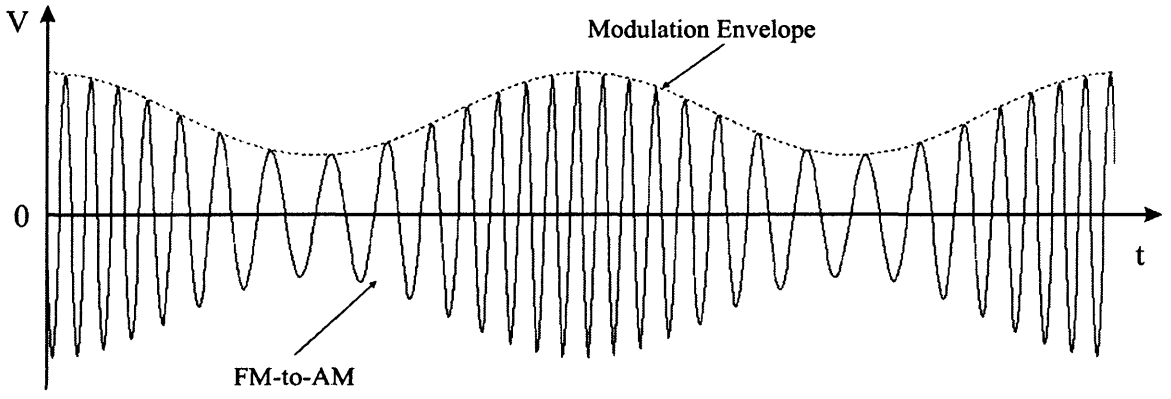

Figure 4.12: The *FM-to-AM* waveform.

The output signal would still have the *FM* frequency variations but with the addition of amplitude changes proportional to v_m. The information signal of the *FM-to-AM* waveform can be extracted using a diode detector (Figure 4.13)[30, 31].

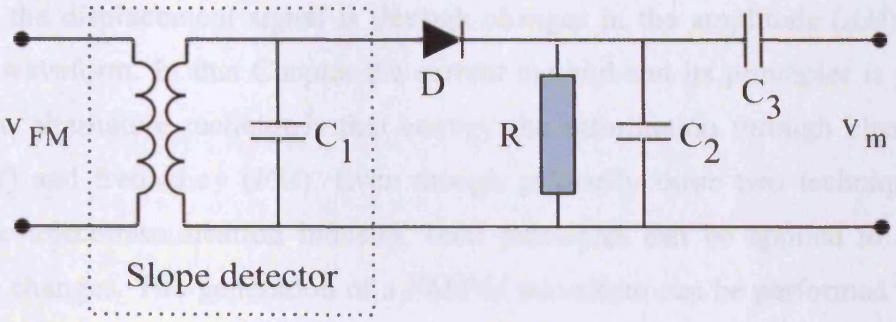

Figure 4.13: FM discriminator[30, 31].

Mathematically the output of the slope detector is the derivative of the *FM* waveform of Eq. 4-21[30, 31]:

$$v_{sd} = \frac{d(v_{FM})}{dt} = V_c \cdot (\omega_c + m_{FM} \cdot \omega_m \cdot \cos(\omega_m \cdot t)) \cdot \sin(\omega_c \cdot t + m_{FM} \cdot \sin(\omega_m \cdot t)) \qquad 4\text{-}54$$

Passing the output of the slope detector, v_{sd}, through an envelope detector such as the Hilbert transform will produce the information signal[30, 31].

In the case of phase modulated waveforms the demodulation takes place by inputting the *PM* signal (Eq. 4-18) through an integrating component[32]:

$$v_{\text{int}} = \int v_{PM}\, dt = \frac{V_c}{(\omega_c + m_{PM} \cdot \omega_m \sin(\omega_m \cdot t))} \cdot \sin(\omega_c \cdot t + m_{PM} \cdot \omega_m \cos(\omega_m \cdot t)) \qquad 4\text{-}55$$

This creates a *PM-to-AM* waveform that carries the information signal as phase and amplitude changes. Inputting the *PM-to-AM* signal in an envelope detector, v_m is found.

4.7 Summary

As part of an electronic circuit the bilayer sensor acts as an inductor, *L*. Any changes ΔL may influence the alternating current (*AC*) that is used to excite the magnetic material, hence the properties of the output voltage signal. The current method of

conveying the displacement signal is through changes in the amplitude (*AM*) of the excitation waveform. In this Chapter the current method and its principles is portrait against two alternative techniques that convey the information through changes in phase (*PM*) and frequency (*FM*). Even though primarily these two techniques are used in the telecommunication industry, their principles can be applied to convey inductance changes. The generation of a *FM/PM* waveform can be performed using a device/circuit whose sinusoidal output undergoes a phase or frequency deviation proportional to the change in the sensor reactance. This is a novel application for these two modulation techniques.

References

[1] H. S. Black, "Modulation theory", Van Nostrand Reinhold: New York, 1953, Ch. 2, pp. 11-13.
[2] A. B. Carlson et al, "Communication systems", McGraw-Hill: Singapore, 1986, Ch. 1, pp. 5-11.
[3] L. Mehnen, et al, "Magnetostrictive amorphous bimetal sensors", Journal of Magnetism and Magnetic Materials, Vol. 215-216, 2000, pp. 779-781.
[4] E. Kaniusas et al, "Biomedical applicability of magnetoelastic bilayer sensors", Proclamations of the International Symposium on Applied Electromagnetics and Mechanics (ISEM), Versailles, France, 2003, pp. 236-237.
[5] F. R. Connor, "Modulation", Arnold: London, 1982, Ch. 2, pp. 6-8.
[6] A. B. Cook et al, "Frequency modulation receivers", Prentice Hall: New Jersey, 1968, Ch. 1, pp. 5-11.
[7] T. Ozkul, "Data acquisition and process control using personal computers", Dekker: New York, 1996, Ch. 2, pp. 45.
[8] C. W. DaSilva et al, "Vibration: fundamentals and practice", CRC Press: Boca Raton, 2000, Ch. 9, pp. 592-593.
[9] K. C. Wu, "Transistor circuits for spacecraft power system", Kluwer Academic: Norwell, 2003, pp. 80-81.
[10] J. Kosel, et al, "Non-contact detection of magnetoelastic bilayer position sensors", Sensors and Actuators A, vol. 123, 2004, pp. 349-353.
[11] J. A. Betts, "Signal processing modulation and noise", London: English Universities Press, 1970, Ch. 2, pp. 32-43.
[12] H. S. Black, "Modulation theory", Van Nostrand Reinhold: New York, 1953, Ch. 3, pp. 27-30.
[13] A. B. Carlson et al, "Communication systems", McGraw-Hill: Singapore, 1986, Ch. 7, pp. 236-240.
[14] F. R. Connor, "Modulation", Arnold: London, 1982, Ch. 3, pp. 26-28.
[15] H. S. Black, "Modulation theory", Van Nostrand Reinhold: New York, 1953, Ch. 13, pp. 206-209.
[16] R. Mancini, "Sine-wave oscillators", Texas Instruments: Dallas, 2001, Ch. 15, pp. 15.3-15.9.
[17] A. Basak, "Analogue electronic circuits and systems", Cambridge University Press: Cambridge, 1991, Ch. 4, pp. 157-160.
[18] M. S. Ghausi, "Electronic Devices and Circuits: Discrete and Integrated", Oxford University Press: New York, 1985, Ch. 10, pp. 505-507.
[19] F. R. Connor, "Modulation", Arnold: London, 1982, Ch. 6, pp. 78-82.
[20] M. L. Mead, "Lock-in amplifiers: principles and applications", Peregrinus: Stevenage, 1983: Ch. 2, pp. 7-29.
[21] A. B. Carlson et al, "Communication systems", McGraw-Hill: Singapore, 1986, Ch. 3, pp. 103-105.
[22] R. E. Ziemer et al, "Principles of communications systems, modulation and noise", Wiley: Boston, 1998, Ch. 2, pp. 94-104.
[23] M. Johansson, "The Hilbert transform", Växjö University, Sweden, Thesis, 1999, Ch. 1, pp. 1-2.
[24] S. R. Long et al, "The Hilbert techniques: an alternate approach for non-steady time series analysis", IEEE Geoscience and Remote Sensing Society Newsletter, 1995, pp. 6-11.
[25] F. R. Connor, "Modulation", Arnold: London, 1982, App. A, pp. 112-114.
[26] TN1000-2 Technical notes, Perkin Elmer Instruments Inc., Massachusetts, MA, 2000.
[27] J. H. Scofield, "A frequency-domain description of a lock-in amplifier", American Journal of Physics, vol. 62, 1994, pp. 129-133.
[28] F. R. Connor, "Modulation", Arnold: London, 1982, Ch. 6, pp. 89-95.
[29] J. A. Betts, "Signal processing modulation and noise", London: English Universities Press, 1970, Ch. 3, pp. 67-78.
[30] H. S. Black, "Modulation theory", Van Nostrand Reinhold: New York, 1953, Ch. 13, pp. 209-215.
[31] A. B. Carlson et al, "Communication systems", McGraw-Hill: Singapore, 1986, Ch. 7, pp. 259-263.
[32] F. Froehlich et al, "Encyclopaedia of Telecommunications", Dekker: New York, 1995, Vol. 4, pp. 427-429.

Chapter 5 Measurement System

5.1 System Overview

The measuring system consists of a personal computer (*PC*) based acquisition set-up and a circuit that conveys the sensor displacement signal to the unit, using the *AM*, *PM* or *FM* principles (Figure 5.1).

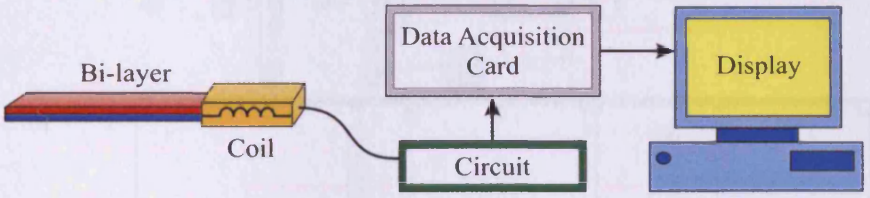

Figure 5.1: Measurement system set-up.

The use of data acquisition packages such as LabVIEW® allow a high degree of software modularity and provide the features necessary for obtaining the sensor signal, processing, analysing it and displaying the results. The signal detection was achieved through the use of LabVIEW® software and a NI-6120 data acquisition card with a maximum sampling rate of 800 kS/s per channel and 16-bit resolution[1]. For the signal processing, analysis and presentation, a program was written using the LabVIEW® graphical programming language. In this program, functions or principles such as Hilbert transform, lock-in amplifier or discriminator are represented mathematically in order to recover the sensor displacement signal. This programming language consists of layers of software termed virtual instruments (*VI*'s) that use the processing power of an ordinary *PC* to convert it to a custom designed instrument. The *VI*'s consist of two main elements the block diagram (Figure 5.2) and the front panel (Figure 5.3). The front panel is the instruments interface and it is used for controlling the *VI* and displaying the data. The block diagram consists of the elements that acquire and process the signal. These *VI*'s can be used as inside other *VI*'s, as *subVI*'s, creating a hierarchical structure[2]. The main code and hierarchy of the measurement system program is located in Appendix C.

G. S. Katranas, "Design and Development of Bilayer Sensor Systems for Biomedical and Automotive Applications", Ph.D. Thesis, Cardiff University.

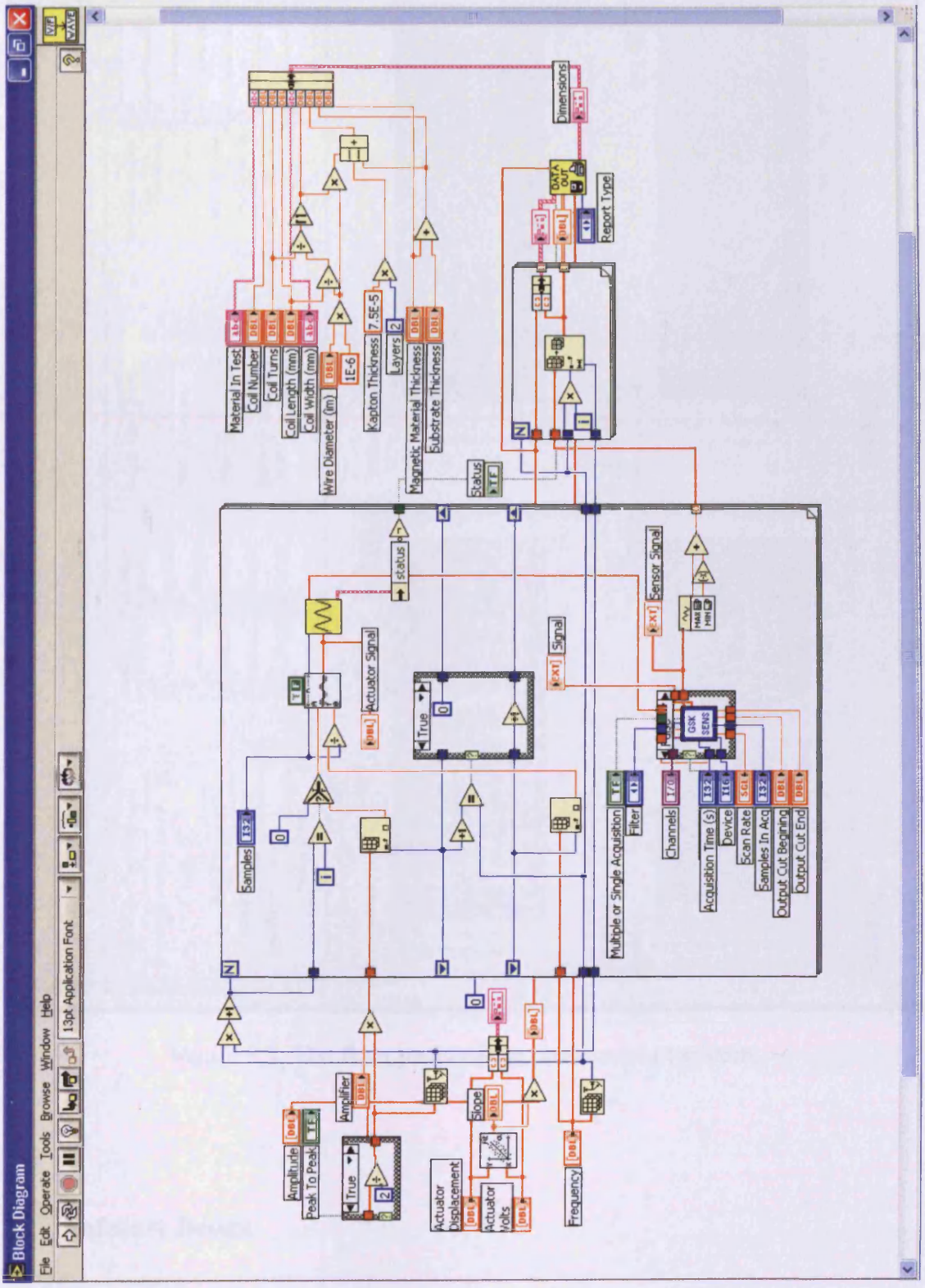

Figure 5.2: The block panel of the measurement system.

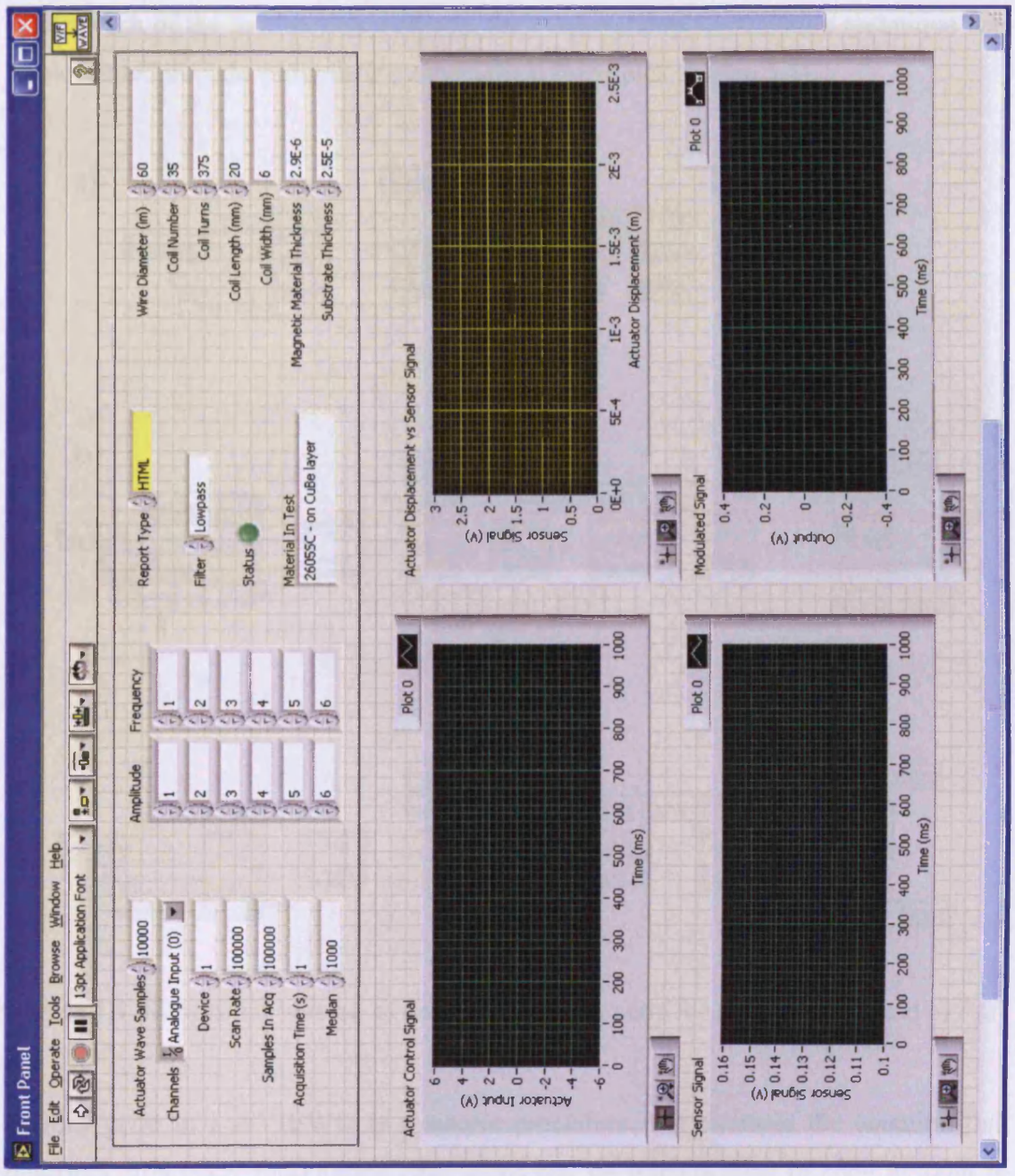

Figure 5.3: The front panel of the measurement system.

5.2 Software Design

The role of the software program is to acquire the modulated waveform (*AM*, *PM*, *FM*) and separate the sensor displacement information, v_m, from the reference signal,

v_c. For each of the modulation methods, their equivalent demodulation technique was implemented in code using their mathematical principles (Figure 5.4).

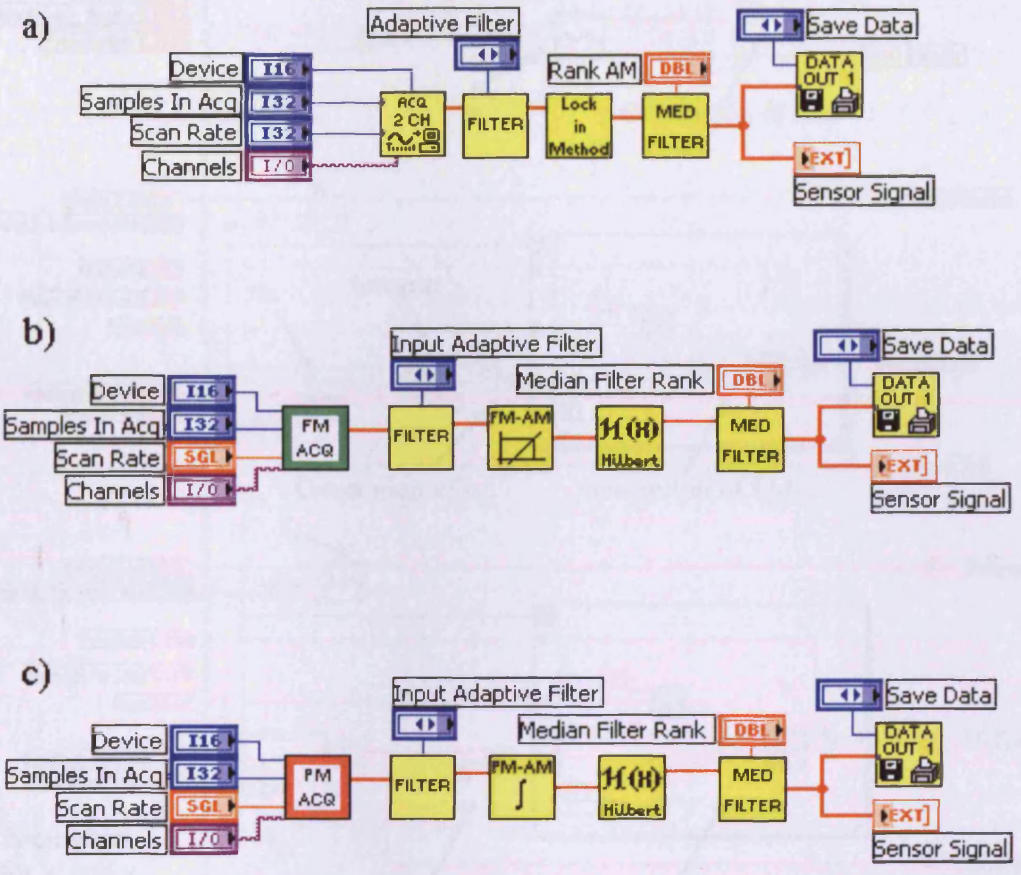

Figure 5.4: Simplified version of the demodulating code for a) *AM*, b) *FM* and c) *PM*.

Writing code in LabVIEW® is a simple procedure. For example the equation that describes frequency modulation (Eq. 4-20) can be implemented in code as seen in Figure 5.5. By inputting values to the parameters on the left, the v_m can be generated, integrated as in Eq. 4-20, multiplied by 2π and then inserted into the v_c as instantaneous frequency change; the output from this *VI* is an *FM* waveform.

The initial step in writing the demodulating program was to simulate the modulated signals (*AM*, *PM* and *FM*), mathematically, with and without superimposed noise signals in order to test the demodulation algorithm of the LabVIEW® code.

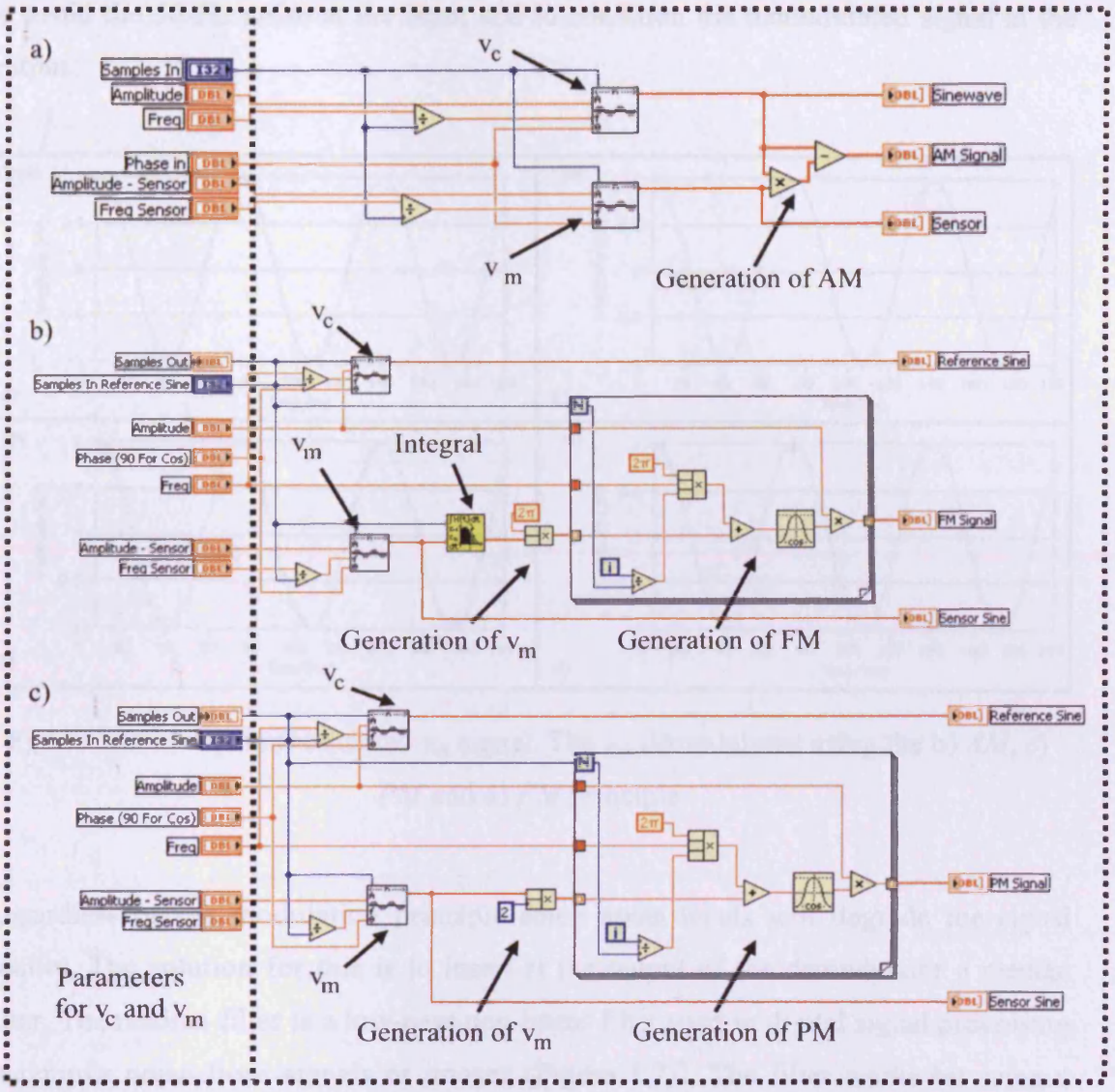

Figure 5.5: Example *VI* that shows the implementation of the mathematical equations of a) *AM*, b) *FM* and c) *PM* using the LabVIEW language.

The results showed that in a simulation situation (ideal condition) the program can demodulate signals as low as 1 pV (Figure 5.6). This value is governed by software/code limitations but does not affect the accuracy of the system as the signals to be detected are above this mark. Thus, the results confirm the correct operation of the demodulation software. The next step was to connect the demodulation program to an Agilent 33250A waveform generator that was configured to output modulated waveforms[3]. From this procedure the behaviour of the system (acquisition time, noise levels etc) under real-time acquisition was examined. The results from the waveform generator acquisition showed the need to include in the program filtering (band-stop)

[3] G. S. Katranas, "Design and Development of Bilayer Sensor Systems for Biomedical and Automotive Applications", Ph.D. Thesis, Cardiff University.

to avoid the 50 Hz noise at the input and to condition the demodulated signal at the output.

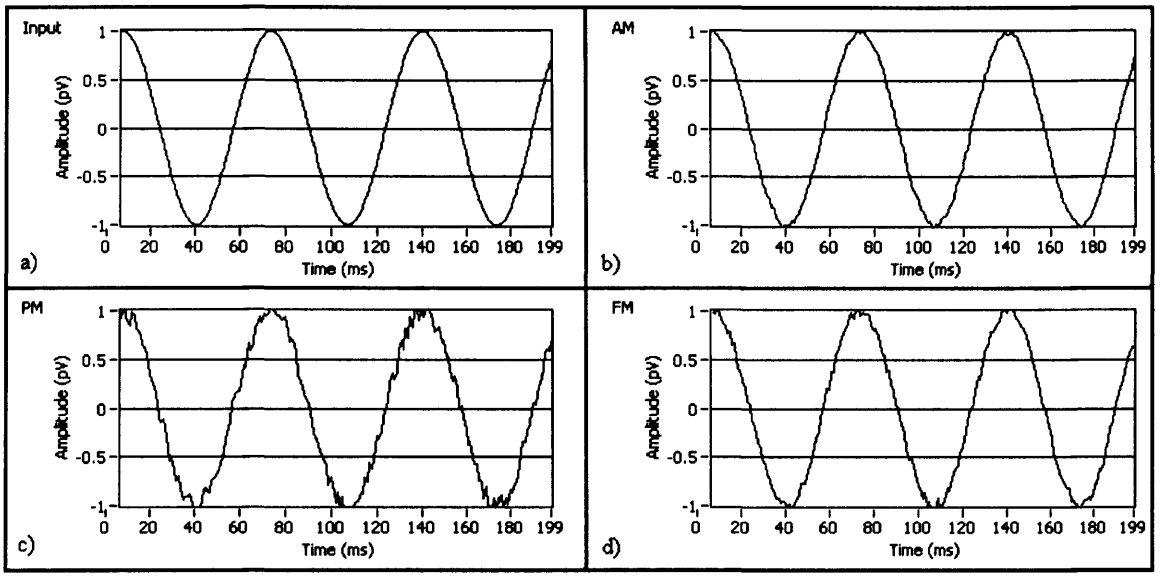

Figure 5.6: a) The unmodulated v_m signal. The v_m demodulated using the b) *AM*, c) *PM* and d) *FM* principle.

Regardless of the modulation principle some noise levels will degrade the signal quality. The solution for this is to insert at the output of the demodulator a median filter. The median filter is a low-pass non-linear filter used in digital signal processing to remove noise from signals or images (Figure 5.7)[4]. The filter works by using a window that consists of an odd number of samples. These points are sorted (ranked) numerically in an ascending order.

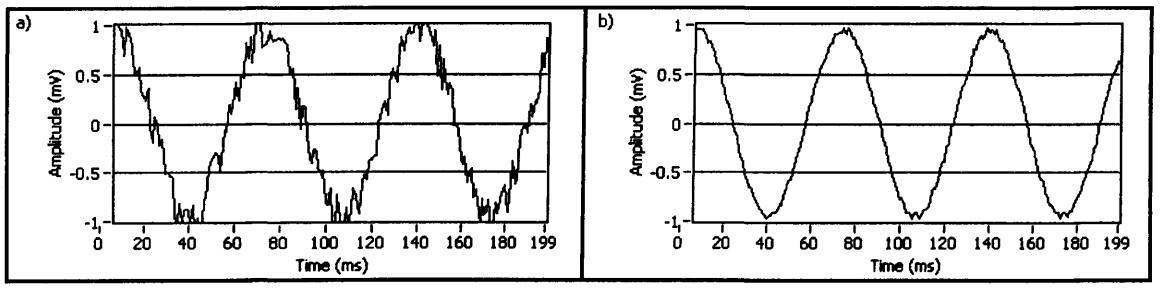

Figure 5.7: A noisy signal (a), filtered via the median filter principle (b).

The number in the centre of the window is termed the median number. The old value is replaced with the new number which is actually the value of a neighbouring point.

G. S. Katranas, "Design and Development of Bilayer Sensor Systems for Biomedical and Automotive Applications", Ph.D. Thesis, Cardiff University.

In this way the median filter isolates and removes all the spurious points (Figure 5.8a) without affecting the neighbouring values (Figure 5.8b). Other filters do equally reduce the noise but the spurious values tend to get averaged along with the unaffected points (Figure 5.8c)[5, 6].

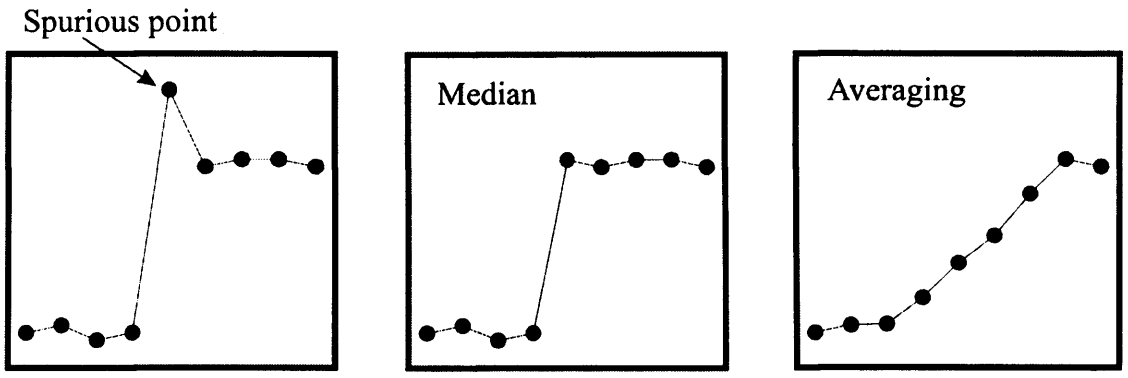

Figure 5.8: The elimination of spurious points via the median filter technique (b) and with the averaging method (c)[5, 6].

After signal conditioning is preformed at the output of the demodulator, which ensures minimum amount of noise interference, the information signal is passed into a *subVI* that handles the presentation and preservation of the data. This section of the system handles the tagging of the data with the sensor configuration (coil and bilayer material dimensions) and the presentation of the information by producing automated reports in *.xls* (Microsoft Excel®) or *.html* format (Appendix C).

5.3 Verification and Comparison

After verifying that the measurement system is able to demodulate simulated and acquired modulation waveforms, it is necessary to quantify the sensor information signal in terms of displacement distance. For this task an LDV V450/1 Shaker System – actuator (Appendix E) was used to provide a controlled displacement of the free end of the bilayer sensor (Figure 5.9).

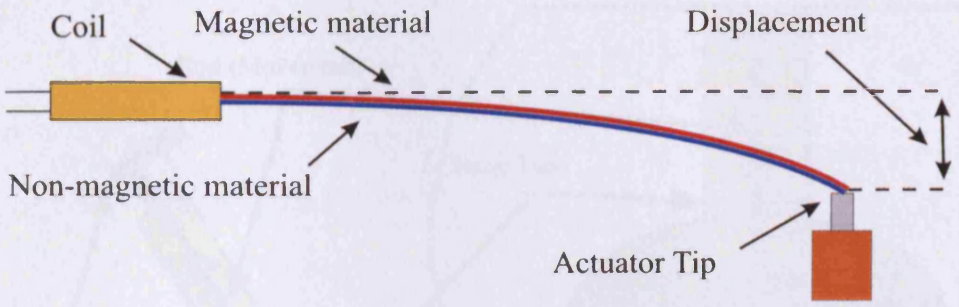

Figure 5.9: The bilayer sensor during bending displacement at the free end.

The maximum peak to peak continuous displacement that the actuator can provide is 19 mm at a 6 V *DC* supply. Using a F. W. Bell 9950 Gauss/Teslameter the maximum magnetic field that is generated from the actuator at its surface was measured to be 2.3 kA/m.

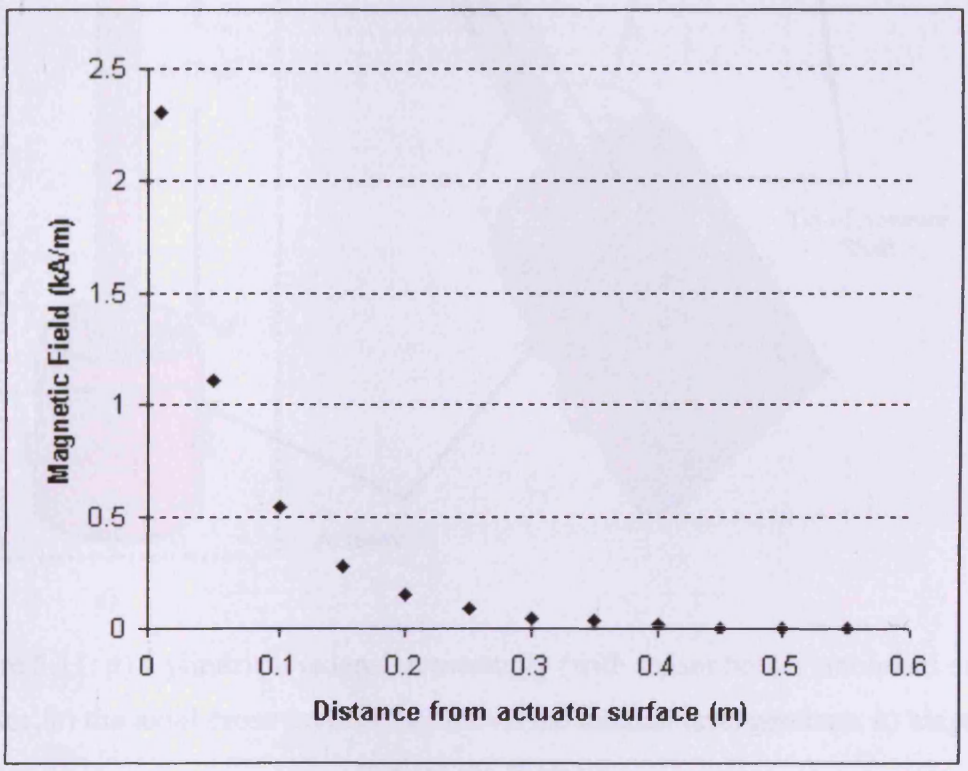

Figure 5.10: The field density becomes zero at a distance of 45 cm away from the surface of the actuator.

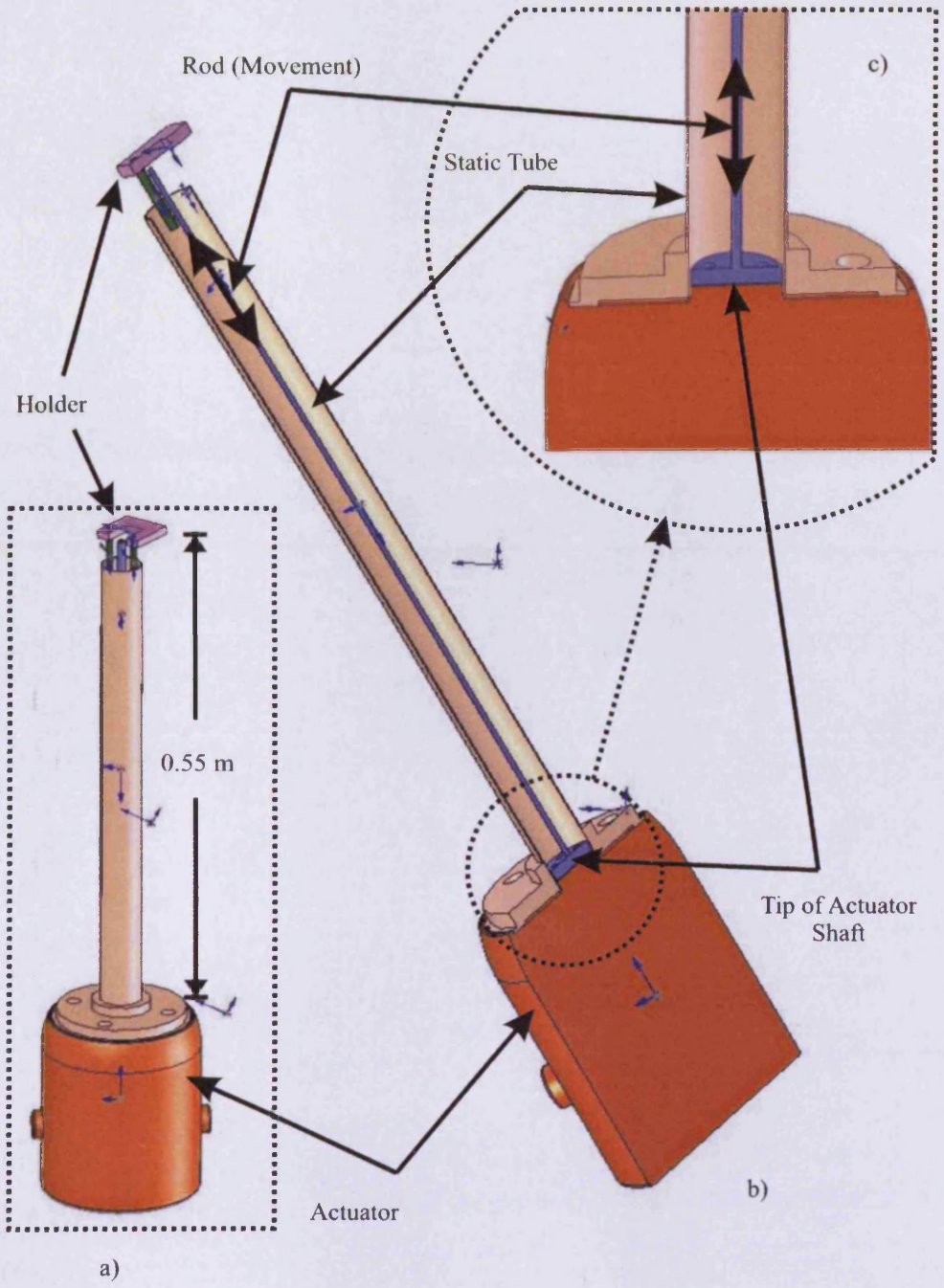

Figure 5.11: a) Cylindrical extension assembly (with sensor holder) mounted on the actuator, b) the axial cross-section that shows the internal arrangements, c) magnified view of the shaft tip.

To avoid any influence from that field (Figure 5.10), the bilayer sensor was placed 55 cm away from the top surface of the actuator with the aid of a non-magnetic stainless steel cylindrical extension assembly (Figure 5.11). It comprises of a (10 mm x 550 mm) rod attached to the actuator's movement (actuator shaft) and housed within a (40 mm x 500 mm) static tube fixed to the top surface of the actuator's body. This

extension also includes a holder base for the sensor that has an adjustable slider to accommodate sensor lengths of 5 mm - 40 mm (Figure 5.12).

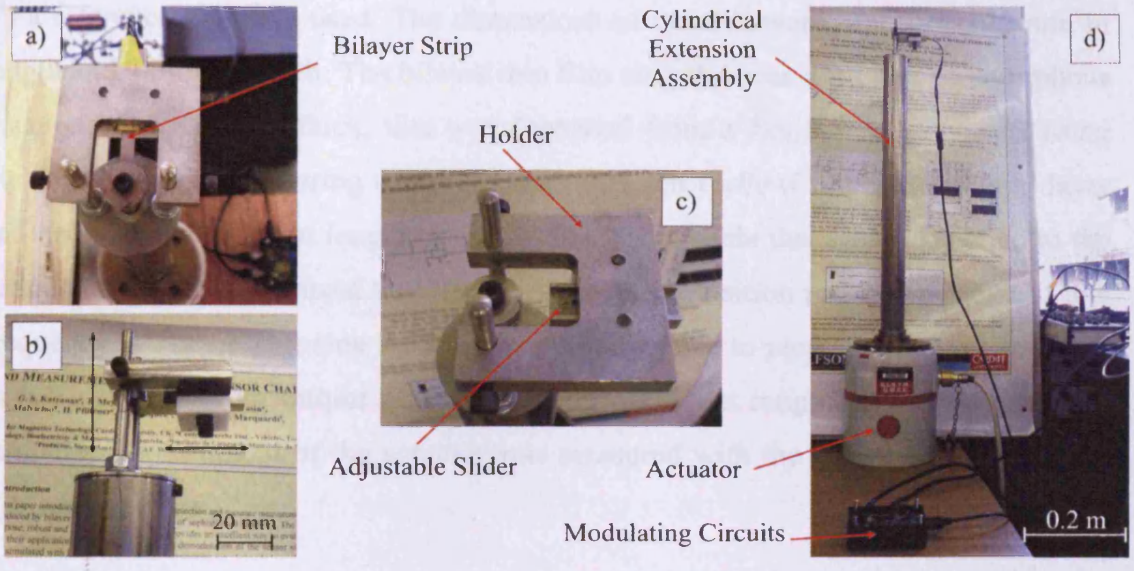

Figure 5.12: a) Sensor mounted for taking measurements, b) two-dimensional movement adjustment of holder and slider, c) magnified view of holder and slider, c) actuator assembly with sensor connected to the modulating circuits.

For protection and easiness of handling, all three modulating circuits were transferred to a two-layer printed circuit board (*PCB*) and placed in a (90 mm x 60 mm x 30 mm) plastic enclosure box (Figure 5.13). In all three circuits an OPA37 ultra-low noise (4.5 nV/√Hz) precision operational amplifier[15].

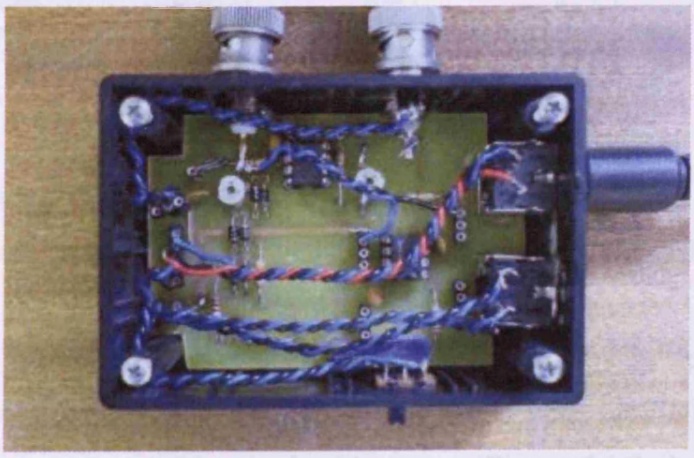

Figure 5.13: The three modulation circuits inside the enclosure box.

G. S. Katranas, "Design and Development of Bilayer Sensor Systems for Biomedical and Automotive Applications", Ph.D. Thesis, Cardiff University.

Extra code was written to the LabVIEW® program in order to supply the actuator with a sinusoidal signal, via an Amcron PSA-2 Power Amplifier. For calibration and comparison purposes between the three modulation principles, (*AM* [7], *FM* [8, 9] and *PM* [10]) a reference coil was used. The dimensions of the coil were 300 turns, 20 mm in length and 7 mm in width. The bilayer thin film strip that was used was an amorphous magnetic film, 2.9 μm thick, that was deposited from a $Fe_{81}B_{13.5}Si_{3.5}C_2$ target using the *RF* magnetron sputtering technique onto a 25 μm *CuBe* (Copper Beryllium) layer and had a size of 40 mm length, 5 mm width. The signals that where supplied to the actuator where synchronised with the sensor data acquisition and had a range of low frequency (1 Hz - 6 Hz) sine waves, with variable peak to peak amplitudes from 1 V to 6 V. The resulting output peak to peak displacement ranged from 0.35 mm to 2 mm. The displacement of the actuator was measured with the aid of a Laser Doppler Vibrometer (*LDV*)[11].

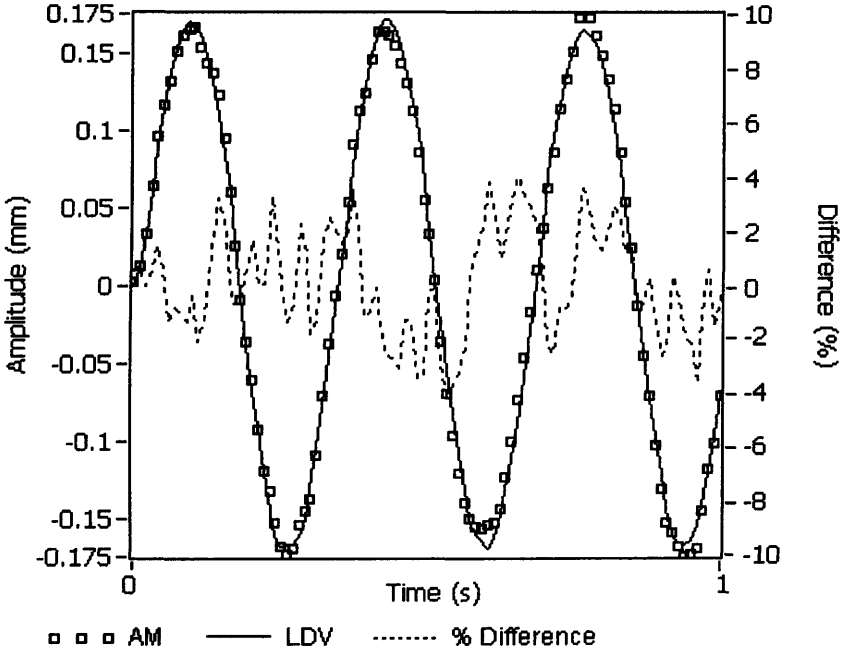

Figure 5.14: A comparison of the a) *AM* information signal and b) the *LDV* output at 0.35 mm peak to peak plotted together with their percentage difference.

As seen in Figure 5.14 the *AM* signal shows an average of 1.7 % deviation with a 3.9 % maximum deviation compared to the output signal from the *LDV*. At the same peak to peak displacement of 0.35 mm, the *PM* signal (Figure 5.15) shows an average

G. S. Katranas, "Design and Development of Bilayer Sensor Systems for Biomedical and Automotive Applications", Ph.D. Thesis, Cardiff University.

1 % deviation with a 2.2 % maximum deviation whereas the *FM* signal (Figure 5.16) shows an average of 0.9 % deviation with a 2 % maximum deviation.

The *AM* signal not only shows almost twice the amount of deviation, at this displacement range, compared to the *PM* or *FM* signal but it also depicts a deteriorated signal quality. This difference is expected to increase at displacements below 0.35 mm peak to peak. From this the influence of the noise effects that usually infest the *AM* method is made apparent. Both angle modulations show similar results but during the acquisition and signal processing there is an increase of 10-15 % in the time it takes for the program to demodulate the *PM* signal and present the data. This is due to the fact that the *PM* circuit suffers from a minor frequency drift/instability (0.1 % more than the *FM* circuit) which imposes the need to increase the sampling rate of the data acquisition card, to 200 kS/s, in order to enhance the quality of the signal. The instability of the *PM* circuit arises from the circuit component tolerances. The *RC* tanks of the *PM* circuit need to be as closely matched as possible to ensure minimal drift.

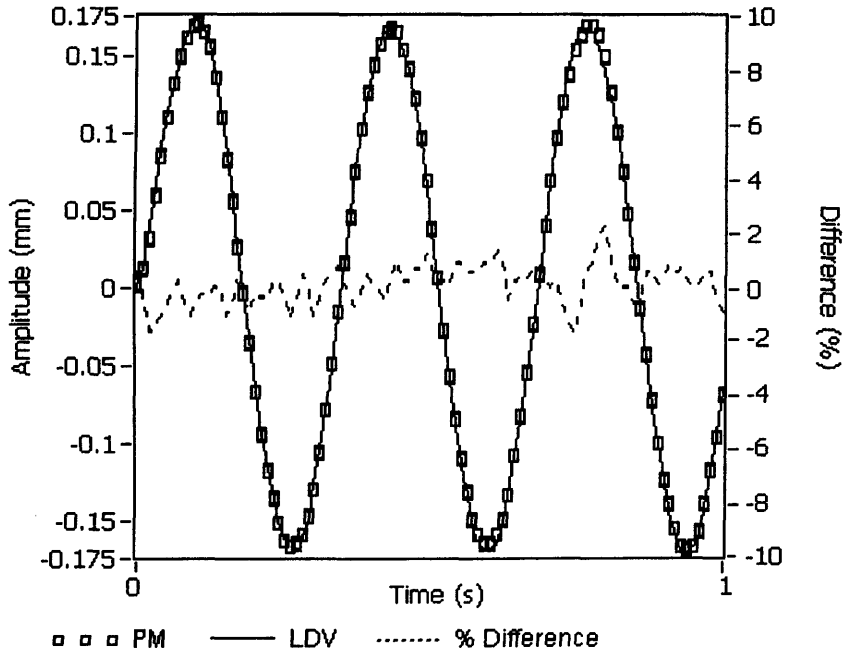

Figure 5.15: A comparison of the a) *PM* information signal and b) the *LDV* output at 0.35 mm peak to peak plotted together with their percentage difference.

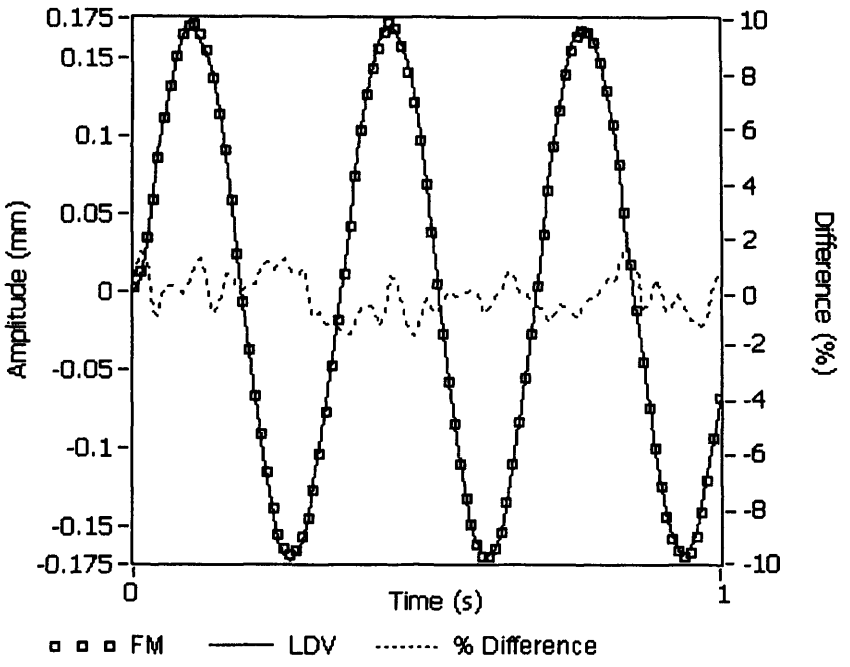

Figure 5.16: A comparison of the a) *FM* information signal and b) the *LDV* output at 0.35 mm peak to peak plotted together with their percentage difference.

The output signal is determined by the degree of bending of the bilayer which can be converted into a displacement reading (Figure 5.17). The average peak to peak signal produced at the displacement range of the actuator, for all three modulation principles, was in the range of 0.8 mV to 4.6 mV. From the performance of the system it was found that it has an average sensitivity of 2.2 mV/mm.

By removing the sensor from and then repositioning it on to the holder for each measurement an understanding on the repeatability was obtained. Repeating five times the measurement, under the same conditions for each modulation principle, the repeatability of the system was examined. For each modulation system an average curve (Figure 5.17) was plotted from the five measurements and the maximum deviation was recorded. For the *AM*, *PM* and *FM* the non-repeatability of the results were 4.6 %, 2.7 % and 2.4 % respectively. Even though the non-repeatability values are within the desired limits[12] of such sensor systems, the repeatability difference between the amplitude and angle modulation techniques is noticeable. Generally a number of factors can influence the quality of the results of a system such as the type of equipment that is used, the operator, environmental or equipment temperature or

G. S. Katranas, "Design and Development of Bilayer Sensor Systems for Biomedical and Automotive Applications", Ph.D. Thesis, Cardiff University.

the presence of electric/magnetic fields[13]. In the *AM* technique this undesirable interference is superimposed on the modulated signal as seen in Eq. 5-1.

$$v_{AM} = [V_c + V_m \cdot \cos(\omega_m \cdot t)] \cdot \cos(\omega_c \cdot t) + \sum V_{noise} \cdot \cos(\omega_{noise} \cdot t) \qquad 5\text{-}1$$

Even though there is a filtering stage in the *AM* demodulation process, the noise influence is still present. Amplitude variations due to the addition of noise on the amplitude of the a *FM* or *PM* signal do not influence the modulation waveform as the sensor information signal is conveyed as changes in frequency or phase. The main sources of any non-repeatability in angle modulation systems are the circuit component fluxuations (flicker noise)[14] and the input noise of the amplifier[15] (Appendix E) that cause minor frequency instability in the oscillator's operation.

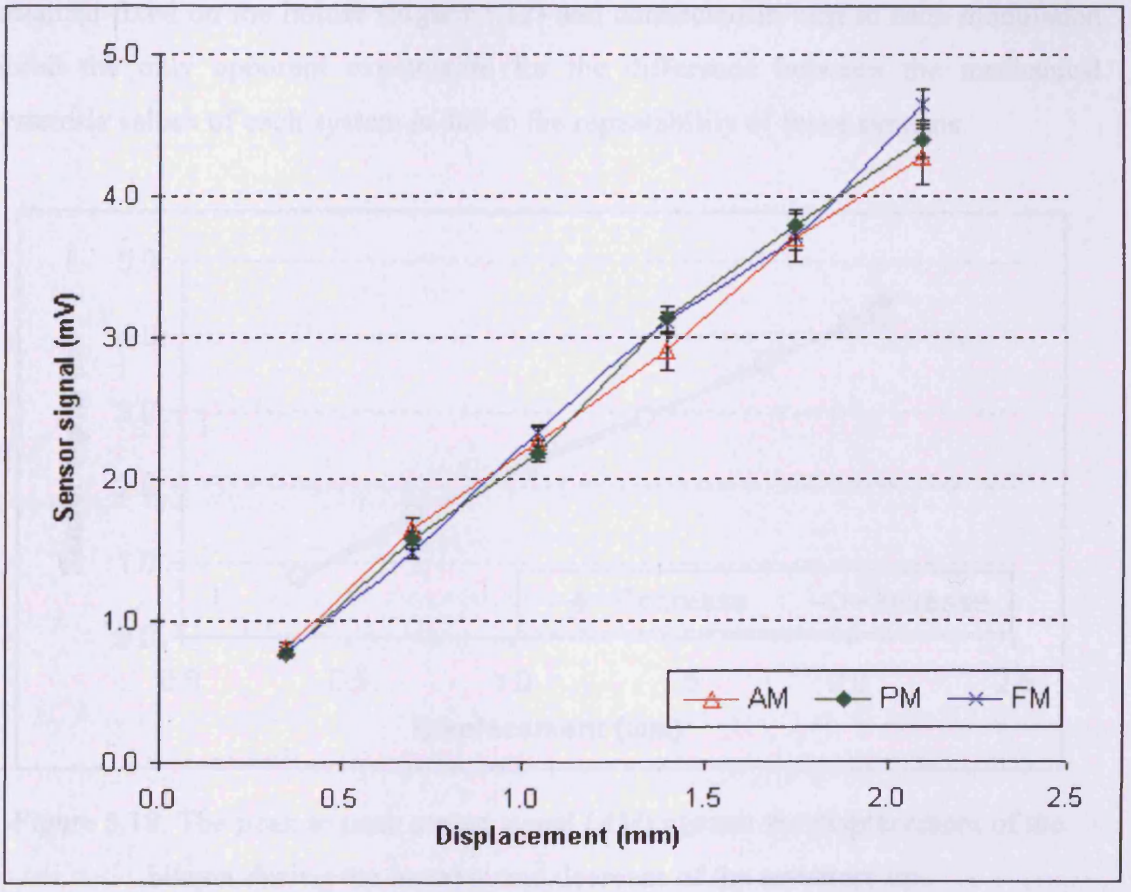

Figure 5.17: The peak to peak output voltage characteristics against peak to peak displacement of the bilayer sensor for all three modulation principles.

G. S. Katranas, "Design and Development of Bilayer Sensor Systems for Biomedical and Automotive Applications", Ph.D. Thesis, Cardiff University.

The results in Figure 5.17 also showed that all three modulation systems have a linear behaviour with a square correlation coefficient value of sc^2 = 0.99. The data examination was performed using standard statistical methods[16].

Materials under the application of a cyclic stress (within their elastic region) may show a distinct difference between the loading and unloading (return) path. This defect in Hooke's law is termed mechanical hysteresis[17]. In order to examine the influence of mechanical hysteresis in the measurement system the difference between the increase and decrease of the amplitude of the actuators tip and hence the increase and decrease of the sensors signal was examined. Five consecutive readings were taken for each modulation principle and the average increase and decrease curves were plotted. The mechanical hysteresis was found to be 3.6 %, 2.2 % and 1.8 % for the *AM* (Figure 5.18), *PM* (Figure 5.19) and *FM* (Figure 5.20) respectively. These values are within the repeatability range of each modulation system. Since the sensor remained fixed on the holder (Figure 5.12) and connected in turn to each modulation circuit the only apparent explanation for the difference between the mechanical hysteresis values of each system is due to the repeatability of these systems.

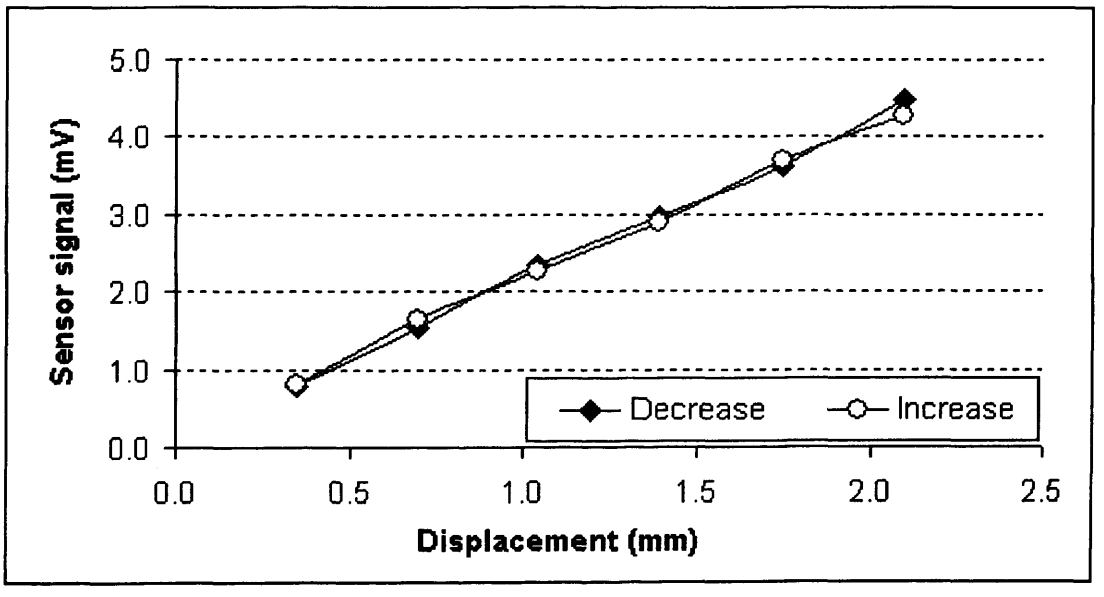

Figure 5.18: The peak to peak sensor signal (*AM*) against the displacement of the bilayer during the increase and decrease of the actuators tip.

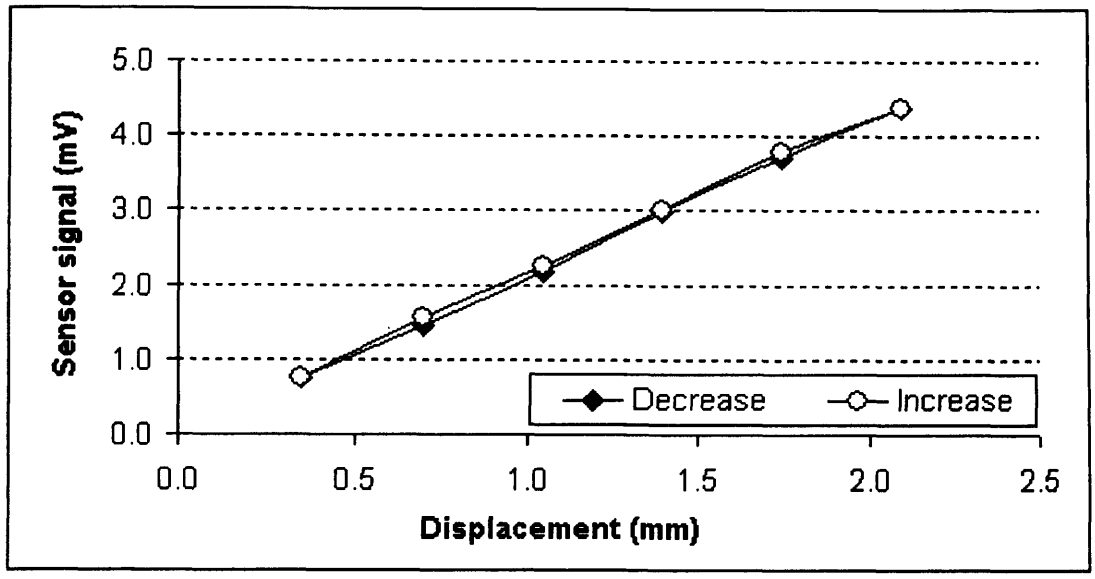

Figure 5.19: The peak to peak sensor signal (*PM*) against the displacement of the bilayer during the increase and decrease of the actuators tip.

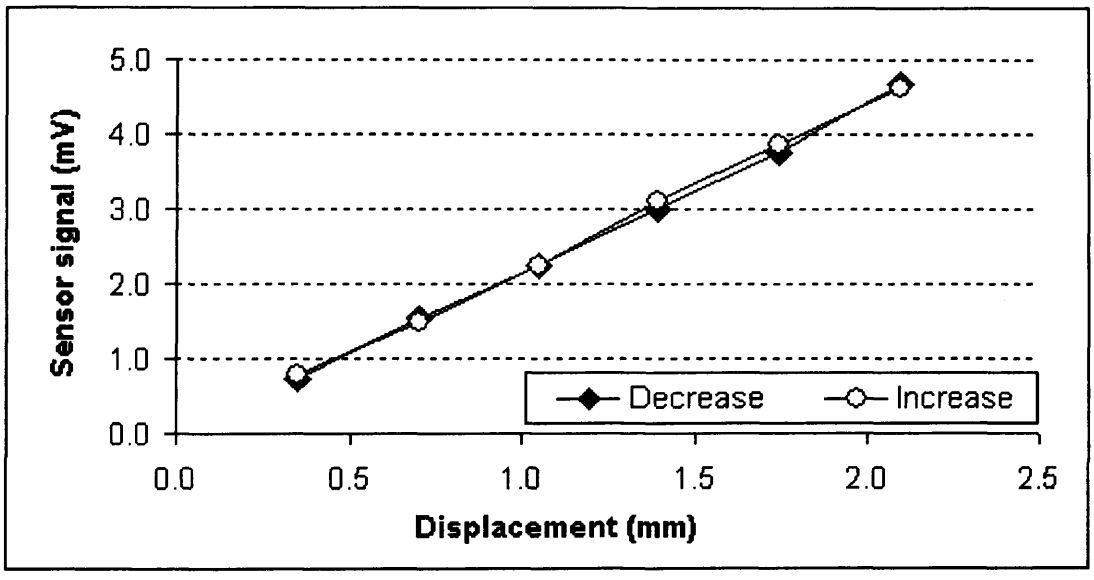

Figure 5.20: The peak to peak sensor signal (*FM*) against the displacement of the bilayer during the increase and decrease of the actuators tip.

By examining the performance of all three modulation techniques in this section (5.3) the preferred method for conveying the bilayer displacement information can be selected. It is important to note that all three principles were used to successfully convey the sensor information signal for displacements in the range of 0.35 mm to 2 mm (Figure 5.14, Figure 5.15, Figure 5.16 and Figure 5.17).

Although the *AM* technique can be effectively used in sensor systems, its susceptibility to noise, especially in the presence of electric or magnetic fields, can deteriorate the signal quality. The effect of noise is made apparent by examining not only the non-repeatability of the *AM* signal (4.6 %) which is almost double of that of the angle modulation (2.7 % for *PM* and 2.4 % for *FM*) but also the modulation parameter deviation. In order to illustrate the effect of noise on each modulation technique the effect of the bilayer sensor displacement on the deviation of modulation parameters in *AM*, *PM* or *FM* needs to be quantified. For example, in the case of the *AM* principle, at a 2 mm displacement the sensor will produce a peak to peak ΔV deviation (20 μV) from V_R (1 V) equal to:

$$\frac{\Delta V}{V_R} = \frac{20\mu V}{1V} = 20 \cdot 10^{-6} \qquad 5\text{-}2$$

In the laboratory environment in which the sensor was tested the ambient noise level was of the order of ~5 μV (peak to peak). This is significant when compared to the 20 μV amplitude variation of the bilayer sensor signal. Therefore when increased levels of electric or magnetic fields are present the bilayer sensor information can be buried within the noise.

In contrast the angle modulation methods display higher deviations that the *AM*. At 2 mm displacement the sensor will produce a 0.1 kHz Δf for the *FM* and a 3.5° $\Delta\phi$ for the *PM*:

$$\frac{\Delta f}{f_R} = \frac{0.1kHz}{5kHz} = 0.02 \qquad 5\text{-}3$$

$$\frac{\Delta \phi}{\phi_R} = \frac{3.5°}{180°} \approx 0.02 \qquad 5\text{-}4$$

The higher change in parameter deviation (Δf_R for *FM* or $\Delta \phi_R$ for *PM*) and the fact that noise interference is not a significant issue in angle modulation, improves the quality of the sensor signal and its sensitivity. In applications such as mapping the hemo-dynamic changes of the carotid artery the essence is to record the exact details

of the heart beat waveform. Thus, it is very important that the sensor information signal deviates as less as possible from the actual displacement caused from the arterial expansion and contraction. The sensor signal "quality" was examined by comparing the deviation between the *LDV* output signal and the *AM*, *PM* and *FM* in Figure 5.14, Figure 5.15 and Figure 5.16 respectively. Comparing with the *LDV* output signal the *AM* waveform showed that it has almost twice the average (1.7 %) and maximum (3.9 %) deviation in contrast to the *PM* (average 1 %, maximum 2.2 %) and *FM* (average 0.9 %, 2 % maximum). Thus, for reasons of noise susceptibility and signal quality, angle modulation is preferred over the *AM*.

Comparing the sensor signal quality (deviation from the *LDV* waveform) between the two angle modulation principles the difference is ~10 % with the *FM* marginally outperforming the *PM*. Also taking in to consideration the *PM* method requires the *RC* tank components to be "hand-picked" to have values as close as possible in order to reduce the oscillator's frequency/phase drift. The drift in the phase modulation technique can be further compensated by increasing the sampling rate of the software. The increase of sampling rate enhances the resolution of the acquired waveform and the software is able to filter the drift more effectively. Increasing the sampling rate causes a rise in the signal processing time as more samples (points) need to be processed. In applications such as airflow measurement in car intake (automotive) or monitoring the cardio-respiratory activity of a patient (biomedical), continuous data acquisition, signal processing and quality are of paramount importance. Hence preferred method for conveying the bilayer displacement information is by the use of the *FM* principle.

5.4 Optimisation of Bilayer Sensor

The bilayer sensor used in the measurement system was designed according to the principles of the preferred modulation method (*FM*). When placed in the modulation circuit (Colpitts oscillator), the bilayer sensor acts as its inductive component. Any change ΔL in the inductance L of the pickup coil (sensor) will shift the operating/oscillating frequency from f to $f + \Delta f$. Hence, frequency modulation is

achieved. The inductor along with the two parallel capacitors set the frequency of operation of the circuit. The capacitors where chosen to be $C_1 = C_2 = 1$ μF, in order to keep the circuit frequency between 1 kHz to 10 kHz. For signal quality purposes (to avoid signal aliasing) the sampling rate must be 20 samples per Hertz which means that at 10 kHz there will be a need to acquire 200,000 samples per second (200 kS/s). Even though the data acquisition card can accept up to 800 kS/s, the processing time needed is increased rapidly. Taking in consideration the capacitor value and the desired frequency range the combination of coil parameters and excitation current were optimised, to provide the largest change of inductance and hence the largest change of relative permeability.

An essential part of the sensor comparison and parameter optimisation is the standardisation of the fabrication procedure (Figure 5.21a).

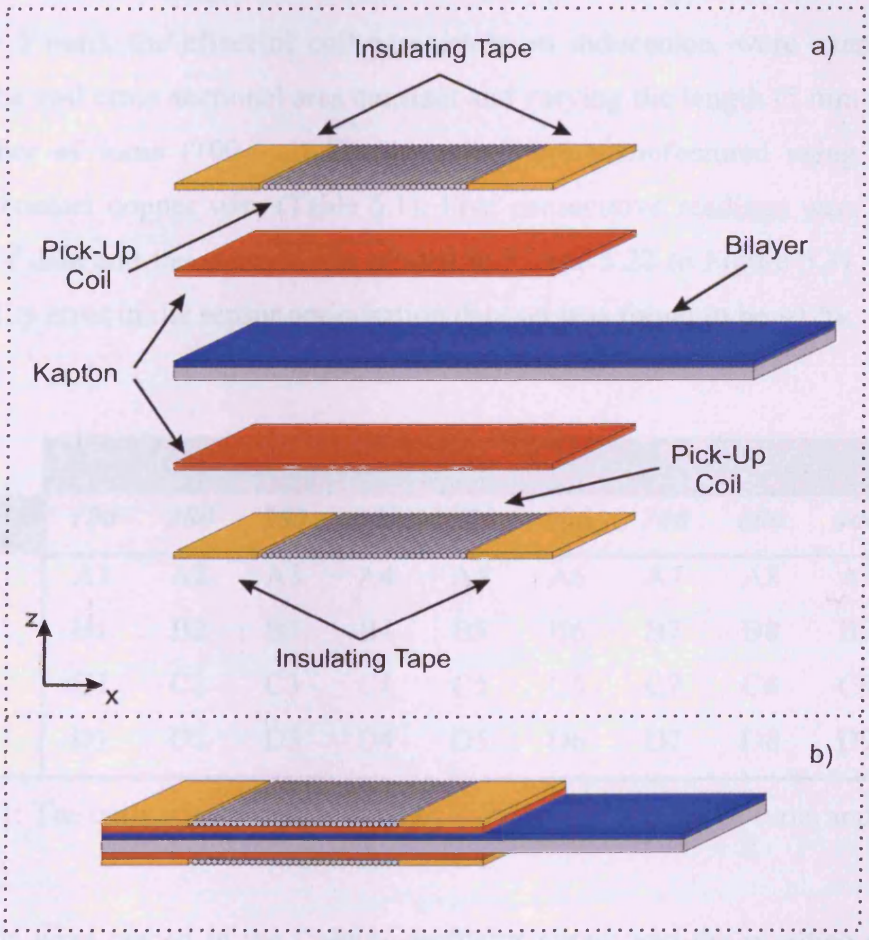

Figure 5.21: A longitudinal cross sectional view in the z-x plane (not in scale) of a) the of sensor components (exploded view) and b) the assembled sensor.

The sensor's former was constructed by placing two Kapton® layers (ℓ = 30 mm, w = 6 mm, th = 75 μm) on each side of the bilayer strip. The Kapton® polyimide film was chosen as a former due to its ability to maintain its excellent mechanical properties at a wide range of temperatures (-269 °C to +400 °C)[18] (Appendix E). The two Kapton® layers were fixed by wrapping layers of narrow width (w = 3 mm) insulating tape around both its ends; the tape layers depend on coil thickness. The area between the two insulating tapes is where the coil will be wound. The tape arrangement also serves as an aid during the winding of the copper wire (coil) as it maintains the desired coil length and holds the turns in place during the sensor operation. The resulting product is a flexible flat coil that can maintain its shape (Figure 5.21b). The sensor design also provides a fast and easy way to interchange bilayer strips with different magnetic characteristics.

Using as a reference magnetic material a 28 μm thick Metglas® 2605SC[19] (ℓ = 40 mm, w = 5 mm), the effect of coil parameters on inductance, were examined. By keeping the coil cross sectional area constant and varying the length (5 mm – 20 mm) and number of turns (100 – 1000), 40 coils were manufactured using a 60 μm diameter enamel copper wire (Table 5.1). Five consecutive readings were taken for each set of data and the average was plotted in Figure 5.22 to Figure 5.31. The non-repeatability error in the sensor optimisation data set was found to be ~1 %.

	Turns									
Length	***100***	***200***	***300***	***400***	***500***	***600***	***700***	***800***	***900***	***1000***
5 mm	A1	A2	A3	A4	A5	A6	A7	A8	A9	A10
10 mm	B1	B2	B3	B4	B5	B6	B7	B8	B9	B10
15 mm	C1	C2	C3	C4	C5	C6	C7	C8	C9	C10
20 mm	D1	D2	D3	D4	D5	D6	D7	D8	D9	D10

Table 5.1: The coils were manufactured by varying the number of turns and length.

These coils were placed in the Colpitts oscillator circuit and the resulting operating frequency and current through the coil were measured. An approximation of the

G. S. Katranas, "Design and Development of Bilayer Sensor Systems for Biomedical and Automotive Applications", Ph.D. Thesis, Cardiff University.

relative permeability value was calculated from the measured frequency and current and through the use of Eq. 5-5 (Eq. 4-37) and Eq. 5-6 (Eq. 3-15):

$$f = \frac{1}{2\pi \cdot \sqrt{\frac{L \cdot C_1 \cdot C_2}{C_1 + C_2}}} \qquad 5\text{-}5$$

$$L = \mu_0 \mu_r \cdot \frac{N^2 A}{\ell} \qquad 5\text{-}6$$

It is these values, illustrated in Figure 5.22 - Figure 5.26, that give an indication of the optimum coil parameters for the magnetic material in question. By looking at Figure 5.22 it can be seen that high values of relative permeability are recoded on longer coils at low numbers of turns, following Eq. 5-6.

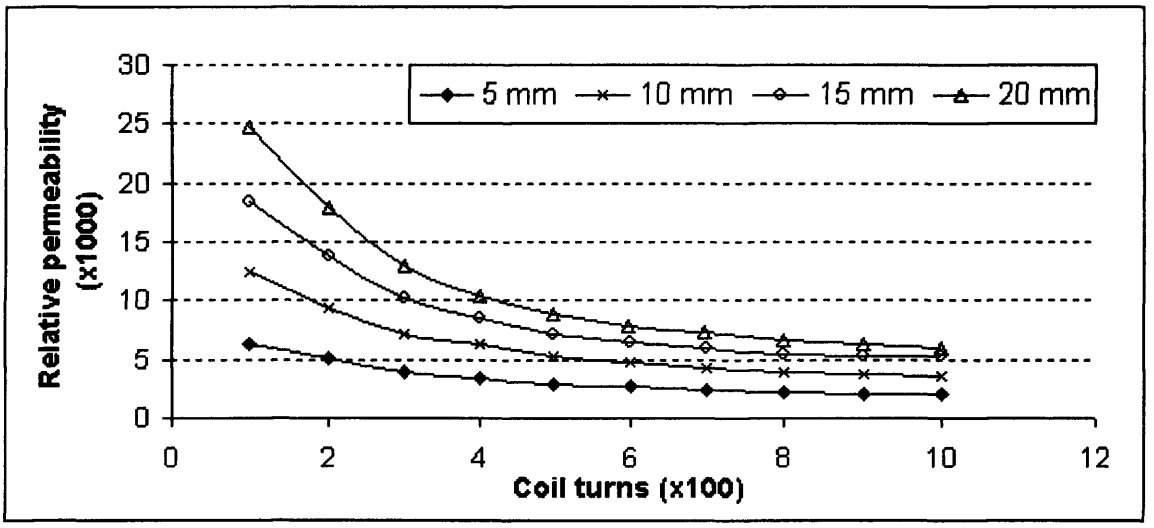

Figure 5.22: The effect of variation of coil length and number of turns on relative permeability (Sample 2605SC - 28 μm).

Figure 5.23 confirms that low turn coils (N = 200 - 400) are more suitable for sensors, since they display high values of current (compared with coils of high N), but it also shows that I increases as ℓ decreases as is expected from Eq. 5-7 (Eq. 3-1).

$$H = N\frac{I}{\ell} \qquad 5\text{-}7$$

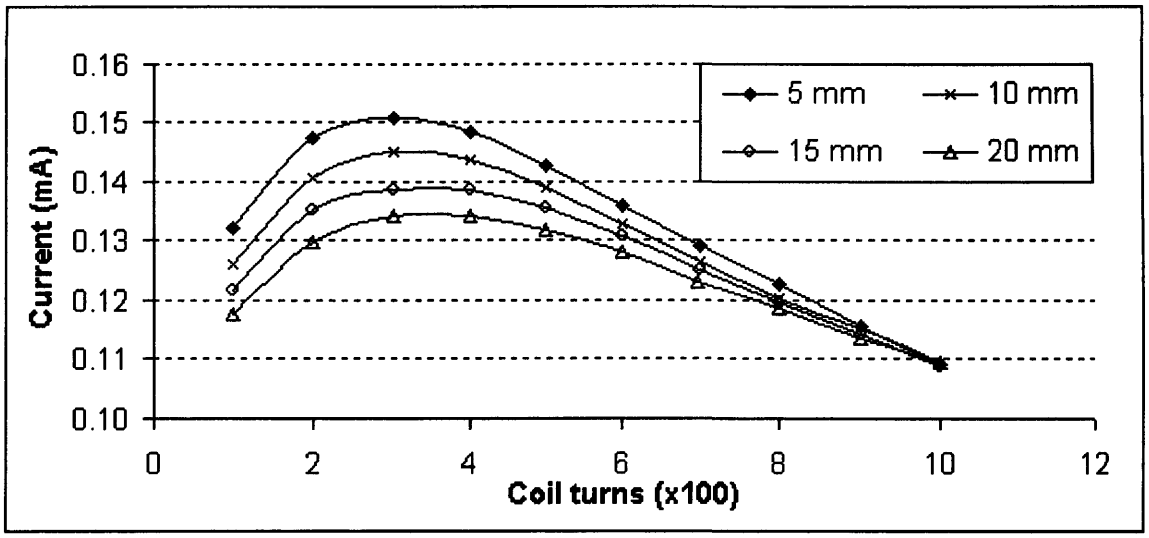

Figure 5.23: The effect of variation of coil length and number of turns on excitation current (Sample 2605SC - 28 μm).

From the results shown in Figure 5.22 and Figure 5.23 it is apparent that low number of turns is a desired parameter for the design of the sensor coil (using the 2605SC - 28 μm sample) as current reaches a peak using coils of 200 - 400 turns, regardless of coil length.

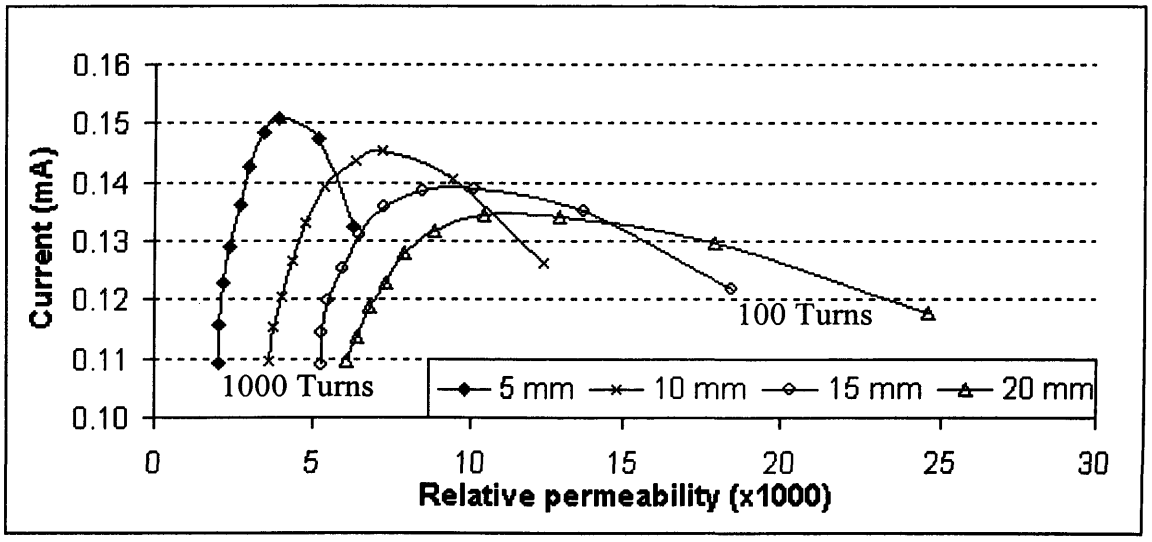

Figure 5.24: The effect of variation of coil length and number of turns on relative permeability and excitation current (Sample 2605SC - 28 μm).

The relationship between the current and relative permeability (Figure 5.24) reveals the optimum number of turns (using the 2605SC - 28 μm sample) which is found to be $N \approx 300$. Current and relative permeability need to be high as to ensure high levels of sensor sensitivity as expected in Eq. 5-6 and Eq. 5-8 (3-13):

$$v = -\mu_0 \mu_r \cdot \frac{N^2 A}{\ell} \cdot \frac{dI}{dt} \qquad 5\text{-}8$$

The data points on Figure 5.24 represent the number of turns which increases from right ($N = 100$) to left ($N = 1000$).

The next parameter to be decided was the length of the coil. Plotting I against μ_r (Figure 5.24) shows that, at 300 turns, longer coils may have lower current values (9 %) than the shorter but they present much higher amounts of μ_r (72 %). If the relative permeability is high then the $\Delta\mu_r$ will be high (high ΔL) and hence the sensor sensitivity will increase. Thus, a coil of N = 300 and ℓ = 20 mm would have the optimum dimensions needed for a sensor.

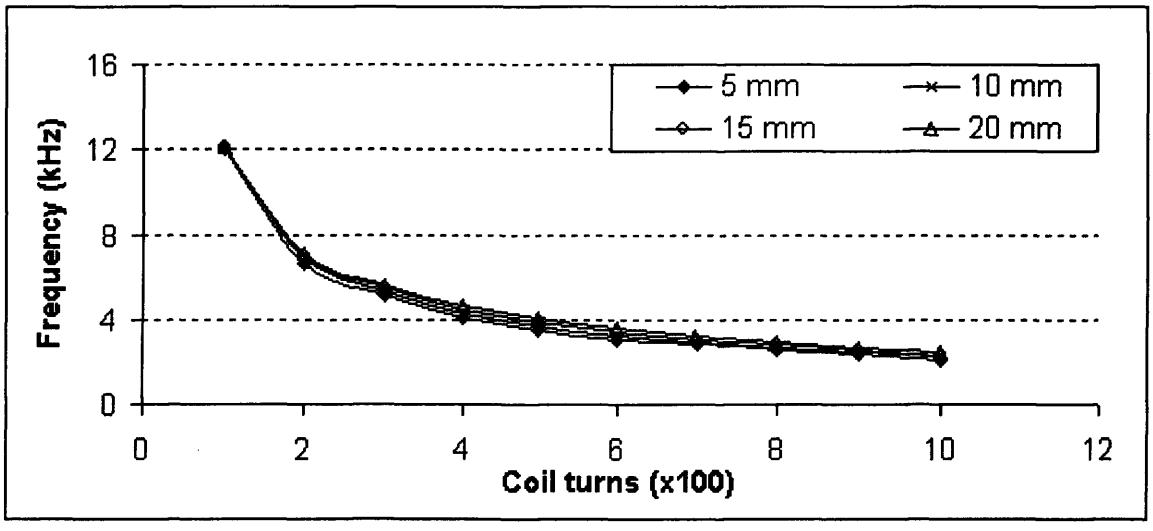

Figure 5.25: The effect of variation of coil length and number of turns on operating frequency (Sample 2605SC - 28 μm).

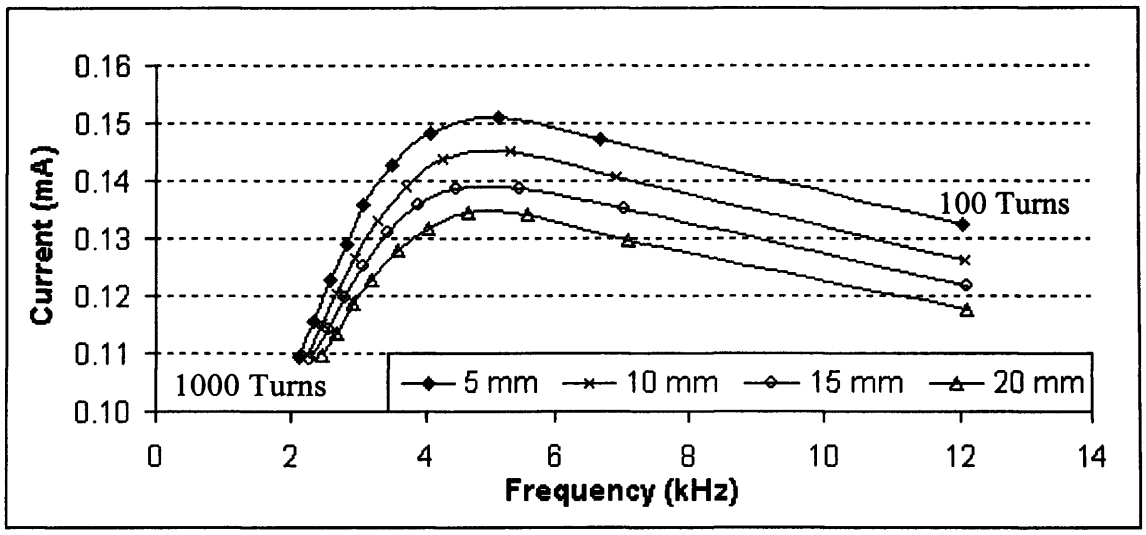

Figure 5.26: The effect of variation of coil length and number of turns on excitation current and operating frequency (Sample 2605SC - 28 μm).

From Figure 5.25 it can be seen that the operating frequency does change (decrease) with the increase of N, as expected from Eq. 5-5 and Eq. 5-6 but also from Figure 5.26 is evident that using a 300 – 400 turn coil the current peaks at 5 kHz.

The data points on Figure 5.26 represent the number of turns which increases from right ($N = 100$) to left ($N = 1000$).

At this operating frequency the sampling rate will be 100 kS/s which will approximately take 1 - 2 seconds for the software to display the information signal ensuring continuous real-time acquisition and process of the data. The data shown on Figure 5.22 to Figure 5.26 show the optimum parameter selection only for the 2605SC – 28 μm sample.

The measurement system can be used not only for the detection of stress/displacement but also for the evaluation of bilayer magnetic material for sensor applications. Hence, a comparison was made between two materials of different saturation magnetostriction at a range of thicknesses to conclude to an optimum coil dimension and magnetic material for the sensor. The materials used for this comparison were Metglas® 2605SC ($\lambda_s \approx 30 \cdot 10^{-6}$)[19] and Metglas® 2705M ($\lambda_s \approx 0$) [19] (Table 5.2) [20].

G. S. Katranas, "Design and Development of Bilayer Sensor Systems for Biomedical and Automotive Applications", Ph.D. Thesis, Cardiff University.

Metglas® Material	2605SC ($\lambda_s \approx 30 \cdot 10^{-6}$)			2705M ($\lambda_s \approx 0$)		
Metglas® Thickness (μm)	28	12	2.9	24	5	2.9
Substrate	*Al*	*Al*	*CuBe*	*Al*	*CuBe*	*AlMg*
Substrate Thickness (μm)	75	75	25	75	25	30
Bilayer Fabrication	Adhesive	Adhesive	*RF*	Adhesive	*RF*	*RF*

Table 5.2: Bilayer strip fabrication method and layer thickness.

The 28 μm thick 2605SC was reduced in thickness down to 12 μm by means of mechanical polishing. As expected from Eq. 5-6 the reduction in cross sectional area of the sensor due to the decrease of magnetic material thickness increases the values of relative permeability (Figure 5.27). The exponential decrease of relative permeability with the increase of number of turns is mainly due to the N^2 term in Eq. 5-6. The highest values of relative permeability are recorded between $N = 100 - 300$.

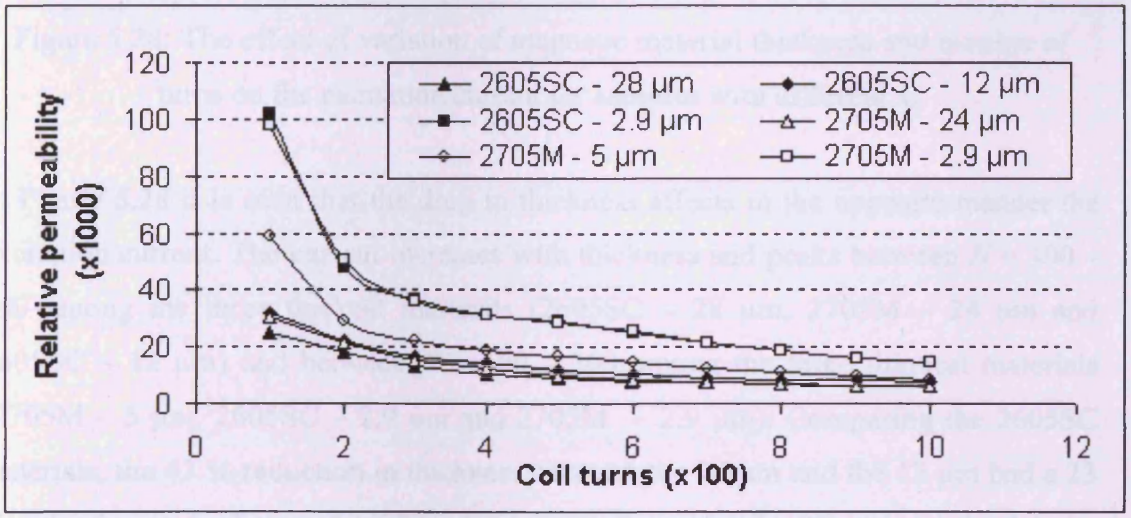

Figure 5.27: The effect of variation of magnetic material thickness and number of turns on the relative permeability for samples with different λ_s.

In Figure 5.27 the effect of magnetic material choice (2605SC, 2705M) and its thickness (28 μm – 2.9 μm) on the resulting relative permeability is studied. An indication of the effect of thickness on relative permeability can be seen by comparing the 2605SC – 28 μm and the 2605SC - 2.9 μm. For this material the ~10 times reduction in thickness showed a ~3 times (averaged from $N = 100 - 1000$) increase in μ_r. This difference is non-linear and depends on the materials properties, operating

frequency and the current induced in the coil. A comparison between strips that have similar dimensions and are of different magnetic material (2705M – 2.9 μm and 2605SC - 2.9 μm) can also be made. On average the 2705M displayed a μ_r 2.4 % higher than 2605SC due to its greater as cast *DC* permeability [19, 20].

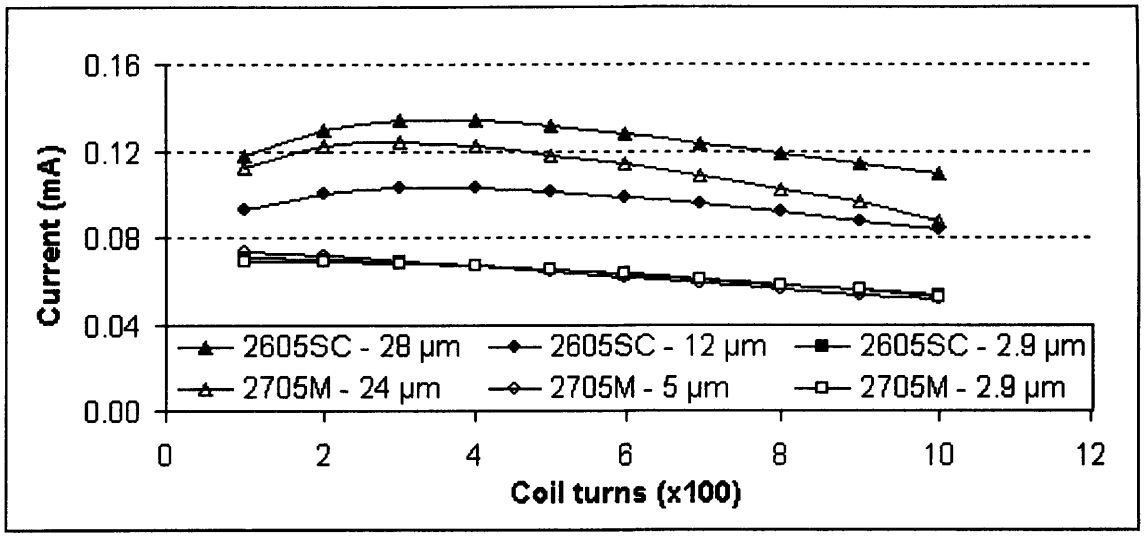

Figure 5.28: The effect of variation of magnetic material thickness and number of turns on the excitation current for samples with different λ_s.

In Figure 5.28 it is seen that the drop in thickness affects in the opposite manner the excitation current. The current increases with thickness and peaks between N = 300 – 400 among the three thickest materials (2605SC – 28 μm, 2705M – 24 μm and 2605SC – 12 μm) and between N = 100 – 300 among the three thinnest materials (2705M – 5 μm, 2605SC – 2.9 μm and 2705M – 2.9 μm). Comparing the 2605SC materials, the 43 % reduction in thickness between the 28 μm and the 12 μm had a 23 % reduction in *I* whereas the 90 % decrease in *th* among the 28 μm and the 2.9 μm produced about 50 % less current. From the examination of the 2507M materials the reduction of thickness by 79 % (from 24 μm and the 5 μm) leads to a 43 % current fall and the decrease of *th* by 88 % (from 24 μm and the 2.9 μm) shows a 44 % drop in *I*. The effect of thickness reduction to current between the 2605SC and the 2705M can be performed by comparing both the 2.9 μm samples. The difference between these is below the 1 % repeatability of the data, hence the 2605SC – 28 μm and 2705M – 24 μm were examined instead. Even though there is a 4 μm difference between the two materials, the thickness reduction from 28 μm and 24 μm to 2.9 μm is of similar level

89 ± 1 %. It can be seen that even though the 2705M displays less current loss, the 2605SC does display higher values of λ which gives an advantage for selection as the magnetic material for the bilayer sensors.

Both Figure 5.27 and Figure 5.28 show that the highest amounts of I and μ_r occur as expected with low turn coils. By plotting the excitation current against the relative permeability, the effects of thickness and number of turns are made evident (Figure 5.29). The data points on Figure 5.29 represent the number of turns which increases from right (N = 100) to left (N = 1000). The first thing that is made apparent from the I versus μ_r relationship is that thinner materials (2705M – 5 μm, 2605SC – 2.9 μm and 2705M – 2.9 μm) display large amounts of relative permeability and smaller quantity of current compared to the thicker samples (2605SC – 28 μm, 2705M – 24 μm and 2705M – 12 μm).

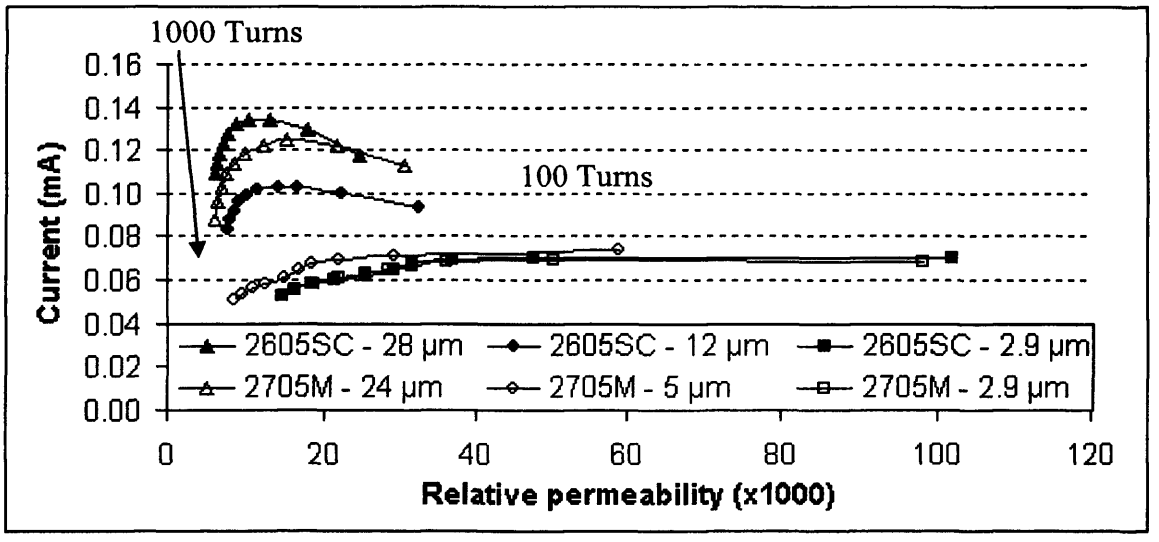

Figure 5.29: The effect of variation of magnetic material thickness and number of turns on I and μ_r for samples with different λ_s.

The behaviour of the system shows that the current is reversely proportional to the relative permeability (Eq. 5-8). Therefore a "balance" between current and relative permeability will define the optimum coil dimensions and material for the bilayer sensor system. From the results it is estimated that low turn coils (N = 100 - 400) are more suitable for sensors, since they display high values of I and μ_r (compared with coils of high N).

By examining Figure 5.30 and Figure 5.29 it can be seen that the low turn coils (N = 100 – 300) do produce high μ_r but they also generate operating frequencies above 10 kHz depending on the thickness of the sample. An operating frequency above 10 kHz reduces significantly the data processing of the software and continuous real-time acquisition and process of the data is no longer possible. This upper frequency limit of the system shows that a sensor using magnetic material under ~5 μm in thickness can have as a minimum 300 turns; less turns will have f > 10 kHz.

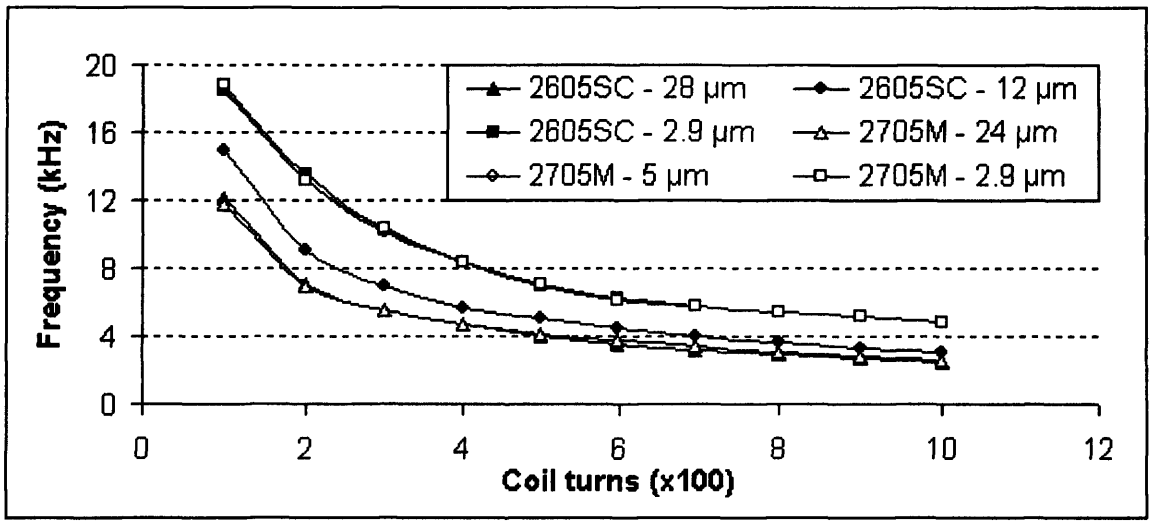

Figure 5.30: The effect of variation of magnetic material thickness and number of turns on the operating frequency for samples with different λ_s.

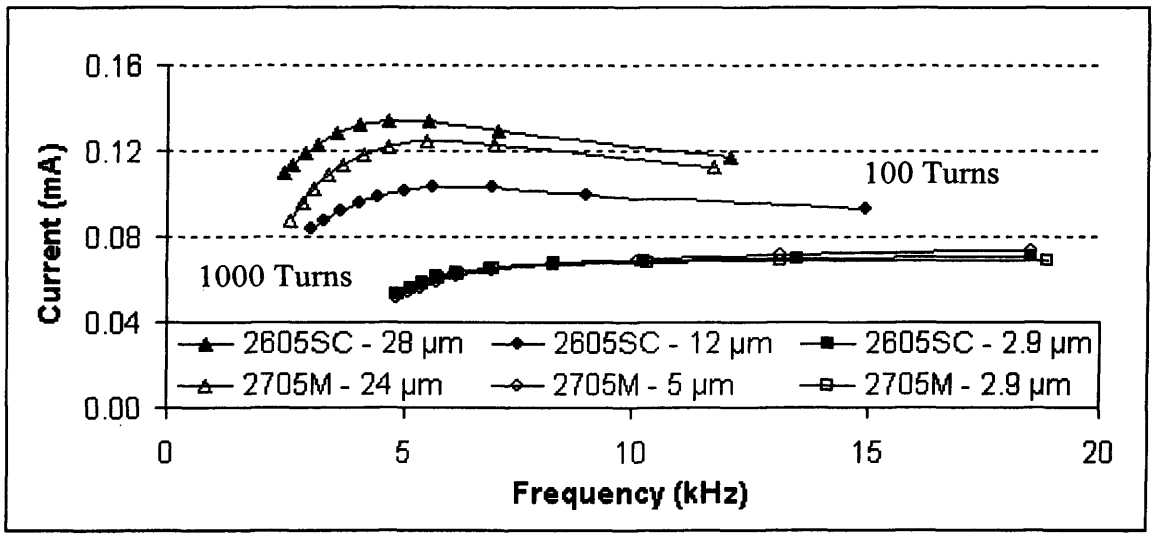

Figure 5.31: The effect of variation of magnetic material thickness and number of turns on current and frequency for samples with different λ_s.

The examination of Figure 5.31 shows that the samples with less thickness, and hence less cross sectional area of magnetic material in the coil, produce higher operating frequencies as its expected from Eq. 5-6 and Eq. 5-5. Taking in consideration the limit of the system that prevents the use of coils that generate $f > 10$ kHz it can be seen that the maximum current occurs at ~300 turns for all samples. The operating frequency with $N = 300$ for the 2605SC – 28 μm, 2705M – 24 μm and 2705M – 12 μm samples will be around 5.5 kHz whereas for the 2705M – 5 μm, 2605SC – 2.9 μm and 2705M – 2.9 μm it will be approximately at the 10 kHz limit.

In the investigation of the data illustrated from Figure 5.22 to Figure 5.31 the coil's length, thickness, number of turns and magnetic material were varied and the performance behaviour (current, relative permeability and frequency) was examined in order to optimise the design of bilayer sensor. From the parameters used in the measurement system and the materials and sample thickness tested (Table 5.2), the optimum coil number of turns and length were $N = 300$ and $\ell = 20$ mm. To further verify that these are the optimum coil parameters, four sensor configurations (Table 5.3) were selected to be tested using the measurement system with the actuator set-up (Figure 5.32). Another parameter to be evaluated will be the performance of the two materials (2605SC and 2705M) and the effect of thickness on the sensor sensitivity.

	(*i*)	(*ii*)	(*iii*)	(*iv*)	(*v*)
Metglas® Material	2605SC				2705M
Metglas® Thickness (μm)	28	2.9	28	28	2.9
Turns	300	300	300	1000	300
Length (mm)	20	20	5	20	20

Table 5.3: The four coils used in the measurement system to verify the selected optimum coil parameters.

As expected from Eq. 5-6, sensor (*i*) displays increased voltage output (average increase of ~10 times) than (*ii*) since the thickness and hence the cross sectional area of the magnetic material in the coil is ~10 times higher. The thicker material may have higher sensitivity but a thin strip has lower stiffness and hence will bend to smaller displacements (low forces). This is useful in applications such as detecting the hemo-dynamic changes of the heart beat where the skin curvature changes are dependant on the blood pressure in the vessel. If a material of high stiffness is used,

the bending force exerted on the bilayer from the skin curvature changes will be too small and unable to bend the strip.

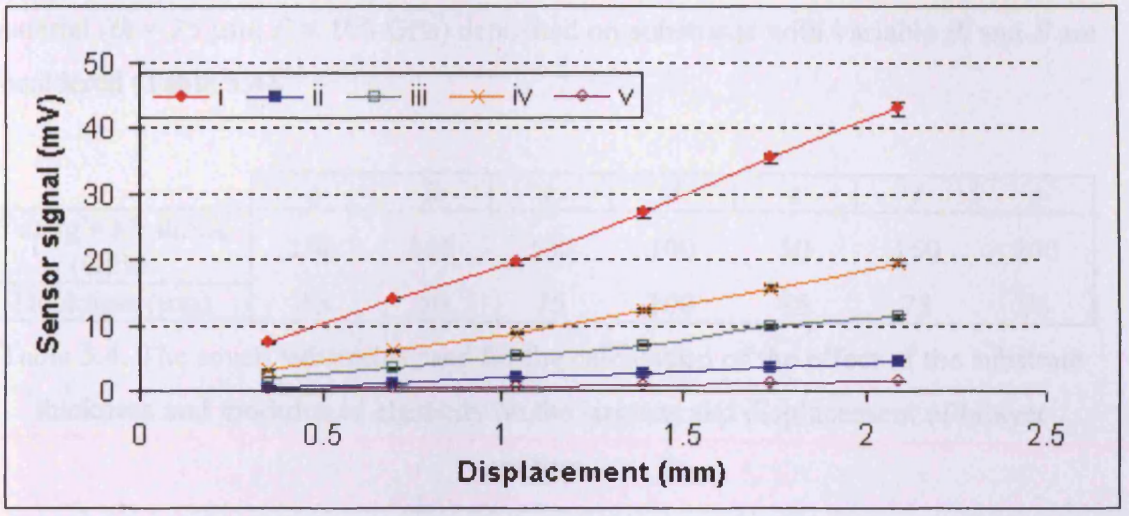

Figure 5.32: The peak to peak output voltage characteristics against peak to peak displacement of bilayer sensors, using the configurations seen in Table 5.3.

Comparing sensor (*i*) and (*iii*) the effect of coil length reduction does produce lower output voltage (average ~26 %) which is explained by Eq. 5-7 and the results from Figure 5.24. Increasing the number of turns on a coil will decrease the output voltage (average ~47 %) as seen from sensor (*i*) and (*iv*), which verifies the results of Figure 5.29. Also from Figure 5.32 it was seen that sensor (*ii*) with the 2605SC ($\lambda \approx 30 \cdot 10^{-6}$) outperformed by ~65 % the (*v*) with the 2705M ($\lambda \approx 0$). Thus, the effect of materials with high saturation magnetostriction was noted, and the 2605SC was chosen for use in bilayer sensors. The selected optimum coil parameters seem to give the highest output voltage compared with other configurations.

5.5 Effect of Substrate Parameters on Stress and Displacement

Regarding the selection of the optimum thickness of the magnetic material or the substrate, that will depend on the application of the bilayer sensor (desired strip elasticity) as well as any need for its miniaturisation. By performing a brief theoretical examination using finite element modelling software (*FEM*), on the effect of the

substrate thickness and modulus of elasticity on the stresses and displacement of bilayer sensors, useful conclusions can be drawn[21]. For this assessment seven bilayer strips (ℓ = 20 mm, w = 5 mm), in cantilever configuration, with a random magnetic material (th = 25 μm, E = 100 GPa) deposited on substrates with variable th and E are considered (Table 5.4).

	a	*b*	*c*	*d*	*e*	*f*	*g*
Young's Modulus (GPa)	100	100	100	100	50	150	200
Thickness (μm)	25	50	75	100	75	75	75

Table 5.4: The seven substrates used for the calculation of the effect of the substrate thickness and modulus of elasticity on the stresses and displacement of bilayer sensors.

By using a force of F = 0.1 N, Eq. 5-9 (Eq. 2-32) and Eq. 5-10 (Eq. 2-33) will give the maximum stress (in the magnetic layer) and tip displacement for each of the bilayer strips:

$$\sigma_t = M \cdot y \cdot \left(\frac{E_1 + E_2 + \cdots + E_n}{E_1 \cdot In_1 + E_2 \cdot In_2 + E_n \cdot In_n} \right) \qquad 5\text{-}9$$

$$\zeta = \frac{F \cdot \ell^3}{3 \cdot (E_1 \cdot In_1 + E_1 \cdot In_1 + \cdots + E_n \cdot In_n)} \qquad 5\text{-}10$$

By keeping F (and therefore σ constant) and increasing E from 50 GPa to 200 GPa, (strips *e*, *c*, *f*, *g*), the stresses on the magnetic material rise while the displacement is reduced due to the growing bilayer stiffness (Figure 5.33). The four times increase of E caused a 60 % decrease in displacement, ζ, and a 28 % increase in stress. Since the output voltage of the measurement system is dependant on stress then it will follow accordingly.

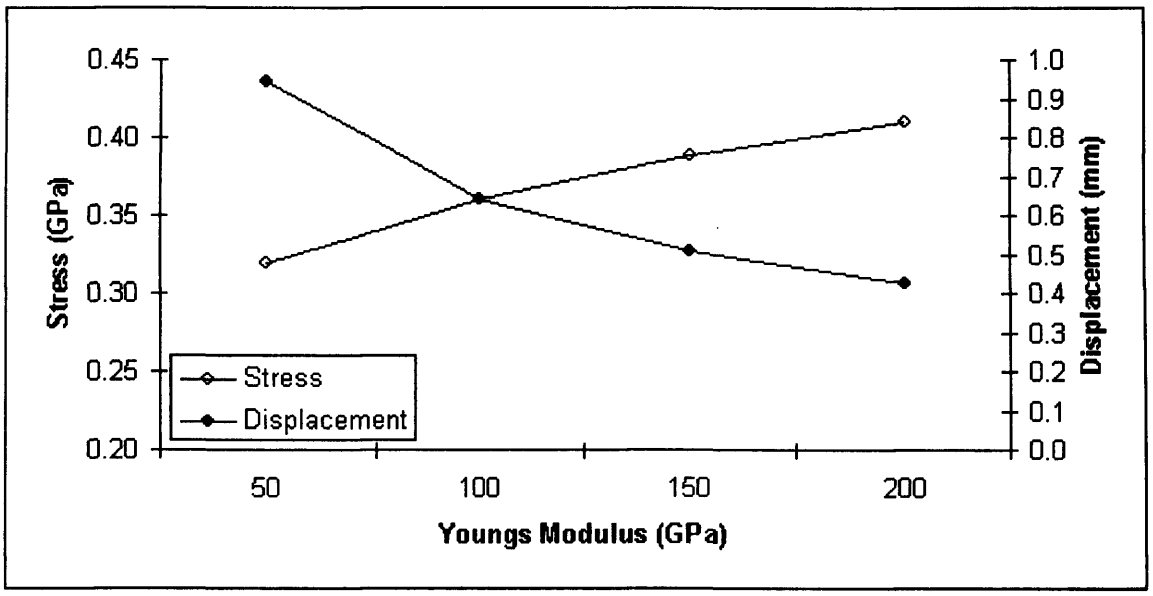

Figure 5.33: The stress and tip displacement plotted as a function of the substrates' modulus of elasticity.

A substrate with higher E does not imply that this bilayer can be used in all the sensor applications. In situations where the displacement force is small (heartbeat rate monitoring), a stiff bilayer will suppress it without bending; resulting in little or no sensor signal.

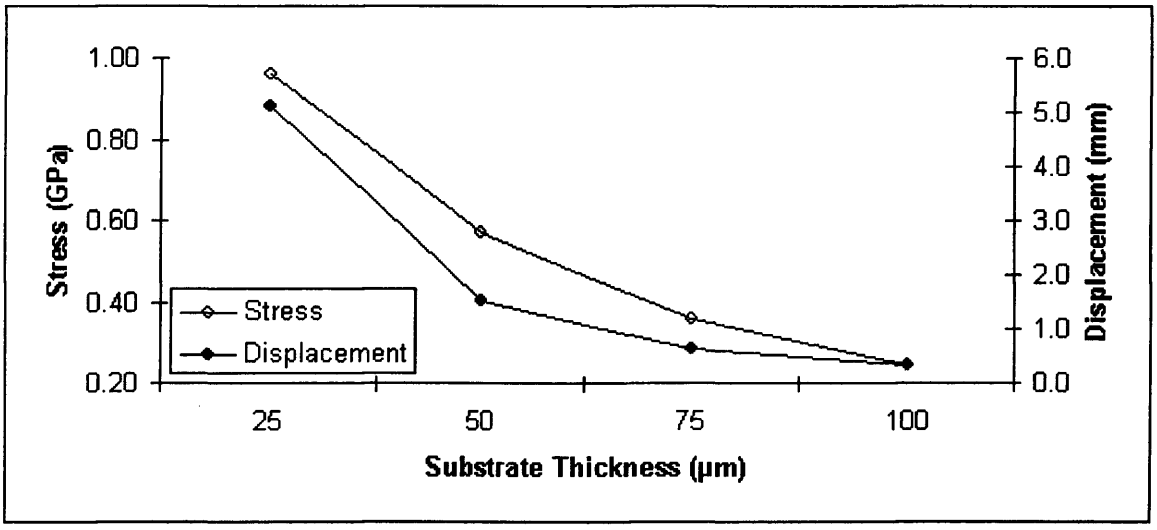

Figure 5.34: The stress and tip displacement plotted as a function of the substrates' thickness.

Increasing the thickness of the substrate from 25 μm to 100 μm (strips *a*, *b*, *c*, *d*), and keeping *F* constant, will give rise to the cross sectional area of the bilayer strip, Eq. 5-11 (Eq. 2-17) and Eq. 5-12 (Eq. 2-19), and hence change the value of inertia (Figure 5.34):

$$In_{y'} = d^2 \cdot A + In_y + In_c \qquad 5\text{-}11$$

$$In = \frac{w \cdot h^3}{12} \qquad 5\text{-}12$$

Since the stiffness of a material is defined according to the product of $E \cdot In$ (Chapter 2), the increase of the inertia due to the four times increase of *th*, will produce 75 % lower stress (Eq. 5-9 and Eq. 5-10). At the same time the tip displacement of the bilayer strip will be reduced by 94 % as the substrate thickness grows. A substrate with high thickness should be selected for applications where the displacement forces are large, such as measuring airflow in a car engine intake. These forces are usually large enough to bend a bilayer strip, of high stiffness, thus producing a voltage output which can be translated into an information signal for airflow measurements.

5.6 Thermal Stability

To ensure thermal stability of bi-layer thin films the materials need to have approximately identical thermal expansion coefficients, *e*. If the thermal expansion coefficients of the materials are chosen to be notably different then due to a temperature increase the material with the largest *e* will expand disproportionally from the other, thus producing unwanted curvature increase in the strip. This is the reason why, in previous works, bilayer sensors have been used as thermal sensors[22, 23].

In order to examine the thermal stability of the sensors and *FM* measurement system, a bilayer strip was fabricated with two materials with different thermal expansion coefficients using the *RF* sputtering method. The bilayer sensor used consisted of an

amorphous magnetic film, 2.9 μm thick, deposited from a $Fe_{81}B_{13.5}Si_{3.5}C_2$ target (Metglas 2605SC) using the *RF* magnetron sputtering technique onto a 25 μm non-magnetic layer *CuBe* layer. The strip was inserted in an $N = 300$ turn, $\ell = 20$ mm coil made without the insulating tape as it cannot withstand the temperature range that the sensor will be subjected to. The thermal expansion coefficients of the bilayer strip were $e_1 = 5.9 \cdot 10^{-6}$ K^{-1} for the amorphous magnetic film 2605SC[19] and $e_2 = 17 \cdot 10^{-6}$ K^{-1} for the substrate *CuBe*[24]. The sensor and the actuator set-up were placed inside an environmental chamber[25] and subjected to a temperature increase up to 180 °C (Figure 5.35). The actuator was supplied with a range of low frequency (1 Hz - 6 Hz) sine waves, with variable peak to peak amplitudes from 1 V to 6 V. The resulting output peak to peak displacement ranged from 0.35 mm to 2 mm and gave an average peak to peak signal of 0.8 mV to 4.6 mV.

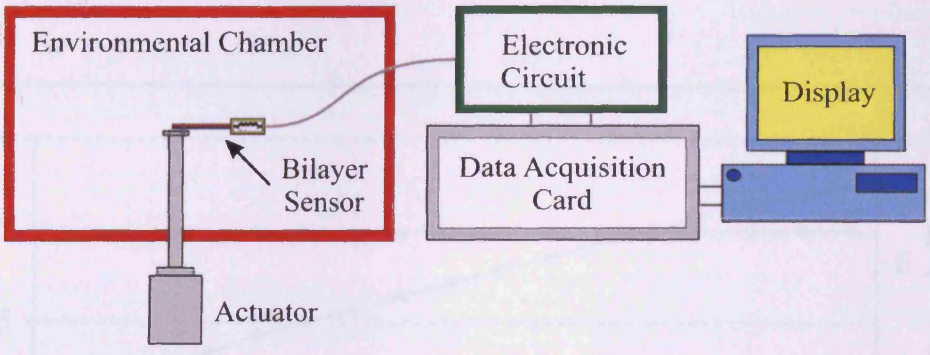

Figure 5.35: The bilayer sensor placed inside an environmental chamber[26, 27].

The output signal is determined by the degree of bending of the bi-layer which can be converted into a displacement reading. A comparison between the output at 25 °C and 180 °C showed that the repeatability of the results was 2.7 %. The results were linear in this temperature region with a square correlation coefficient value of $sc^2 = 0.99$ (Figure 5.36). The sensor signal at 180 °C shows average absolute values of 1.7 % deviation, and a 2.3 % maximum deviation, compared to the signal taken at 25 °C. These values are within the repeatability percentage of the *FM* system.

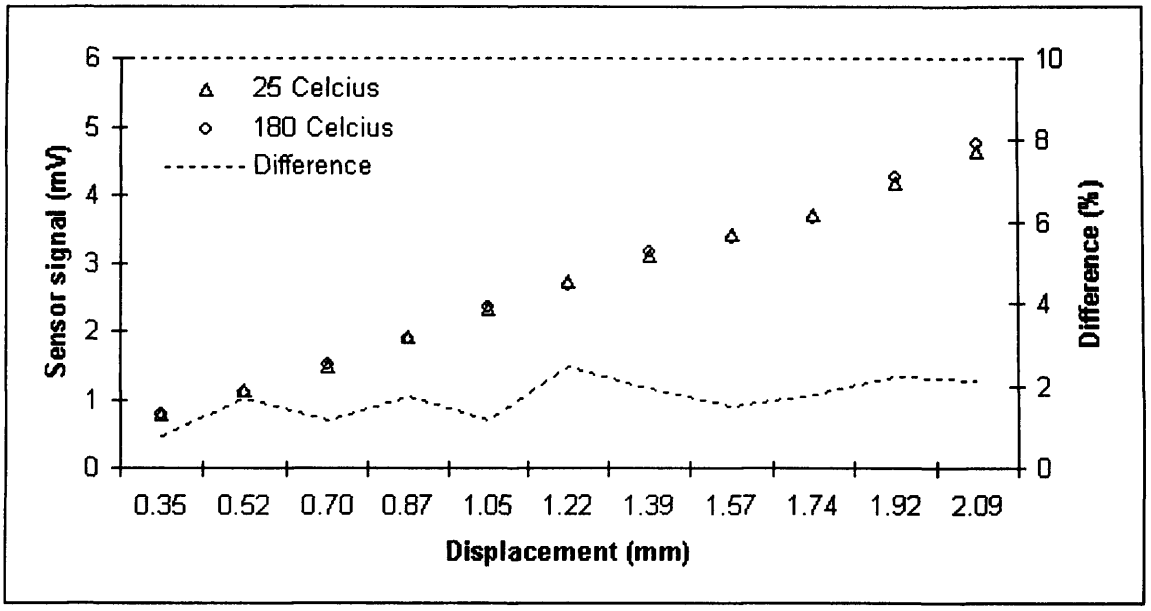

Figure 5.36: A comparison of the sensor signal at 25 °C and at 180 °C plotted together with the absolute value of their percentage difference.

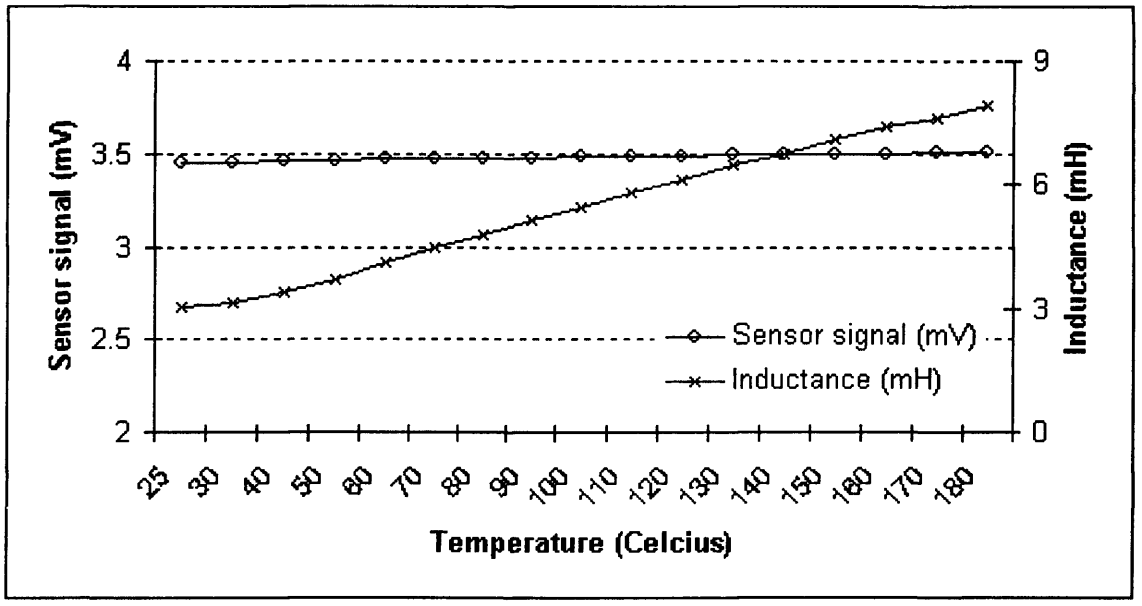

Figure 5.37: The rise of inductance due to temperature increase has minute effect to the peak to peak sensor signal taken at ~1.6mm peak to peak displacement.

As seen in Figure 5.37 the temperature increase caused a sharp and approximately linear rise, in region, of the inductance value, reaching 63 % change in inductance, ΔL, at 180 °C. This high ΔL increase is explained by the notable different thermal expansion coefficients of the two materials of the bi-layer strip. In contrast the peak to

peak sensor signal starts at 3.45 mV (at 25 °C) and shows a 1.7 % increase at 180 °C with a 0.009 % per 1 °C increase of temperature.

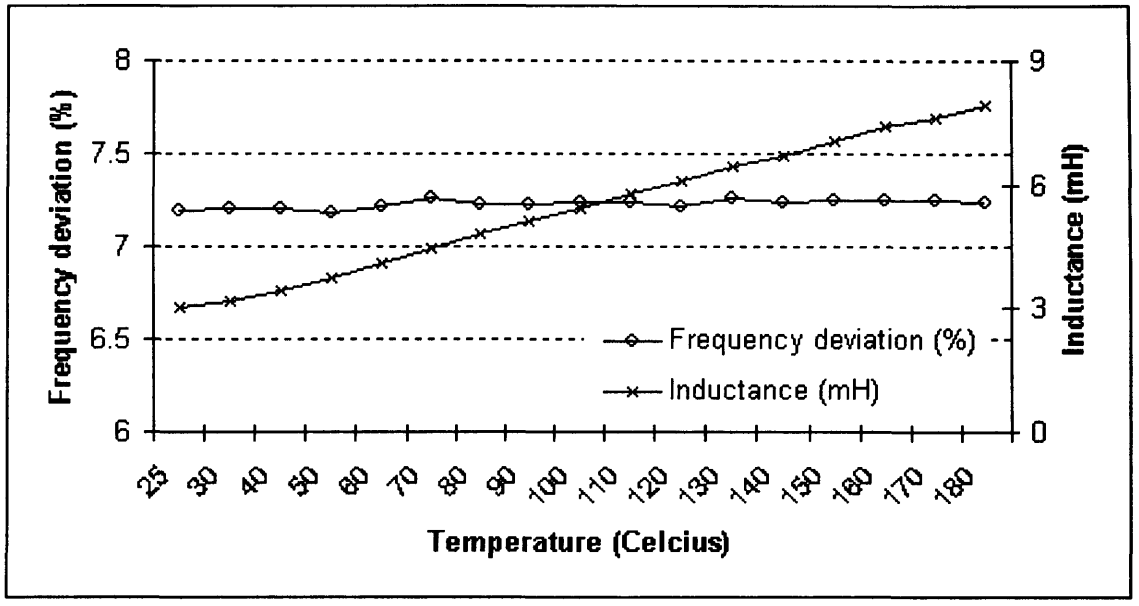

Figure 5.38: The frequency dependence on temperature remains relatively uninfluenced from the rise of inductance due to temperature increase (displacement was set at ~1.6mm peak to peak).

As inductance increases with temperature the reference frequency, f_c, is also increasing but the percentage change ΔL remains approximately constant, thus Δf follows proportionally at 7.2 % (Figure 5.38). With the system settings used the frequency deviation (Figure 5.38) is 7.19 % at 25 °C and it was raised to 7.26 % at 180 °C due to the increase of the inductance value; the frequency deviation percentage does not change significantly with the increase of inductance, due to temperature rise. Hence, the sensor signal is relatively uninfluenced by the increase of temperature as found experimentally[26, 27]. These findings allow the design and construction of temperature independent sensor families (in the range up to 180 °C) as required by industry[28].

5.7 Summary

To be able to extract and recover the sensor information/displacement signal from the modulated waveforms, software was written using the LabVIEW® programming package. The written code contained methodologies primarily used in electronic circuitry (envelope detector, discriminator, low pass filter) and mathematical concepts (lock-in amplifier, Hilbert transform, median filter) in order to perform the acquisition, signal processing and presentation of the data. After verifying that the measurement system is able to demodulate simulated and acquired modulation waveforms, it was necessary to quantify the sensor information signal in terms of displacement distance. For this task an actuator set-up was designed and used to provide a controlled displacement of the free end of the bilayer sensor. This enabled the direct comparison and evaluation of the three modulation principles against the results obtained from a laser Doppler Vibrometer (*LDV*). The comparison between the *AM*, *PM* and *FM* principles and the *LDV* was performed by looking at the relationship between the signal output versus displacement and the mechanical hysteresis for each modulation method. From the results it was deduced that the *FM* principle outperforms in quality the *AM* method and is noticeably faster than the *PM* modulation. Another well known advantage of the *FM* technique is that it is not influenced by noise as much as the *AM*. Thus, the chosen method for conveying the bilayer displacement information was the *FM* principle. The system alone encompasses techniques that make it so adaptable that it can even be successfully used with alternative non-bilayer sensor configurations[29].

The examination of the effects of bilayer sensor physical dimensions and parameters paved the way in its optimisation. In this investigation it was found that a coil of N = 300 and ℓ = 20 mm would have the optimum dimensions needed for a sensor used in conjunction with the *FM* system. The correctness of the chosen parameters was also confirmed by the system output where sensors of different sizes and characteristics were compared. The measurement system was used not only for the detection of stress/displacement but also for a brief evaluation of bilayer magnetic material for sensor applications. Comparing the two materials of different saturation magnetostriction (th = 2.9 μm) it was found that the signal output from a sensor with

the 2605SC ($\lambda \approx 30 \cdot 10^{-6}$) will outperform by 65 % the one with the 2705M ($\lambda \approx 0$). Thus, the effect of materials with high saturation magnetostriction was noted, and the 2605SC was chosen for use in bilayer sensors. Further investigation on the effect of substrate choice showed that high modulus of elasticity and high overall thickness, increases, as expected, the stiffness of the bilayer strip. Hence, in situations where the displacement force is weak (heartbeat rate monitoring), a stiff bilayer will suppress it without bending; resulting in little or no sensor signal. A substrate with high thickness should be selected for applications where the displacement forces are large, such as measuring airflow in a car engine intake; where as for functions where weak forces are to be measured the stiffness should be kept at low levels.

As part of examining the performance of the bilayer sensor, the thermal stability was tested over the temperature range of up to 180 °C. By placing the bilayer sensor and the actuator set-up inside an environmental chamber it was seen that although the temperature rise did cause inductance change, the sensor signal remained relatively unaffected due to the nature of the frequency modulation method. Thus, a bi-layer thin film sensor, using materials of different thermal expansion coefficients, can be used and have a good thermal stability over a range of temperatures up to 180 °C. A temperature independent sensor is needed in industry especially for application in car engines for measuring exhaust fume flow.

References

[1] DAQ PCI-6115/6120 Data Acquisition Card, User Manual, National Instruments Inc., Austin, USA, 2004.
[2] LabVIEW 7 User Manual, National Instruments Inc., Austin, USA, 2004.
[3] 33250A Arbitrary Waveform Generator User Manual, Agilent Inc., Palo Alto, USA, 2004.
[4] K. Najarian, "Biomedical signal and image processing", CRC Press: Boca Raton, 2006, Ch. 3, pp. 54-58.
[5] I. Pitas et al, "Non linear digital filters: principles and applications", Kluwer Academic Publishers: Massachusetts, 1990, Ch. 4, pp. 63-112.
[6] P. Mather, "Computer processing of remotely sensed images: an introduction", Wiley: West Sussex, 1988, Ch. 7, pp. 186-187
[7] G. S. Katranas et al, "Simulation and measurement of bilayer sensor characteristics", Sensors and Actuators A: Physical Vol. 129, 2006, pp. 243-246.
[8] G. S. Katranas et al, "A novel frequency modulation based system using bilayer thin film displacement sensors", IEEE Magnetics society, International Magnetism Conference (INTERMAG), 2006, San Diego (USA), Digest, pp. 517a-517b.
[9] G. S. Katranas et al, "A frequency modulation based system using bi-layer thin film displacement sensors", IEEE Transactions on Magnetics, Vol. 43-3, 2006, pp. 1035-1039.
[10] G. S. Katranas et al, "A novel phase modulation based system using bi-layer thin film displacement sensors", Journal of Magnetism and Magnetic Materials, International Conference on Magnetism (ICM), 2006, Kyoto (Japan), in print.
[11] OFV-303/OFV-3001 Single Point Laser Doppler Vibrometer, User Manual, Polytec GmbH, Germany, 2002.
[12] R. Boll et al, "Sensors: a comprehensive survey", VCH: Weinheim, 1989, Vol. 5, Ch. 4, pp. 98-147.
[13] G. Vasilescu, "Electronic noise and interfering signals", Springer: Berlin, 1999, Ch. 14-16, pp. 443-582.
[14] G. Vasilescu, "Electronic noise and interfering signals", Springer: Berlin, 1999, Ch. 3, pp. 45-68.
[15] OPA37 Ultra-Low Noise, Precision Operational Amplifier, Data Sheet, Texas Instruments Inc, USA, 2004.
[16] W. M. Harper, "Statistics", Pitman: London, 1991, Ch. 14, pp. 172-183.
[17] A. E. Love, "Treatise on the Mathematical Theory of Elasticity", Dover Publications: New York, 1944, Ch. 4, pp. 112-124.
[18] Kapton VN, Polyimide Film, DuPont Inc., Circleville, USA, 2004.
[19] 2605SC Magnetic Alloy Data Sheet, Metglas Inc., Conway, USA, 2004.
[20] 2705M Magnetic Alloy Data Sheet, Metglas Inc., Conway, USA, 2004.
[21] Comsol Structural Mechanics 3.1 User Manual, Comsol AB, Stockholm, Sweden, 2004.
[22] E. Kaniusas et al, "Magnetostrictive amorphous bilayers and trilayers for thermal sensors", Journal of Magnetism and Magnetic Materials, Vol. 254-255, 2003, pp. 624-626.
[23] E. Kaniusas et al, "Optimisation of sensitivity and time constant of thermal sensors based on magnetoelastic amorphous bilayers", Journal of Alloys and Compounds, Vol. 369, 2004, pp. 198-201.
[24] $Cu_{98}Be_2$, Data Sheet, Goodfellow Cambridge Ltd, Cambridge, UK, 2006.
[25] Environmental Chamber (Bespoke), Carbolite Ltd, Sheffield, UK,
[26] G. S. Katranas et al, "Thermal Stability of Bi-Layer Thin Film Displacement Sensors", Sensor Letters, European Conference on Magnetic Sensors and Actuators (EMSA), 2006, Bilbao (Spain), in print.
[27] G. S. Katranas et al, "Thermal Stability of Bi-Layer Thin Film Displacement Sensors Systems", Sensors and Actuators A: Physical, in print.
[28] A. M. Merlo, Private communication, Centro Ricerche Fiat, Torino, Italy, 2004.
[29] G. S. Katranas et al, "A Hybrid Magnetic Sensor System for Measuring Dynamic Forces", IEEE Transactions on Magnetics, 2006, Vol. 42-10, pp. 3288-3290.

Chapter 6 Bilayer Sensor Measurement System Applications

6.1 Introduction

The simple principle by which the bilayer sensors operate yields a wide range of applications that include bending, force or displacement in their operation. The applications of bilayer sensors are concentrated on biomedical monitoring and on the automotive sector, two fields where this new sensor concept shows interest due to the low sensor mass and the flat sensor design[1].

Physiological measurements concentrate on "sleep laboratory" (Polysomnography) sensors for the detection and long-term monitoring of breathing, leg movement, heart activity, blood pressure, eye-lid movements by applying sensors on the human body. At present, no *FM* based system or bilayer sensor principle is available which can be applied in a comparably universal way.

In the automotive sector, the bilayer is intended to be applied on steering wheels for angle and torque measurements, for driver status monitoring and for airflow observation of the car engine intake.

6.2 Biomedical

The non-disturbing monitoring of the cardio-respiratory activity of the human body is an important parameter during biomedical tests, such as Polysomnography (*PSG*). This is a comprehensive recording of the physiological changes that occur during sleep. This diagnostic test monitors many medical techniques including electroencephalography (*EEG*), rapid eye movement (*REM*), electromyography (*EMG*), electrocardiogram (*ECG*), and respiratory activity while the patient is sleeping. During the sleep study the breathing; oxygen levels, tracing of heartbeat

[1] G. S. Katranas, "Design and Development of Bilayer Sensor Systems for Biomedical and Automotive Applications", Ph.D. Thesis, Cardiff University.

waveform, and the different levels of sleep are recorded. A qualified sleep technician performs the test and monitors the patient's sleep through the night. The sleep technician will place electrodes on the head and face to monitor levels of sleep, apply *ECG* patches to the chest to monitor the heartbeat, and place a flow sensor under the nose to monitor airflow. In addition, soft straps are placed around the chest and abdomen to monitor the rise and fall of the chest to determine whether the patient is breathing appropriately during sleep. These sensors, electrodes and straps can potentially disturb the patients sleep.

This section of the thesis describes the application of the measuring system, using bilayer sensors originally used for the detection of bending, in order to measure with minimum disturbance the physiological activities that involve the dynamic deformations of the curvature of the skin (Figure 6.1)[2]. Internal physiological activities are mirrored on the human body in the form of active variations of the skin curvature. As an example, when the heart beats it pumps blood to the body, the arteries (i.e. carotid) expand and their radius, r, changes to $r + \Delta r$. The tissue around the artery will expand accordingly, forcing the surrounding skin area to change its curvature from c_1 to c_2 ($c_1 < c_2$). Hence the hemo-dynamic changes of the carotid artery (blood pressure) can be acquired using a displacement sensor placed on the skin surface.

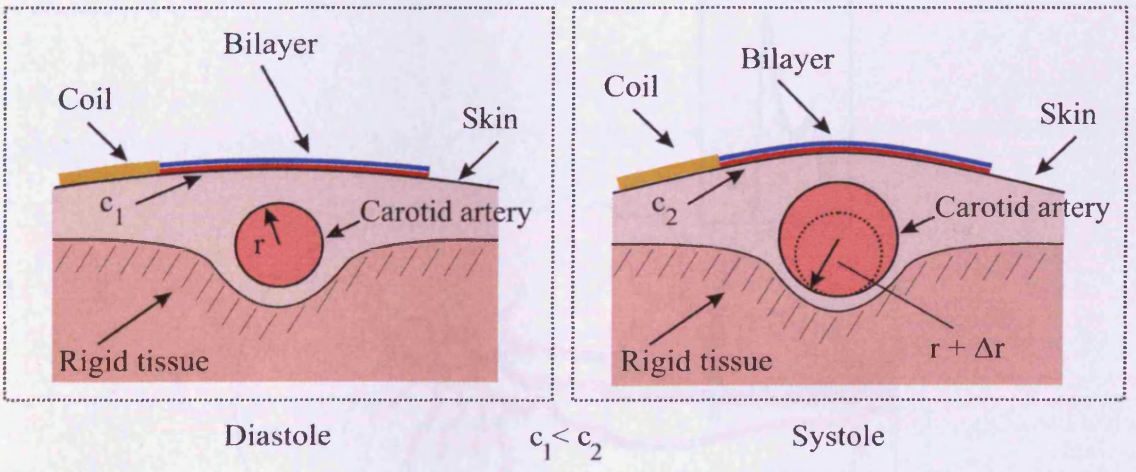

Figure 6.1: The change of the carotid artery radius during the systolic/diastolic contractions of the heart alters the curvature of the skin[7].

G. S. Katranas, "Design and Development of Bilayer Sensor Systems for Biomedical and Automotive Applications", Ph.D. Thesis, Cardiff University.

Depending on the body region that the sensor is placed, the signals that can be acquired due to skin curvature changes will consist of three main components, cardiac activity s_C (carotid artery systolic/diastolic contractions), lung ventilation s_R (rib cage movement during air inhale/exhale) and body movements s_M (muscle activation from active/aware stimulation or passive/sleep disturbance)[3].

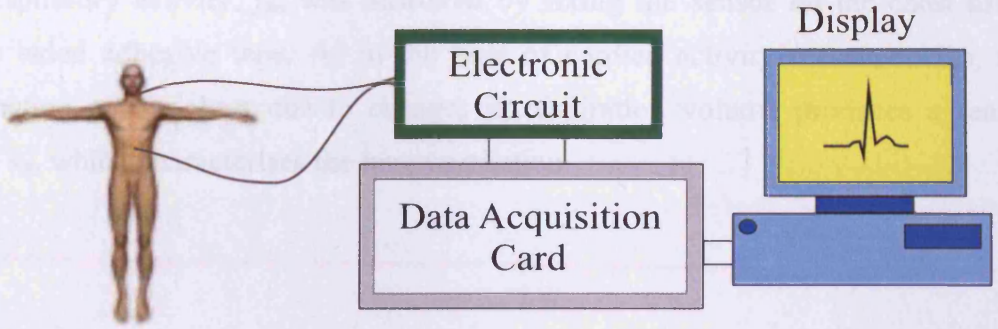

Figure 6.2: Bilayer sensor system for registering cardio-respiratory activity[4, 5].

Here the measurement set-up consisted of the *FM* system and the bilayer sensor placed on the patient; the location of which depends on the activity to be measured. The bilayer sensor used consisted of an amorphous magnetic film, 2.9 μm thick, deposited from a $Fe_{81}B_{13.5}Si_{3.5}C_2$ target (Metglas 2605SC) using the *RF* magnetron sputtering technique onto a 25 μm non-magnetic layer *CuBe* layer.

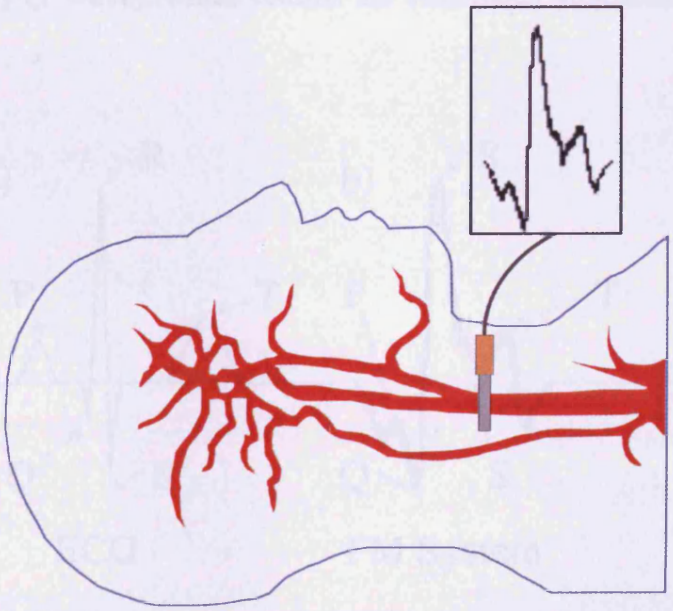

Figure 6.3: Application of the bilayer thin film sensor over the carotid artery.

G. S. Katranas, "Design and Development of Bilayer Sensor Systems for Biomedical and Automotive Applications", Ph.D. Thesis, Cardiff University.

For the detection of the heartbeat rate, f_C, the sensor was attached on the neck over the carotid artery with the aid of double sided adhesive tape (Figure 6.3). Cardiac activity transmits blood pressure waves through the arterial system which result in the cyclic alteration of the vessel's radius, r. This deformation is transmitted to the skin, through the surrounding tissue, resulting in change of curvature, Δc, proportional to Δr [6].

The respiratory activity, f_R, was measured by fixing the sensor on the chest using double sided adhesive tape. As in the case of cardiac activity measurements, the deformation of the chest due to changes in respiration volume produces a sensor signal, s_R, which characterises the lung ventilation.

6.2.1 Hemo-dynamics and Cardiac Rate

An Electrocardiogram (*ECG*) is an illustration produced by an Electrocardiograph, which measures the electrical potential between points of the body in order to show the electrical activity in the heart. Up to 12 contacts (electrodes) are usually affixed to the arms, legs and chest on clean, shaven skin areas. The typical *ECG* wave (Figure 6.4a) starts with the spread of the heart stimulation through the atria (*P* wave), triggering the ventricular activation (*Q*, *R* and *S* wave), and then ending up to the ventricular recovery (*T* wave), which returns the stimulated ventricular muscle to its resting state.

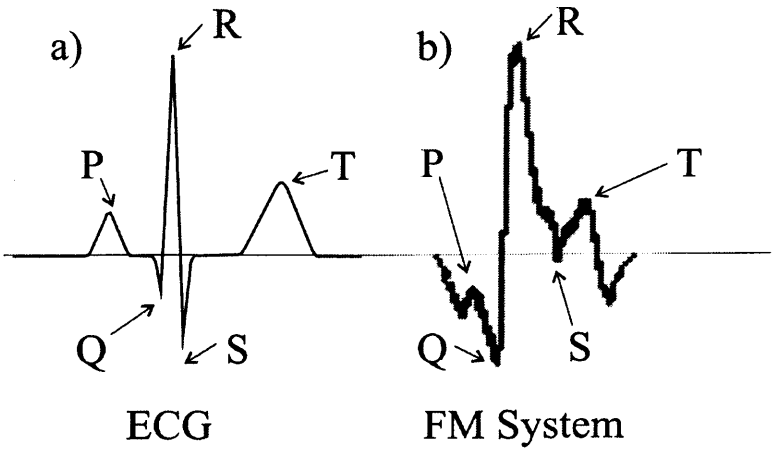

Figure 6.4: Comparison between the basic *ECG* output and the acquired heartbeat from the *FM* system[4, 5].

G. S. Katranas, "Design and Development of Bilayer Sensor Systems for Biomedical and Automotive Applications", Ph.D. Thesis, Cardiff University.

Figure 6.4b shows the hemo-dynamic activity at the carotid artery caused by the pumping of the heart. As the heart pumps blood at different pressures, (during its systolic/diastolic contractions), the artery changes in diameter accordingly. This diameter change is reflected on the skin as skin curvature change (Figure 6.1).

A bilayer curvature sensor system was used for the first time not only to monitor but also to map the five characteristic waves of the normal heartbeat rate (*P*, *Q*, *R*, *S* and *T* wave). This provided additional medical information about the cardiac activity and the blood pressure waveform of the patient that other magnetic bilayer sensor systems can not provide[7]. The shape and size of the *P*, *Q*, *R*, *S* and *T* waves (heartbeat waveform) can provide medical doctors with valuable information regarding the patient's health[8, 9]:

- Arterial blood clots or blocked artery (occlusion)
- Heart valve defects and congenital heart disease
- Narrowing (stenosis) of an artery
- Heart condition - ischemia and infarction, pericarditis, ventricular hypertrophy, bundle branch block, and cerebral disease, ventricular strain, hypertrophy of the ventricle, obstructive septal hypertrophy etc.

The *FM* bilayer sensor system can accurately and clearly reproduce the pressure changes of the carotid artery and give vital information regarding the condition of the heart or that of the arteries. Hence information such as heart arrhythmia or clotting of the carotid artery can be determined in a quick and inexpensive way. Also compared to the *ECG*, the bilayer sensor system only needs one contact to the body (the bilayer sensor) and there is no need for the preparation of the skin area.

Figure 6.5a demonstrates a characteristic pulse train, f_C, acquired from the *FM* system that corresponds to ~81 beats per minute. The normal resting heart rate for adults is between 60-100 beats per minute. The signal s_C is usually influenced from other signals, s_R and s_M, that arise from respiration or body movements. The ramp increase of the cardiac waveform in Figure 6.5a arises from the change of the neck circumference and muscle motion during slow intake of air in the lungs.

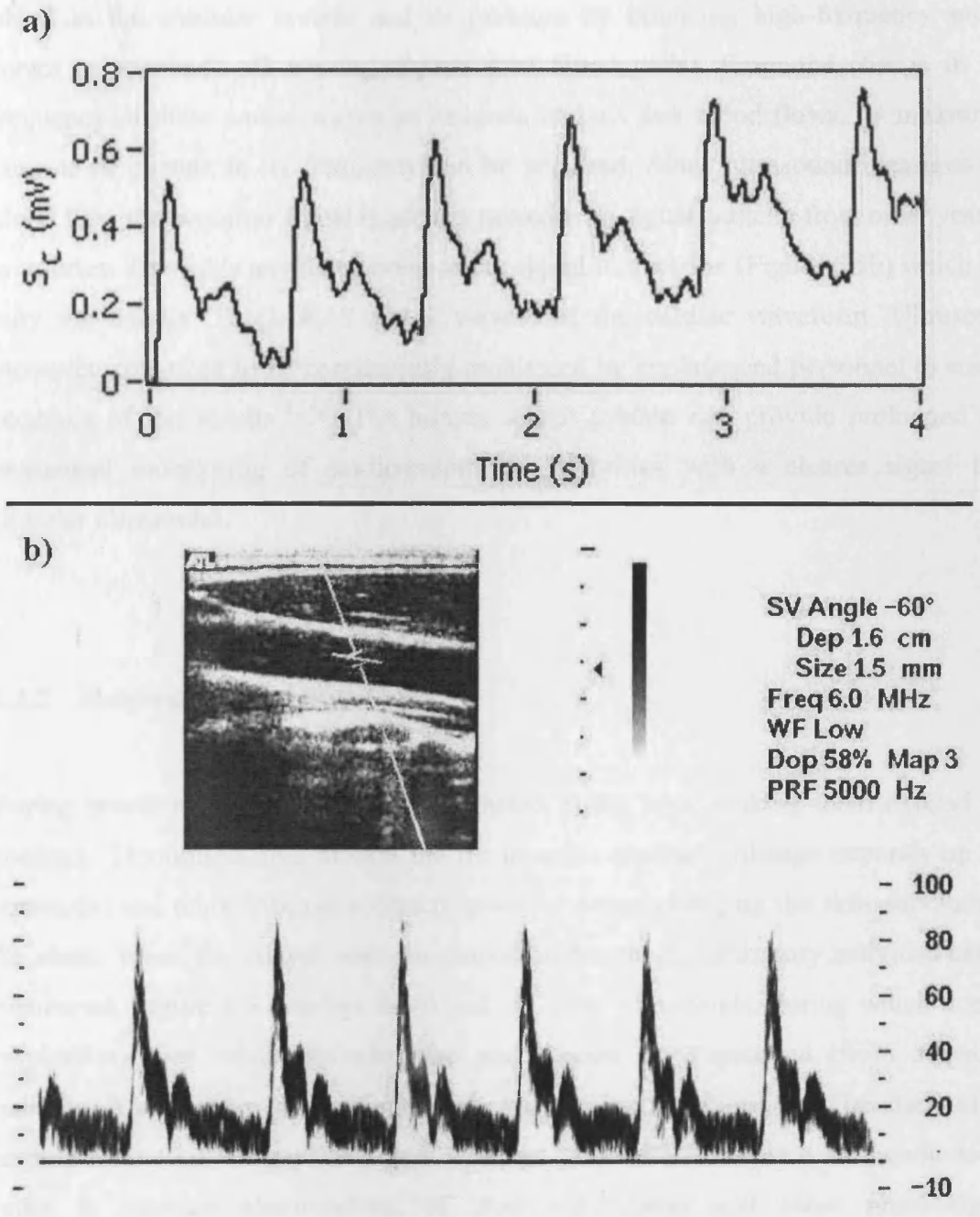

Figure 6.5: A detected pulse train segment, from the carotid artery displaying the hemo-dynamics of the carotid artery, using a) the bilayer sensor measurement system[4, 5] and b) ultrasound (normal Doppler spectrum)[10].

When the patient is holding his breath and immobile (Figure 6.5b), only the signal from the cardiac activity, s_C, is detected. The Figure 6.5b shows the hemo-dynamic activity of the carotid artery acquired by ultrasound[10] (Doppler spectrum) normal to

G. S. Katranas, "Design and Development of Bilayer Sensor Systems for Biomedical and Automotive Applications", Ph.D. Thesis, Cardiff University.

the vessel (90°). Ultrasound is a non-invasive test that can is used to assess the flow of blood in the vascular system and its pressure by bouncing high-frequency sound waves (ultrasound) off moving objects (red blood cells). From the change in the frequency of these sound waves an estimate of how fast blood flows, by measuring the rate of change in its frequency can be acquired. Since ultrasound measures the blood flow the acquired signal is usually mixed with signals arising from other vessels or arteries. This adds unwanted noise to the signal in question (Figure 6.5b) which can bury the details (*P*, *Q*, *R*, *S* and *T* waves) of the cardiac waveform. Ultrasound measurements need to be continuously monitored by experienced personnel to ensure accuracy of the results[11, 12]. The bilayer sensor system can provide prolonged and unmanned monitoring of cardio-respiratory activities with a clearer signal than Doppler ultrasound.

6.2.2 Respiratory Activity

During breathing, air is inspired and exhaled in the lugs, making them expand and contract. Throughout this motion the rib muscles contract (ribcage expands up and outwards) and relax (ribcage contracts inwards) hence changing the skin curvature of the chest. When the bilayer sensor is placed on the chest, respiratory activities can be monitored. Figure 6.6 displays the signal, s_R, over 55 seconds, during which normal respiration, deep inhalation/exhalation and apnoea were recorded (from a healthy individual) with clear differentiation between respiratory activities. The study of the respiratory activity is important as it is a part of the *PSG* tests that are conducted in order to monitor abnormalities of sleep/wakefulness and other physiological parameters related to it. Generally the study of respiratory activities can reveal the following conditions[13, 14]:

- Apnoea (absence of spontaneous respiration)
- Bradypnoea (abnormally slow rate of respiration)
- Cheyne-Stokes respiration (alternating periods of hyperpnoea and apnoea)
- Dyspnoea (shortness of breath)
- Hyperpnoea (increase in the depth and rate of respiration)

- Hypopnoea (slow respiration)
- Hyperventilation (abnormally rapid deep breathing)

During the *PSG* test the respiratory activity is monitored by placing two Velcro® straps, one placed around the chest under the breast area and one around the abdomen. This serves to determine chest wall and abdominal movements during breathing. A piezoelectric transducer is incorporated to this set-up and connected on each strap. The displacement force of the chest causes the expansion on the straps and hence stresses the transducer; this alters the signal to the physiological recorder. Along with the straps an airflow sensor (thermocouple) is placed under the nose to record airflow. The measurements of the straps and the airflow sensor are combined for the evaluation of respiratory activities. Attaching both the straps and the airflow sensor to the body will hinder any movement during sleep which will wake or disturb the patient and hence the monitoring[3].

Since the application of the bilayer sensor is a non-invasive and a non-disturbing method (only one sensor needed) for monitoring respiratory activities, i.e. with minimum inconvenience to the patient, then the system can be used for prolonged, undisturbed and successful monitoring.

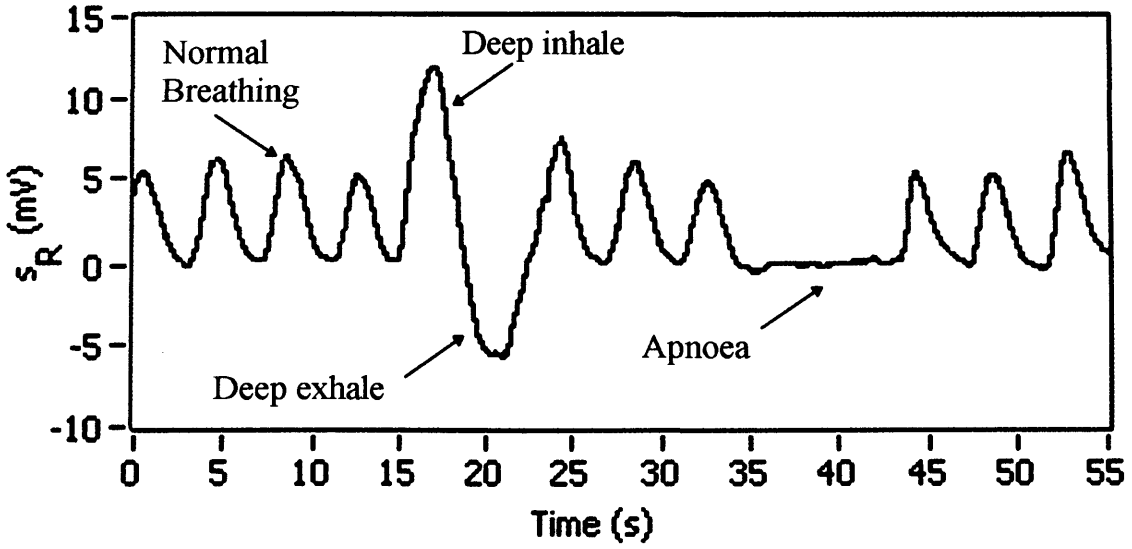

Figure 6.6: Respiratory activities using the bilayer thin film sensor system[4, 5].

G. S. Katranas, "Design and Development of Bilayer Sensor Systems for Biomedical and Automotive Applications", Ph.D. Thesis, Cardiff University.

6.3 Airflow

The ability to quantify the flow of air or liquids, quickly and accurately, is greatly needed by industry. Applications of flow sensors can vary from measuring blood flow through the human artery system to determining the air flow through the intake of a car engine[1, 15]. The means to monitor the air flow through a car engine led to the introduction of electronic fuel injection systems that replaced carburettors that could not rapidly change the air-to-fuel ratio in order compensate for changes in atmospheric conditions. Thus, the electronic fuel injection system improved fuel economy and reduced exhaust emissions. Airflow sensors can also be a vital part of a condition monitoring system which together with an electronic processor it can analyse data and in turn warn the user for equipment fatigue and failure or to automatically control the apparatus i.e. by changing the air stream through pipes, vents etc, in order to correct any problems. The application of a novel system using bilayer sensors, originally used for the detection of bending, is described in this section. Based on the principle of bending bilayer sensors the system is able to measure the speed of an air stream through a cylindrical tube[16]. The measuring system was connected to a setup comprised of a cylindrical tube where the sensor is placed inside and a tank with compressed air that supplied the air flow (Figure 6.7).

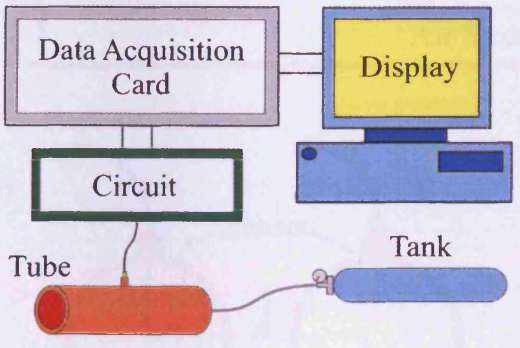

Figure 6.7: The bilayer sensor setup for airflow measurements.

The bilayer sensor used consisted of an amorphous magnetic film (Metglas 2605SC), 28 μm thick, and agglutinated onto a 75 μm non-magnetic layer *Al* layer. The bilayer sensor was inserted in the middle of a cylindrical tube 70 mm long with 30 mm diameter. The orientation of the sensor was parallel to the radius of the tube with the

G. S. Katranas, "Design and Development of Bilayer Sensor Systems for Biomedical and Automotive Applications", Ph.D. Thesis, Cardiff University.

broad face of the bilayer strip placed orthogonally to the air stream and the tip of its free end located in the centre of the tube (Figure 6.8a, b). The air stream was supplied to the tube from a compressed air tank with 8 bar (115 psi) maximum working pressure. An anemometer was placed at the other end of the tube to measure the air flow in order to correlate the sensor signal to the wind speed. The performance of the sensor was tested at air speeds up to 25 m/s and at a range of distances from the centre of the tube (reducing the bilayer strip length inside the tube) (Figure 6.8b). The tube diameter and the air speed range was chosen as such as to achieve a slightly turbulent flow through the tube with a Reynolds number of R_e = 6324 at 3.9 m/s up to R_e = 40541 at 25 m/s using Eq. 6-1 (Eq. 2-39):

$$R_e = \frac{u \cdot dm}{\nu_d} = \frac{25 \cdot 0.03}{1.85 \cdot 10^{-7}} = 40541 \qquad 6\text{-}1$$

where ν_d is the dynamic viscosity of air equal to $1.85 \cdot 10^{-5}$ Pa·s at 25 °C[17].

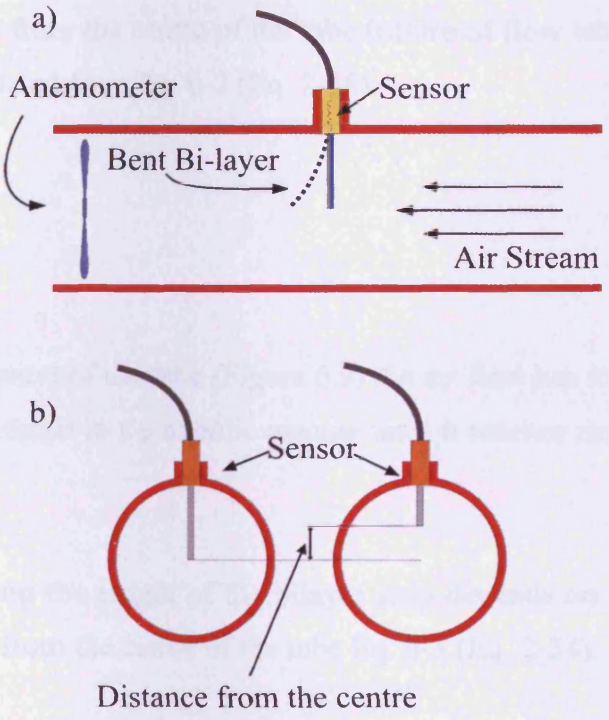

Figure 6.8: The bilayer sensor configuration inside the cylindrical tube.

In a straight tube when the Reynolds number is above 4000 then the flow is turbulent[18]. The reason behind this choice was to examine the performance of the sensor in conditions found in engine intakes where the flow is usually turbulent[19].

6.3.1 Sensor Tip Distance from Centre of Flow

In order to relate the sensor signal to the air flow, the environment inside the tube and the forces that displace the bilayer strip need to be considered. This was performed by modelling the sensor inside the tube using *FEM* (Comsol Structural Mechanics® package)[20]. A model of the tube and strip arrangement was designed in *FEM*, applying parameters such as the air flow speed and the mechanical characteristics of the bilayer (Young's modulus).

The nature of the air flow (air velocity) in a tube is parabolic (Figure 6.9) and depends on the radial distance from the centre of the tube (centre of flow where air speed is at maximum)[21] as calculated from Eq. 6-2 (Eq. 2-38):

$$u = u_{\max}\left(1-\left(\frac{r'}{r}\right)^2\right) \qquad 6\text{-}2$$

Hence at 0 mm, the centre of the tube (Figure 6.9) the air flow has its maximum speed of 25 m/s. This value drops in a parabolic manner until it reaches zero at 15 mm (tube wall).

The force exerted along the length of the bilayer strip depends on the air speed and hence on the distance from the centre of the tube Eq. 6-3 (Eq. 2-34):

$$P_t = P_s + \frac{\rho \cdot u^2}{2} \qquad 6\text{-}3$$

where the static pressure, P_s, is equal to zero since the tube is not pressurised.

G. S. Katranas, "Design and Development of Bilayer Sensor Systems for Biomedical and Automotive Applications", Ph.D. Thesis, Cardiff University.

Thus, the force will show a maximum value at the centre of the tube (0.265 N at 25 m/s) and will display a bell shaped drop down to zero at 15 mm.

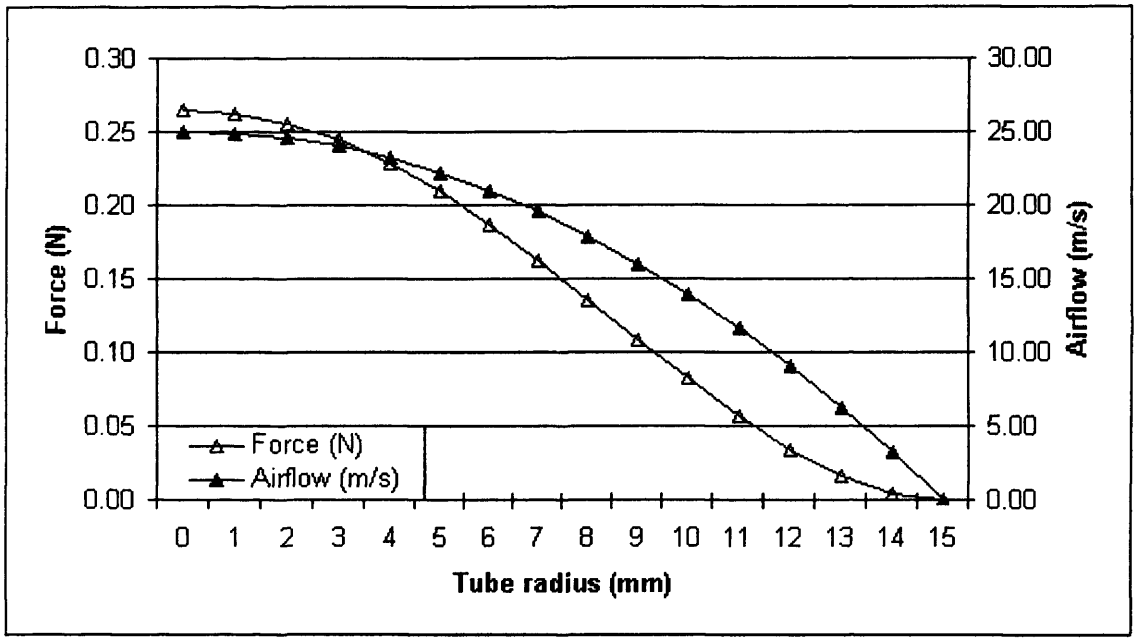

Figure 6.9: The dependence of the airflow and force on the distance from the centre of the tube (FEM Results).

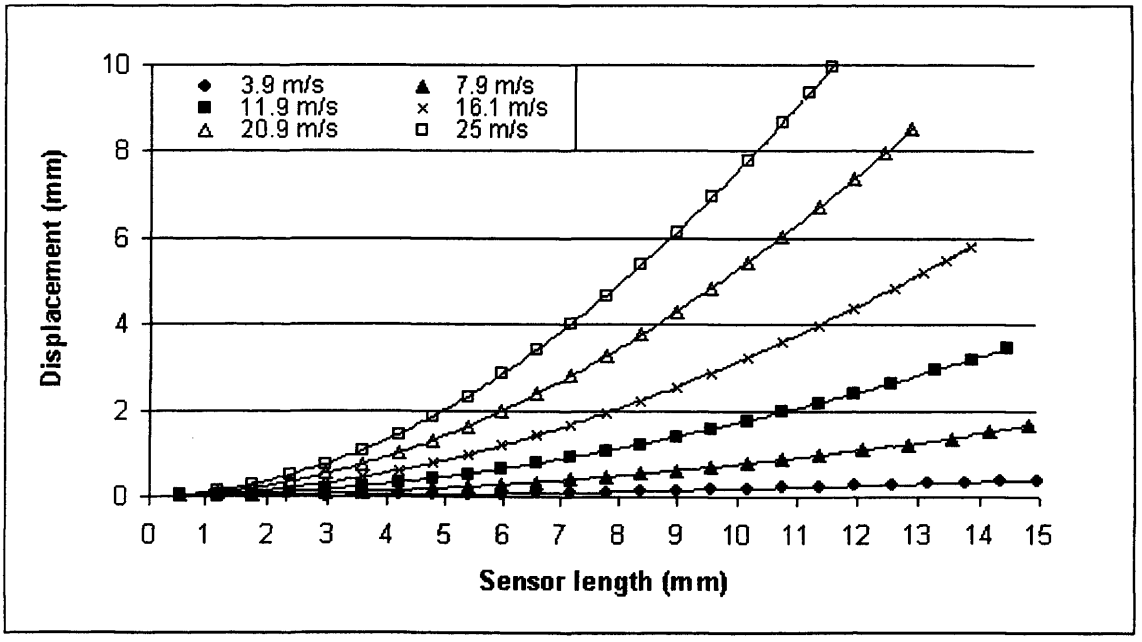

Figure 6.10: The bilayer sensor curvature and displacement at a range of air speeds up to 25 m/s (FEM Results).

The data shown in Figure 6.9 were inserted in the *FEM* calculations and the results obtained were plotted on Figure 6.10 to Figure 6.12 and represent the theoretical behaviour of the bilayer strip in the tube under the application of airflow up to 25 m/s.

When the bilayer is inserted in the tube the air flow, and hence the force, will be applied vertically to the longitudinal axis of the strip and throughout its length. The magnitude of the force will vary along the length of the strip according to Eq. 6-3. Since the force is applied throughout the bilayer's length (Figure 6.10) rather than concentrated on its tip, the curvature at a point ℓ along the strip will be calculated using Eq. 6-3 and Eq. 6-4 (Eq. 2-25):

$$\zeta = \frac{F \cdot \ell^3}{3 \cdot E \cdot In} \qquad 6\text{-}4$$

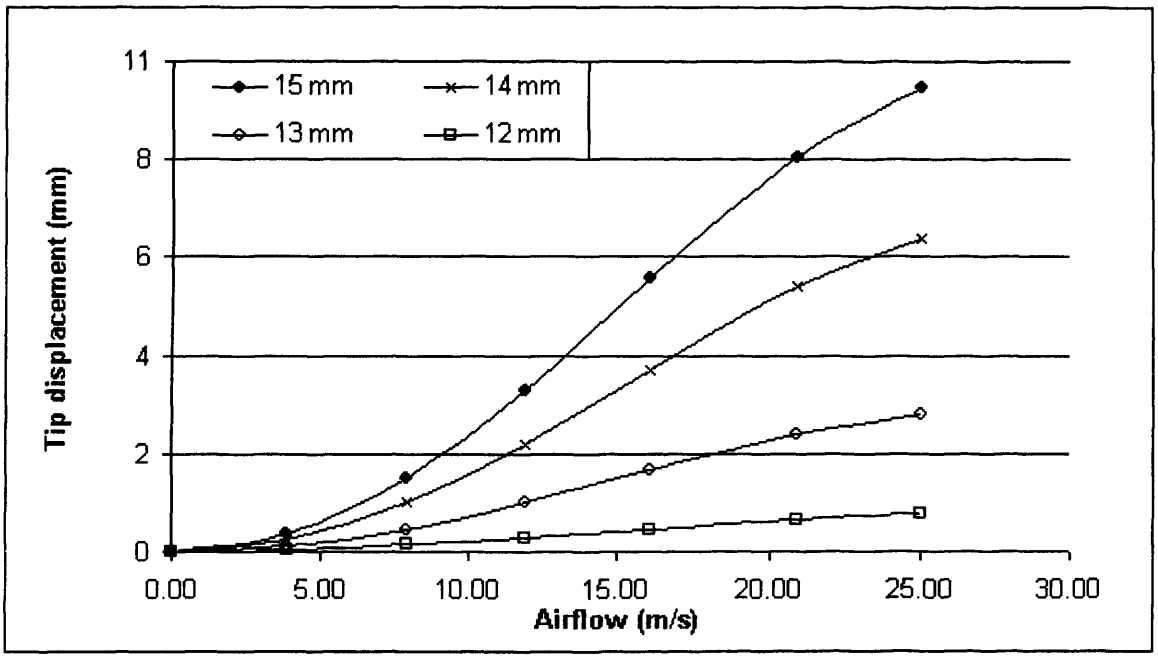

Figure 6.11: Bilayer length effect on tip displacement at speeds up to 25 m/s (FEM Results).

By moving the sensor away from the centre of the tube (reducing the length) and hence away from the point where the air force is at its maximum, it can be seen from the modelling results that the tip displacement of the bilayer strip displacement is dramatically reduced 12.5 times at 25 m/s (Figure 6.11 and Figure 6.12) as expected from Eq. 6-2 and Eq. 6-3. This is not only because the force decreases towards the

tube wall but also because the length of the strip affects the amount by which it can be displaced (Eq. 6-4). Figure 6.12 demonstrates that in order to displace by the same amount two bilayer strips of different length, higher amounts of force are required for the shorter strip.

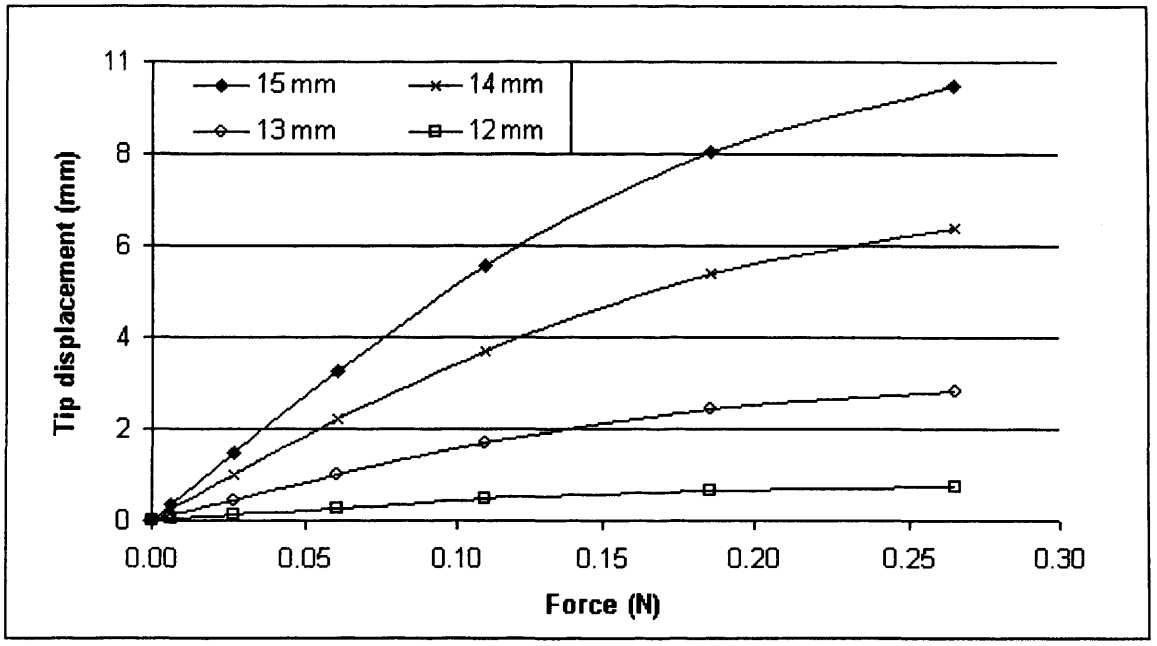

Figure 6.12: The bilayer sensor curvature and displacement at a range of air speeds up to 25 m/s.

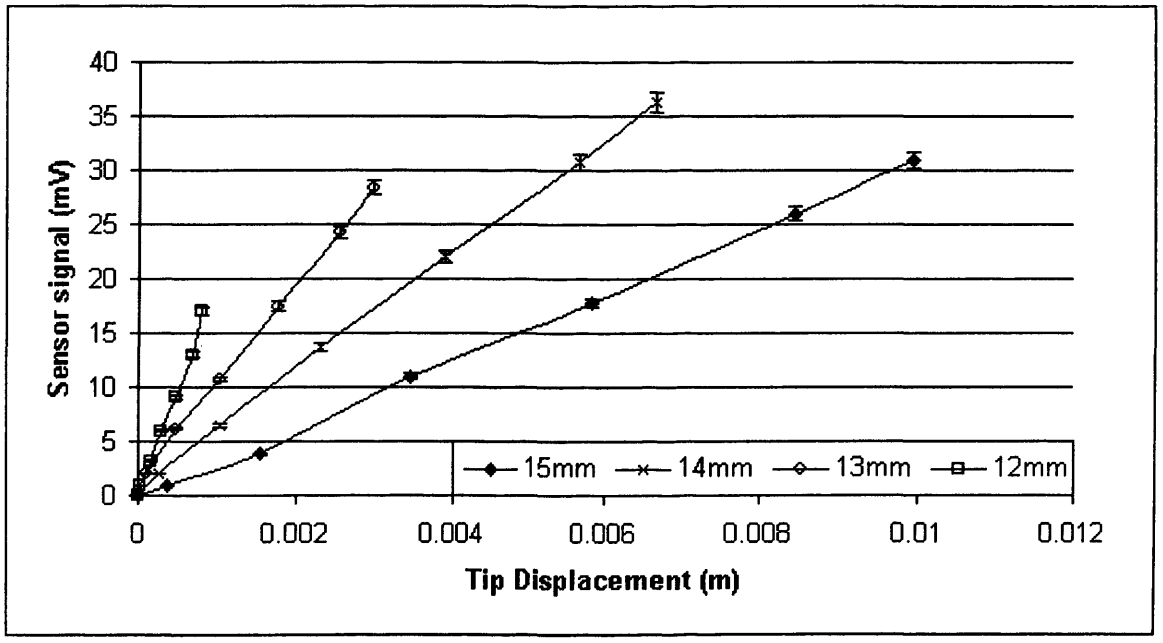

Figure 6.13: The output voltage characteristics against the tip displacement of the bilayer sensor at a range of air speeds up to 25 m/s..

The bilayer strip was inserted in the tube and subjected to a range of air flows up to 25 m/s. The acquired sensor signal was recorded and plotted against the tip displacement. Measurements were also taken by reducing the strip length in the tube from 15 mm to 12 mm in 1 mm steps. The results were repeated five times and the average values were plotted in Figure 6.13. The linearity was found to have a square correlation coefficient of 0.99 and the non-repeatability (2.4 %) of the data is within that of the *FM* system. The closer the bilayer's tip it to the centre of the tube the bigger the displacement of the trip. This is due to the higher air flow levels towards the centre and the fact that more strip area is present in the tube, subjected to additional force and hence increased displacement. This is explained in Eq. 6-4 where displacement is proportional to ℓ^3. High levels of displacement will increase the stresses within the material which in turn will show elevated sensor signal. A bilayer, with its tip away from the centre of the tube will require much higher airflow to show the same tip displacement as a longer strip. Higher forces induce higher stresses in the magnetic material which in turn cause increased change in ΔL and hence increased levels of signal. This is observed in Figure 6.13 where at a 12 mm length the strip needs 25 m/s air flow to achieve a 0.8 mm displacement in contrast to a 15 mm length which reaches the same ζ with ~5 m/s. Nevertheless, at ζ = 0.8 mm a 12 mm length the stresses are high and a 17 mV signal is recorded against the ~4 mV (76 % less signal) that arises at a 15 mm length. Hence even though shorter strip length gives less displacement it can be used in conditions where there is a high air flow rate. Longer strip lengths should be used in conditions of low air flow to increase the sensitivity.

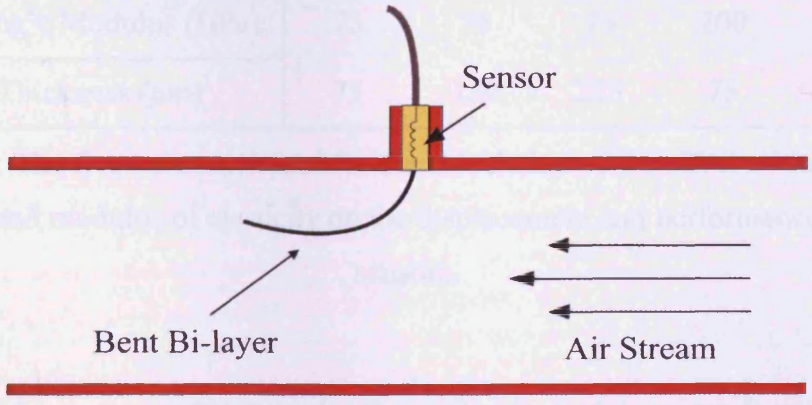

Figure 6.14: At sufficiently high flow rates the sensor is deflected at around 90° to lie parallel to the flow direction.

At sufficiently high flow rates the longitudinal axis of the sensor is deflected at around 90° (bends backwards) to lie parallel to the flow direction (Figure 6.14). During this condition a further increase in the airflow will not result to a further increase of the sensor signal because there is no further bending/stressing on the material. This can be corrected by either reducing the sensor length in the tube or by increasing the substrate thickness in order to increase the stiffness of the bilayer.

6.3.2 Effect of Substrate Thickness and Material

In Chapter 5, section 5.5, with the aid of *FEM* the effect of substrate thickness and modulus of elasticity on the displacement of bilayer strips was conducted. The sensor was inserted into the tube and subjected to a range of air flows up to 25 m/s. By placing in the sensor coil, strips constructed from substrates of different thickness or modulus of elasticity the theoretical finds from the *FEM* can be verified.

Five bilayers made by agglutinating an amorphous magnetic film (Metglas 2605SC), 28 μm thick, onto a range of non-magnetic layers of difference thickness and material were constructed (Table 6.1):

Substrate Material	*Al*			*HAVAR*	
Young's Modulus (GPa)	75	75	75	200	200
Thickness (μm)	75	150	225	75	100

Table 6.1: The five substrates used for the calculation of the effect of the substrate thickness and modulus of elasticity on the displacement and performance of bilayer sensors.

In section 5.5 it was noted that, under the application of the same force, as stiffness increases the tip displacement of the bilayer strip will decrease. Figure 6.15 verifies the theoretical investigation conducted with the FEM that as the thickness of the

substrate increases the tip displacement decreases. This is due to the fact that the increase of thickness is directly linked to the inertia of the bilayer strip, Eq. 6-5 (Eq. 2-19), which in turn affects the stiffness of the material, Eq. 6-6 (Eq. 2-32):

$$In = \frac{w \cdot h^3}{12} \qquad 6\text{-}5$$

$$\sigma_t = M \cdot y \cdot \left(\frac{E_1 + E_2 + \cdots + E_n}{E_1 \cdot In_1 + E_2 \cdot In_2 + E_n \cdot In_n} \right) \qquad 6\text{-}6$$

By comparing the two bilayers with the 75 μm and 225 μm *Al* substrate, it can be seen that a 3 times increase in the thickness gave a 76 % decrease in displacement due to the increase of inertia 96 % higher. Thus, having a material with higher stiffness will require increased amounts of force (airflow) to be displaced further. Similarly the comparison between the 75 μm *Al* (E = 75 GPa) and 75 μm *HAVAR* (E = 200 GPa) shows that as the modulus of elasticity increases the tip displacement decreases. Here a 2.6 times increase in E caused a 20 % decrease in the sensor tip displacement.

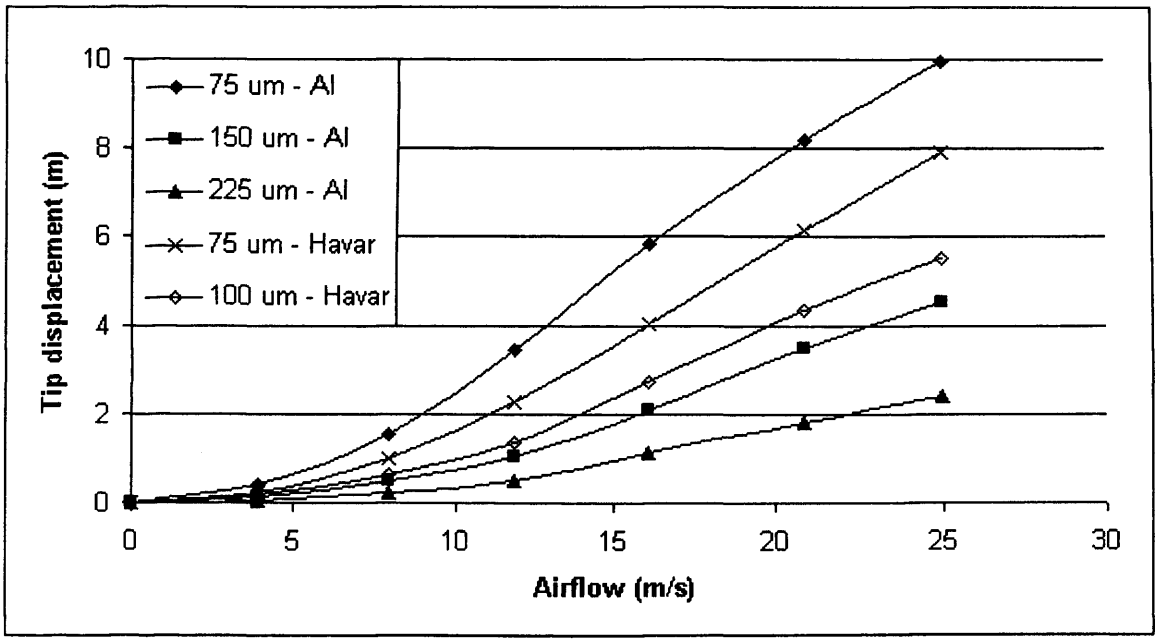

Figure 6.15: The effect of varying the substrate thickness and its modulus of elasticity, on bilayer tip displacement at speeds up to 25 m/s.

This is due to the fact that stiffness is defined as the product of the modulus of elasticity with the moment of inertia (Chapter 2, page 19). The results of Figure 6.16 show that the sensor signal is influenced by the bilayer dimensions and by the displacement/stress induced on the strip. It is seen that comparing the two bilayers with the 75 μm and 225 μm *Al* substrate, the 3 times increase in thickness displayed a 35 % drop in the sensor signal at 25 m/s. From Figure 6.15 the airflow needed to displace the samples with the 75 μm and 225 μm *Al* substrate at a 2 mm tip displacement is 8.9 m/s and 22.3m/s respectively. This demonstrates that the magnitude of the force applied on the bilayer tip needs to be increased in order to achieve the same amount of displacement due to the increased thickness (Eq. 6-4 and Eq. 6-5). To quantify this, a 2.5 times increase in airflow is needed (compared to the 75 μm *Al*) to displace the tip of the 225 μm *Al* to 2 mm. From Figure 6.16 it is seen that at 2 mm tip displacement the 75 μm *Al* substrate will show 5.5 mV of signal whereas the 225 μm *Al* displays 24 mV. So the 3 times increase of thickness produced a 4.4 times rise in output. This is due to the fact that the increase of force will increase the stress and hence give a rise to the sensor signal (Eq. 6-6).

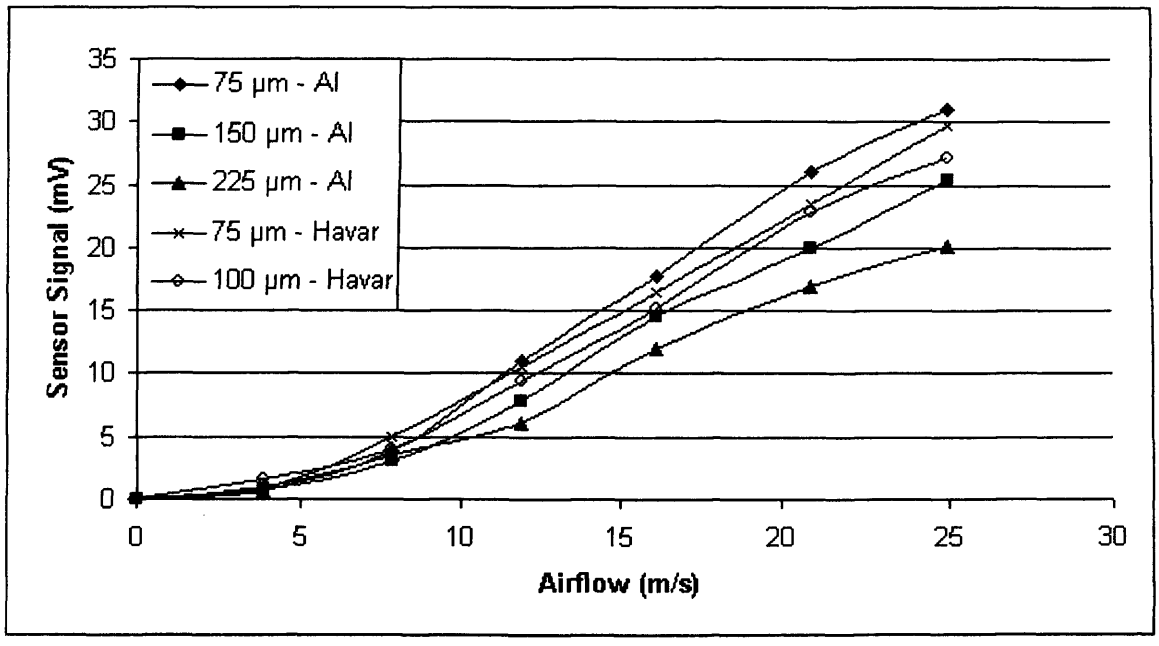

Figure 6.16: The effect of varying the substrate thickness and its modulus of elasticity, on bilayer signal output at speeds up to 25 m/s.

Accordingly, looking at the 75 μm *Al* (E = 75 GPa) and the 75 μm *HAVAR* (E = 200 GPa), a 2.6 times increase in E showed a 4 % decrease in sensor signal at 25 m/s, this

is due to the increase in stiffness that gives rise to the stress in the bilayer strip. By comparing the 75 μm *Al* and the 75 μm *HAVAR* (Figure 6.15), at 2 mm tip displacement, it is found that the airflow is 8.9 m/s and 11.2 m/s respectively, showing a 26 % increase. This produces a 7.1 mV signal for the 75 μm *Al* and a 9.5 mV output for the 75 μm *HAVAR*. Therefore the 2.6 times increase in E will show a 34 % increase in voltage signal. At low airflow where sensitivity is needed a sample with reduced thickness or with low E is desired. Whereas in conditions of high airflow a thick material with a high E, (and hence high stiffness), is necessary. Therefore by choosing the *th* or E of a bilayer according to the magnitude of the applied force, the strip not only will be able to withstand higher forces without bending excessively (Figure 6.14) but also be sensitive enough to record a strong signal.

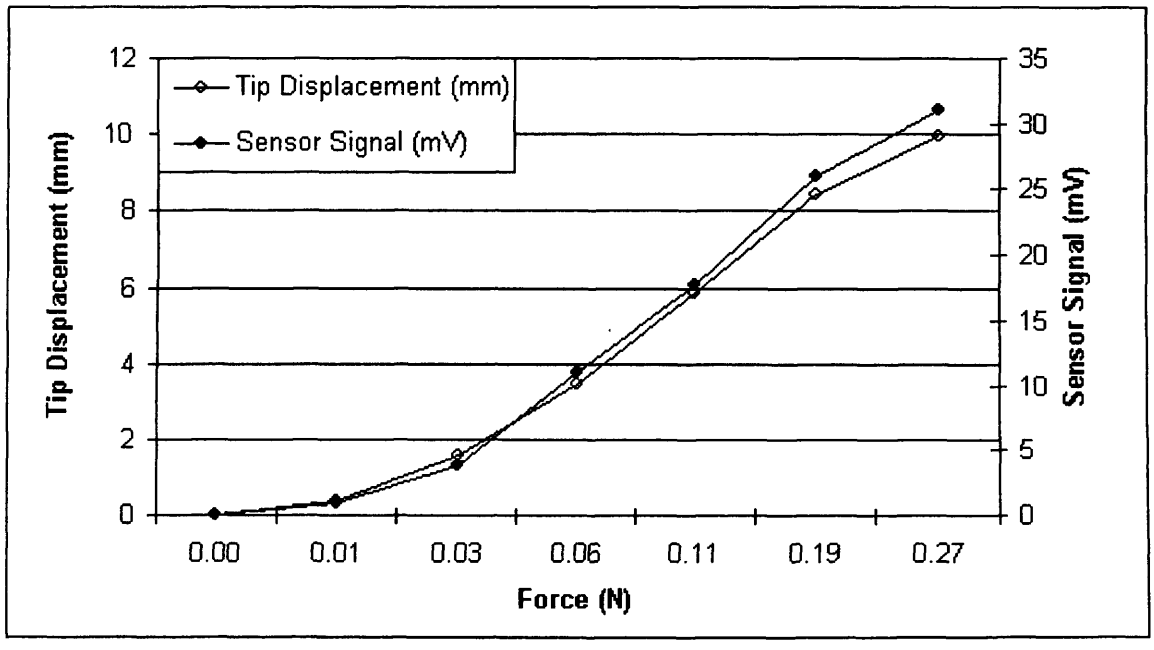

Figure 6.17: The output voltage characteristics and the tip displacement of the bilayer sensor vs. the force exerted on the strip.

By plotting the acquisition results (sensor signal) against the tip displacement of the bilayer strip it can be seen that the relationship has a linear behaviour with a square correlation coefficient value of $sc^2 = 0.99$ (Figure 6.13). The results present this linearity even at speeds up to 25 m/s where the conditions in the tube are turbulent. A direct connection between the sensor signal and the tip displacement of the bilayer strip from the airflow was plotted in Figure 6.17. By plotting both the sensor tip

displacement against force and the sensor signal versus force it can be seen that the responses closely follow each other. This further indicates that the sensor output signal faithfully replicates tip displacement position. Hence the bilayer sensor system can be used in air flow measurements as needed by industry[19].

6.4 Summary

In Chapter 6 the bilayer sensor measurement system was used to observe physiological functions, such as the cardio-respiratory activities, and also to monitor and quantify the flow of air.

The results showed that the various physiological activities that are mirrored on the human body in the form of active variations of skin curvature can be successfully detected. In fact a bilayer curvature sensor system was used for the first time not only to monitor but also to map the five characteristic waves of the normal heartbeat rate (*P*, *Q*, *R*, *S* and *T* wave), hence providing additional medical information about the cardiac activity of the patient that other magnetic bilayer sensor systems can not provide. Compared to commercial equipment such as the *ECG*, the bilayer sensor system only needs one contact to the body (the bilayer sensor) and there is no need for the preparation of the skin area. The *FM* bilayer sensor system can accurately and clearly reproduce the hemo-dynamic pressure changes of the carotid artery and give vital information regarding the condition of the heart or that of the arteries. Hence information such as heart arrhythmia or clotting of the carotid artery can be determined in a quick and inexpensive way.

When the bilayer sensor was placed on the chest a range of respiratory activities were monitored. These activities included normal respiration, deep inhalation/exhalation and apnoea which were recorded with a clear differentiation. The study of the respiratory activity is important as it is a part of the Polysomnography tests that are conducted in order to monitor abnormalities of sleep/wakefulness and other physiological parameters related to it. Since the application of the sensor is a non-invasive and a non-disturbing method for monitoring respiratory activities, i.e. with

minimum inconvenience to the patient, then the system can be used for prolonged, undisturbed and successful monitoring.

Based on the principle of bending, the bilayer sensor measuring system is able to measure the speed of an air stream through a cylindrical tube. Sensor signals were recorded with the bilayer tip at a range of distances away from the centre of the tube, where the airflow is at its maximum. It was found that in order to displace by the same amount, two bilayer strips of different length, higher amounts of force are required for the shorter strip. The higher forces induce higher stresses in the magnetic material which in turn cause increased change in ΔL and hence increased levels of signal. A strip with high stiffness or short in length can be used in conditions where sufficiently high flow rates can deflected the longitudinal axis of the sensor at around 90° (bends backwards) to lie parallel to the flow direction. This is due to the fact that the thickness and the modulus of elasticity are directly linked to the stiffness of the material. Depending on the strength of the airflow and the sensitivity needed, accordingly the substrate needs to be chosen. It was also noted that the relationship between the sensor signal and the tip displacement of the bilayer strip has a linear behaviour presented even at speeds of 25 m/s where the conditions in the tube are turbulent. Hence, a direct connection between the sensor signal and the force exerted on the bilayer strip from the airflow can be made apparent.

References

[1] L. Mehnen et al, "Magnetostrictive bilayer sensors – a survey", Journal of Alloys and Compounds, Vol. 369, 2004, pp. 202-204.
[2] E. Kaniusas et al, "First magnetic materials with sensitivity for the physical quantity "curvature" ", Journal of Materials Processing Technology, Vol. 181, 2007, pp. 186-189.
[3] E. Kaniusas et al, "A magnetostrictive acceleration sensor for registration of chest wall displacements", Journal of Magnetism and Magnetic Materials, Vol. 215-216, 2000, pp. 776-778.
[4] G. S. Katranas et al, "A novel bi-layer thin film sensor system for registering cardio-respiratory activity," Sensor Letters, European Conference on Magnetic Sensors and Actuators (EMSA), 2006, Bilbao (Spain), in print.
[5] G. S. Katranas et al, "Applications of the Bi-Layer Thin Film Sensor System for Registering Cardio-respiratory Activity", Sensors and Actuators A: Physical, in print.
[6] E. Kaniusas et al, "Magnetoelastic bilayer concept for skin curvature sensor", Ultrasound, Vol. 3-52, 2004, pp. 42-46.
[7] E. Kaniusas et al, "Method for continuous nondisturbing monitoring of blood pressure by magnetoelastic skin curvature sensor and ECG", IEEE Sensors Journal, Vol. 6-3, 2006, pp. 819-828.
[8] L. P. Cahalin, "Cardiovascular and Pulmonary Physical Therapy: an evidence-based approach", McGraw-Hill: New York, 2004, Ch. 2, pp. 95-122.
[9] C. Cannon, "The ECG: A Two-Step Approach to Diagnosis", Springer: Berlin, Ch. 2-8, pp. 13-100.
[10] Department of Diagnostic Radiology and Organ Imaging, Prince of Wales Hospital, Shatin, Hong Kong, 2006.
[11] N. Bornstein, "The limitations of diagnosis of carotid occlusion by Doppler ultrasound", Annals of Surgery, Vol. 207-3, 1988, pp. 315–317.
[12] P. N. Burns, "Quantitative flow measurements with Doppler ultrasound: techniques, accuracy, and limitations", The Radiologic Clinics of North America, Vol. 23, pp. 641-657.
[13] C. L. Schroeder, "Introduction to Medical Terminology", Delmar Publishers: New York, 2000, Ch. 7, pp. 122-159.
[14] M. B. Wang, "NMS Physiology", Lippincott Williams and Wilkins: New York, 2001, Ch. 16, pp. 199-226.
[15] T. Meydan, "Amorphous materials in sensor applications, magnetic materials for sensors and actuators", IEE Colloquium on New Magnetic Materials, Vol. 183, 1994, pp. 1-3.
[16] G. S. Katranas et al, "A bilayer sensor system for measuring airflow", Joint AIP 10th MMM/ IEEE INTERMAG Conference, 2007, Baltimore (USA), in print.
[17] M. W. Denny, "Air and Water: The Biology and Physics of Life's Media", Princeton University Press: Princeton Ch. 5, pp. 58-83.
[18] N. P. Cheremisinoff, "Practical fluid mechanics for engineers and scientists", Technomic Pub. Co: Lancaster, 1990, Ch. 5, pp. 124-125.
[19] A. M. Merlo, Private communication, Centro Ricerche Fiat, Torino, Italy, 2004.
[20] Comsol Structural Mechanics 3.1 User Manual, Comsol AB, Stockholm, Sweden, 2004.
[21] R. Baker, "An introductory guide to industrial flow", Mechanical Engineering Publication Ltd: London, 1996, Ch. 3, pp. 53-61.

Chapter 7 Conclusions and Outlook

The conclusions of the work presented in this thesis are given, linking it to the larger context of the use of magnetic bilayer sensors and their measurement systems in the biomedical and automotive industry. Potential future research directions are explored.

7.1 Conclusions

The work concerned the development of a new type of bilayer sensor measurement system and its possible application in dissimilar areas such as the observation of human physiological activities and monitoring of the airflow inside a car engine.

The central questions were:

i. How to develop a measurement system that would have the ability to recover with detail weak signals, such as the heartbeat waveform, and simultaneously be adaptable to other applications that may have different parameters?
ii. What parameters in the design and manufacturing of bilayer sensors could be critical in augmenting their performance, sensitivity and possible miniaturisation?

To cover the topic and the factors involved proved difficult as it encompassed a wide range of disciplines such as electronics, magnetism, material science, mechanics, physiology and software programming. It is hoped however, that the reader is left with an overview of the subject and a general intent for the many opportunities that remain to be explored and exploited.

From the investigation that was carried out, the following conclusions were derived:

- An algorithm was designed and developed that was able to extract and recover the sensor information/displacement signal from all three modulated waveforms (*AM*, *PM* and *FM*). This program was written on the LabVIEW® platform. The measurement system is able to demodulate simulated and acquired modulation waveforms and quantify the sensor information signal in terms of displacement distance. The written code contained methodologies primarily used in electronic circuitry (envelope detector, discriminator, low pass filter) and mathematical concepts (lock-in amplifier, Hilbert transform, median filter) in order to perform the acquisition, signal processing and presentation of the data. Extra code was written in order to supply the actuator with a sinusoidal signal that was used in order to provide a synchronised and controlled displacement to the bilayer strip.

- From the direct comparison between the *AM*, *PM* and *FM* signals it was deduced that the bilayer sensor measurement system can produce signals proportional to the displacement of its free end. All three principles were used to successfully convey the sensor information signal for displacements in the range of 0.35 mm to 2 mm. However it was shown that the *PM* and *FM* principles are less susceptible to noise and hence outperform in quality the *AM* method. It was also found that the *FM* technique is noticeably faster than the *PM* principle, due to phase drift problems that require higher sampling/acquisition rates. Thus, the chosen method for continuously conveying the bilayer displacement information was the *FM* principle. From the performance of the system it was found that along the region of 0.8 mV to 4.6 mV, it has a linearity of $sc^2 = 0.99$, non-repeatability of 2.4 % and an average sensitivity of 2.2 mV/mm.

- It was deduced from the examination of the effects of bilayer sensor physical dimensions and parameters that a coil of $N = 300$ and $\ell = 20$ mm would have the optimum dimensions needed to be used in conjunction with the *FM* system. The correctness of the chosen parameters was also confirmed by the system output voltage where sensors of different sizes and characteristics were compared.

- The measurement system was used not only for the detection of stress/displacement but also for a brief evaluation of bilayer magnetic material for sensor applications. It was seen that a sensor with the 2605SC (*th* =2.9 μm, $\lambda \approx 30 \cdot 10^{-6}$) outperformed by ~65 % the 2705M (*th* =2.9 μm, $\lambda \approx 0$). Thus, the effect of materials with high saturation magnetostriction was noted, and the 2605SC was chosen for use in bilayer sensors. The selected optimum coil parameters seem to give the highest output voltage compared with other configurations.

- Further investigation on the effect of substrate choice showed that high modulus of elasticity and high thickness, increases, as expected, the stiffness of the bilayer strip. Hence, in situations where the displacement force is weak (heartbeat rate monitoring), a stiff bilayer will suppress it without bending; resulting in little or no sensor signal. A substrate with high thickness would be selected for applications where the displacement forces are large, such as measuring airflow in a car engine intake; where as for functions where weak forces are to be measured the stiffness should be kept at low levels.

- The bi-layer thin film sensor, using materials of different thermal expansion coefficients, showed a good thermal stability over a range of temperatures up to 180 °C. The sensor signal remained relatively uninfluenced by the increase of temperature, due to the nature of the frequency modulation method, as found experimentally. A temperature independent sensor is needed in industry especially for application for measuring air flow in intake in car engines

- A bilayer curvature sensor system was used for the first time not only to monitor but also to map the five characteristic waves of the normal heartbeat rate (*P*, *Q*, *R*, *S* and *T* wave), hence providing additional medical information about the cardiac activity of the patient that other magnetic bilayer sensor systems can not provide. Compared to commercial equipment such as the *ECG*, the bilayer sensor system only needs one contact to the body (the bilayer sensor) and there is no need for the preparation of the skin area. The *FM* bilayer sensor system can accurately and clearly reproduce the hemo-dynamic pressure changes of the carotid artery and give vital information regarding the condition of the heart or that of the arteries.

Hence information such as heart arrhythmia or clotting of the carotid artery can be determined in a quick and inexpensive way.

- It was seen that when the bilayer sensor was placed on the chest a range of respiratory activities were detected. These activities included normal respiration, deep inhalation/exhalation and apnoea which were recorded with a clear differentiation. Compared to existing methods the use of the bilayer sensor is a non-invasive and a non-disturbing method for monitoring respiratory activities, i.e. with minimum inconvenience to the patient, then the system can be used for prolonged, undisturbed and successful monitoring.

- The bilayer sensor system was used successfully to measure airflow up to 25 m/s through a cylindrical tube. Sensor signals were recorded with the bilayer tip at a range of distances away from the centre of the tube, where the airflow is at its maximum. It was found that in order to displace by the same amount, two bilayer strips of different length, higher amounts of force are required for the shorter strip. A strip with high stiffness or short in length can be used in conditions where sufficiently high flow rates can deflected the longitudinal axis of the sensor at around 90° (bends backwards) to lie parallel to the flow direction. The relationship between the sensor signal and the tip displacement of the bilayer strip has a linear behaviour with $sc^2 = 0.99$. This linearity is presented even at speeds of 25 m/s where the conditions in the tube are turbulent.

- As expected the tip displacement and the sensor signal are affected by varying the bilayer strip thickness and the modulus of elasticity of the materials that it is comprised of. Depending on the strength of the force applied on the bilayer's tip and the sensitivity needed, accordingly the substrate needs to be chosen.

This is the first application of angle modulation (*PM, FM*) principles for use in bilayer sensors. The application of this system to biomedical and automotive applications showed the universality and adaptability of the bilayer sensors. It is hoped that the bilayer sensor measurement system will lend its self to other applications.

7.2 Outlook

The bilayer sensor and its measurement system showed that it can measure displacement/stress and that it can be used in many different applications. This universality is very attractive for industry.

Fields such as sleep monitoring laboratories can use an array of these sensors for multiple monitoring of physiological activities. The automotive industry may apply this sensor system not only for fluid control (air, water) but also for monitoring the drivers' health via sensors placed on the steering wheel, the safety belt or the back of the seat. These sensors could be connected to a neural network system that can evaluate whether the driver is falling asleep or suffering from a condition that prevents him from driving safely. Further developments of this sensor system may include an all hardware realisation of the measurement system in order to achieve portability as a hand held device. This can be of use to the medical profession for quick observation of the hemo-dynamics of the blood and hence the health condition of the heart. Further clinical testing will enable the medical community to correlate the results obtained from the bilayer measurement system with known medical conditions. The system could also be designed as a wireless stress monitoring sensor system with applications such as monitoring the structural integrity of installations such as power generation or chemical plants or even oil pipes.

The investigation of the application of the bilayer sensor system for airflow measurements showed promising future. Further tests will be necessary to fully record the effects of airflow on the bilayer sensor and perhaps propose new configurations depending on the area of application. These tests will require to be conducted under specialised airflow dynamics laboratory for precise characterisation of the full abilities of the bilayer sensor.

Finally an interesting evolution of the bilayer sensors would be their miniaturisation and perhaps incorporation in micromechanical systems. The small size and very low power consumption can be used in every day consumer applications such as toothbrushes (applied pressure) or in less common devices like space exploration probes (displacement/stress).

It seems that there are plenty of opportunities to be explored and it is hoped that the reader might find the information presented here interesting and useful.

Appendix A: Mechanical Analysis – Derivations

- **Calculation of the deflection of a nth layer cantilever beam**

Calculation of the deflection of an nth layer cantilever beam

In order to calculate the deflection of an nth layer cantilever beam loaded at the free end with a concentrated load, the centroid of the composite structure and the area moment of inertia of each layer need to be determined.

The centroid of an area is the centre of mass of an object of uniform density. Most composite or geometrically complex shapes can be considered to be made up by combining several shapes together. This can be used to locate the position of the centroid. If a complex area can be considered to be a composite of two or more simple areas, the centroid and hence the neutral axis, can be found by applying the principle that the product of the total area times the distance to the centroid of the total area is equal to the sum of the products of the area of each component part times the distance to its centroid. For the calculation of ξ_n, the point of reference is the centroid of layer n (Figure A.1).

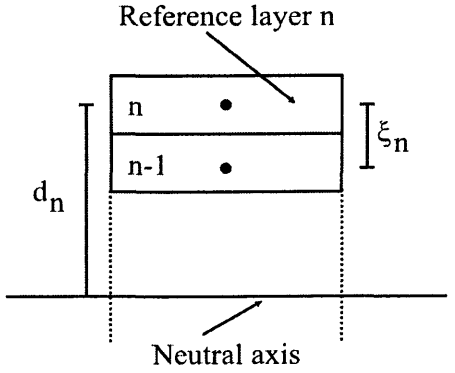

Figure A.1: Calculation of ξ_n and d_n.

Stating this mathematically[1]:

[1] G. S. Katranas, "Design and Development of Bilayer Sensor Systems for Biomedical and Automotive Applications", Ph.D. Thesis, Cardiff University.

$$\sum_n (A_n)\cdot d_n = \sum_n (A_n \cdot \xi_n) \Rightarrow d_n = \frac{\sum_n (A_n \cdot \xi_n)}{\sum_n (A_n)} \qquad \textbf{A-1}$$

Beams that are made of different materials (different Young's Modulus) need to be treated with the "equivalent width technique" (Figure A.2a). An assumption is made where by the width of each component parallel to the principal axis of bending is increased in the same proportion that the modulus of elasticity of the n^{th} component (E_n) makes with the modulus of elasticity (E_1) of the assumed material. This proportionality is written as:

$$w_n = \frac{E_n}{E_1}\cdot w_1 \qquad \textbf{A-2}$$

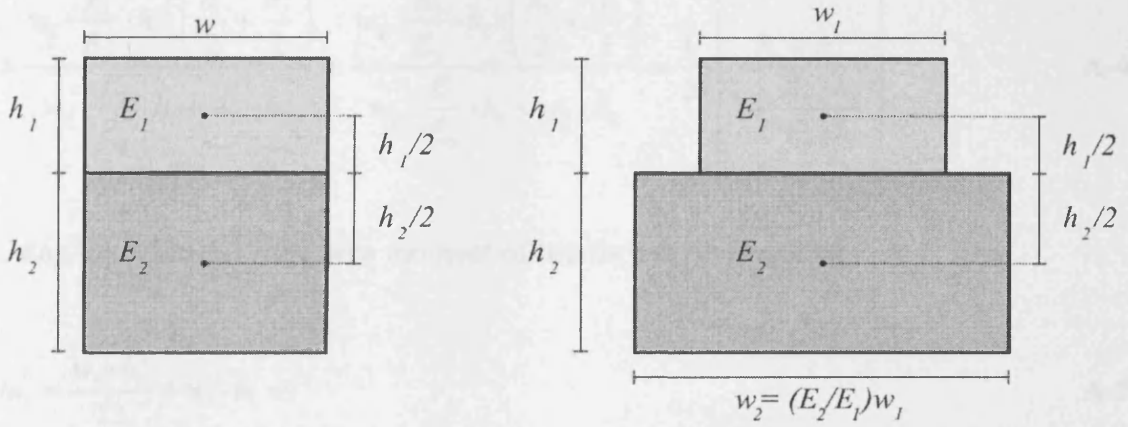

Figure A.2: Cross sections of a) bilayer beam, b) the equivalent width technique applied to a).

In the case of a bilayer strip with a cross section as shown in Figure A.2, Eq. A-1 will become[1,2]:

$$d_1 = \frac{A_1 \cdot \xi_1 + A_2 \cdot \xi_2}{A_1 + A_2} = \frac{w_1 \cdot h_1 \cdot \xi_1 + w_2 \cdot h_2 \cdot \xi_2}{w_1 \cdot h_1 + w_2 \cdot h_2} = \frac{w_1 \cdot h_1 \cdot 0 + w_2 \cdot h_2 \cdot \left(\frac{h_1}{2} + \frac{h_2}{2}\right)}{w_1 \cdot h_1 + w_2 \cdot h_2} =$$

$$= \frac{w_1 \cdot \frac{E_2}{E_1} \cdot h_2 \cdot \left(\frac{h_1}{2} + \frac{h_2}{2}\right)}{w_1 \cdot h_1 + w_1 \cdot \frac{E_2}{E_1} \cdot h_2} = \frac{1}{2} \cdot \left[\frac{h_1 + h_2}{1 + \frac{E_1 \cdot h_1}{E_2 \cdot h_2}}\right] \qquad \textbf{A-3}$$

and

$$d_2 = \frac{A_1 \cdot \xi_1 + A_2 \cdot \xi_2}{A_1 + A_2} = \frac{w_1 \cdot h_1 \cdot \xi_1 + w_2 \cdot h_2 \cdot \xi_2}{w_1 \cdot h_1 + w_2 \cdot h_2} = \frac{w_1 \cdot h_1 \cdot \left(\frac{h_1}{2} + \frac{h_2}{2}\right) + w_2 \cdot h_2 \cdot 0}{w_1 \cdot h_1 + w_2 \cdot h_2} =$$

$$= \frac{w_2 \cdot \frac{E_1}{E_2} \cdot h_1 \cdot \left(\frac{h_1}{2} + \frac{h_2}{2}\right)}{w_2 \cdot \frac{E_1}{E_2} \cdot h_1 + w_2 \cdot h_2} = \frac{w_2 \cdot \frac{E_1}{E_2} \cdot h_1 \cdot \left(\frac{h_1}{2} + \frac{h_2}{2}\right)}{w_2 \cdot \frac{E_1}{E_2} \cdot h_1 + w_2 \cdot h_2} = \frac{1}{2} \cdot \left[\frac{h_1 + h_2}{1 + \frac{E_2 \cdot h_2}{E_1 \cdot h_1}}\right] \qquad \textbf{A-4}$$

Using Equation 2-17 the area moment of inertia can be found as:

$$In_1 = \frac{w_1 \cdot h_1^3}{12} + w_1 \cdot h_1 \cdot d_1^2 \qquad \textbf{A-5}$$

and

$$In_2 = \frac{w_2 \cdot h_2^3}{12} + w_2 \cdot h_2 \cdot d_2^2 \qquad \textbf{A-6}$$

From Eq. A-5, Eq. A-6 and Eq. 2-33 the deflection of the cantilever bilayer beam will be as follows:

$$\zeta = \frac{F \cdot \ell^3}{3 \cdot (E_1 \cdot In_1 + E_2 \cdot In_2)} \qquad \textbf{A-7}$$

References

[1] R. L. Mott, "Applied strength of materials", Englewood Cliffs: Prentice-Hall, 1976, Ch. 8, pp. 179-184.
[2] J. Kosel et al, "Theoretical investigation of magnetostrictive bilayers sensitive to bending or temperature changes", Proceedings of the IEEE, Sensors 2004, Vol. 3, pp. 1086-1089.

Appendix B: Oscillator – Derivations

B.1 Phase shift oscillator

B.2 Phase shift oscillator with bilayer sensor

B.3 Colpitts oscillator

B.1 Phase shift oscillator

A three section *RC* network is used to achieve a phase shift of 180^0. The loop gain can be found by breaking the feedback loop at *x-x'* (Figure B-1).

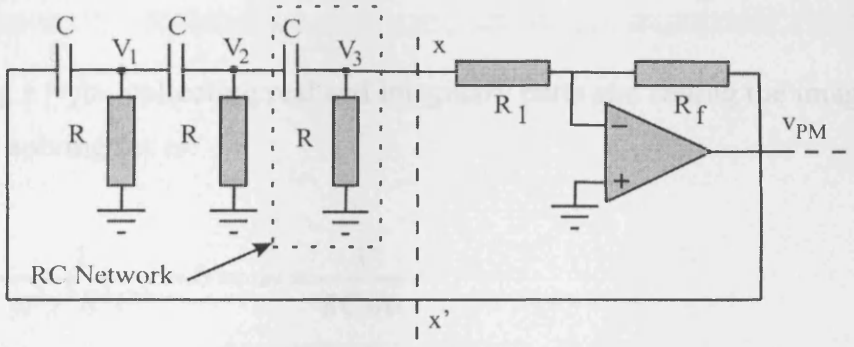

Figure B.1: Phase shift oscillator

Using Ohm's and Kirchoff's laws, the network equations become:

$$V_1(s2C+G) - V_2 sC + 0 = V_{out} sC \qquad \text{B-1}$$

$$-V_1 sC + V_2(s2C+G) - V_{in} sC = 0 \qquad \text{B-2}$$

$$0 - V_2 sC + V_{in}(sC+G) = 0 \qquad \text{B-3}$$

where $V_{in} = V_3$, $s = j\omega$ and $G=1/R$.

Using Cramer's Rule to solve for $\beta = V_{in} / V_{out}$:

$$D=\begin{vmatrix} 2sC+G & -sC & 0 \\ -sC & 2sC+G & -sC \\ 0 & -sC & sC+G \end{vmatrix} \Rightarrow D=s^3C^3+6Gs^2C^2+5G^2sC+G^3=V_{out} \qquad \text{B-4}$$

$$D_z=\begin{vmatrix} 2sC+G & -sC & sC \\ -sC & 2sC+G & 0 \\ 0 & -sC & 0 \end{vmatrix} \Rightarrow D_z=s^3C^3=V_{in} \qquad \text{B-5}$$

$$\beta=\frac{V_{in}}{V_{out}}=\frac{s^3C^3}{s^3C^3+6Gs^2C^2+5G^2sC+G^3}=\frac{1}{\left(1+\frac{6}{sRC}+\frac{5}{s^2R^2C^2}+\frac{1}{s^3R^3C^3}\right)} \qquad \text{B-6}$$

Substituting $s=j\omega$, collecting real and imaginary parts and setting the imaginary part to zero and solving for ω:

$$\frac{6}{\omega\ j\ RC}+\frac{1}{\omega^3 j^3R^3C^3}=0 \Rightarrow \omega=\frac{1}{RC\sqrt{6}} \qquad \text{B-7}$$

Substituting Eq. B-7 to the real part of Eq. B-6:

$$\beta=1-\frac{5}{\omega^2R^2C^2}=1-\frac{5}{\frac{R^2C^2}{R^2C^2(\sqrt{6})^2}} \Rightarrow \beta=-29 \qquad \text{B-8}$$

From Eq. B-7 the circuit will oscillate at:

$$\omega=\frac{1}{RC\sqrt{6}} \Rightarrow f=\frac{1}{2\pi RC\sqrt{6}} \qquad \text{B-9}$$

$$\beta = \frac{V_{in}}{V_{out}} = \frac{s^3C^3}{s^3C^3 + 6Gs^2C^2 + 5G^2sC + Ws^2C^2 + 3WGsC + WG^2 + G^3} =$$

$$= \frac{1}{\left(1 + \frac{6}{sRC} + \frac{5}{s^2R^2C^2} + \frac{1}{s^3R^3C^3} + \frac{1}{s^2CL} + \frac{3}{s^3C^2RL} + \frac{1}{s^4C^3R^2L}\right)} \quad \text{B-15}$$

Substituting $s = j\omega$, collecting real and imaginary parts and setting the imaginary part to zero and solving for ω:

$$\frac{6}{sRC} + \frac{1}{s^3R^3C^3} + \frac{3}{s^3C^2RL} = 0 \Rightarrow \omega = \frac{\sqrt{3R^2C + L}}{RC\sqrt{6L}} \quad \text{B-16}$$

From the above calculations the circuit will oscillate at:

$$\omega = \frac{\sqrt{3R^2C + L}}{RC\sqrt{6L}} \Rightarrow f = \frac{\sqrt{3R^2C + L}}{2\pi RC\sqrt{6L}} \quad \text{B-17}$$

B.3 Colpitts oscillator

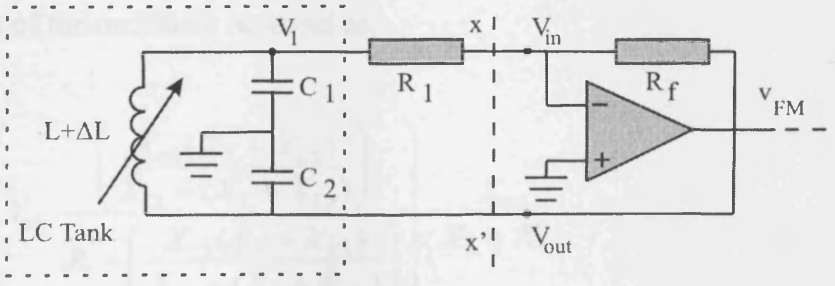

Figure B.3: Colpitts oscillator

By breaking the feedback loop at *x-x'* and treating it as a voltage divider, comprised of reactive components, the oscillator gain and operating frequency can be found:

$$V_{out} = V_1 \cdot \frac{X_{C2}}{X_L + X_{C2}} \qquad \text{B-18}$$

$$X_0 = \frac{X_{C1}(X_L + X_{C2})}{X_{C1} + (X_L + X_{C2})} \qquad \text{B-19}$$

$$V_1 = V_{in} \cdot \frac{X_0}{R_1 + X_0} \qquad \text{B-20}$$

Combining Eq. B-19 and Eq. B-20:

$$V_1 = V_{in} \cdot \frac{\left(\frac{X_{C1}(X_L + X_{C2})}{X_{C1} + (X_L + X_{C2})}\right)}{R_1 + \left(\frac{X_{C1}(X_L + X_{C2})}{X_{C1} + (X_L + X_{C2})}\right)} \qquad \text{B-21}$$

From Eq. B-21, Eq. B-18 becomes:

$$V_{out} = \left(V_{in} \cdot \frac{\left(\frac{X_{C1}(X_L + X_{C2})}{X_{C1} + (X_L + X_{C2})}\right)}{R_1 + \left(\frac{X_{C1}(X_L + X_{C2})}{X_{C1} + (X_L + X_{C2})}\right)} \right) \cdot \frac{X_{C2}}{X_L + X_{C2}} \qquad \text{B-22}$$

The gain, β, of the oscillator is found as:

$$\beta = \frac{V_{out}}{V_{in}} = \frac{\left(V_{in} \cdot \frac{\left(\frac{X_{C1}(X_L + X_{C2})}{X_{C1} + (X_L + X_{C2})}\right)}{R_1 + \left(\frac{X_{C1}(X_L + X_{C2})}{X_{C1} + (X_L + X_{C2})}\right)} \right) \cdot \frac{X_{C2}}{X_L + X_{C2}}}{V_{in}} =$$

$$= \frac{\left(\frac{X_{C1}(X_L + X_{C2})}{X_{C1} + (X_L + X_{C2})}\right) \cdot \frac{X_{C2}}{X_L + X_{C2}}}{R_1 + \left(\frac{X_{C1}(X_L + X_{C2})}{X_{C1} + (X_L + X_{C2})}\right)} =$$

$$= \frac{X_{C1} \cdot X_{C2}}{R_1 \cdot (X_{C1} + X_{C2} + X_L) + X_{C1} \cdot X_{C2} + X_{C1} \cdot X_L)} \qquad \text{B-23}$$

Replacing the reactance values of Eq. B-23 with:

$$X_C = \frac{1}{j\omega C} \qquad \text{B-24}$$

$$X_L = j\omega L \qquad \text{B-25}$$

$$\beta = \frac{\frac{1}{j\omega C_1} \cdot \frac{1}{j\omega C_2}}{R_1 \cdot \left(\frac{1}{j\omega C_1} + \frac{1}{j\omega C_2} + j\omega L\right) + \frac{1}{j\omega C_1} \cdot \frac{1}{j\omega C_2} + \frac{j\omega L}{j\omega C_1}} =$$

$$= \frac{\frac{-1}{\omega^2 C_1 C_2}}{R_1 \cdot \left(\frac{1}{j\omega C_1} + \frac{1}{j\omega C_2} + j\omega L\right) + \frac{-1}{\omega^2 C_1 C_2} + \frac{L}{C_1}} \qquad \text{B-26}$$

Setting the imaginary part to zero and solving for ω:

$$\frac{1}{j\omega C_1} + \frac{1}{j\omega C_2} + j\omega L = 0 \Rightarrow \underbrace{\frac{1}{C_1} + \frac{1}{C_2}}_{\frac{1}{C_T}} = \omega^2 L \Rightarrow \frac{1}{C_T} = \frac{1}{\omega^2 L} \Rightarrow \omega = \frac{1}{\sqrt{LC_T}} \qquad \text{B-27}$$

Therefore the frequency is:

$$f = \frac{1}{2\pi\sqrt{LC_T}} = \frac{1}{2\pi\sqrt{L\dfrac{C_1C_2}{C_1+C_2}}} \qquad \text{B-28}$$

Substituting Eq. B-27 to the real part of Eq. B-26:

$$\beta = \frac{\dfrac{-1}{\omega^2 C_1C_2}}{\dfrac{-1}{\omega^2 C_1C_2}+\dfrac{L}{C_1}} = \frac{\dfrac{-1}{\dfrac{C_1C_2}{L\dfrac{C_1C_2}{C_1+C_2}}}}{\dfrac{-1}{\dfrac{C_1C_2}{L\dfrac{C_1C_2}{C_1+C_2}}}+\dfrac{L}{C_1}} = \frac{\dfrac{-L}{C_1+C_2}}{\dfrac{L}{C_1}-\dfrac{L}{C_1+C_2}} = -\frac{C_1}{C_2} \qquad \text{B-29}$$

For $C_1 = C_2$ then $\beta = -1$, which means that the amplifier must be in an inverting configuration (as in Figure B.3) with and the feedback gain at least 1 in order to oscillate.

Appendix C: Software Hierarchy and Main Code

- **Measurement system hierarchy**
- **Main system *VI*'s**
- **Demodulation and signal processing code for the *AM*, *PM* and *FM* techniques**
- **Data output and report generation code**

For the signal processing, analysis and presentation, a program was written using the LabVIEW® graphical programming language. This programming language consists of layers of software termed virtual instruments (*VI*'s) that use the processing power of an ordinary *PC* to convert it to a custom designed instrument. These *VI*'s can be used as inside other *VI*'s, as *subVI*'s, creating a hierarchical structure (Figure C.1). The LabVIEW Class Hierarchy window displays a graphical representation of the inheritance of LabVIEW classes.

The role of the main software program (Figure C.2) is to acquire the modulated waveform (*AM*, *PM*, *FM*) that arises from the sensor circuit and separate the sensor displacement information from the reference signal. Extra code was written to the LabVIEW® program in order to supply the actuator with a sinusoidal signal that was used in order to provide a controlled displacement to the bilayer strip. For each of the modulation methods, their equivalent demodulation technique was implemented in code using their mathematical principles (Figure C.3 to Figure C.5).

After signal conditioning is preformed the information signal is passed into a *subVI* that handles the presentation and preservation of the data (Figure C.7). This section of the system handles the tagging of the data with the sensor configuration (coil and bilayer material dimensions) and the presentation of the information by producing automated reports in *.xls* (Microsoft Excel®) or *.html* format.

Measurement system hierarchy

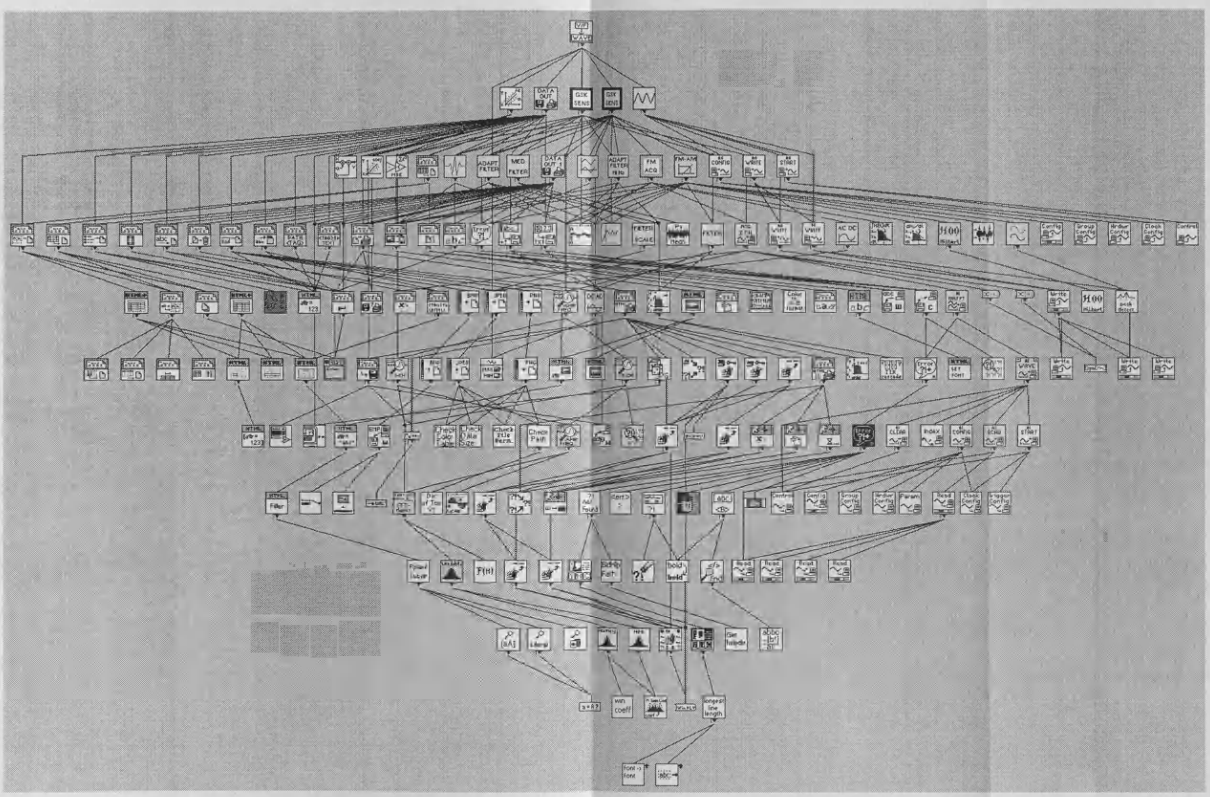

Figure C.1: The 10-layer hierarchy of the measurement system code.

Main system *VI*

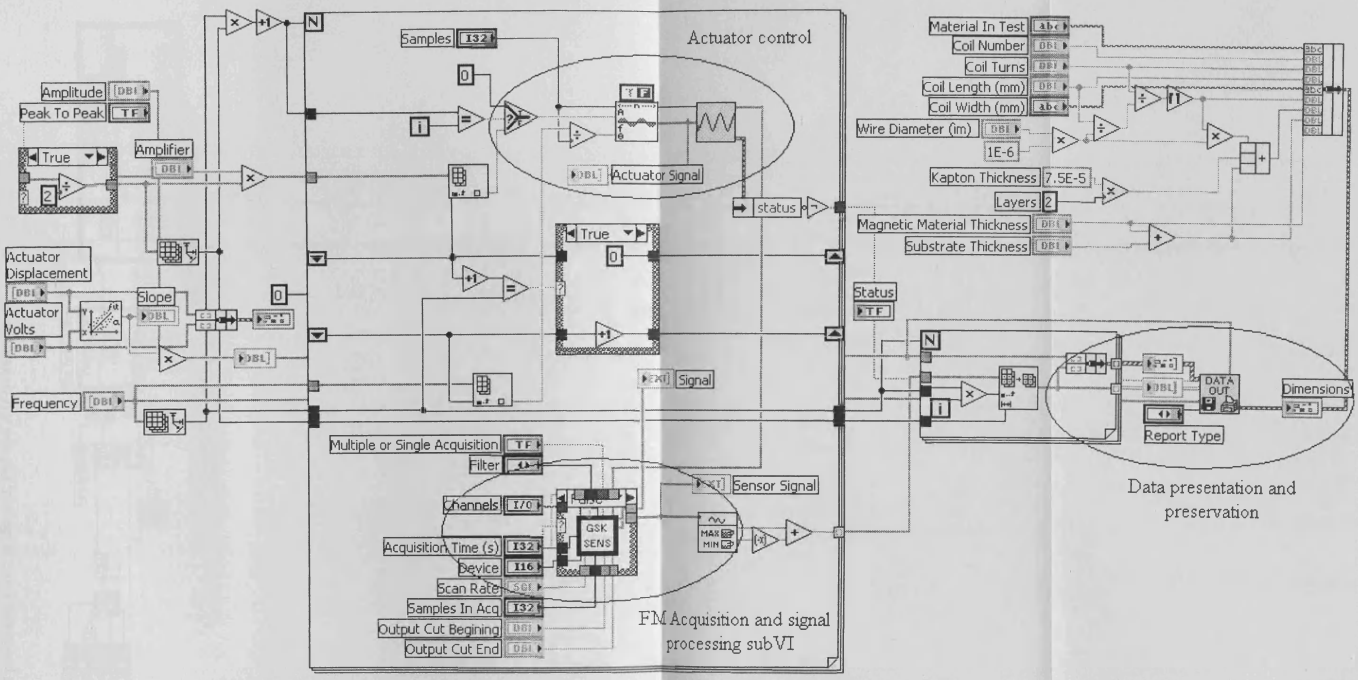

Figure C.2: The measurement system code incorporating the *FM* principle.

Demodulation and signal processing code for the *AM*, *PM* and *FM* techniques.

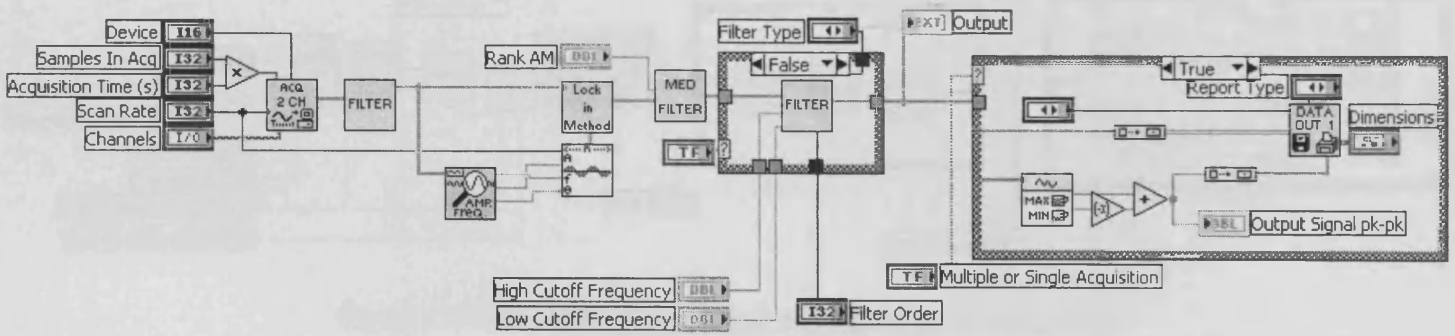

Figure C.3: The *AM* demodulation and signal processing code.

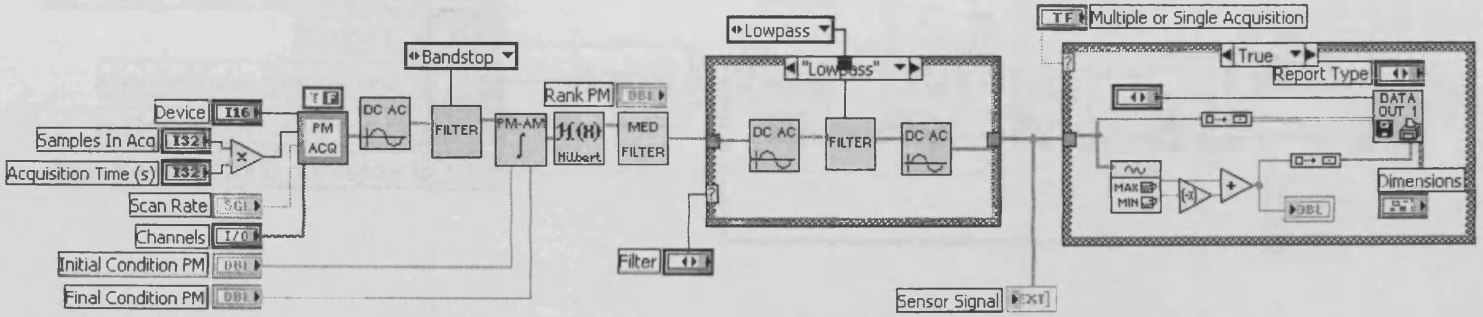

Figure C.4: The *PM* demodulation and signal processing code.

G. S. Katranas, "Design and Development of Bilayer Sensor Systems for Biomedical and Automotive Applications", Ph.D. Thesis, Cardiff University.

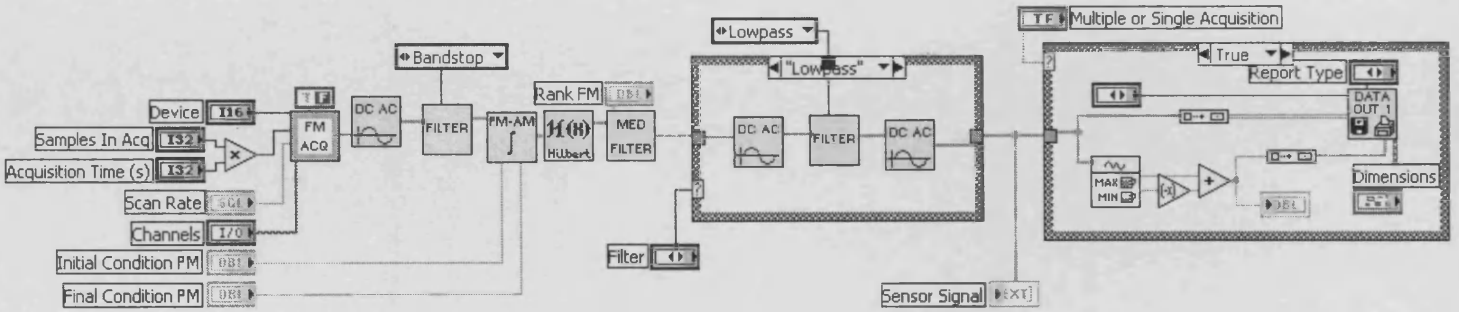

Figure C.5: The *FM* demodulation and signal processing code.

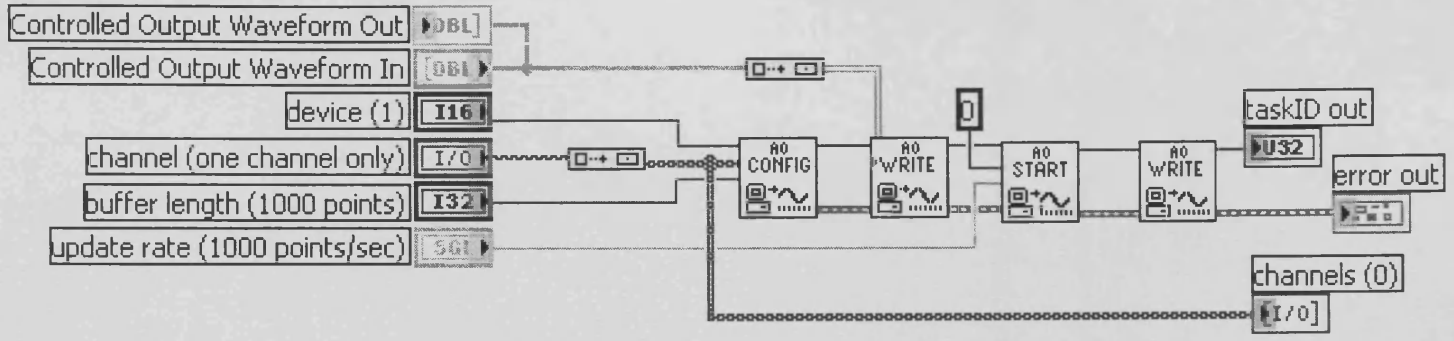

Figure C.6: The control code for the actuator

G. S. Katranas, "Design and Development of Bilayer Sensor Systems for Biomedical and Automotive Applications", Ph.D. Thesis, Cardiff University.

Data output and report generation code

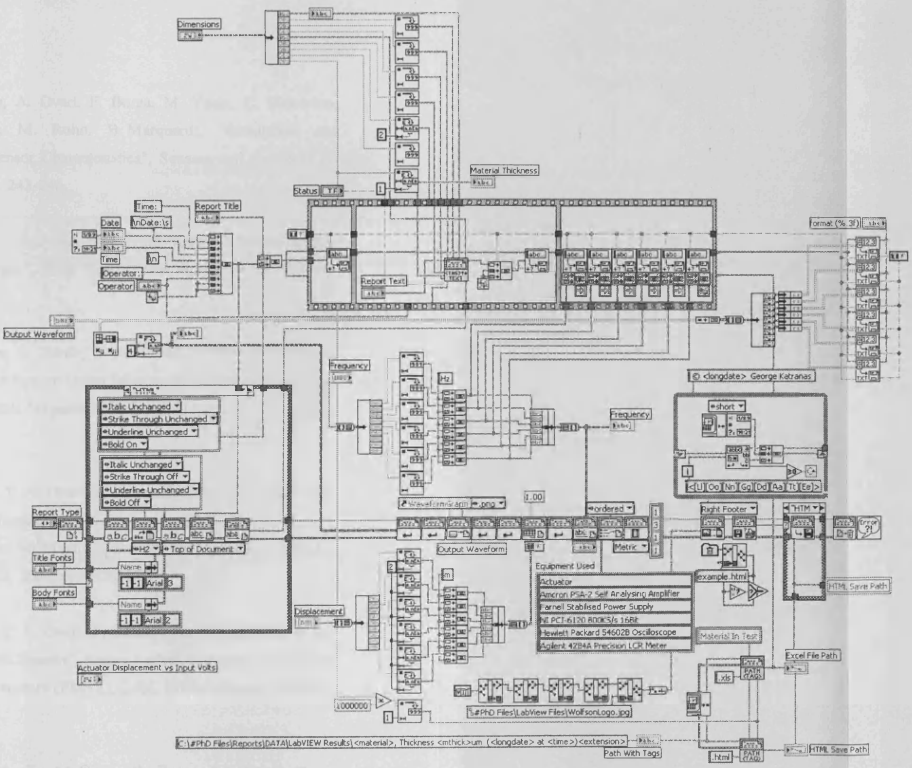

Figure C.7: The *subVI* that handles the presentation and preservation of the data.

Appendix D: Publications

Publication List

1. G. S. Katranas, T. Meydan, A. Ovari. F. Borza, M. Yasin, C. Malvicino, H. Pfützner, M. Vázquez, M. Rohn, B. Marquardt, "Simulation and Measurement of Bi-layer Sensor Characteristics", Sensors and Actuators A: Physical Vol. 129, 2006, pp. 243-246.

2. P. Bartlett, G. S. Katranas, T. Meydan, "A Hybrid Magnetic Sensor System for Measuring Dynamic Forces", IEEE Transactions on Magnetics, Vol. 42-10, 2006, pp. 3288-3290.

3. G. S. Katranas, T. Meydan, S. Zurek, T. A. Ovari, F. Borza, "A Novel Frequency Modulation Based System Using Bi-layer Thin Film Displacement Sensors", Proceedings of IEEE Magnetics Society, INTERMAG, San Diego, CA, 2006, pp. 517a-517b.

4. G. S. Katranas, T. Meydan, T. A. Ovari, F. Borza, "A Novel Bi-Layer Thin Film Sensor System for Registering Cardio-respiratory Activity", Sensor Letters, European Conference on Magnetic Sensors and Actuators (EMSA), 2006, Bilbao (Spain), Vol. 5-1, 2007, pp. 215-217.

5. G. S. Katranas, T. Meydan, T. A. Ovari, F. Borza, "Thermal Stability of Bi-Layer Thin Film Displacement Sensors", Sensor Letters, European Conference on Magnetic Sensors and Actuators (EMSA), 2006, Bilbao (Spain), Vol. 5-1, 2007, pp. 102-104.

6. G. S. Katranas, T. Meydan, T. A. Ovari, F. Borza, "A Novel Phase Modulation Based System Using Bi-layer Thin Film Displacement Sensors", Journal of Magnetism and Magnetic Materials, International Conference on Magnetism (ICM), 2006, Kyoto (Japan), Vol. 310-2, 2007, pp. e986-e988.

7. G. S. Katranas, T. Meydan, "A Bi-layer Sensor System for Measuring Airflow", IEEE Transactions on Magnetics, Vol. 43-6, 2007, pp. 2382 - 2384.

8. G. S. Katranas, T. Meydan, T. A. Ovari, F. Borza, "A Frequency Modulation Based System Using Bi-layer Thin Film Displacement Sensors", IEEE Transactions on Magnetics, Vol. 43-3, 2006, pp. 1035-1039.

9. G. S. Katranas, T. Meydan, A. Ovari. F. Borza, "Applications of the Bi-Layer Thin Film Sensor System for Registering Cardio-respiratory Activity", Sensors and Actuators A: Physical, in print.

10. G. S. Katranas, T. Meydan, A. Ovari. F. Borza, "Thermal Stability of Bi-Layer Thin Film Displacement Sensors Systems", Sensors and Actuators A: Physical, in print.

11. G. S. Katranas, T. Meydan, F. Borza, "Bi-Layer Thin Film Sensor System for Medical Applications", UK Magnetics Society Seminar: Magnetics in Medicine, Vol. 1, 2007, pp. 3-6.

12. G. S. Katranas, T. Meydan, "Parameter Optimisation for the Bi-Layer Sensor Used in the Frequency Modulation Based System", Soft Magnetic Materials Conference SMM 18, abstract accepted and paper is submitted for publication.

Available online at www.sciencedirect.com
SCIENCE DIRECT
Sensors and Actuators A 129 (2006) 243–246
SENSORS AND ACTUATORS A PHYSICAL
www.elsevier.com/locate/sna

Simulation and measurement of bilayer sensor characteristics

G.S. Katranas[a,*], T. Meydan[a], A. Ovari[a], F. Borza[a], M. Yasin[a], C. Malvicino[b], H. Pfützner[c], M. Vázquez[d], M. Rohn[e], B. Marquardt[f]

[a] *Wolfson Centre for Magnetics Technology, Cardiff University, UK*
[b] *Centro Ricerche Fiat–Vehicles, Torino, Italy*
[c] *Vienna University of Technology, Bioelectricity and Magnetism Lab, Austria*
[d] *Instituto de Ciencia de Materiales de Madrid, CSIC, Spain*
[e] *Profactor, Steyr, Austria*
[f] *ELCAT, Wolfratshausen, Germany*

Received 6 July 2004; received in revised form 1 September 2005; accepted 19 September 2005
Available online 3 March 2006

Abstract

This paper introduces a novel approach to the detection and accurate measurement of extremely small signals, produced by bilayer thin films without the use of sophisticated hardware. The implementation of this measuring system is based on the LabVIEW graphical programming. This general purpose, robust and low-cost signal detector, provides an excellent way to evaluate magnetostrictive materials and their application in magnetic sensors. Initially the complete system was first simulated in LabVIEW software with the simulated signal superimposed with noise signals and the correct performance of the program was successfully confirmed. Later the software was incorporated together with the simple modulating circuit of the sensor. The results from the acquisition proved that the system provides a quick and excellent way to evaluate magnetostrictive materials and their application in magnetic sensors.

Keywords: Magnetostriction; Bilayer thin film sensors; Data acquisition; LabVIEW

1. Introduction

Magnetic sensors are devices that receive a stimulus and convert it to an electrical output signal by utilizing the laws of electromagnetism and effects in electromagnetic fields in order to achieve their goal. Materials such as the soft magnetic amorphous ribbon exhibit discrete amounts of magnetostriction. These materials display a property, which is known as the magnetoelastic effect. Depending on the sign of the sample's magnetostrictive constant, the application of mechanical tensile stress, σ, (or strain ε) to bilayer thin film sensors, results in changes in the relative permeability, μ_r, of the material [1,2]. When a magnetostrictive amorphous ribbon is bent, the changes in the relative permeability, μ_r, are not as large as expected, because there is a reduction due to the fact that the effect of tension in the first half of the material is counterbalanced by the effect of compression in the second half. Bilayer strips consist of two layers, one layer that contains the magnetostrictive amorphous ribbon and a non-magnetic counter layer. The purpose of this configuration is to shift the neutral bending area out of the amorphous ribbon, hence impose the same sign stress throughout the amorphous ribbon [3]. The permeability changes are detected by a pickup coil, wrapped around one end of the bilayer sensor, which establishes the sensor signal as a change of inductance, ΔL [4]. Bilayer sensors are cost-effective and easy to operate and they have been developed to detect various measurement categories such as displacement, bending, temperature, etc. [5]. These sensors can be used for a variety of applications such as automotive industry, aerospace, environmental monitoring, earthquake prevention and especially biomedical for signal acquisition for monitoring physiological activities [6–8]. So far, the sensor signals have been detected and analysed using sophisticated electronic circuits and costly measuring systems [9]. The system described in this paper uses a PC-based system that consists of a simple external circuit used for the modulation of the sensor signal and the National Instruments LabVIEW software

* Corresponding author. Tel.: +44 2920 875934; fax: +44 2920 876729.
E-mail address: katranasg@cf.ac.uk (G.S. Katranas).

0924-4247/$ – see front matter © 2006 Elsevier B.V. All rights reserved.
doi:10.1016/j.sna.2005.09.059

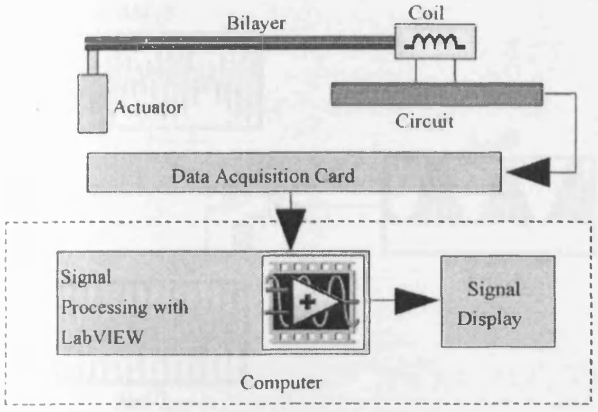

Fig. 1. Measurement system.

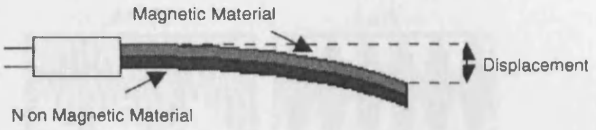

Fig. 2. Bilayer sensor during bending.

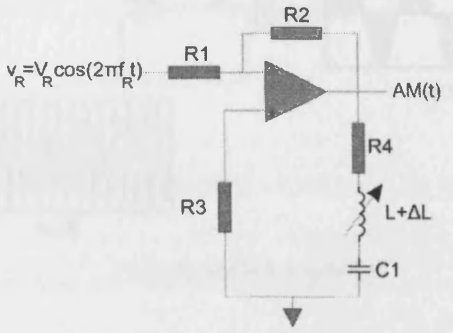

Fig. 3. Voltage-controlled current source.

and acquisition card. The detection of the signal was conducted by using the LabVIEW software that acquired the modulated signal from the circuit and demodulated it into its components via a technique known as the lock-in amplification. The use of the versatile LabVIEW software provided a user-friendly method for accurately obtaining, analysing and displaying data, in a cost-effective way.

2. Experimental method

The measuring system consists of a simple circuit, that modulates the sensor displacement with a reference signal, and a PC-based acquisition setup, as seen in Fig. 1.

The bilayer thin film that was used in the sensor consists of a magnetostrictive layer and a counter layer of non-magnetic nature (mica). The 2 μm thickness magnetic material (Metglas 2605SC) was deposited on the 150 μm counter layer by using the magnetron sputtering technique.

In order to provide a controlled displacement, the free end of the bilayer sensor was attached mechanically to the tip of an actuator. This displacement was also monitored with the aid of a laser scanning Doppler vibrometer, in order to verify the correct operation of the measurement system.

When the bilayer is mechanically bend at the free end, the relative permeability, μ_r, of the magnetostrictive layer changes, leading to a change ΔL in the inductance, L, of the pickup coil and hence its reactance, X_L. Thus, the change in ΔL corresponds to the displacement of the bilayer sensor (Fig. 2).

The pickup coil of the sensor was supplied with a voltage $v_R = V_R \cos(2\pi f_R t)$. The change in ΔL of the coil varies accordingly the amplitude, V_R. Thus, the voltage v_R becomes an amplitude-modulated signal (AM), and it is described as:

$$\mathrm{AM}(t) = [V_R + v_S(t)]\cos(2\pi f_R t) \quad (1)$$

Where $v_S(t)$ is the information signal (sensor displacement). For the measurement system the actuator is setup to displace the bilayer according to:

$$v_S(t) = V_S \cos(2\pi f_S t) \quad (2)$$

In the measurement setup, the amplitude I_R, of the excitation current $i_R = I_R \sin(2\pi f_R t)$ is held constant with the aid of a voltage controlled current source (Fig. 3).

A PC with a NI-4472 card from National Instruments was used to acquire the data. The card used has a maximum sampling rate of 102.4 kS/s and provides a 24-bit resolution. The LabVIEW virtual instruments (VI's) are layers of software that use the processing power of an ordinary PC to convert it to a custom designed instrument. The VI's consist of two main elements the front panel and the block diagram. The front panel is the instruments interface and it is used for controlling the VI and displaying the data. The block diagram consists of the elements that acquire and process the signal [10].

The design was initiated with the simulation of the complete system in LabVIEW. This included the modulation of two sine waves, a reference and a sensor signal under the amplitude modulation principle, and their demodulation via the lock-in technique. The correct performance of the simulated system was successful. The principal steps of the block diagram can be seen on the flowchart in Fig. 4. The core of the demodulation process is the lock-in technique and there are two mathematical

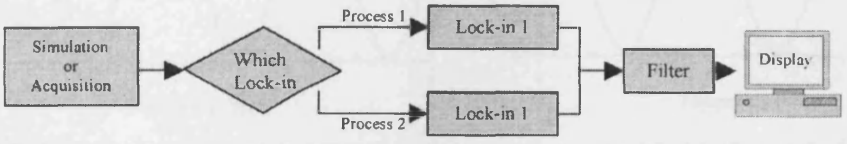

Fig. 4. Flowchart of the measurement system.

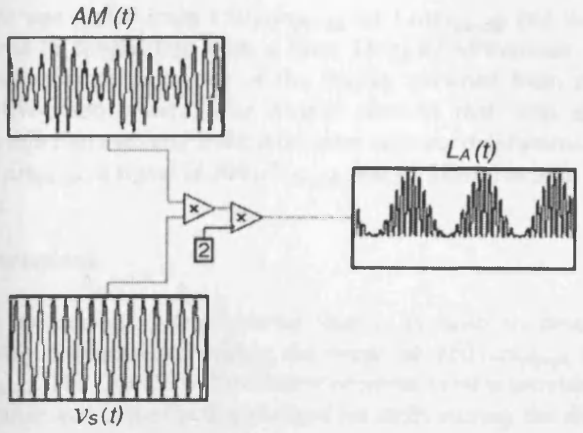

Fig. 5. First lock-in technique.

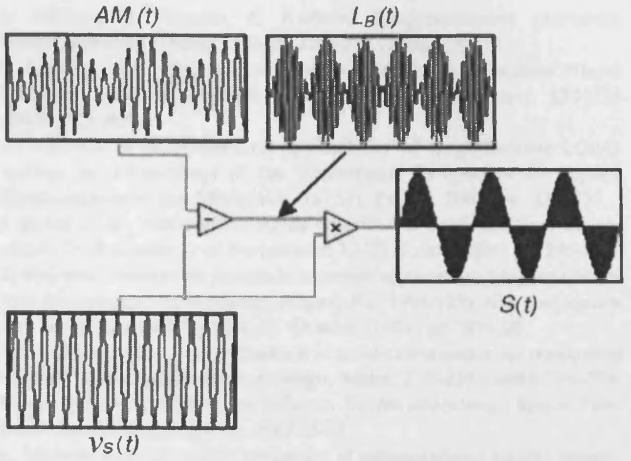

Fig. 6. Second lock-in technique.

processes of performing it. Both are incorporated within the LabVIEW program for evaluation purposes.

The first process is the multiplication of the amplitude-modulated signal with the reference signal [11] as seen in Fig. 5.

$$L_A(t) = 2\cos(2\pi f_R t)\mathrm{AM}(t) \quad (3)$$

After filtering the high frequency component through a low pass filter the remaining signal is the sensor signal with a DC component, which is then easily removed in LabVIEW. The second process is the subtraction from the amplitude-modulated signal, the component which in this case is the reference signal, as seen in Fig. 6.

$$L_B(t) = \mathrm{AM}(t) - V_R\cos(2\pi f_R t) \quad (4)$$

The signal now consists of two components, a low frequency component which is the sensor signal and a high frequency component, $\cos(2\pi f_R t)$ that originates from the reference signal. By multiplying $L_B(t)$ with the reference signal, $v_R(t)$, the high frequency component is then squared.

$$S_M(t) = V_s\cos(2\pi f_S t)V_R\cos^2(2\pi f_R t) \quad (5)$$

This creates a signal $S(t)$ as seen in Fig. 6. By passing $S(t)$ through a low pass filter the high frequency component was removed. In both lock-in techniques care is taken so that the AM and the reference signal have the same phase between them to ensure correct demodulation.

3. Results

The software program was first tested by simulating the amplitude-modulated waveform AM(t) and demodulating it into its components via a technique known as the lock-in amplification. In ideal conditions the software program will demodulate the AM(t) to its components, as it can be seen comparing the simulated sensor displacement $v_S(t)$ (input) in Fig. 7a, with the demodulated sensor displacement (output) in Fig. 7b. Tests were also run by adding noise components to the AM(t) signal and then successfully demodulating it as seen in Fig. 7c.

For the acquisition, the measurement system was set at $V_R = 1$ V, $f_R = 20$ kHz and $f_S = 3$ Hz, the displacement of the

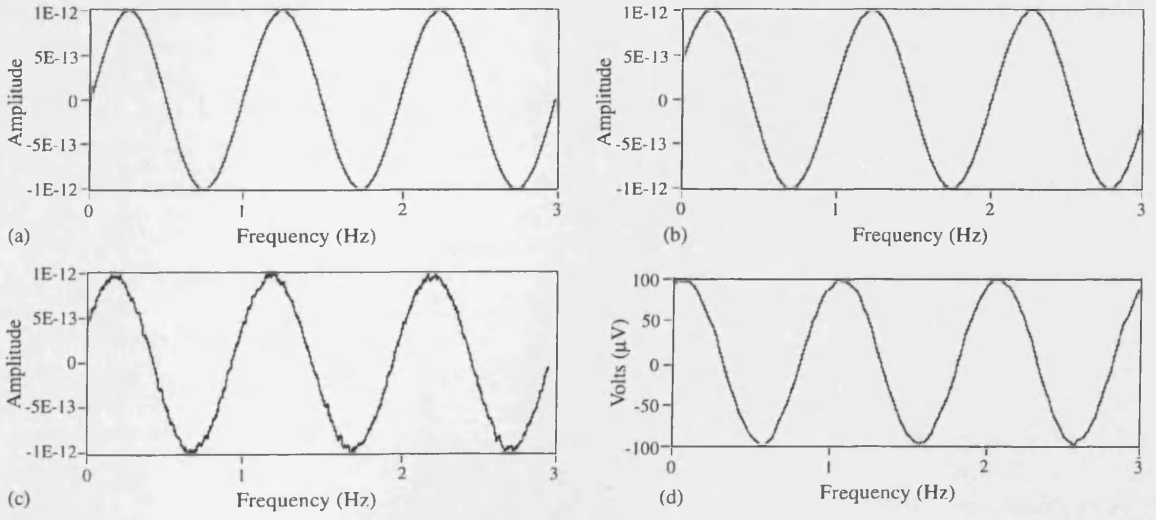

Fig. 7. (a) simulated sensor displacement $v_s(t)$ (input); (b) demodulated sensor displacement (output); (c) demodulated sensor displacement (output) after the addition of noise parameters to the AM(t) signal; and (d) acquisition results.

actuator was varied from 150 μm_{pk-pk} to 1 mm_{pk-pk} and was measured in conjunction with a laser Doppler vibrometer in order to verify the accuracy of the results obtained from the LabVIEW-based system. The results showed that with the bilayer thin film used and at the minimum actuator displacement of 150 μm_{pk-pk}, a signal of 200 μV_{pk-pk} was produced as seen in Fig. 7d.

4. Conclusions

The measuring system proved that it is able to detect accurately displacements within the range of 150 μm_{pk-pk} to 1 mm_{pk-pk}. The LabVIEW-based measurement system provided an accurate and cost-effective method for determining the displacement of the bilayer sensor.

References

[1] R. Boll, K.J. Overshott (Eds.), Magnetic Sensors, vol. 5, VCH, Weinheim, 1989.
[2] L. Mehnen, H. Pfützner, E. Kaniusas, Magnetostrictive amorphous bimetal sensors, J. Magn. Mater. 215–216 (2000) 779–781.
[3] L. Mehnen, et al., Displacement sensor based on an amorphous bilayer including a magnetostrictive component, J. Magn. Mater. 254–255 (2003) 627–629.
[4] E. Kaniusas et al. Biomedical applicability of magnetoelastic bilayer sensors, in: Proceedings of the International Symposium on Applied Electromagnetics and Mechanics (ISEM), France, 2003, pp. 236–237.
[5] J. Kosel et al., Non-contact signal detection of multifunctional bilayer sensor, in: Proceedings of Eurosensors XVIII, Rome, 2004, pp. 593–594.
[6] T. Meydan, Amorphous materials in sensor applications, Magnetic Materials for Sensors and Actuators (Digest No. 1994/183), IEE Colloquium on New Magnetic Materials, 11 October, 1994, pp. 2/1–2/3.
[7] E. Kaniusas, et al., A magnetostrictive acceleration sensor for registration of chest wall displacements, J. Magn. Mater. 215–216 (2000) 776–778.
[8] EU-Project, Magnetostrictive Bilayers for Multifunctional Sensor Families, http://bsens.gte.tuwien.ac.at/ 2002.
[9] L. Mehnen et al., Dynamic properties of magnetoelastic bilayer sensors, 16th Soft Magnetic Materials Conference, Germany, 2003.
[10] National Instruments, LabVIEW 7 user manual, 2003.
[11] P. Kromer, PC-Based Digital Lock-In Detection of Small Signals in the Presence of Noise, University of Texas, USA, NIWeek Competition, 2002, Available at http://mrflip.com/papers/LIA/#Implementation.

A Hybrid Magnetic Sensor System for Measuring Dynamic Forces

Paul A. Bartlett, George S. Katranas, and Turgut Meydan

Wolfson Centre for Magnetics, Cardiff School of Engineering, Cardiff University, Cardiff CF24 3AA, U.K.

This paper describes a hybrid device that comprises of both a magnetostrictive rod and an amorphous wire magnetic sensor that could be used for force sensing applications. The amorphous sensor uses a frequency modulation technique to detect changes in the wire's permeability. These permeability changes were a result of stress-induced changes in magnetization in a dynamically compressed magnetostrictive rod that was in close proximity to the amorphous sensor.

Index Terms—**Amorphous wire, force measurement, frequency modulation, magnetostrictive sensor.**

I. Introduction

THE measurement of applied stress has been shown to be possible through the use of magnetostrictive materials such as Terfenol-D. A change in the applied stress to such materials results in a change in their magnetization; this is known as the Villari Effect [1].

There are a number of ways to measure the change in magnetization in a rod of Terfenol-D [2]. The typical way is to wind a sensing "pick-up coil" co-axially on the sensor's Terfenol-D rod. However, in this paper a novel amorphous-wire sensor system is described that can detect the changes in magnetization induced by an externally applied stress. These magnetization changes are then related to the force that was applied to the transducer thereby enabling the calibration of the sensor.

II. Experiment

A. A Hybrid Magnetostrictive Material/Amorphous Wire Sensor System

1) Sensor Design: The main component of the force sensor was a 15 mm in diameter and 50 mm in length rod of Terfenol-D. It was housed in a cylindrical Tufnol former which enabled the alignment of the sensor within the external test-rig whilst also giving support to the amorphous wire sensor. This sensor comprised of a 30 mm long FeCoSiB amorphous wire that was surrounded by a 350 turn excitation coil (see Fig. 1). The amorphous wire sensor was bent so that it would follow the circumference of the 1 mm thick Tufnol former that surrounded the Terfenol-D rod.

The coil that was wound around the amorphous wire was supplied with a sinusoidal carrier signal of 5 kHz. Stress induced changes in the magnetization state of the Terfenol-D rod produces a field that alters the impedance of the amorphous-material sensor which in turn shifts the frequency of the carrier signal by Δf, hence producing a frequency modulated (FM) waveform. By demodulating the FM signal, the amplitude of the peak-to-peak signal could be measured and then related to the equivalent drive signal produced by applying a sinusoidal stress to the hybrid sensor [2].

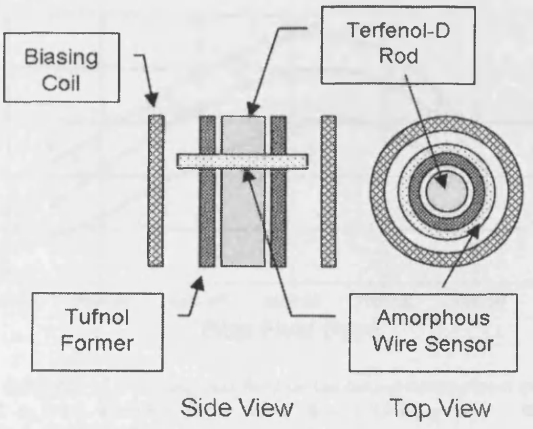

Fig. 1. Schematic of the hybrid sensor.

The hybrid sensor was placed in a solenoid of 1375 turns, with an inner diameter of 55 mm, outer diameter 84 mm and length 100 mm. This solenoid was incorporated so that a "biasing field" could be applied to the hybrid sensor.

It is considered that the biasing field moves the operating point of the Terfenol-D rod into a region of the strain versus induction curve where the $dB/d\lambda$ is greatest, where the value of the magnetic induction B, is a result of an externally applied stress-induced strain λ. Therefore a change in applied stress at a favorable operating point will result in a greater change in magnetization than that produced in a region of lower $dB/d\lambda$. It must also be noted that the transduction performance of Terfenol-D is also dependent on any applied pre-stress.

The Terfenol-D rod was positioned so that it was in the middle of a biasing solenoid that had a length twice that of the magnetostrictive component. A biasing coil of this length was used in order to improve applied field uniformity in the region of the Terfenol-D rod. At both ends of the Terfenol-D rod, brass "push rods" enabled the positioning of it in the former whilst also allowing the application of mechanical stress from an external source.

2) Test Rig: The main aim of these experiments was to determine whether is was possible to calibrate the hybrid sensor

Digital Object Identifier 10.1109/TMAG.2006.879745

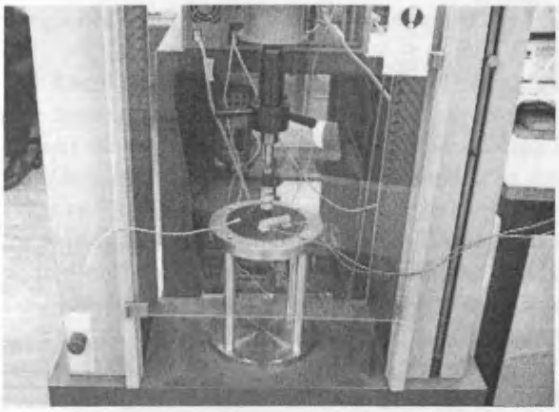

Fig. 2. Hybrid sensor mounted in the RSA 50 test machine. The bias coil is not present in this image.

against a known sensor, so that it could detect a dynamic force that was applied to it. To achieve this, the hybrid sensor was installed in a Schenk RSA 50 Electromechanical Universal Testing Machine. By moving the RSA 50's cross-head it was possible to apply a known dynamic force (and hence a strain) to the Terfenol-D rod in the hybrid sensor (see Fig. 2).

The force that was applied to the sensor was then directly measured via the RSA 50's integral PM 63 k load cell that could measure loads up to 63 kN, via a Schenk M1602 display unit. The output signal from the load cell was processed by the RSA 50's DP 151 control monitor unit before being recorded on an Agilent 54 624A oscilloscope where peak-to-peak force values could be identified.

A low-frequency dynamic force (~1.7 Hz) was applied to the hybrid sensor with the amplitude of oscillation being controlled via the RSA 50's FP 151, 153, and FG 152 control modules. This was the highest frequency of oscillation that could be produced from the RSA 50. The force was applied so that it ranged from zero to its maximum value without an additionally applied pre-stress.

3) Signal Processing: The FM signal measurement system consisted of a personal computer (PC) based acquisition arrangement. The detection of the FM signal was conducted through the LabVIEW package and a National Instruments PNI-6120 data acquisition card with a maximum sampling rate of 800 kS/s and 16-bit resolution [3].

Changes in the state of magnetization of the Terfenol-D rod caused co-responding FM to the carrier signal that was applied to the amorphous sensor. By demodulating this signal, the peak to peak amplitude could be calculated by the LabVIEW system and then related to the equivalent drive signal produced by the IPM 63 k load cell as measured by the Agilent 54 624A. This could then be related to the applied force through calibration data that was obtained for the PM 63k's load cell.

B. Low-Frequency Force Measurements

It is understood that the performance of Terfenol-D in a sensor configuration is dependent on the applied stress, applied biasing field and the magnetic history of the active element. As a result, it was certain that the output voltage from the hybrid sensor would be influenced by these factors. Therefore,

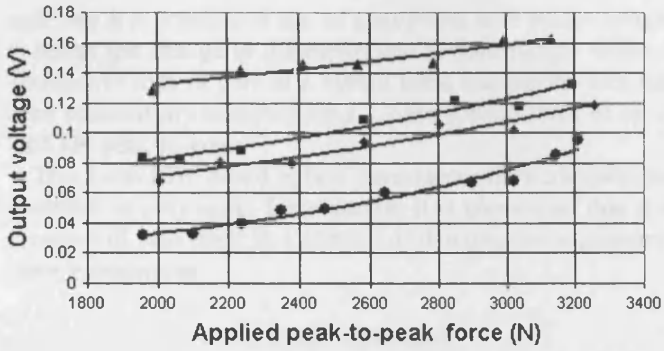

Fig. 3. Measured output voltages from the hybrid sensor system for different applied forces at a frequency of 1.7 Hz with the following bias fields: ▲ = 4.13 kA/m, ■ = 3.50 kA/m, ♦ = 3.34 kA/m, • = 2.65 kA/m.

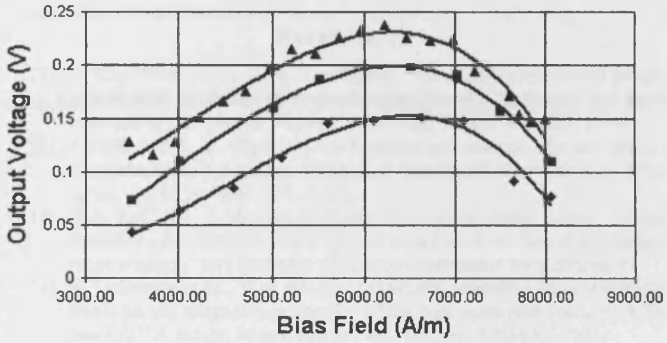

Fig. 4. Influence of a varying bias field on the output voltage from the hybrid sensor at a fixed dynamic stress value. ♦ = 1.46 kN p-to-p, ■ = 1.97 kN p-to-p, ▲ = 2.39 kN p-to-p.

measurements were made of the voltage output from the sensor system were made for different peak-to-peak amplitudes of the 1.7 Hz applied force (see Fig. 3).

For each data point, five sensor output voltage measurements were made and averaged for each force amplitude. In each of the plots shown, different biasing fields were applied to the Terfenol-D rod. As can be seen, changing the bias field offsets the output voltage versus applied force curve. To investigate this further, the hybrid sensor was subjected to fixed amplitude dynamic forces of 1.46, 1.97, and 2.65 kN and the bias field that was applied to the device was altered between ~ 3.5–8 kA/m (see Fig. 4).

It was noted here that increasing the dynamic force causes an offset of the sensor output curve. This is to be expected as Fig. 3 demonstrates that an increase in the dynamic applied force results in an increase in sensor output. It must be noted that in this system configuration, the "effective" average force for each dynamic stress increases as the peak-to-peak force value increases. It has been shown [4] that Terfenol-D's performance can be improved through the suitable application of a pre-stress. It is possible that the performance of the sensor is influenced by this factor and an improvement to the device would be the application of an additional pre-stress. Further work will be undertaken to optimize pre-stress levels for the hybrid sensor operation.

Inspection of Fig. 4 also shows that there seems to be a maximum value of sensor output voltage for a given dynamic force in the region of 6–7 kA/m for each curve. It is considered that this is due to the operating point of the transducer moving away

rom a region of the B versus λ curve where $dB/d\lambda$ is at a maximum.

It was found that both very high levels of stress and low agnetic biasing levels resulted in distortions in the signal utput from the sensor. When the sinusoidal applied stress' mplitude is great enough, it can cause a change in magnetiation that result in the detected stress-induced magnetic field anges passing through a minimum value. If this occurs, then roportion of the signal output will be "frequency doubled." his can be mitigated against by supplying sufficient magnetic asing so that any change in stress-induced magnetization does ot occur near this minimum. It was also noted that for some rger values of dynamic applied stress, the shape of one half of e sensor output signal was "flattened." It is considered that in is case the Terfenol-D's Villari effect is being saturated as a sult of the high applied forces. It is possible that selection of appropriate pre-stress could improve the performance of the nsor and increase the applied force value at which saturation ccurs.

Although the dynamic force-spectrum that was applied to this nsor was limited to 1.7 Hz, it is not considered that there ould be any difficulty in significantly increasing the operation equency of the sensing system. Indeed, it has been shown in that such devices can operate at least to 3 kHz.

III. Conclusion

In this paper, a hybrid magnetostrictive force sensor has been scribed. Experiments have been carried out to prove the principle that it is possible to use an amorphous wire sensor system to detect the change in magnetization in dynamically stressed Terfenol-D rods as part of a hybrid force transducer. This has been successfully achieved for a 1.7 Hz applied force of up to 2.65 kN peak-to-peak.

This LabVIEW based hybrid transducer offers considerable potential as a dynamic force sensor. It is considered that this system will lend itself to a number of dynamic force measurement applications.

Acknowledgment

The authors would like to thank S. J. Eaton of QinetiQ Ltd. for supplying the Rare Earth Products Ltd. Terfenol-D rods used in this study.

References

[1] S. Chakraborty and G. R. Tomlinson, "An initial experimental investigation into the change in magnetic induction of a Terfenol-D rod due to external stress," *Smart. Mater. Struct.*, vol. 12, pp. 763–768, 2003.

[2] J. Pratt and A. B. Flatau, "Development and analysis of a self-sensing magnetostrictive actuator design," *J. Intelligent Material Syst. Structures*, vol. 6, pp. 639–648, 1995.

[3] G. S. Katranas, T. Meydan, S. Zurek, T. A. Ovari, and F. Borza, "A novel frequency modulation based system using bi-layer thin film displacement sensors," INTERMAG 2006 Conf, submitted for publication.

[4] N. Galloway *et al.*, "The effects of magnetic annealing and compressive stress on the magnetic-properties of the rare-earth iron compound Terfenol-D," *J. Magn. Magn. Mater.*, vol. 119, pp. 107–114, 1993.

Manuscript received March 13, 2006 (e-mail: Bartlettpa1@cf.ac.uk).

A Novel Frequency Modulation Based System Using Bi-Layer Thin Film Displacement Sensors . .

G. S. Katranas[1], T. Meydan[1], S. Zurek[1], T. A. Ovari[1] and F. Borza[1]
1. Wolfson Centre for Magnetics, School of Engineering, Cardiff University, Cardiff, South Glamorgan, United Kingdom

Introduction

A novel method has been used for accurately measuring low voltage signals (~10^{-4}V) associated with inductance changes of bi-layer thin film sensors under bending stress, without the use of sophisticated hardware. Bi-layer thin films form the building blocks for a new generation of multifunctional sensors. They consist of a magnetic layer deposited on a non magnetic layer that is used to enhance the changes in the relative permeability of the magnetic material, caused by tensile or compressive stresses. Bi-layer sensors are cost effective and easy to operate and they have been developed to detect various parameters such as displacement, temperature, stress etc [1]. Previous methods for detecting and analyzing sensor signals required the use of costly measurement systems such as Laser Scanning Doppler Vibrometer [2].

Frequency modulation based system

The bending sensor used is a bi-layer strip, which consists of a high positive magnetostrictive amorphous layer and a non-magnetic counter-layer (Copper Beryllium - CuBe). The amorphous magnetic film, 2.9μm thick, was deposited from a $Fe_{81}B_{13.5}Si_{3.5}C_2$ ribbon target using the RF magnetron sputtering technique onto a 25μm CuBe layer. The measuring system consists of a personal computer (PC) based acquisition set up and a circuit that modulates the sensor displacement signal with a reference signal, using the frequency modulation (Fig. 1a). Signal detection was achieved through the use of LabVIEW® software and a NI-6120 data acquisition card (800kS/s 16-bit) which allows a high degree of software modularity [3]. In the frequency modulation (FM) scheme the sensor signal is not significantly influenced by noise. The FM was achieved using a Colpitts oscillator. The output is a sine wave at a frequency which is defined by the values of the circuit components L and C. The bi-layer sensor acts as the inductive component of the Colpitts oscillator. Any change ΔL in the inductance L of the pickup coil will shift the oscillator's frequency f by Δf. Hence, frequency modulation is achieved. An alternating sinusoidal force was applied to the free end of the bi-layer using a mechanical actuator operating at 3Hz to simulate the average maximum heart rate (180 beats per minute) expected in a healthy 40 year old person [4]. In order to demodulate the FM signal it needs to be input through a differentiator followed by an envelope detector. The envelope detector used here was based on the Hilbert transform [5].

Capability of the system

Low frequency (3Hz) sine waves, with variable peak to peak amplitudes from 1V to 6V, were applied to the actuator. The resulting output peak to peak displacement ranged from 0.35mm to 2mm. The displacement of the actuator was first tested with the aid of a Laser Doppler Vibrometer (LDV) for calibration purposes. As seen in Fig. 1b the frequency modulated signal (FM) shows an average 0.9% deviation with a 2% maximum deviation compared to the expected signal from the LDV. The output signal is determined by the degree of bending of the bi-layer which can be converted into a displacement reading. The average peak to peak signal corresponding to the displacement range of the actuator was in the range of 0.8mV to 4.6mV. The results are linear with a square correlation coefficient value of 0.99 (Fig. 1c). The system has a good performance with an average sensitivity of 2.2mV/mm while the repeatability of the results was 2.4%.

Conclusion

A new type of measuring system incorporating bi-layer displacement sensors has been developed. The system is capable of detecting peak to peak displacements using the frequency modulation scheme in the range of 0.35mm to 2mm. It has been shown that the measurement system, together with the bi-layer sensors, provides an accurate and low-cost method for determining displacement. It is expected that this system will lend itself to a number of applications including biometric measurements. References

1. J. Kosel et al., "Non-Contact Signal Detection of Multifunctional Bi-layer Sensor," Proc. of Eurosensors XVIII, Italy, Rome, 2004, pp. 593-594.
2. L. Mehnen et al., "Dynamic properties of magnetostrictive bilayer sensors," 16th Soft Magnetic Materials Conference, Dusseldorf, Germany, 2003, to be published
3. DAQ PCI-6115/6120 User Manual, S-Series Simultaneous-Sampling Multifunction Device for PCI, National Instruments, 2004.
4. G. F. Fletcher et al., "Exercise standards for testing and training: a statement for healthcare professionals," American Heart Association, Circ., 2001, pp.1694-1740.
5. S. R. Long et at., "The Hilbert techniques: an alternate approach for non-steady time series analysis," IEEE Geoscience and Remote Sensing Society Newsletter, pp. 6-11, March 1995.

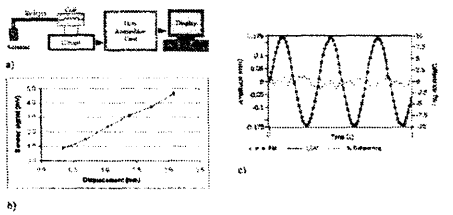

Fig. 1. Frequency modulation based system a) block diagram, b) a comparison between the sensor signal and the LDV output at 0.35mm peak to peak, plotted together with their percentage difference and c) the output voltage against the displacement of the bi-layer sensor.

SENSOR LETTERS
Vol. 5, 1–3, 2007

A Novel Bi-Layer Thin Film Sensor System for Registering Cardio-Respiratory Activity

G. S. Katranas, T. Meydan*, T. A. Ovari, and F. Borza

Wolfson Centre for Magnetics, Cardiff School of Engineering, Cardiff University, Queens Buildings, Cardiff University, Cardiff, CF243AA, UK

(Received: Xx Xxxxx Xxxx. Accepted: Xx Xxxxx Xxxx)

A novel method has been used for accurately measuring physiological parameters associated with body movements, such as cardiac and respiratory activities, using bi-layer thin-film sensors. A bi-layer curvature sensor system was used the first time not only to monitor but also to map the five characteristic waves of the normal heartbeat rate (P, Q, R, S, and T wave), hence providing additional medical information about the cardiac activity of the patient. Also during monitoring of lung ventilation, parameters such as normal respiration, deep inhalation/exhalation and apnoea were easily distinguishable in the output signal. The bi-layer thin films used are the building blocks for a new generation of multi-functional sensor families. They consist of a magnetic layer and a non magnetic counter layer that is used to enhance the changes in the relative permeability of the material caused by tensile or compressive stresses during bending. The measuring system utilizes a personal computer based system using the LabVIEW® graphical programming package. This allows a high degree of software modularity and provides the features necessary for acquiring the sensor signal, analysing it and displaying the results. The results demonstrate that this system provides a robust, cost effective solution to monitoring cardio-respiratory activity with minimum inconvenience to the patient, which is necessary for prolonged, undisturbed monitoring.

Keywords: Data Acquisition, Frequency Modulation, Physiological Sensors, Thin Films, Transducer.

RESEARCH ARTICLE

1. INTRODUCTION

The non-disturbing monitoring of the cardio-respiratory activity of the human body is an important parameter during biometrical tests, such as polysomnography. This is a comprehensive recording of the physiological changes that occur during sleep. This diagnostic test monitors many medical techniques including electroencephalography (EEG), rapid eye movement (REM), electromyography (EMG), electrocardiogram (ECG), and respiratory activity while the patient is sleeping. During the sleep study the breathing; oxygen levels, heart tracing, and the different levels of sleep are recorded. A qualified sleep technician performs the test and monitors the patient's sleep through the night. The sleep technician will place electrodes on the head and face to monitor levels of sleep, apply ECG (electrocardiogram) patches to the chest to monitor the heartbeat, and place a flow sensor under the nose to monitor airflow. In addition, soft straps are placed around the chest and abdomen to monitor the rise and fall of the chest to determine whether the patient is breathing appropriately during sleep. These sensors, electrodes, and straps can potentially disturb the patients sleep.

This paper describes the application of a novel system using bi-layer thin film sensors, originally used for the detection of bending.[1] The system can also be used to measure, with minimum disturbance, physiological activities that involve the dynamic deformations of the curvature of the skin.

2. EXPERIMENTAL DETAILS

2.1. Measurement System

Bi-layer sensors are constructed from a ferromagnetic magnetostrictive layer that can be crystalline, nano crystalline or amorphous magnetic materials on a non-magnetic layer. Bi-layer sensors are cost effective and easy to operate and they have been developed to detect parameters such as displacement, temperature, curvature, stress, etc.[2] In this paper, a bi-layer with amorphous

*Corresponding author; E-mail: Meydan@cf.ac.uk

 1546-198X/2007/5/001/003 doi:10.1166/sl.2007.075

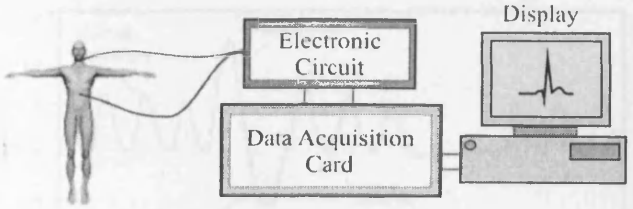

Fig. 1. Bi-layer sensor system for registering cardio-respiratory activity.

magnetostrictive layer is used because of its lack of magneto-crystalline anisotropy and high mechanical strength.[3,4] Soft magnetic amorphous ribbons and thin films may exhibit high magnetostriction and therefore strong magneto-elastic effects. When a bi-layer thin film sensor is physically bent, stress develops along its length that is dependant by the geometry of the cantilever and its curvature, c. The changes in stress result in changes in the relative permeability of the material. These changes are detected by a pick-up coil, wound around one end of the bi-layer sensor, which produces the sensor signal, s, as a result of changes in the inductance, ΔL, and hence its reactance X_L.[5,6] Thus, the change in ΔL corresponds to the change of skin curvature, Δc, where the sensor is applied. The bending sensor used is a bi-layer strip, which consists of a magnetostrictive layer on a non-magnetic layer (Copper Beryllium—CuBe). The magnetostrictive layer is an amorphous magnetic film, 2.9 μm thick, was deposited from a $Fe_{81}B_{13.5}Si_{3.5}C_2$ target using the RF magnetron sputtering technique onto a 25 μm CuBe layer. The measuring system consists of a personal computer (PC) based acquisition set-up and an electronic circuit that modulates the sensor displacement signal with a reference signal, using the frequency modulation (FM) principle (Fig. 1).[1]

Signal detection was achieved through the use of LabVIEW® software and a NI-6120 data acquisition card with a maximum sampling rate of 800 kS/s per channel and 16-bit resolution.[7]

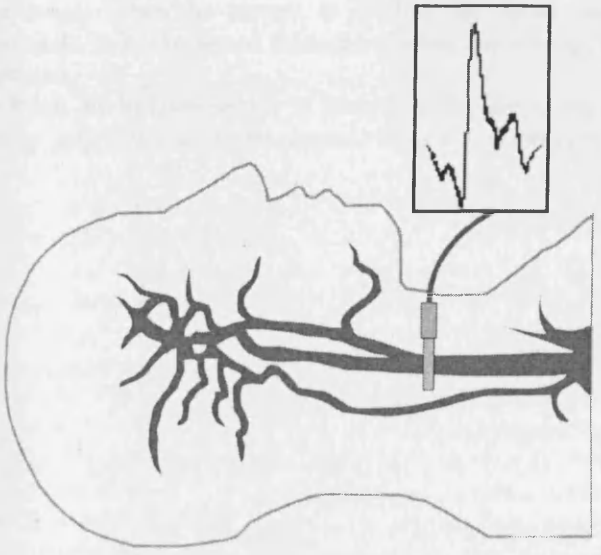

Fig. 2. Application of the bi-layer thin film sensor over the carotid artery.

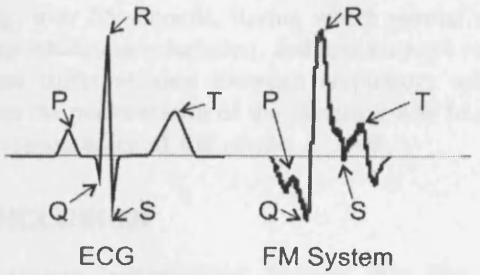

Fig. 3. Comparison between the basic ECG output and the acquired heartbeat from the FM system.

2.2. Sensor Application

Internal physiological activities are mirrored on the human body in the form of active variations of the skin curvature, c. Depending on the body region these signals consist of three main components, cardiac activity, s_C, lung ventilation, s_R, and body movements, s_M.[8] For the detection of the heartbeat rate, f_C, the sensor was attached on the neck over the carotid artery with the aid of double sided adhesive tape (Fig. 2). Cardiac activity transmits blood pressure waves through the arterial system which result in the cyclic alteration of the vessel's radius, r. This deformation is transmitted to the skin, through the surrounding tissue, resulting in change of curvature, Δc, proportional to Δr.[9] The respiratory activity, f_R, was measured by fixing the sensor on the chest using double sided adhesive tape. As in the case of cardiac activity measurements, the deformation of the chest due to changes in respiration volume produces a sensor signal, s_R, which characterizes the lung ventilation.

3. RESULTS

An Electrocardiogram (ECG) is an illustration produced by an Electrocardiograph, which measures the electrical potential between points of the body in order to show the electrical activity in the heart. Up to 12 contacts (electrodes) are usually affixed to the arms, legs, and chest on clean, shaven skin areas. The typical ECG wave starts

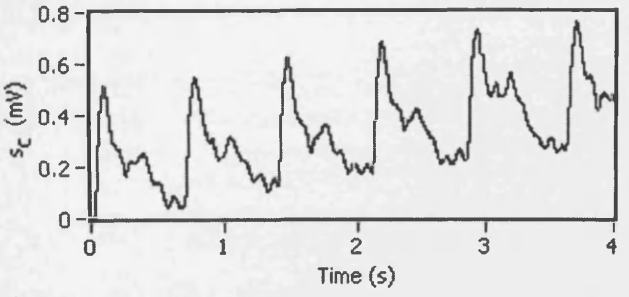

Fig. 4. A detected pulse train segment, from the carotid artery, using the bi-layer thin film sensor system.

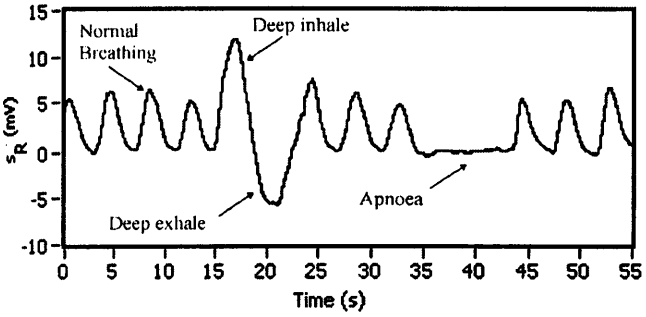

Fig. 5. Respiratory activities using the bi-layer thin film sensor system.

with the spread of the heart stimulation through the atria (P wave), triggering the ventricular activation (Q, R, and S wave), and then ending up to the ventricular recovery (T wave), which returns the stimulated ventricular muscle to its resting state.

Figure 3 shows the hemo-dynamic activity at the carotid artery caused by the pumping of the heart. A bi-layer curvature sensor system was used for the first time not only to monitor but also to map the five characteristic waves of the normal heartbeat rate (P, Q, R, S, and T wave), hence providing additional medical information about the cardiac activity of the patient that other magnetic bi-layer sensor systems can not provide. Compared to the ECG, the bi-layer sensor system only needs one contact to the body (the bi-layer sensor) and there is no need for the preparation of the skin area.

Figure 4 demonstrates a characteristic pulse train, f_C, acquired from the FM system that corresponds to 81 beats per minute. The normal resting heart rate for adults is between 60–100 beats per minute. The signal s_C is usually influenced from other signals, s_R, and s_M, that arise from body movements including in this case from the change of the neck circumference during slow intake of air in the lungs. When the patient is holding his breath and immobile, only the signal from the cardiac activity, s_C, is detected.

When the bi-layer sensor is placed on the chest, respiratory activities can be monitored. Figure 5 displays the signal, s_R, over 55 seconds, during which normal respiration, deep inhalation/exhalation, and apnoea were recorded with clear differentiation between respiratory activities. Also from the performance of the system it was found that the non repeatability of the results is 2.4%.

4. CONCLUSION

A new system incorporating bi-layer thin film curvature sensors has been developed. The system is capable of detecting cardio-respiratory activities using the frequency modulation principle. It has been shown that the LabVIEW® based measurement system, together with the bi-layer thin film sensors, provides an accurate, robust, and low-cost method for monitoring physiological parameters that arise from the change of skin curvature. This sensor system also provides minimum inconvenience to the patient, which is essential for prolonged, undisturbed monitoring.

References and Notes

1. G. S. Katranas, T. Meydan, S. Zurek, T. A. Ovari, and F. Borza, Intermag, San Diego, USA (**2006**).
2. J. Kosel, H. Pfutzner, L. Mehnen, E. Kaniusas, T. Meydan, M. Vázquez, M. Rohn, A. M. Merlo, and B. Marquardt, *Proceedings of Eurosensors XVIII*, Italy, Rome (**2004**).
3. L. Mehnen, E. Kaniusas, J. Kosel, J. C. Téllez-Blanco, H. Pfützner, T. Meydan, M. Vázquez, M. Rohn, C. Malvicino, and B. Marquardt, *J. Alloys Comp.* 369, 202 (**2004**).
4. T. Meydan, *IEE Colloq. New Magn. Mater.* 183 (**1994**).
5. L. Mehnen, H. Pfützner, and E. Kaniusas, *J. Magn. Magn. Mater.* 215–216, 779 (**2000**).
6. E. Kaniusas, H. Pfützner, L. Mehnen, J. Kosel, J. C. Téllez-Blanco, G. Varoneckas, A. Alonderis, T. Meydan, M. Vázquez, M. Rohn, R. Seccardini, and B. Marquardt, *Proc. Inter. Symp. Appl. Electromagnetics Mechanics*, Versailles (**2003**).
7. DAQ PCI-6115/6120 User Manual, S-Series Simultaneous-Sampling Multifunction Device for PCI, National Instruments (**2004**).
8. E. Kaniusas, L. Mehnen, C. Krell, and H. Pfutzner, *J. Magn. Magn. Mater.* 215–216, 776 (**2000**).
9. E. Kaniusas, H. Pfützner, L. Mehnen, J. Kosel, G. Varoneckas, A. Alonderis, T. Meydan, M. Vázquez, M. Rohn, A. M. Merlo, and B. Marquardt, *J. Ultragarsas (Ultrasound)* 3, 52 (**2004**).

RESEARCH ARTICLE

SENSOR LETTERS
Vol. 5, 1–3, 2007

Thermal Stability of Bi-Layer Thin Film Displacement Sensors

G. S. Katranas, T. Meydan*, T. A. Ovari, and F. Borza

Wolfson Centre for Magnetics, Cardiff School of Engineering, Cardiff University, Queens Buildings, Cardiff University, Cardiff, CF24 3AA, UK

(Received: Xx Xxxxx Xxxx. Accepted: Xx Xxxxx Xxxx)

The measuring system utilizes a personal computer based system using the LabVIEW® graphical programming package. The sensor is connected to a circuit that modulates the bi-layer thin film sensor signal, which arises from a controlled displacement, with a reference signal using the frequency modulation principle. This setup allows a high degree of software modularity and provides the features necessary for acquiring the sensor signal, analyzing, it and displaying the results. The bi-layer thin film sensor was placed within an environmental chamber where its thermal stability was tested over the temperature range of up to 180 °C. The temperature rise does cause inductance change, but the sensor signal remains unaffected due to the nature of the frequency modulation method, hence making it a temperature independent sensor that is needed in industry. Thus, having two materials, with different thermal coefficients of expansion in a bi-layer thin film sensor does not adversely influence the sensor signals.

Keywords: Data Acquisition, Frequency Modulation, Magnetostriction, Thin Films, Transducer.

RESEARCH ARTICLE

1. INTRODUCTION

Bi-layer displacement sensors based on thin film technology consist of magnetostrictive thin film deposited onto a non-magnetic layer in order to enhance the bending stress dependence of the relative permeability of the material. Such sensors can also operate at high temperatures for prolonged periods of time unlike agglutinated bi-layers that depend on the working temperature of the adhesive used. The bi-layer thin films used are the building blocks for a new generation of multi-functional sensor families. Industry today needs sensors that are cost effective and easy to operate and are able to detect multiple parameters such as displacement, temperature, curvature, and stress; this is the reason why bi-layer sensors were developed.[1] The ferromagnetic magnetostrictive layer can be crystalline, nano-crystalline, or amorphous magnetic material. In the system described in this paper, an amorphous magnetostrictive layer is used because of its lack of magneto-crystalline anisotropy and high mechanical strength.[2,3] Amorphous magnetic ribbons and thin films may exhibit high magnetostriction and therefore strong magneto-elastic effects. When a bi-layer magnetostrictive thin film sensor is physically bent, stress develops along its length that is influenced by the geometry of the cantilever and its curvature. The changes in stress result in changes in the relative permeability of the material which are detected by a pick-up coil, wound around one end of the bi-layer sensor. These changes produce the sensor signal which arises as a result of changes in the inductance, ΔL, and hence its reactance X_L.[4,5] Thus, the change in ΔL corresponds to the displacement of the free end of the bi-layer sensor. To ensure thermal stability of bi-layer thin films the materials need to have approximately identical thermal expansion coefficients, α. If the thermal expansion coefficients of the materials are chosen to be notably different then due to a temperature increase the material with the largest α will expand disproportionally from the other, thus producing unwanted curvature increase in the strip.[6,7] The paper shows how, due to the nature of the frequency modulation (FM) system, a bi-layer thin film sensor, using materials of different α, can be used and have a good thermal stability over a range of temperatures up to 180 °C.

2. EXPERIMENTAL DETAILS

A magnetostrictive layer on a non-magnetic layer (Copper Beryllium—CuBe) is the two components that consist the bi-layer strip of the bending sensor. The amorphous

*Corresponding author; E-mail: Meydan@cf.ac.uk

 1546-198X/2007/5/001/003 doi:10.1166/sl.2007.073

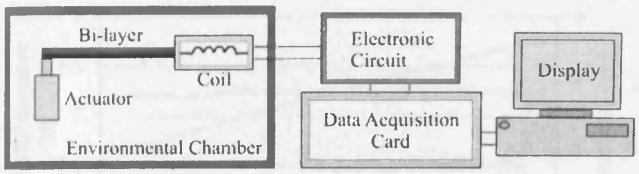

Fig. 1. The Bi-layer sensor during the bending displacement of the free end.

magnetic film, 2.9 μm thick, was deposited from a $Fe_{81}B_{13.5}Si_{3.5}C_2$ ribbon target using the RF magnetron sputtering technique onto a 25 μm CuBe layer. The thermal expansion coefficients are $\alpha_1 = 5.9 \cdot 10^{-6}$ K^{-1} for the amorphous magnetic film and $\alpha_2 = 17 \cdot 10^{-6}$ K^{-1} for the CuBe layer. An electronic circuit that modulates the sensor displacement with a reference signal, using the FM principle is connected to a personal computer (PC) based acquisition set-up (Fig. 1).[8]

The detection of the signal was achieved through the use of LabVIEW® software and a NI-6120 data acquisition card with a maximum sampling rate of 800 kS/s per channel and 16-bit resolution.[9] A Colpitts oscillator circuit was used to produce the FM signal (Fig. 2).[8]

This circuit utilizes an LC tank with an inductor connected in parallel to two series capacitors. The output is a sine wave at a frequency, f_R, which is defined by the values of L and C:

$$f_R = \frac{1}{2\pi\sqrt{L(C_1C_2)/(C_1+C_2)}} \quad (1)$$

The bi-layer sensor acts as the inductive component of the Colpitts oscillator, L. Any change ΔL in the inductance L of the pickup coil will shift the frequency proportionally from f_R by Δf. Hence, frequency modulation is achieved.[10]

$$\mathrm{FM}(t) = V_R \cos\left[2\pi_R t + 2\pi_f K_f \int_o^t v_s(t)dt\right] \quad (2)$$

where K_f is the modulation constant and $v_s(t)$ the sensor displacement signal. An actuator is set up to displace the free end of the bi-layer according to $v_s(t) = V_s\cos(2\pi f_s t)$. To optimize performance of the system, a range of coil configurations were investigated before deciding on the final specification of 300 turns, 20 mm in length and in 7 mm width. The FM signal is demodulated via a differentiator followed by an envelope detector based on the Hilbert transform.[11,12]

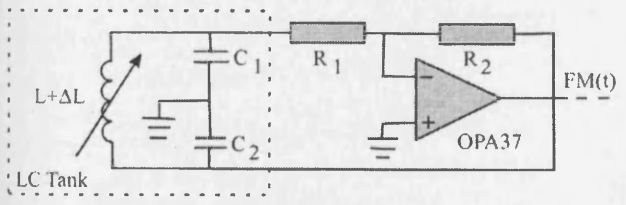

Fig. 2. The Colpitts oscillator schematic diagram. The component values used were: R_1 = 10 kΩ, R_2 = 100 kΩ, $C_1 = C_2$ = 1 μF, and L = 3.02 mH.

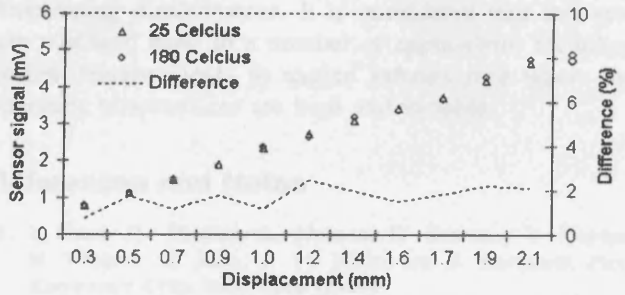

Fig. 3. A comparison of the sensor signal at 25 °C and at 180 °C plotted together with the absolute value of their percentage difference.

3. RESULTS

The sensor was placed inside an environmental chamber and subjected to a temperature increase up to 180 °C. Sine waves, with variable peak to peak amplitudes from 1 V to 6 V, were applied to the actuator. The resulting output peak to peak displacement ranged from 0.35 mm to 2 mm. The output signal is determined by the degree of bending of the bi-layer which can be converted into a displacement reading (Fig. 3). The average peak to peak signal produced at the displacement of the actuator, was in the range of 0.8 mV to 4.6 mV. From the performance of the system it was found that it has an average sensitivity of 2.2 mV/mm while the repeatability of the results was 2.7%. The results were approximately linear in this temperature region with a square correlation coefficient value of 0.99.[13]

The sensor signal at 180 °C shows average absolute values of 1.7% deviation, and a 2.3% maximum deviation, compared to the signal taken at 25 °C. These values are within the repeatability percentage of the FM system. As seen in Figure 4 the temperature increase caused a sharp and approximately linear rise in this temperature region, of the inductance value, reaching 163% change in inductance, ΔL, at 180 °C.

This high ΔL increase is explained by the notable different thermal expansion coefficients of the two materials of the bi-layer strip ($\alpha_1 = 5.9 \cdot 10^{-6}$ K^{-1} for the amorphous magnetic film and $\alpha_2 = 17 \cdot 10^{-6}$ K^{-1} for the CuBe layer). In contrast the peak to peak sensor signal remains quite uninfluenced by the increase of temperature. As inductance

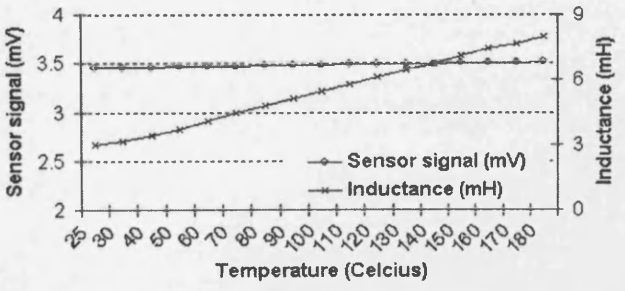

Fig. 4. The rise of inductance due to temperature increase has minute effect to the peak to peak sensor signal taken at ~1.6 mm peak to peak displacement.

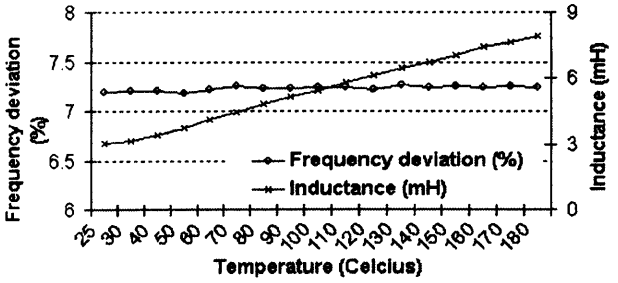

Fig. 5. The frequency dependence on temperature remains relatively uninfluenced from the rise of inductance due to temperature increase (displacement was set at ~1.6 mm peak to peak).

increases with temperature the reference frequency, f_R, is also increasing but the percentage change ΔL remains approximately constant, thus Δf follows proportionally at 7.2% (Fig. 5). With the system settings used the frequency deviation showed to be not very susceptible to the increase of the inductance value; hence the sensor signal is relatively uninfluenced by the increase of temperature.

These findings allow the design and construction of temperature independent sensor families (in the range up to 180 °C) as required by industry.

4. CONCLUSION

The LabVIEW® based system was developed capable of detecting peak to peak displacements using the frequency modulation scheme. Since the sensor signal is transmitted through changes in phase and not in amplitude, the FM scheme has the advantage that it is not as affected by noise as the AM scheme. It has been shown that the LabVIEW® based measurement system, together with the bi-layer sensors, provides an accurate and low-cost method for determining displacement. It is considered that this system will lend itself to a number of applications including airflow measurements in engine exhaust pipe where the operating temperatures are high and variable.

References and Notes

1. J. Kosel, H. Pfutzner, L. Mehnen, E. Kaniusas, T. Meydan, M. Vázquez, M. Rohn, A. M. Merlo, and B. Marquardt, *Proc. Eurosensors XVIII*, Italy, Rome (**2004**).
2. L. Mehnen, E. Kaniusas, J. Kosel, J. C. Téllez-Blanco, H. Pfützner, T. Meydan, M. Vázquez, M. Rohn, C. Malvicino, and B. Marquardt, *J. Alloys Comp.* 369, 202 (**2004**).
3. T. Meydan, *IEE Colloq. New Magn. Mater.* 183 (**1994**).
4. L. Mehnen, H. Pfützner, and E. Kaniusas, *J. Magn. Magn. Mater.* 215–216, 779 (**2000**).
5. E. Kaniusas, H. Pfützner, L. Mehnen, J. Kosel, J. C. Téllez-Blanco, G. Varoneckas, A. Alonderis, T. Meydan, M. Vázquez, M. Rohn, R. Seccardini, and B. Marquardt, *Proc. Inter. Symp. on Applied Electromagnetics and Mechanics (ISEM)*, Versailles (**2003**).
6. E. Kaniusas, L. Mehnen, and H. Pfützner, *J. Magn. Magn. Mater.* 254–255, 624 (**2003**).
7. E. Kaniusas, H. Pfützner, L. Mehnen, J. Kosel, J. C. Téllez-Blanco, E. Mulasalihovic, T. Meydan, M. Vázquez, M. Rohn, C. Malvicino, and B. Marquardt, *J. Alloys Comp.* 369, 198 (**2004**).
8. G. S. Katranas, T. Meydan, S. Zurek, T. A. Ovari, and F. Borza, to be presented in Intermag San Diego, USA (**2006**).
9. DAQ PCI-6115/6120 User Manual, S-Series Simultaneous-Sampling Multifunction Device for PCI, National Instruments (**2004**).
10. J. D. Gibson, The Communications Handbook, 2nd edn., CRC Press, Boca Raton (**2002**), Section VI, pp. 68.1–68.14
11. B. P. Lathi, Signal Processing and Linear Systems, Oxford University Press, New York (**1998**), Chap. 4, pp. 289–299.
12. S. R. Long, N. E. Huang, C. Tung, M. C. Wu, R. Lin, E. Mollo-Christensen, and Y. Juan, *IEEE Geoscience and Remote Sensing Society Newsletter* (**1995**).
13. W. M. Harper, Statistics, 7th edn., Pitman, London (**1991**), Chap. 4, pp. 172–183.

RESEARCH ARTICLE

Available online at www.sciencedirect.com
ScienceDirect
Journal of Magnetism and Magnetic Materials 310 (2007) e986–e988
Journal of magnetism and magnetic materials
www.elsevier.com/locate/jmmm

A novel phase modulation-based system using bi-layer thin film displacement sensors

T. Meydan*, G.S. Katranas, T.A. Ovari, F. Borza

Wolfson Centre for Magnetics, Cardiff University, Queens Buildings, Newport Road, Cardiff CF24 3AA, UK

Available online 21 November 2006

Abstract

A novel method has been used for accurately measuring low-voltage signals ($\sim 10^{-4}$ V) associated with inductance changes of bi-layer thin-film sensors under bending stress. Bi-layer sensors consist of a magnetic layer and a non-magnetic counter layer that is used to enhance the changes in the relative permeability of the material, caused by tensile or compressive stresses. The measuring system utilizes a personal computer-based system using the LabVIEW® graphical programming package. The results from the acquisition proved that this system provided a robust, cost-effective solution (as compared to hardware-based systems) to evaluate magnetostrictive materials and their application in magnetic sensors.

PACS: 07.07.D; 75.70; 75.70.K; 85.70.K

Keywords: Data acquisition; Phase modulation; Magnetostriction; Thin film; Transducer

1. Introduction

Industry today needs sensors that are cost-effective and easy to operate and are able to detect multiple parameters such as displacement, temperature, curvature and stress; this is the reason why bi-layer sensors were developed [1]. When a bi-layer magnetostrictive thin film sensor is physically bent, stress develops along its length that is influenced by the geometry of the cantilever and its curvature. The changes in stress result in changes in the relative permeability of the material, which are detected by a pick-up coil wound around one end of the bi-layer sensor. These changes produce the sensor signal that arises as a result of changes in the inductance, ΔL, and hence its reactance XL. Thus, the change in ΔL corresponds to the displacement of the free end of the bi-layer sensor [2].

*Corresponding author. Tel.: +44 2920 875923; fax: +44 2920 879538.
E-mail address: Meydan@cf.ac.uk (T. Meydan).

0304-8853/$ - see front matter © 2006 Elsevier B.V. All rights reserved.
doi:10.1016/j.jmmm.2006.10.1030

2. Experimental

2.1. Measurement system

The bending sensor used is a bi-layer strip, which consists of an amorphous magnetostrictive layer on a non-magnetic layer (copper beryllium—CuBe). The amorphous magnetic film, 2.9 μm thick, was deposited from a $Fe_{81}B_{13.5}Si_{3.5}C_2$ target using the RF magnetron sputtering technique onto a 25 μm CuBe layer. The measuring system consists of a personal computer (PC)-based acquisition set up and a circuit that modulates the sensor displacement signal with a reference signal, using the phase modulation. Signal detection was achieved through the use of LabVIEW® software and a NI-6120 data acquisition card with a maximum sampling rate of 800 kS/s per channel and 16 bit resolution [3].

2.2. Phase modulation

For phase modulation, (PM), the instantaneous phase of the sine wave will deviate from the reference phase Φ_R by an amount $\Delta\Phi$, proportional to the instantaneous

value of ΔL [4]:

$$\mathrm{PM}(t) = V_R \cos[2\pi f_R t + K_P v_S(t)], \quad (1)$$

where K_P is the modulation constant, $v_S(t)$ the sensor displacement signal and $\Phi_R = K_P v_S(t)$. The PM was achieved using a phase shift oscillator (as seen in Fig. 1). This circuit utilizes three RC tanks with one of them having an inductor connected in parallel to two series capacitors. The output is a sine wave at a frequency, which is defined by the values of L and C:

$$f = \frac{\sqrt{3CR^2 + L}}{2\pi CR\sqrt{6L}}. \quad (2)$$

The bi-layer sensor acts as the inductive component of the phase shift oscillator. Any change ΔL in the inductance L of the pick-up coil will shift from Φ_R by $\Delta\Phi$. Hence, phase modulation is achieved. For the measurement system, an actuator is set up to displace the bi-layer according to $v_S(t) = V_S \cos(2\pi f_S t)$. To optimize performance, a range of coil configurations were investigated before deciding on the final specification of 300 turns, 20 mm length and 7 mm width. The PM signal is demodulated via a differentiator followed by an envelope detector based on the Hilbert transform [5].

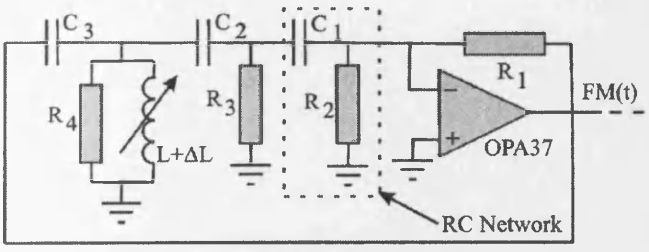

Fig. 1. The phase shift oscillator schematic diagram.

3. Results

Low-frequency (3 Hz) sine waves, with variable peak-to-peak amplitudes from 1 to 6 V, were applied to the actuator. The resulting output peak-to-peak displacement ranged from 0.35 to 2 mm. The displacement of the actuator was measured with the aid of a laser Doppler Vibrometer (LDV) [6].

As seen in Fig. 2 the phase modulated signal (PM) shows an average 1% deviation with a 2.2% maximum deviation compared with the expected signal from the LDV. The output signal is determined by the degree of bending of the bi-layer which can be converted into a displacement reading (Fig. 3). The average peak-to-peak signal produced at the displacement range of the actuator, was in the range of 0.8 to 4.4 mV. From the performance of the system it was found that it has an average sensitivity of 2.2 mV/mm, whereas the repeatability of the results was 2.7%. The results were linear with a square correlation coefficient value of 0.99 [7]. The mechanical hysteresis, i.e. the difference between the increase and decrease in

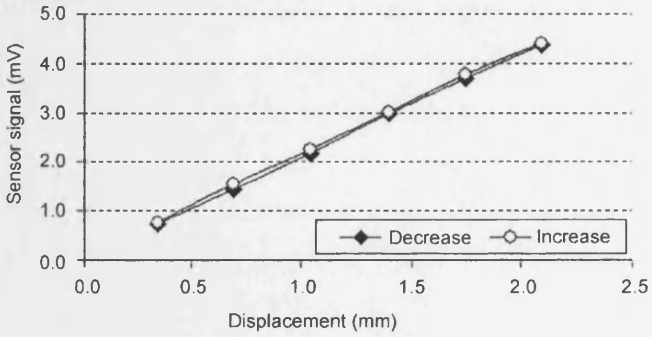

Fig. 3. The peak-to-peak output voltage characteristics against the displacement of the bilayer during the increase and decrease of the actuators displacement.

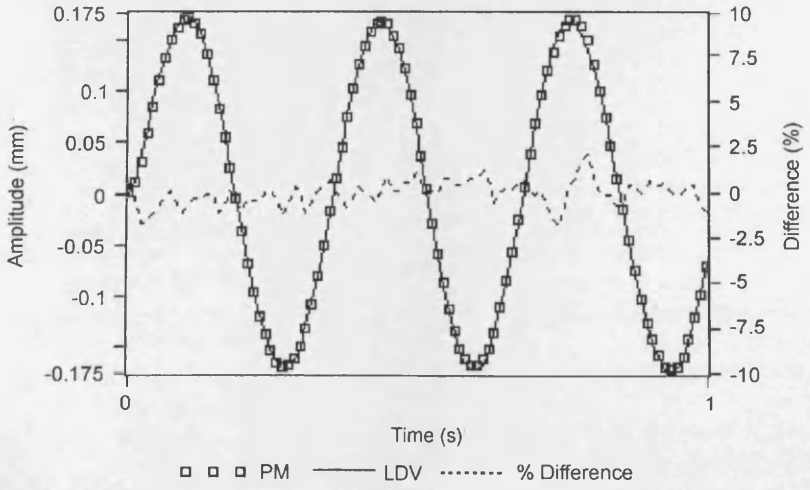

Fig. 2. A comparison of (a) sensor signal and (b) the LDV output at 0.35 mm peak to peak plotted together with their percentage difference.

the amplitude of the actuators displacement and hence the increase and decrease in the sensors signal was 2.23% (Fig. 3).

4. Conclusions

A new type of system incorporating bi-layer stress sensors was developed. The LabVIEW®-based system was developed capable of detecting peak-to-peak displacements using the phase modulation scheme in the range of 0.35 mm to 2 mm. It was shown that the LabVIEW®-based measurement system, together with the bi-layer sensors, provides an accurate and low-cost method for determining displacement. It is considered that this system will lend itself to a number of applications including biometric measurements.

References

[1] L. Mehnen, E. Kaniusas, J. Kosel, J.C. Téllez-Blanco, H. Pfützner, T. Meydan, M. Vázquez, M. Rohn, C. Malvicino, B. Marquardt, J. Alloys Compds. 369 (2004) 202.
[2] E. Kaniusas, H. Pfützner, L. Mehnen, J. Kosel, J.C. Téllez-Blanco, G. Varoneckas, A. Alonderis, T. Meydan, M. Vázquez, M. Rohn, R. Seccardini, B. Marquardt, in: Proceedings of the . International Symposium on Applied Electromagnetics and Mechanics (ISEM), Versailles, 2003, p. 236.
[3] DAQ PCI-6115/6120 User Manual, S-Series Simultaneous-Sampling Multifunction Device for PCI, National Instruments, 2004.
[4] J. Dunlop, Telecommun. Eng., Third ed, CRC Press, Boca Raton, FL, 1994.
[5] S.R. Long, N.E. Huang, E. Mollo-Christensen, C.C. Tung, R.Q. Lin, M.L. Wu, Y. Yuan, IEEE-GRS-S Newslett. 3 (1995) 6.
[6] OFV-303/OFV-3001, User Manual, Single Point, Laser Doppler Vibrometer, Polytec GmbH, 2002.
[7] W.M. Harper, Statistics, 7th ed, Pitman, London, 1991.

A Bilayer Sensor System for Measuring Air Flow

G.S. Katranas and T. Meydan

Wolfson Centre for Magnetics, Cardiff School of Engineering, Cardiff University, Cardiff CF24 3AA, U.K.

A bilayer magnetostrictive sensor is inserted into a cylindrical tube where air flows at a controlled rate. A circuit connected to the sensor conveys a signal that arises from changes in frequency as a function of displacement using the frequency modulation principle. The performance of the sensor was tested at air stream speeds up to 25 m/s and at a range of distances from the center of the tube. The acquired response of the sensor was compared against a displacement simulation model designed using the Comsol Structural Mechanics package. The results demonstrate that this system provides a robust solution to the problem of monitoring variable airflows as needed by the automotive and biomedical industry.

Index Terms—**Airflow, data acquisition, frequency modulation, transducer.**

I. Introduction

THE ability to quantify the flow of air or liquids quickly and accurately is greatly needed by the automotive and biomedical industry. Applications for flow sensors can vary from measuring blood flow through the human artery system to determining the air flow through the intake of a car engine [1], [2]. For example, the means to monitor the air flow through a car engine led to the introduction of electronic fuel injection systems, which replaced carburettors that could not rapidly change the air-to-fuel ratio in response to changes in atmospheric conditions. This improved fuel economy and reduced exhaust emissions. Airflow sensors can also be a vital part of a condition monitoring system that collects data and warns the user of equipment fatigue and failure or automatically controls the apparatus by controlling the air stream through pipes and vents to correct problems. The application of a novel system using bilayer sensors, originally used for the detection of bending, is described in this paper [3]. By bending bilayer sensors, the system is able to measure the speed of an air stream through a cylindrical tube.

II. Experiment

A. Measurement System

Bilayer sensors are cost effective, easy to operate, and have been developed to detect various parameters such as displacement, temperature, curvature, and stress [4], [5]. When a bilayer sensor is physically bent, stress develops along its length which is dependent on the geometry and curvature of the cantilever. The sensor consists of a magnetostrictive layer on a nonmagnetic layer. The magnetostrictive layer is an amorphous magnetic film ($Fe_{81}B_{13.5}Si_{3.5}C_2$), 28 μm thick, agglutinated onto a 75-μm aluminium layer. Details of the sensor design and measurement system can be found in [3]. Changes in stress result in changes in the relative permeability of the material. These changes are detected by a pick-up coil wound around one end of the bilayer sensor, which produces the sensor signal as a result of changes in the inductive reactance X_L, [6], [7]. Thus, the change in inductance corresponds to the change of bilayer curvature, which is due to the applied force from the air stream on the sensor tip.

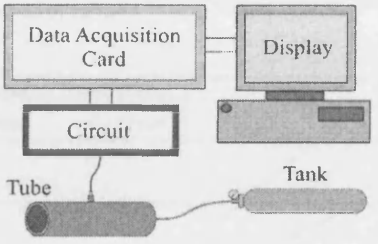

Fig. 1. Bilayer sensor setup for airflow measurements.

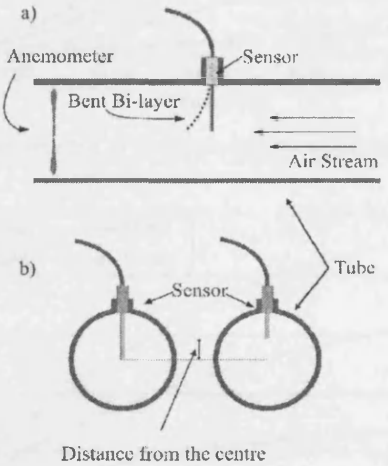

Fig. 2. Bilayer sensor position inside cylindrical tube.

The measuring system (see Fig. 1) consists of a cylindrical tube with the sensor mounted inside, a tank with compressed air that generates the air flow, a PC-based acquisition system, and a circuit that conveys the sensor signal as changes in frequency using frequency modulation. The position and location of the sensor in the tube can be seen in Fig. 2. Signal detection and processing was achieved using a program written in LabVIEW[1]

[1]Registered trademark.

Digital Object Identifier 10.1109/TMAG.2007.893301

Color versions of one or more of the figures in this paper are available online at http: //ieeexplore.ieee.org.

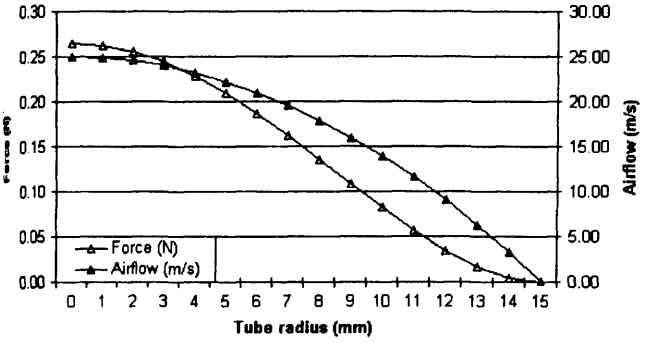

Fig. 3. Dependence of airflow and force on distance from center of tube.

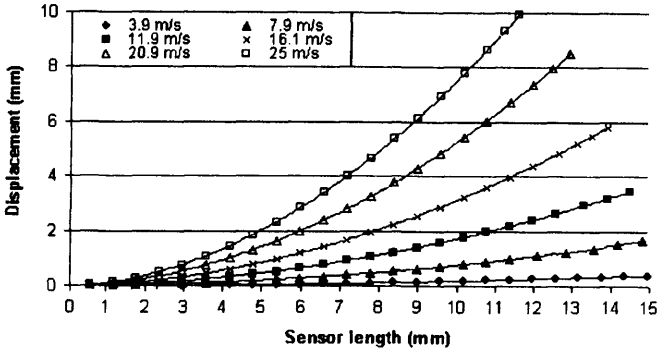

Fig. 4. Bilayer sensor curvature and displacement versus sensor length for a range of air speeds up to 25 m/s.

software and a NI-6120 data acquisition card with a maximum sampling rate of 800 kS/s per channel and 16-bit resolution [8].

B. Sensor Application

The bilayer sensor was inserted into the middle of a cylindrical tube 70 mm long with a 30-mm diameter. The orientation of the sensor was parallel to the radius of the tube with the broad face of the bilayer strip orthogonal to the air stream and free end in the center of the tube [Fig. 2(a) and (b)]. The air stream was supplied to the tube from a compressed air tank with an eight-bar (115 psi) maximum working pressure. An anemometer was placed at the end of the tube to measure the air flow in order to correlate the sensor signal to the wind speed. The performance of the sensor was tested for a range of air speeds from 0 to 25 m/s and at a range of distances from the center of the tube that effectively reduced the bilayer strip length inside the tube [Fig. 2(b)]. The tube diameter and the air speed range were chosen to achieve a slightly turbulent flow through the tube with a Reynolds number of up to Re = 40541 at 25 m/s. The flow is turbulent in a straight tube when the Reynolds number is above 4000 [9]. The reason behind this choice was to examine the performance of the sensor in conditions found in engine intakes where the flow is usually turbulent.

C. Results

In order to relate the sensor signal to the air flow, the environment inside the tube and the forces that displace the bilayer strip need to be calculated. This was performed by modelling the sensor inside the tube using the Comsol Structural Mechanics[2] package [10]. The nature of the air flow (air velocity) in a tube is parabolic (Fig. 3) and depends on the radial distance from the center of the tube (center of flow where air speed is at maximum) [11]. The force exerted along the length of the bilayer strip depends on the air speed and hence on the distance from the center of the tube.

The results from the simulation are shown in Fig. 4 where the application of an air speed range up to 25 m/s displaces the free end of the 15-mm-long bilayer strip, changing its curvature.

By moving the sensor away from the center of the tube and away from the point where the air force is at its maximum, it

[2]Registered trademark.

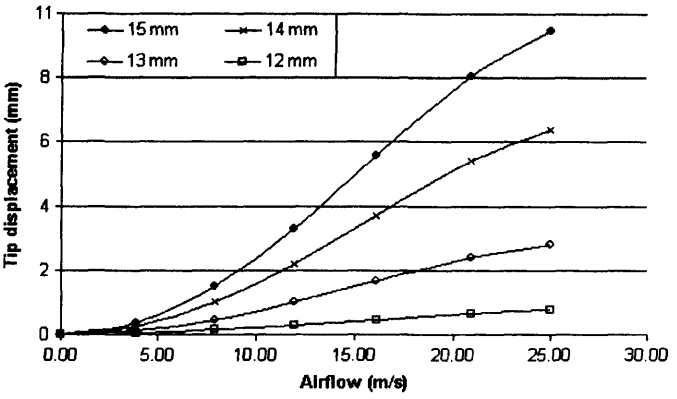

Fig. 5. Bilayer length effect on tip displacement for speeds up to 25 m/s.

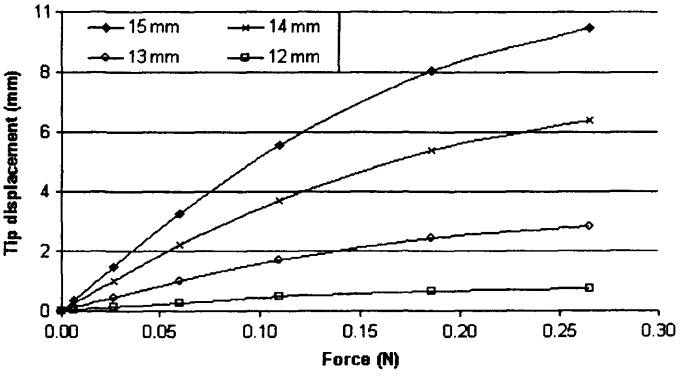

Fig. 6. Bilayer sensor curvature and displacement versus force exerted on strips.

can be seen from the modelling data that the displacement of the bilayer strip is dramatically reduced (Figs. 5 and 6).

As the airflow is increased, the longitudinal axis of the sensor is bent. This curvature increases accordingly with the increase of the airflow. At the same time that the sensor is curved, the area vertical to the airflow is reduced until the longitudinal axis of the sensor is deflected at around 90° (parallel to the flow direction). In the case of Fig. 5, at around 20 m/s the area of the sensor is reduced to such an extent that higher airflows will result in an incremental increase in tip displacements. Hence, the tip displacement increases and then tails off.

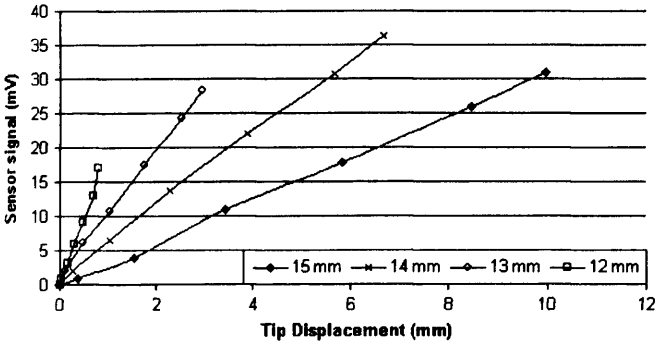

Fig. 7. Output voltage versus tip displacement of bilayer sensor.

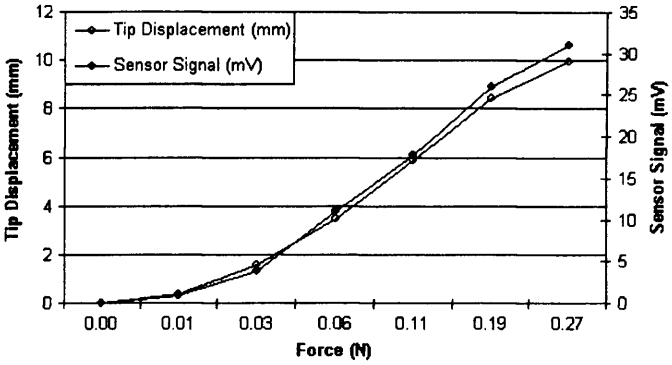

Fig. 8. Output voltage and tip displacement versus force exerted on strip.

Fig. 6 demonstrates that given the same amount of displacement for two bilayer strips of different length, more force is required for the shorter strip. In this case, higher forces induce higher stresses in the magnetic material, which in turn cause increased change in inductance and hence increased levels of signal, as in Fig. 7. This is useful when at sufficiently high flow rates the longitudinal axis of the sensor is deflected at around 90°. During this condition, a further increase in the airflow will not result to a further increase of the sensor signal. This can be corrected by reducing the sensor length in the tube. By plotting the acquisition results (sensor signal) against the tip displacement of the bilayer strip it can be seen that the relationship is almost linear, with a square correlation coefficient value of $r^2 = 0.99$ (Fig. 7).

By plotting both the sensor tip displacement against force and the sensor signal versus force it can be seen that the responses closely follow each other. This further indicates that the sensor output signal faithfully replicates tip displacement position (Fig. 8).

III. Conclusion

A new system incorporating bilayer magnetostrictive air flow sensors has been developed. It has been shown that the LabVIEW-based measurement system, in conjunction with bilayer sensors, provides an accurate and robust method for quantifying the flow of air, even when minor turbulence is present. It is expected that this system will lend itself to a diverse range of applications from automotive (engine gases) to biomedical (blood flow) applications.

References

[1] L. Mehnen, "Magnetostrictive bilayer sensors—A survey," *J. Alloys Comp.*, vol. 369, pp. 202–204, 2004.
[2] T. Meydan, "Application of amorphous materials to sensors," *J. Magn. Magn. Mater.*, vol. 133, no. 1–3, pp. 525–532, 1994.
[3] G. S. Katranas, T. Meydan, T. A. Ovari, and F. Borza, "A novel frequency modulation based system using bilayer thin film displacement sensors," in *Proc. IEEE Magnetic Soc., INTERMAG*, San Diego, CA, 2006, pp. 517a–517b.
[4] J. Kosel, "Non-contact signal detection of multifunctional bilayer sensor," in *Proc. Eurosensors XVIII*, Rome, Italy, 2004, pp. 593–594.
[5] L. Mehnen, H. Pfützner, and E. Kaniusas, "Magnetostrictive amorphous bimetal sensors," *J. Magn. Magn. Mater.*, vol. 215-216, pp. 779–781, 2000.
[6] E. Kaniusas, "Biomedical applicability of magnetoelastic bilayer sensors," in *Proc. Int. Symp. Applied Electromagnetics Mechanics (ISEM)*, Versailles, France, 2003, pp. 236–237.
[7] G. S. Katranas, "Simulation and measurement of bilayer sensor characteristics," in *Sens. Actuators A: Phys.*, 2006, vol. 129, pp. 243–246.
[8] 2004, DAQ PCI-6115/6120 User Manual, S-Series Simultaneous-Sampling Multifunction Device for PCI, National Instruments.
[9] N. P. Cheremisinoff, *Practical Fluid Mechanics for Engineers and Scientists*. Lancaster, U.K.: Technomic, 1990, ch. 5, pp. 124–125.
[10] *Comsol Structural Mechanics 3.1*, Comsol, 2004.
[11] R. Baker, *An Introductory Guide to Industrial Flow*. London, U.K.: Mechanical Engineering, 1996, pp. 53–61.

Manuscript received October 30, 2006 (e-mail: KatranasG@cf.ac.uk).

A Frequency Modulation Based System Using Bilayer Thin-Film Displacement Sensors

G. S. Katranas, T. Meydan, T. A. Ovari, and F. Borza

Wolfson Centre for Magnetics, Cardiff School of Engineering, Cardiff University, Cardiff CF24 3AA, U.K.

A novel method has been used for accurately measuring low voltage signals ($\sim 10^{-4}$ V) associated with inductance changes of bilayer thin-film sensors under bending stress. In this paper the architecture of the system is first presented, and then the design ideas and key technologies are followed. Initially, the frequency modulated signals were simulated with superimposed noise signals to test the demodulation performance of the written program. From the results, the expected output of the program was confirmed. Following this, the frequency modulation technique was used with actual sensor signals to measure the displacement of a bilayer thin film sensor. The results from the acquisition were compared with a previously developed amplitude modulation based setup, and it proved that the frequency modulation system provided a robust and accurate solution to evaluate magnetostrictive materials and their application in magnetic sensors.

Index Terms—**Amorphous magnetic films, frequency modulation, magnetic sensors, magnetostriction.**

I. Introduction

THE technological advances of the personal computer (PC) have enabled it to become a very efficient signal acquisition and analysis system. Out of the many software acquisition packages commercially available, LabVIEW provides a powerful tool for signal analysis. By using the developed software and a few external components, the system can be used to detect low voltage signals that are related to the displacement of bilayer sensors. Magnetic sensors are devices that receive a stimulus and convert it to an electrical output signal by utilizing the laws of electromagnetism and effects in electromagnetic fields in order to achieve their goal. The bilayer thin films used are the building blocks for a new generation of multifunctional sensor families. They consist of a magnetic layer and a nonmagnetic counter layer that is used to enhance the changes in the relative permeability of the material, caused by tensile or compressive stresses. Bilayer sensors are constructed from a ferromagnetic magnetostrictive layer which can be crystalline, nanocrystalline, or amorphous, deposited on a nonmagnetic layer. In the system described in this paper, an amorphous magnetostrictive layer is used because of its lack of magnetocrystalline anisotropy and high mechanical strength [1], [2]. Soft magnetic amorphous ribbons and thin films may exhibit high magnetostriction and therefore strong magneto-elastic effects.

When a magnetostrictive amorphous ribbon is physically bent at its free end, a tensile stress, σ, develops along its length. The changes in the relative permeability, μ_r, are not as large as expected [3], because there is a reduction due to the effect of tension in one half of the material which is counterbalanced by the effect of compression in the other half.

Digital Object Identifier 10.1109/TMAG.2006.888857

Color versions of one or more of the figures in this paper are available online at http://ieeexplore.ieee.org.

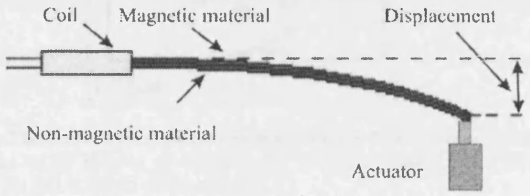

Fig. 1. The bilayer sensor during the bending displacement of the free end.

Bilayer strips consist of two layers, one layer that contains the magnetostrictive amorphous ribbon and a nonmagnetic counter layer. The purpose of this configuration is to shift the neutral bending area out of the amorphous ribbon, hence impose the same sign stress throughout the amorphous ribbon [4], [5]. Bending this bilayer will result in changes in the relative permeability, μ_r, of the material. The permeability changes are detected by a pickup coil, wound around one end of the bilayer sensor, which produces the sensor signal as a result of changes in the inductance ΔL, and hence its reactance X_L [6], [7] (Fig. 1).

Thus, the change in ΔL corresponds to the displacement of the free end of the bilayer sensor.

Bilayer sensors are easy to operate and have been developed to detect various parameters such as displacement, stress, etc. [8]. These sensors can be used for a variety of applications such as automotive industry, aerospace, environmental monitoring, earthquake detection, and especially biomedical for signal acquisition for monitoring physiological activities [9], [10]. Previous methods for detecting and analyzing sensor signals have been conducted using bilayer thin films with the amplitude modulation scheme, which can be susceptible to noise [6], [8], [11]. In this paper, we report on a frequency modulation technique to measure the sensor signal. Also, a comparison is made between both modulation schemes.

II. Experimental Setup

A. Sensor Design

The bending sensor used is a bilayer strip, which consists of a magnetostrictive layer on a nonmagnetic layer (Copper Beryl-

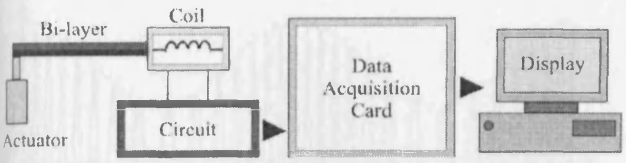

Fig. 2. Frequency modulation based system for the measurement of displacements.

lium, CuBe). The amorphous magnetic film, 2.9 μm thick, was deposited from a $Fe_{81}B_{13.5}Si_{3.5}C_2$ target using the RF magnetron sputtering technique onto a 25 μm CuBe layer [12]. The dimensions of the coil that was used for these measurements were 300 turns, 20 mm in length, and 7 mm in width. The bilayer thin film strip that was used had a size of 40 mm length, 5 mm width. This results in an inductance value of $L = 3.02$ mH.

B. Measurement System

The measuring system consists of a PC-based acquisition setup and a circuit that modulates the sensor displacement signal with a reference signal, using the frequency modulation (Fig. 2).

Signal detection was achieved using the written software and a NI-6120 data acquisition card with a maximum sampling rate of 800 kS/s per channel and 16-bit resolution [13].

In order to compare the two systems (AM and FM system) and examine the performance of the frequency modulation their principle of operation is briefly explained in Sections II-C and II-D, respectively. Depending on the modulation principle used, (amplitude or frequency), the sensor is connected to the corresponding circuit [14].

C. Amplitude Modulation

In amplitude modulation the instantaneous amplitude, V_R, of the carrier waveform is varied linearly by the information signal, $v_S(t)$, i.e., the change in Δ L. A sinusoidal carrier waveform, v_R, is mathematically represented by

$$v_R = V_R \cdot \cos(2\pi f_R t). \tag{1}$$

When the carrier signal is modulated by the information signal, (1) becomes

$$\mathrm{AM}(t) = [V_R + v_s(t)]\cos(2\pi \cdot f_R t) \tag{2}$$

where $v_S(t)$ is the information signal (sensor displacement signal). The details of the AM operation are described in [14]. By replacing R_L with the bilayer sensor in Fig. 3, the sensor will act as the load impedance of the voltage-to-current circuit (VCC). The resistive element of the inductor which is its reactance X_L, ($X_L = 2 \cdot \pi \cdot f \cdot L$) will act as the load resistance of the VCC. For the AM technique, the settings were $V_1 = v_R$ and $V_2 = 0$ (ground).

D. Frequency Modulation

For frequency modulation, FM, the instantaneous frequency of the sine wave will shift from the reference frequency f_R by

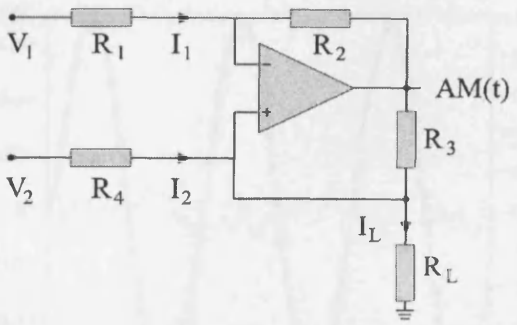

Fig. 3. The VCC used in the amplitude modulation technique.

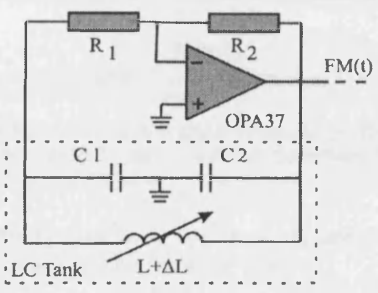

Fig. 4. The Colpitts oscillator schematic diagram. The component values used were: $R_1 = 10$ kΩ, $R_2 = 100$ kΩ, $C_1 = C_2 = 1$ μF, L = 3.02 mH, and ΔL = 60 μH at 2 mm displacement.

an amount Δf, proportional to the instantaneous value of ΔL [15]

$$\mathrm{FM}(t) = V_R \cos\left[2\pi \cdot f_R \cdot t + 2\pi \cdot K_f \int_0^t v_S(t)dt\right] \tag{3}$$

where K_f is the modulation constant and $v_S(t)$ is the sensor displacement signal. The FM was achieved using a Colpitts oscillator (as seen in Fig. 4).

This circuit utilizes an LC tank with an inductor connected in parallel to two series capacitors. The output is a sine wave at a frequency, f, which is defined by the values of L and C

$$f = \frac{1}{2\pi \cdot \sqrt{\frac{L \cdot C_1 \cdot C_2}{C_1 + C_2}}}. \tag{4}$$

The bilayer sensor acts as the inductive component of the Colpitts oscillator. Any change ΔL in the inductance L of the pickup coil will shift from f_R by Δf. Hence, frequency modulation is achieved.

For the measurement system, the actuator is set up to displace the bilayer according to

$$v_S(t) = V_S \cdot \cos(2\pi f_S t). \tag{5}$$

An alternating sinusoidal force was applied to the free end of the bilayer using a mechanical actuator operating at 3 Hz to simulate the average maximum heart rate (180 beats per minute) expected in a healthy 40-year-old person [16].

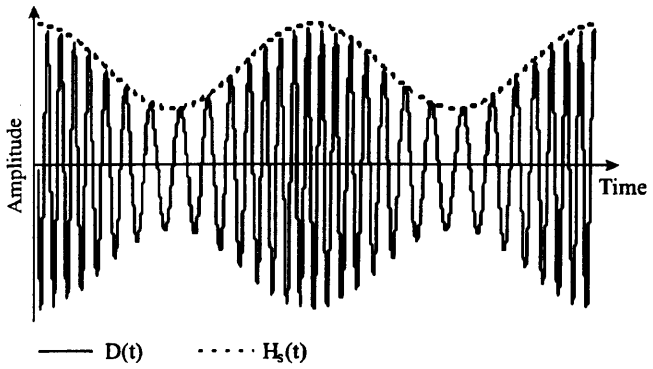

Fig. 5. The output signal of the differentiator, $D(t)$, is a composite signal that consists of the amplitude (AM) and frequency (FM) modulation schemes.

E. Demodulation Technique

The core of the AM demodulation process is the lock-in technique. The mathematical process for performing the lock-in is known to be an accurate method to measure the displacements of bilayer sensors [6], [14].

In order to demodulate the FM signal, it needs to be input through a differentiator followed by an envelope detector. Rewriting (3) gives

$$\mathrm{FM}(t) = V_R \cos\left[\omega_R \cdot t + \underbrace{\frac{K_f V_s}{f_s}}_{m_{\mathrm{FM}}} \cdot \sin(\omega_s t)\right] \tag{6}$$

where m_{FM} is the modulation index. The derivative of $\mathrm{FM}(t)$ can be written as

$$\frac{d\mathrm{FM}(t)}{dt} = D(t) = -\underbrace{V_R \cdot \sin\left(\omega_R \cdot t + m_{\mathrm{FM}} \cdot \sin(\omega_s t)\right)}_{\mathrm{FM}(t)} \cdot \left(\omega_R + 2\pi \cdot K_f \cdot \underbrace{V_s \cdot \sin(\omega_s t)}_{v_s(t)}\right). \tag{7}$$

As seen in from (7), the differentiation of the FM signal has been converted to a composite waveform that comprises the $\mathrm{FM}(t)$ and the $v_s(t)$ signals [17]. $D(t)$ has become an amplitude modulated signal whose reference and modulating waveforms are the $\mathrm{FM}(t)$ and the v_s (t) (Fig. 5).

An envelope detector can be used to demodulate this signal and extract the sensor displacement signal. The envelope detector used for the $D(t)$ was based on the Hilbert transform. A signal $s(t)$ has a Hilbert transform denoted by $s(t)$ and is obtained by shifting the frequency components of $s(t)$ by $\pi/2(90°)$) [18]. A function $s(t)$ and its Hilbert transform $s(t)$ can form together a complex signal [19]

$$S(t) = s(t) + j \cdot \hat{s}(t). \tag{8}$$

Let $\hat{D}(t)$ be the Hilbert transform of $D(t)$

$$\hat{D}(t) = -V_R \cdot \underbrace{\cos}_{90° \text{ shift}} (\omega_R \cdot t + m_{\mathrm{FM}} \cdot \sin(\omega_s t)) \cdot (\omega_R + 2\pi \cdot K_f \cdot V_s \cdot \sin(\omega_s t)). \tag{9}$$

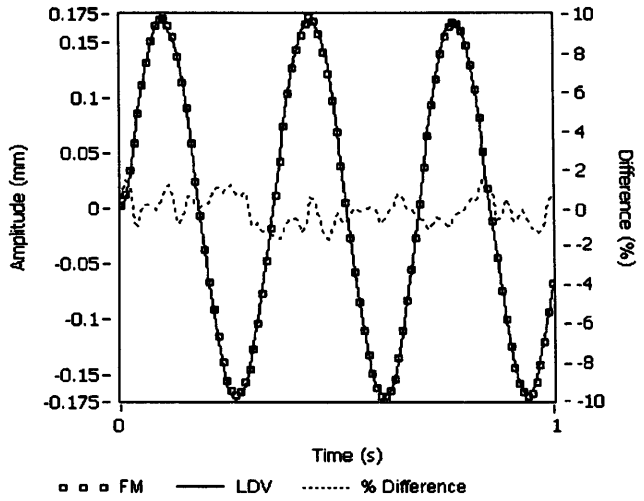

Fig. 6. A comparison of: (a) sensor signal (FM) and (b) the LDV output at 0.35 mm peak to peak plotted together with their percentage difference.

From trigonometry $(\sin^2 x + \cos^2 x = 1)$ and (8), the sensor displacement signal can be found as [18]

$$\begin{aligned} H_S(t) &= |D(t) + j\hat{D}(t)| = \sqrt{D^2(t) + \hat{D}^2(t)} \Rightarrow (H_S(t))^2 \\ &= (V_R \cdot \sin(\omega_R t + m_{\mathrm{FM}} \cdot \sin(\omega_s t)) \\ &\quad \cdot (\omega_R + 2\pi K_f \cdot V_s \cdot \sin(\omega_s t)))^2 \\ &\quad + (V_R \cdot \cos(\omega_R t + m_{\mathrm{FM}} \cdot \sin(\omega_s t)) \\ &\quad \cdot (\omega_R + 2\pi K_f \cdot V_s \cdot \sin(\omega_s t)))^2 \\ &= [V_R \cdot (\omega_R + 2\pi \cdot K_f \cdot V_s \cdot \sin(\omega_s t))]^2. \end{aligned} \tag{10}$$

Hence

$$H_s(t) = V_R \cdot \left(\omega_R + 2\pi \cdot K_f \cdot \underbrace{V_s \cdot \sin(\omega_s t)}_{v_s(t)}\right). \tag{11}$$

From (11), it can be seen that the information signal $v_s(t)$ has been recovered. The dc component that the signal is superimposed on can easily be removed in software.

III. Results

Low-frequency (3 Hz) sine waves, with variable peak-to-peak amplitudes from 1 to 6 V, were applied to the actuator. The resulting output peak to peak displacement ranged from 0.35 to 2 mm. The displacement of the actuator was measured with the aid of a laser Doppler vibrometer (LDV) [20]. As seen in Fig. 6, the frequency modulated signal (FM) shows an average of 0.9% deviation with a 2% maximum deviation compared to the output signal from the LDV.

The output signal is determined by the degree of bending of the bilayer which can be converted into a displacement reading (Fig. 7).

The average peak-to-peak signal produced at the displacement range of the actuator was in the range of 0.8 to 4.6 mV. From the performance of the system it was found that it has an average sensitivity of 2.2 mV/mm, whereas the nonrepeatability of the results is 2.4%. The data examination was performed using standard statistical methods [21]. The results showed

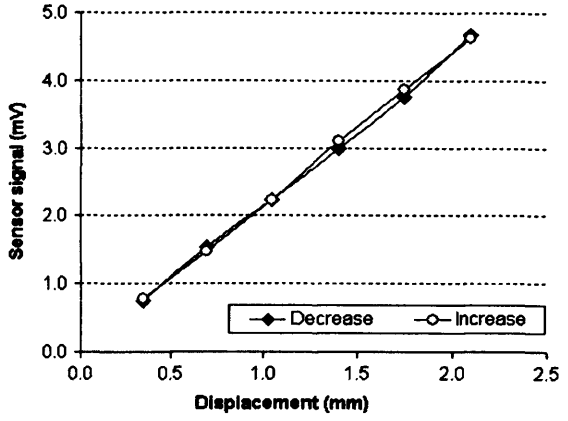

Fig. 7. The output voltage characteristics against the displacement of the bilayer during the increase and decrease of the actuators displacement.

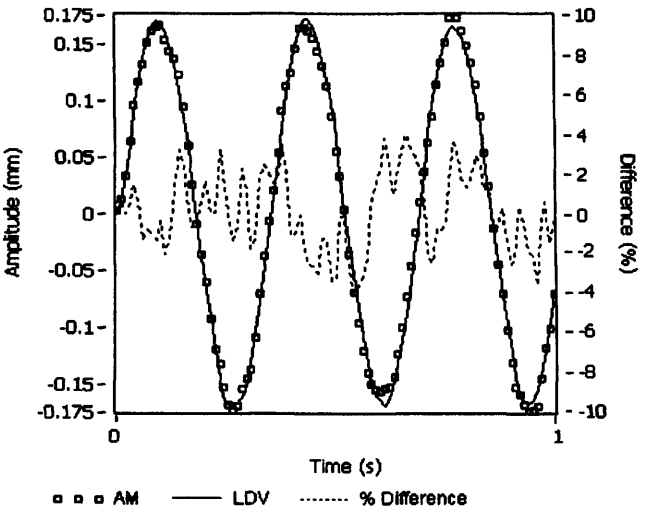

Fig. 8. A comparison of: (a) sensor signal (AM) and (b) the LDV output at 0.35 mm peak to peak plotted together with their percentage difference.

an almost linear behavior with a square correlation coefficient value of $r^2 = 0.99$.

The mechanical hysteresis, i.e., the difference between the increase and decrease of the amplitude of the actuators displacement and hence the increase and decrease of the sensors signal, is 1.85% (Fig. 7).

As seen in Fig. 8, the amplitude modulated signal (AM) shows an average of 1.7% deviation with a 3.9% maximum deviation compared to the output signal from the LDV. The AM signal not only shows twice the amount of deviation, at this displacement range, compared to the FM signal but it also depicts a deteriorated signal quality. This difference is expected to increase at displacements lower than 0.35 mm. Also, at 2 mm displacement the AM shows a deviation of

$$\frac{\Delta V}{V_R} = \frac{20\,\mu\text{V}}{1\text{ V}} = 20 \cdot 10^{-6}. \tag{12}$$

Hence, the information signal can easily be buried in noise. The FM technique, on the other hand, has

$$\frac{\Delta f}{f_R} = \frac{0.1\text{ kHz}}{5\text{ kHz}} = 0.02. \tag{13}$$

From this, it can be seen that the FM method has a high sensitivity compared to the AM.

Another aspect of the FM technique is that if the sensor is placed in the presence of a dc field the Δf change increases (until the magnetic material reaches saturation) as the sensor approaches the source. This has an amplifying effect to signal; hence, the presence of a small permanent magnet can amplify signals that arise from small displacements. In the AM method, the presence of a dc field will augment the present noise levels which in turn cover the information signal.

As part of examining the performance of the measurement system, the thermal stability was tested over the temperature range of up to 180 °C by placing the bilayer sensor and the actuator setup inside an environmental chamber. It was seen that although the temperature rise did cause inductance change, and hence frequency increase, the percentage change of Δf remained approximately constant [22]. Thus, the sensor signal remained relatively unaffected due to the nature of the frequency modulation method. A bilayer thin film sensor, using materials of different thermal expansion coefficients, can be used and have a good thermal stability over a range of temperatures up to 180 °C. A temperature independent sensor is needed in industry, especially for application in car engines for measuring exhaust fume flow.

IV. Conclusion

A bilayer displacement sensor measurement system has been developed. The system is capable of detecting peak to peak displacements using the frequency modulation scheme in the range of 0.35 to 2 mm. It has been shown that the measurement system, together with the bilayer sensors, provides an accurate method for determining displacement. Also, the FM system showed that it has better performance than the AM system. It is considered that this system will lend itself to a number of applications such as stress, airflow measurements in engine exhaust pipes, monitoring physiological parameters that arise from the change of skin curvature such as cardio-respiratory activities.

References

[1] L. Mehnen, "Magnetostrictive bilayer sensors—A survey," *J. Alloys Comp.*, vol. 369, pp. 202–204, 2004.
[2] T. Meydan, "Amorphous materials in sensor applications, magnetic materials for sensors and actuators," *IEE Colloq. New Magn. Mater.*, vol. 183, pp. 1–3, 1994.
[3] Z. M. Wu, "A new frequency-modulation-type MI sensor," *IEEE Trans. Magn.*, vol. 41, no. 10, pp. 3694–3696, Oct. 2005.
[4] J. Kosel, "Theoretical investigation of magnetostrictive bilayers sensitive to bending or temperature changes," in *Proc. IEEE Sensors*, 2004, vol. 3, pp. 1086–1089.
[5] L. Mehnen, "Magnetostrictive bilayer sensors," in *Proc. IEEE Sensors*, 2004, vol. 1, pp. 326–328.
[6] L. Mehnen, H. Pfützner, and E. Kaniusas, "Magnetostrictive amorphous bimetal sensors," *J. Magn. Magn. Mater*, vol. 215–216, pp. 779–781, 2000.

[7] E. Kaniusas, "Biomedical applicability of magnetoelastic bilayer sensors," in *Proc. Inter. Symp. on Applied Electromagnetics and Mechanics (ISEM)*, Versailles, France, 2003, pp. 236–237.
[8] J. Kosel, "Non-contact signal detection of multifunctional bi-layer sensor," in *Proc. Eurosensors XVIII*, Rome, Italy, 2004, pp. 593–594.
[9] E. Kaniusas, "Magnetoelastic skin curvature sensor for biomedical applications," in *Proc. IEEE Sensors*, 2004, vol. 3, pp. 1484–1487.
[10] E. Kaniusas, "A magnetostrictive acceleration sensor for registration of chest wall displacements," *J. Magn. Mater.*, vol. 215–216, pp. 776–778, 2000.
[11] C. M. Cai, "Frequency-modulation-type MI sensor using amorphous wire and CMOS inverter multivibrator," *IEEE Trans., Magn.*, vol. 40, no. 1, pp. 161–163, Jan. 2004.
[12] T. Meydan, "Magneto-elastic bilayer films," in *Proc. 16th Soft Magnetic Materials Conf.*, Dusseldorf, Germany, 2003, vol. 2, pp. 633–637.
[13] *"DAQ PCI-6115/6120 User Manual,"* National Instruments Inc., 2004.
[14] G. S. Katranas, "Simulation and measurement of bilayer sensor characteristics," *Sens. Actuators A: Phys.*, vol. 129, pp. 243–246, 2006.
[15] J. D. Gibson, *The Communications Handbook*, 2nd ed. Boca Raton, FL: CRC, 2002, pp. 68.1–68.14.
[16] G. F. Fletcher, "Exercise standards for testing and training: A statement for healthcare professionals," *American Heart Association, Circulation*, pp. 1694–1740, 2001.
[17] B. P. Lathi, *Signal Processing and Linear Systems*. New York: Oxford Univ. Press, 1998, pp. 289–299.
[18] S. R. Long, "The Hilbert techniques: An alternate approach for non-steady time series analysis," *IEEE Geoscience and Remote Sensing Society Newsletter*, pp. 6–11, 1995.
[19] F. R. Connor, *Modulation*. London, U.K.: Arnold, 1982, pp. 112–114, App. A.
[20] *"OFV-303/OFV-3001, User Manual, Single Point Laser Doppler Vibrometer,"* Polytec GmbH.
[21] W. M. Harper, *Statistics*, 7th ed. London, U.K.: Pitman, 1991, pp. 172–183.
[22] G. S. Katranas, "Thermal stability of bi-layer thin film displacement sensors," in *Eur. Conf. Magnetic Sensors and Actuators (EMSA)*, Bilbao, Spain, 2006.

Manuscript received July 27, 2006; revised November 28, 2006. Corresponding author: G. S. Katranas (e-mail: KatranasG@cf.ac.uk).

Applications of the Bi-Layer Thin Film Sensor System for Registering Cardio-respiratory Activity

G. S. Katranas[a]*, T. Meydan[a], T. A. Ovari[a], F. Borza[a]
[a]Wolfson Centre for Magnetics, Cardiff University, Queens Buildings,Newport Road, Cardiff CF24 3AA,UK

Abstract
A novel bi-layer thin film sensor system was used for accurately registering physiological parameters associated with body movements, such as cardiac and respiratory activities. The bi-layer curvature sensor system can provide additional medical information about the cardiac activity of the patient by mapping the five characteristic waves of the normal heartbeat rate (P, Q, R, S and T wave). This system was also used for registering physiological parameters such as the monitoring of lung ventilation which can give a range of information about the patients health, (normal respiration patterns, deep inhalation/exhalation and apnoea), easily distinguishable in the output signal. The bi-layer thin films used consist of a magnetic layer and a non magnetic counter layer that is utilized to enhance the changes in the relative permeability of the material caused by tensile or compressive stresses during bending. The measuring system is based on a personal computer in conjunction with the LabVIEW® graphical programming package. The nature of this configuration provides the necessary features for sensor signal acquisition, analysis and data presentation. The results from the sensor application on patients demonstrate that this system can provide a robust, cost effective solution to monitoring cardio-respiratory activity with minimum inconvenience to the patient, which is necessary for prolonged, undisturbed monitoring.

Keywords: Data acquisition; Frequency modulation; Physiological sensors; Thin films; Transducer;

* Corresponding author. Tel.: +44-2920-875923; fax: +44-2920-879538.
E-mail address: KatranasG@cf.ac.uk.

1. Introduction

Polysomnography is a diagnostic and comprehensive recording of the physiological changes that occur during sleep. This biometrical test includes medical techniques such as electroencephalography (EEG), rapid eye movement (REM), electromyography (EMG), electrocardiogram (ECG), and the patient's respiratory activity during sleep. The non-disturbing monitoring of the human body activities during sleep and especially the cardio-respiratory activity is an important parameter. Body functions such as breathing, oxygen levels, heart tracing, and the different levels of sleep are recorded during the sleep study.

The test and monitoring of the patient's sleep through the night is performed by a qualified sleep technician. Electrodes are placed on the head and face to monitor levels of sleep, ECG (electrocardiogram) patches will be applied to the chest to monitor the heartbeat, and a flow sensor is placed under the nose to monitor airflow. The respiratory activities are monitored by soft straps placed around the chest and abdomen that record the rise and fall of the chest to determine whether the patient is breathing appropriately during sleep. The patient's sleep could probably be disturbed from the sensors, electrodes and straps.

This paper describes the applications of a novel system using bi-layer thin film sensors, originally used for the detection of bending [1]. The physiological activities that involve the dynamic deformations of the curvature of the skin can be measured, with minimum disturbance, by this system.

2. Experimental

Measurement System

The bi-layer sensors are assembled from a ferromagnetic magnetostrictive layer that can be crystalline, nanocrystalline or amorphous magnetic materials on a non-magnetic layer. These sensors are cost effective, easy to operate and they have been developed to detect parameters such as displacement, temperature, curvature, stress etc [2]. Due to the lack of magneto-crystalline anisotropy and high mechanical strength [3, 4] an amorphous magnetostrictive layer was used for the bi-layer. Soft magnetic amorphous ribbons and thin films may exhibit rather high magnetostriction and therefore strong magneto-elastic effects. During the bending of a bi-layer thin film sensor, stress develops along its length that is dependent on the geometry of the cantilever and its curvature, c. Changes in stress cause changes in the relative permeability of the material. These variations are detected by a pick-up coil, wound around one end of the bi-layer sensor, which produces the sensor signal, s, as a result of changes in the inductance, ΔL, and hence its reactance X_L [5, 6]. Thus, the change in ΔL corresponds to the change of skin curvature, Δc, where the sensor is applied. The bi-layer strip used in the bending sensor consists of a magnetostrictive layer on a non-magnetic layer (Copper Beryllium - CuBe). The magnetostrictive layer is an amorphous magnetic film, 2.9 μm thick, was deposited from a $Fe_{81}B_{13.5}Si_{3.5}C_2$ target using the RF magnetron sputtering technique onto a 25 μm CuBe layer. The measuring system consists of a personal computer (PC) based acquisition set-up and an electronic circuit that modulates the sensor displacement signal with a reference signal, using the frequency modulation (FM) principle (Fig. 1) [1].

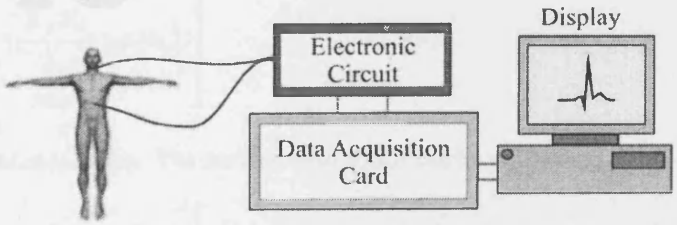

Fig. 1. Bi-layer sensor system for registering cardio-respiratory activity.

Using the LabVIEW® software and a NI-6120 data acquisition card the detection of the signal was achieved. This card has a maximum sampling rate of 800 kS/s per channel and 16-bit resolution [7].

In order to achieve frequency modulation, FM, the instantaneous frequency of the sine wave shifts from the reference frequency f_R by an amount Δf, proportional to the instantaneous value of ΔL [8]:

$$FM(t) = V_R \cos[2\pi \cdot f_R \cdot t + 2\pi \cdot K_f \int_0^t v_S(t)dt] \qquad (1)$$

where K_f is the modulation constant and $v_S(t)$ the sensor displacement signal. The FM was achieved using a Colpitts oscillator (as seen in Fig. 2).

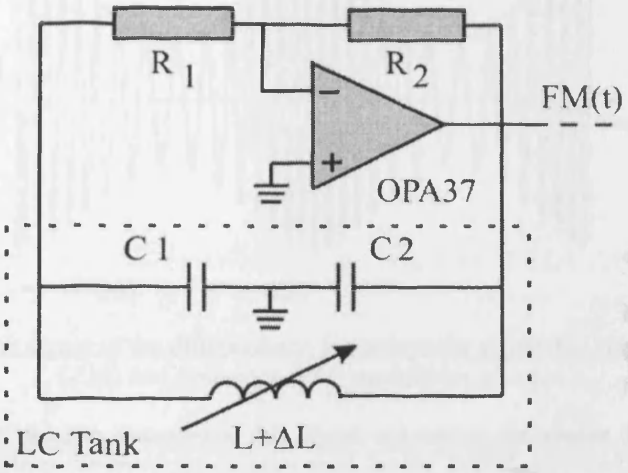

Fig. 2. The Colpitts oscillator schematic diagram. ($R1$ = 10 kΩ, $R2$ = 100 kΩ, $C1 = C2$ = 1 μF, L = 3.02 mH and ΔL = 60 μH at 2 mm displacement).

An LC tank is utilized in this circuit with an inductor connected in parallel to two series capacitors. The output is a sine wave at a frequency, f, which is defined by the values of L and C:

$$f = \frac{1}{2\pi \cdot \sqrt{\frac{L \cdot C_1 \cdot C_2}{C_1 + C_2}}} \qquad (2)$$

The bi-layer sensor acts as the inductive component of the Colpitts oscillator. Any change ΔL in the inductance L of the pickup coil will shift from f_R by Δf. Hence, frequency modulation is achieved.

Demodulation Technique

The demodulation of the FM signal becomes feasible when the waveform is input through a differentiator followed by an envelope detector. Rewriting Eq. 1 gives:

$$FM(t) = V_R \cos\left[\omega_R \cdot t + \underbrace{\frac{K_f V_s}{f_s}}_{m_{FM}} \cdot \sin(\omega_s t)\right] \qquad (3)$$

where m_{FM} is the modulation index. The derivative of $FM(t)$ can be written as:

$$\frac{dFM(t)}{dt} = D(t) = \underbrace{-V_R \cdot \sin(\omega_R \cdot t + m_{FM} \cdot \sin(\omega_s t))}_{FM(t)} \cdot$$

$$\cdot \left(\omega_R + 2\pi \cdot K_f \cdot \underbrace{V_s \cdot \sin(\omega_s t)}_{v_s(t)}\right) \qquad (4)$$

From Fig. 3 it can be seen that the differentiation of the FM signal creates a composite waveform that comprises of the *FM(t)* and the $v_S(t)$ signals [9]. D(t) has become an amplitude modulated signal whose reference and modulating waveforms are the *FM(t)* and the $v_S(t)$ (Fig. 3).

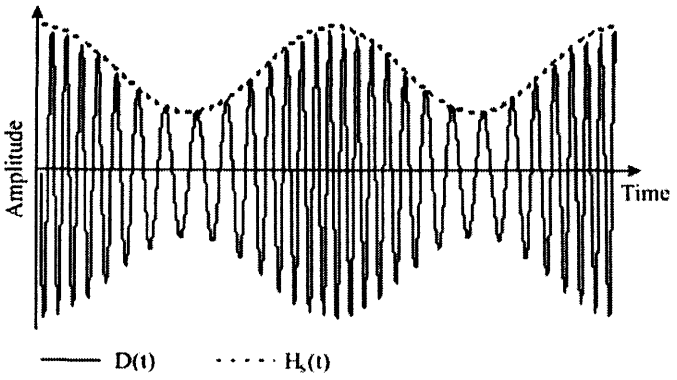

Fig. 3. D(t), the output signal of the differentiator, is a composite signal that consists of the amplitude (AM) and frequency (FM) modulation schemes.

The envelope detector is used to demodulate this signal and extract the sensor displacement signal. The Hilbert transform principle is the envelope detector used for the *D(t)*. A signal *s(t)* has a Hilbert transform denoted by $\hat{s}(t)$ and is obtained by shifting the frequency components of *s(t)* by $\pi/2$ (90^0) [10]. A function *s(t)* and its Hilbert transform $\hat{s}(t)$ can form together a complex signal [11]:

$$S(t) = s(t) + j \cdot \hat{s}(t) \tag{5}$$

Let $\hat{D}(t)$ be the Hilbert transform of *D(t)*:

$$\hat{D}(t) = -V_R \cdot \underbrace{\cos}_{90^0 shift}\left(\omega_R \cdot t + m_{FM} \cdot \sin(\omega_s t)\right) \cdot$$

$$\cdot \left(\omega_R + 2\pi \cdot K_f \cdot V_s \cdot \sin(\omega_s t)\right) \tag{6}$$

From trigonometry ($\sin^2 x + \cos^2 x = 1$) and Eq. 5, the sensor displacement signal can be found as [10]:

$$H_S(t) = \left| D(t) + j\hat{D}(t) \right| = \sqrt{D^2(t) + \hat{D}^2(t)} \Rightarrow (H_S(t))^2 =$$

$$= \left(V_R \cdot \sin(\omega_R t + m_{FM} \cdot \sin(\omega_s t)) \cdot \left(\omega_R + 2\pi K_f \cdot V_s \cdot \sin(\omega_s t)\right)\right)^2 +$$

$$+ \left(V_R \cdot \cos(\omega_R t + m_{FM} \cdot \sin(\omega_s t)) \cdot \left(\omega_R + 2\pi K_f \cdot V_s \cdot \sin(\omega_s t)\right)\right)^2 =$$

$$= \left[V_R \cdot \left(\omega_R + 2\pi \cdot K_f \cdot V_s \cdot \sin(\omega_s t)\right)\right]^2 \tag{7}$$

Hence,

$$H_s(t) = V_R \cdot \left(\omega_R + 2\pi \cdot K_f \cdot \underbrace{V_s \cdot \sin(\omega_s t)}_{v_s(t)}\right) \tag{8}$$

From Eq. 8 it can be seen that the information signal $v_S(t)$ has been recovered. The superimposed DC component on the information signal can easily be removed in software.

Sensor Application

A range of internal physiological activities are mirrored on the human body in the form of active variations of the skin curvature, c. Depending on the body region these signals consist of three main components, cardiac activity, s_C, lung ventilation, s_R and body movements, s_M [12]. Cardiac activity transmits blood pressure waves through the arterial system which result in the cyclic alteration of the vessel's radius, r. This deformation is transmitted to the skin, through the surrounding tissue, resulting in change of curvature, Δc, proportional to Δr [13]. For the detection of the heartbeat rate, f_C, the sensor was attached on the neck over the carotid artery with the aid of double sided adhesive tape (Fig. 4).

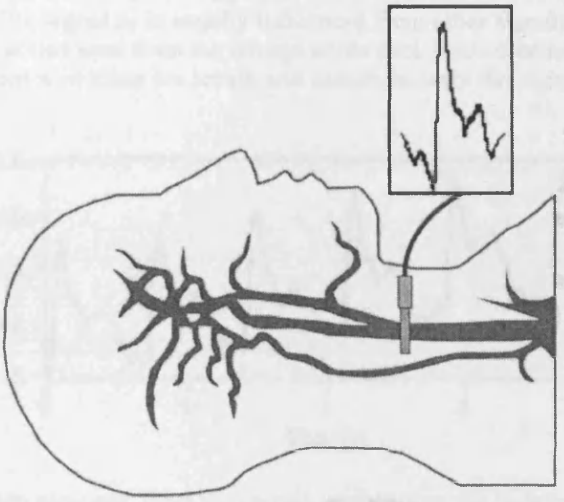

Fig. 4. The bi-layer thin film sensor applied over the carotid artery

As in the case of cardiac activity measurements, the deformation of the chest due to changes in respiration volume produces a sensor signal, s_R, which characterizes the lung ventilation. The respiratory activity, f_R, was measured by fixing the sensor on the chest using double sided adhesive tape.

3. Results

An Electrocardiograph measures the electrical potential between points of the body in order to show the electrical activity in the heart; the data are displayed in the form of an illustration, an Electrocardiogram (ECG) as seen in Fig. 5a. A total of up to 12 contacts (electrodes) are usually affixed to the arms, legs and chest on clean, shaven skin areas. The typical ECG wave starts with the spread of the heart stimulation through the atria (P wave), triggering the ventricular activation (Q, R and S wave), and then ending up to the ventricular recovery (T wave), which returns the stimulated ventricular muscle to its resting state.

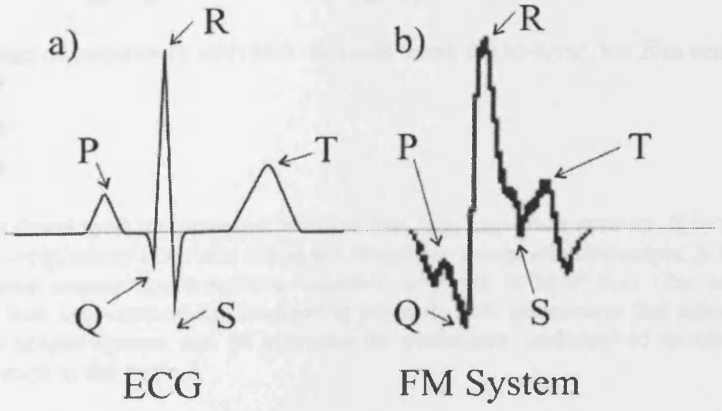

Fig. 5. Comparison between a) the basic ECG output and b) the acquired heartbeat from the FM system.

Fig. 5b shows the hemo-dynamic activity at the carotid artery caused by the pumping of the heart. A bi-layer curvature sensor system was used for the first time not only to monitor but also to map the five characteristic waves of the normal heartbeat rate (P, Q, R, S and T wave), hence providing additional medical information about the cardiac activity of the patient that other magnetic bi-layer sensor systems can not provide. Compared to the ECG, the bi-layer sensor system only needs one contact to the body (the bi-layer sensor) and there is no need for the preparation of the skin area.

Fig. 6 demonstrates a characteristic pulse train, f_C, acquired from the FM system that corresponds to 81 beats per minute. For an adult the normal resting heart rate is between 60-100 beats per minute depending on the physical condition. The signal s_C is usually influenced from other signals, s_R and s_M, that arise from body movements including in this case from the change of the neck circumference during slow intake of air in the lungs. When the patient is holding his breath and immobile, only the signal from the cardiac activity, s_C, is detected.

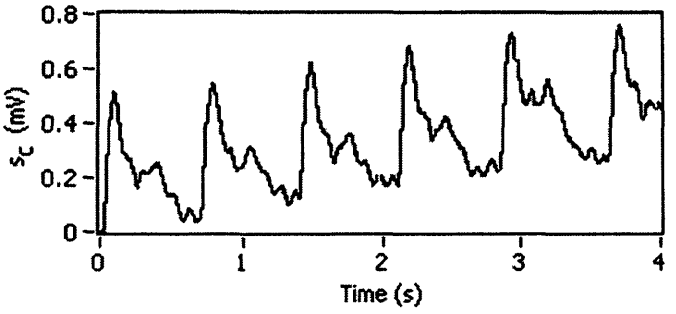

Fig. 6. A detected pulse train segment, from the carotid artery, using the bi-layer thin film sensor system.

The monitoring of respiratory activities is performed by placing the bi-layer sensor on the chest. Fig. 7 displays the signal, s_R, over 55 seconds, during which normal respiration, deep inhalation/exhalation and apnoea were recorded with clear differentiation between respiratory activities. Also from the performance of the system it was found that the non repeatability of the results is 2.4%.

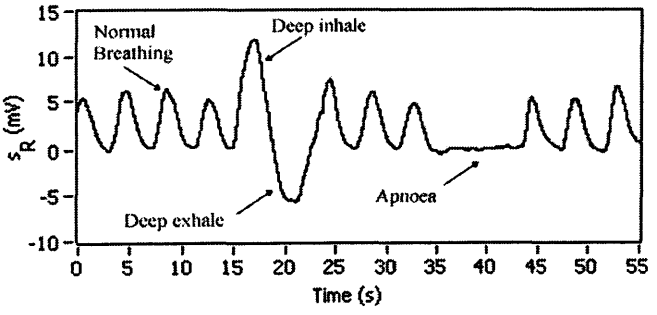

Fig. 7. A range of respiratory activities recorded using the bi-layer thin film sensor system.

4. Conclusions

The system that was developed incorporates bi-layer thin film curvature sensors. It is capable of detecting and recording cardio-respiratory activities using the frequency modulation principle. It has been shown that the LabVIEW® based measurement system, together with the bi-layer thin film sensors, provides an accurate, robust and low-cost method for monitoring physiological parameters that arise from the change of skin curvature. This sensor system can be essential for prolonged, undisturbed monitoring as it provides minimum inconvenience to the patient.

References

1. G. S. Katranas et al. *A novel frequency modulation based system using bilayer thin film displacement sensors*, Tech. Digest, IEEE Intermag San Diego, USA, May. 8 12, 2006.
2. J. Kosel et al. *Non-contact signal detection of multifunctional bilayer sensor*, Proc. of Eurosensors XVIII, Rome, Italy, Sep. 13 15, 2004.
3. L. Mehnen et al. Optimisation of sensitivity and time constant of thermal sensors based on magnetoelastic amorphous bilayers, *J. Alloys Comp. 369* (2004) 198 201.
4. T. Meydan, *Amorphous materials in sensor applications, Magnetic Materials for Sensors and Actuators,* Tech. Digest, IEE Colloq. New Magn. Mater. London, UK, Oct. 11, 1994
5. L. Mehnen et al. Magnetostrictive amorphous bimetal sensors, *J. Magn. Magn. Mater. 215* (2000) 779 781.
6. E. Kaniusas et al. *Biomedical applicability of magnetoelastic bilayer sensors*, Proc. Inter. Symp. on Applied Electromagnetics and Mechanics (ISEM), Versailles, France, May. 12 14, 2003.
7. DAQ PCI-6115/6120 User Manual, S-Series Simultaneous-Sampling Multifunction Device for PCI, National Instruments (2004)
8. J. D. Gibson, *The communications handbook*, CRC Press, Boca Raton, 2nd edn., 2002, p. 68.1.
9. B. P. Lathi, *Signal processing and linear systems*, Oxford University Press, New York, 1998, p. 289.
10. S. R. Long et al, "The Hilbert techniques: an alternate approach for non-steady time series analysis," *IEEE GRSS Newsletter* (1995) 6 11.
11. F. R. Connor, "*Modulation*", Arnold, London, 1982, p. 112.
12. E. Kaniusas et al. A magnetostrictive acceleration sensor for registration of chest wall displacements, *J. Magn. Magn. Mater. 215* (2000) 776 778.
13. E. Kaniusas et al. Magnetoelastic bilayer concept for skin curvature sensor, *J. Ultragarsas (Ultrasound), 3-52* (2004) 42 45.

Author Biography

George S. Katranas was born in Athens, Greece, in 1979. In 2003 he received the Masters of Engineering (MEng Hons.) diploma degree in Electronic Engineering from Cardiff University, UK. He is currently completing his PhD at the Wolfson Centre for Magnetics at Cardiff University and has authored scientific papers in the area of magnetic sensors and their systems. He is a member of the Institution of Engineering and Technology (IET), the Institute of Electrical and Electronic Engineers (IEEE) and associate member of the Institute of Physics (IOP).

Turgut Meydan is a Reader at Cardiff University.

Tibor A. Ovari is now a Researcher at the National Institute of R&D for Technical Physics in Iasi, Romania.

Firuta Borza studied physics at. "Al. I. Cuza" University in Iasi, Romania, received her PhD in 1999 and joined the National Institute of Technical Physics, Iasi, Romania in 1986 where she worked as senior researcher. In 2001 she joined Wolfson Centre for Magnetics, School of Engineering, Cardiff University, UK, where she is currently a lecturer. Her research has mainly been concerned with preparation, characterisation and potential applications of amorphous and nanocrystalline magnetic materials obtained by rapid quenching from the melt (wires, ribbons and thin films) and nanowire arrays.

ipt

Thermal Stability of Bi-Layer Thin Film Displacement Sensors Systems

G. S. Katranas[a]*, T. Meydan[a], T. A. Ovari[a], F. Borza[a]
[a]Wolfson Centre for Magnetics, Cardiff University, Queens Buildings,Newport Road, Cardiff, CF24 3AA,UK

Abstract
The bi-layer thin film measurement system uses the principle of frequency modulation for the detection of displacement. The measuring system utilizes a personal computer based system using the LabVIEW® graphical programming package that provides the features necessary for acquiring the sensor signal, analyzing it and displaying the results. The results from the acquisition were compared with previously developed amplitude and phase modulation based systems to show that the frequency modulation technique provides a robust and accurate solution to evaluate magnetostrictive materials and their application in magnetic sensors. The performance of the bi-layer thin film sensor was examined and its thermal stability, over the temperature range of up to 180^{0}C, was tested in an environmental chamber. The temperature rise does cause inductance change, but the sensor signal remains unaffected due to the nature of the frequency modulation method. Thus, having two materials, with different thermal coefficients of expansion in a bi-layer thin film sensor does not adversely influence the sensor signals. This creates a temperature independent sensor that is needed for applications where there are temperature variations.

Keywords: Data acquisition; Frequency modulation; Magnetostriction; Thin films; Transducer;

* Corresponding author. Tel.: +44-2920-875923; fax: +44-2920-879538.
E-mail address: KatranasG@cf.ac.uk.

1. Introduction

The reason why bi-layer sensors were developed was that industry today needs sensors that are cost effective and easy to operate and are able to detect multiple parameters such as displacement, temperature, curvature and stress [1]. Based on thin film technology, bi-layer displacement sensors consist of magnetostrictive thin film deposited onto a non-magnetic layer in order to enhance the bending stress dependence of the relative permeability of the material. Because of the fact that the two layers are deposited instead of agglutinated, these sensors can operate at high temperatures for prolonged periods of time without depending on the working temperature of the adhesive used. The ferromagnetic magnetostrictive layer that is used for the bi-layer sensor strip can be crystalline, nano-crystalline or amorphous magnetic material. In the system described in this paper, an amorphous magnetostrictive layer is used because of its lack of magneto-crystalline anisotropy and high mechanical strength [2, 3]. When there is a change in stress on the bi-layer strip due to bending, changes in the relative permeability of the material occur which are detected by a pick-up coil, wound around one end of the bi-layer sensor. These changes produce the sensor signal which arises as a result of changes in the inductance, ΔL, and hence its reactance X_L [4, 5]. Thus, the change in ΔL corresponds to the displacement of the free end of the bi-layer sensor. In order for bi-layer thin films to have thermal stability it is necessary for the two materials to have approximately identical thermal expansion coefficients, α. If the thermal expansion coefficients of the chosen materials are notably different then an increase in the temperature will result in the material with the largest α to expand disproportionally with respect to the other, thus producing unwanted curvature increase in the strip [6]. The paper shows how, due to the nature of the frequency modulation (FM) system, a bi-layer thin film sensor, using materials of different α, can be used and have a good thermal stability over a range of temperatures up to 180 ^{0}C.

2. Experimental

A. Measurement System

The bi-layer strip of the bending sensor consists of a magnetostrictive layer on a non-magnetic layer (Copper Beryllium - CuBe). The 2.9 μm thick amorphous magnetic film was deposited from a $Fe_{81}B_{13.5}Si_{3.5}C_2$ ribbon target using the RF magnetron sputtering technique onto a 25 μm CuBe layer. The thermal expansion coefficients are $\alpha_1 = 5.9 \cdot 10\text{-}6\ K^{-1}$ for the amorphous magnetic film and $\alpha_2 = 17 \cdot 10\text{-}6\ K^{-1}$ for the CuBe layer. The sensor is connected to an electronic circuit that modulates the displacement signal with a reference waveform. For each modulation principle there is an equivalent circuit which in turn is connected to a personal computer (PC) based acquisition set-up (Fig. 1) [7].

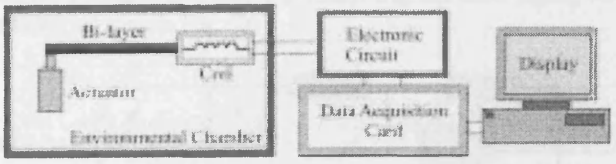

Fig. 1. The Bi-layer sensor during the bending displacement of the free end.

Using the LabVIEW® software and a NI-6120 data acquisition card the detection of the signal was achieved. This card has a maximum sampling rate of 800 kS/s per channel and 16-bit resolution [8].

In order to compare the three systems (AM, PM and FM) and examine their performance, the principles of operation are briefly explained. Depending on the modulation principle used the sensor is connected to the corresponding circuit [10].

B. Amplitude Modulation

In the case of amplitude modulation (AM) the instantaneous amplitude, V_R, of the carrier waveform is linearly varied by the information signal, $v_S(t)$, i.e. the change in ΔL. A sinusoidal carrier waveform, v_R, is mathematically represented by:

$v_R = V_R \cos(2\pi f_R t)$ (1)

When the carrier signal is modulated by the information signal Eq. 1, becomes:

$$AM(t) = [V_R + v_s(t)]\cos(2\pi \cdot f_R t) \quad (2)$$

where $v_S(t)$ is the information signal (sensor displacement signal). Further information of the AM operation is described in ref. [9]. The bi-layer sensor behaves as the load impedance of the VCC when is placed in the place of R_L (Fig. 2). The reactance X_L, ($X_L = 2 \cdot \pi \cdot f \cdot L$) which is the resistive element of the inductor will act as the load resistance of the Voltage-to-Current Circuit (VCC). For the AM technique the settings where $V_1 = v_R$ and $V_2 = 0$ (Ground).

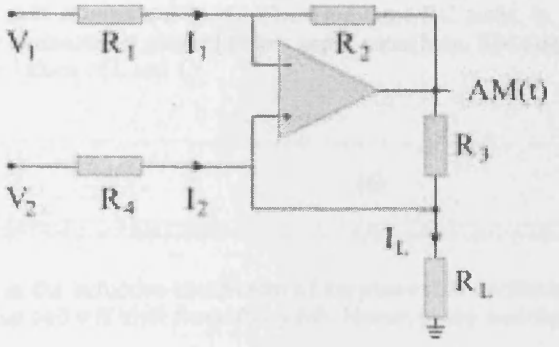

Fig. 2. The Voltage-to-Current Circuit used for the amplitude modulation technique.

C. Frequency Modulation

In order to achieve frequency modulation, FM, the instantaneous frequency of the sine wave shifts from the reference frequency f_R by an amount Δf, proportional to the instantaneous value of ΔL [10]:

$$FM(t) = V_R \cos[2\pi \cdot f_R \cdot t + 2\pi \cdot K_f \int_0^t v_S(t)dt] \quad (3)$$

where K_f is the modulation constant and $v_S(t)$ the sensor displacement signal. For the FM technique a Colpitts oscillator was used (as seen in Fig. 3).

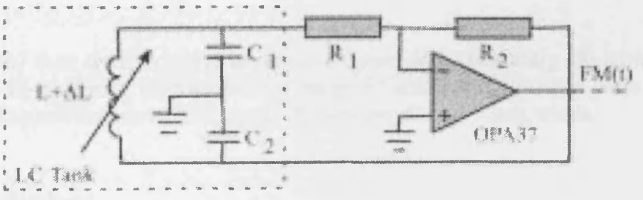

Fig. 3. The Colpitts oscillator schematic diagram. (R1 = 10 kΩ, R2 = 100 kΩ, C1 = C2 = 1 μF, L = 3.02 mH and ΔL = 60 μH at 2 mm displacement).

The LC tank used with the Colpitts oscillator is composed of an inductor connected in parallel to two series capacitors. The output is a sine wave at a frequency, f, which is defined by the values of L and C:

$$f = \frac{1}{2\pi \cdot \sqrt{\frac{L \cdot C_1 \cdot C_2}{C_1 + C_2}}} \quad (4)$$

By replacing the inductive component of the Colpitts oscillator with the bi-layer sensor any change ΔL in the inductance L of the pickup coil will shift from f_R by Δf. Hence, frequency modulation is achieved.

D. Phase Modulation

For phase modulation, PM, the instantaneous phase of the sine wave will deviate from the reference phase Φ_R by an amount ΔΦ, proportional to the instantaneous value of ΔL [11]:

$$PM(t) = V_R \cos[2\pi f_R t + K_P v_S(t)] \quad (5)$$

where K_P is the modulation constant, $v_S(t)$ the sensor displacement signal and $\Phi_R = K_P v_S(t)$. The PM was achieved using a phase shift oscillator (Fig. 4). There are three RC tanks, in the circuit, with one of them having an inductor connected in parallel to two series capacitors. The output is a sine wave with a frequency defined by the values of L and C:

$$f = \frac{\sqrt{3CR^2 + L}}{2\pi CR\sqrt{6L}} \quad (6)$$

The bi-layer sensor acts as the inductive component of the phase shift oscillator. Any change ΔL in the inductance L of the pickup coil will shift from Φ_R by ΔΦ. Hence, phase modulation is achieved.

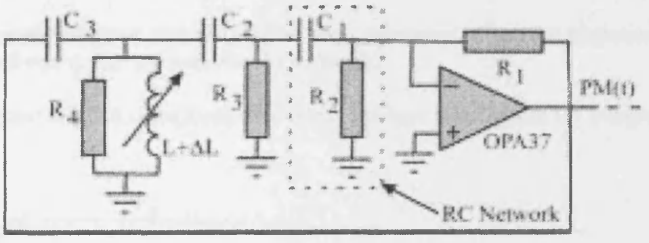

Fig. 4. The phase shift oscillator schematic diagram.

For the measurement system the actuator is set up to displace the bi-layer according to:

$$v_S(t) = V_S \cdot \cos(2\pi f_S t) \quad (7)$$

A mechanical actuator was used in order to apply a controlled alternating sinusoidal force to the free end of the bi-layer. To optimize performance a range of coil configurations were investigated before deciding on the final specification of 300 turns, 20 mm length and 7 mm width.

E. Demodulation Techniques

The core of the AM demodulation process is the lock-in technique. This is known to be an accurate method to measure the displacements of bi-layer sensors [4, 9]. The mathematical process for performing the lock-in is the multiplication of the amplitude modulated signal with the reference signal.

$$L(t) = 2 \cdot \cos(2\pi f_R t) \cdot AM(t) \quad (8)$$

By passing the L(t) through a low pass filter the high frequency component is eliminated and the remaining signal is the sensor signal with a DC component which is then easily removed in LabVIEW.

The demodulation of the FM signal becomes feasible when the waveform is input through a differentiator followed by an envelope detector [7]. The derivative of *FM(t)* can be written as:

$$\frac{dFM(t)}{dt} = D(t) = -\underbrace{V_R \cdot \sin\left(\omega_R \cdot t + m_{FM} \cdot \sin(\omega_s t)\right)}_{FM(t)} \cdot$$

$$\cdot \left(\omega_R + 2\pi \cdot K_f \cdot \underbrace{V_s \cdot \sin(\omega_s t)}_{v_s(t)} \right) \qquad (9)$$

The differentiation of the FM signal creates a composite waveform that comprises of the $FM(t)$ and the $v_S(t)$ signals [12]. $D(t)$ has become an amplitude modulated signal whose reference and modulating waveforms are the $FM(t)$ and the $v_S(t)$.

To demodulate this signal and extract the sensor displacement signal and the Hilbert transform principle is used as an envelope detector for the $D(t)$. Mathematically a signal $s(t)$ has a Hilbert transform denoted by $\hat{s}(t)$ which is obtained by shifting the frequency components of $s(t)$ by $\pi/2$ (90^0) [9]. If $\hat{D}(t)$ is the Hilbert transform of $D(t)$ then:

$$H_S(t) = \left| D(t) + j\hat{D}(t) \right| = \sqrt{D^2(t) + \hat{D}^2(t)} \Rightarrow$$

$$H_s(t) = V_R \cdot \left(\omega_R + 2\pi \cdot K_f \cdot \underbrace{V_s \cdot \sin(\omega_s t)}_{v_s(t)} \right) \qquad (10)$$

Eq. 10 shows that the information signal $v_S(t)$ has been recovered. The superimposed DC component on the information signal can easily be removed in software.

In the case of phase modulated waveforms the demodulation takes place by integrating the PM signal (Eq. 5) [14]:

$$\int PM(t)dt = I(t) = \frac{V_R}{\left(\omega_R + \underbrace{K_P \cdot V_S}_{m_{PM}} \cdot \omega_S \sin(\omega_S \cdot t) \right)} \cdot$$

$$\cdot \sin\left(\omega_c \cdot t + m_{PM} \cdot \omega_m \cos(\omega_m \cdot t)\right) \qquad (11)$$

where m_{PM} is the phase modulation index. This creates a composite waveform that carries the information signal as phase and amplitude changes. Inputting this signal in an envelope detector such as the Hilbert transform, $v_S(t)$ is found.

3. Results

A. Performance

The actuator was supplied with low frequency (3 Hz) sine waves, with variable peak to peak amplitudes from 1 V to 6 V. The resulting output peak to peak displacement ranged from 0.35 mm to 2 mm. A Laser Doppler Vibrometer (LDV) was used to measure the displacement of the actuator [15]. In Fig. 5 the frequency modulated signal (FM) was compared to the output signal from the LDV and showed an average deviation of 0.9 % with a maximum deviation of 2 %.

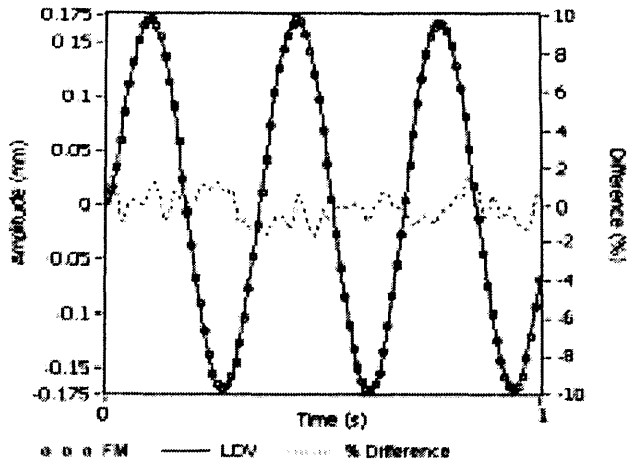

Fig. 5. A comparison of: a) sensor signal (FM) and b) the LDV output at 0.35 mm peak to peak plotted together with their percentage difference.

The output signal is determined by the degree of bending of the bi-layer which can be converted into a displacement reading (Fig. 6).

The average peak to peak signal produced at the displacement range of the actuator, for all three modulation principles, was in the range of 0.8 mV to 4.6 mV. From the performance of the three systems it was found that it has an average sensitivity of 2.2 mV/mm. For the AM, PM and FM the non-repeatability of the results were 4.6 %, 2.7 % and 2.4 % respectively. The mechanical hysteresis, i.e. the difference between the increase and decrease of the amplitude of the actuators tip and hence the increase and decrease of the sensors signal is 3.6 %, 2.2 % and 1.8 % for the AM, PM and FM respectively. Standard statistical methods were performed for the data examination [16]. The results showed a square correlation coefficient value of r^2 = 0.99 and an almost linear behavior. The mechanical hysteresis, i.e. the difference between the increase and decrease of the amplitude of the actuators displacement and hence the increase and decrease of the sensors signal is 1.85 % (Fig. 6).

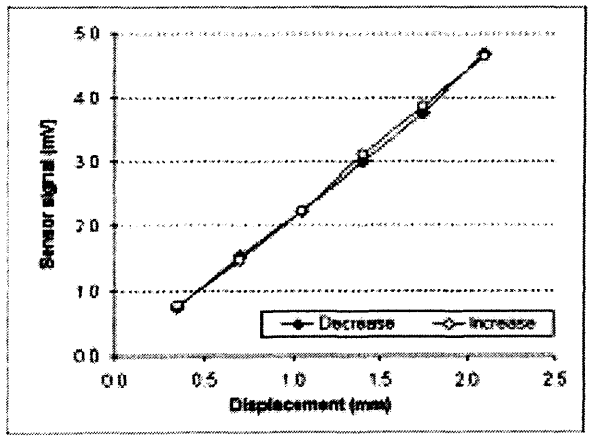

Fig. 6. The output voltage characteristics against the displacement of the bi-layer during the increase and decrease of the actuators displacement (FM System).

Comparing the output signal (AM) with the LDV (Fig. 7) it can be seen that the amplitude modulated signal shows an average of 1.7 % deviation with a 3.9 % maximum deviation.

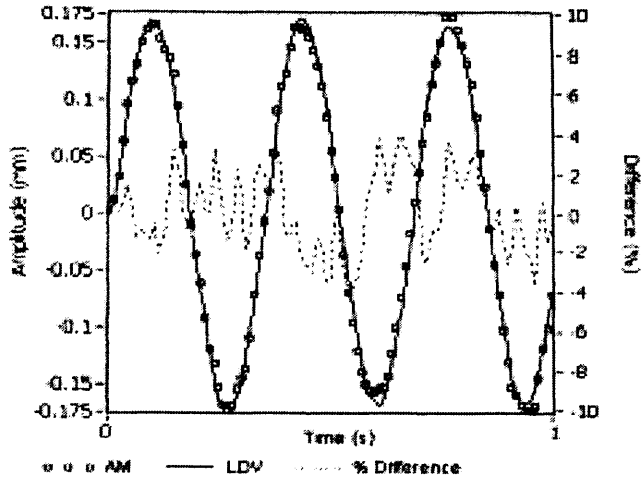

Fig. 7. A comparison of: a) sensor signal (AM) and b) the LDV output at 0.35 mm peak to peak plotted together with their percentage difference.

From the above it can be noticed that the AM signal not only shows twice the amount of deviation, at this displacement range, but also compared to the FM signal it depicts a deteriorated signal quality. This difference is expected to increase at displacements lower than 0.35 mm.

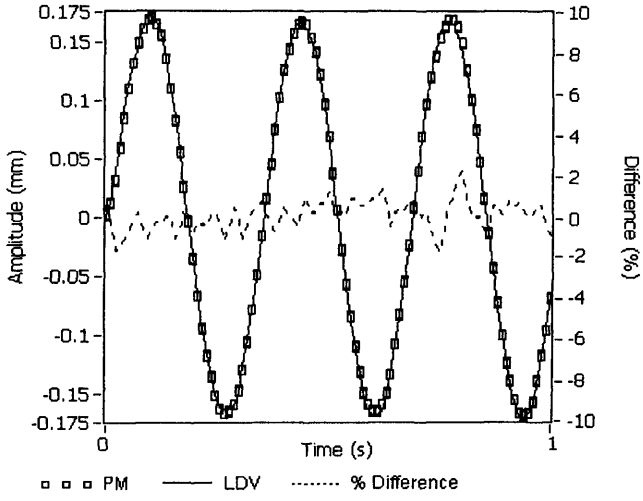

Fig. 8. A comparison of: a) sensor signal (PM) and b) the LDV output at 0.35mm peak to peak plotted together with their percentage difference.

From Fig. 8 the phase modulated signal (PM) shows an average 1% deviation with a 2.2 % maximum deviation compared to the expected signal from the LDV.

Comparing the AM, PM, FM principles against the LDV results and also looking at the relationship between the signal output versus displacement and the mechanical hysteresis for each modulation method, a useful conclusion can be drawn. The FM principle outperforms in quality the other two modulation principles. Thus, the preferred method for conveying the bi-layer displacement information is by the use of the FM principle. Another aspect of the FM and PM techniques is that if the sensor is placed in the presence of a DC field the Δf (or $\Delta\Phi$ for PM) change increases (until the magnetic material reaches saturation) as the sensor approaches the source. Thus, presence of a small permanent magnet has an amplifying effect to signal and it can increase signals that arise from small displacements. In the case of the AM technique the presence of a DC field will augment the present noise levels which in turn cover the information signal.

B. Thermal Stability

As part of examining the performance of the FM measurement system, the thermal stability was tested over the temperature range of up to 180 ^{0}C by placing the bi-layer sensor and the actuator set-up inside an environmental chamber. The sensor was placed inside an environmental chamber and subjected to a temperature increase up to 180 ^{0}C.

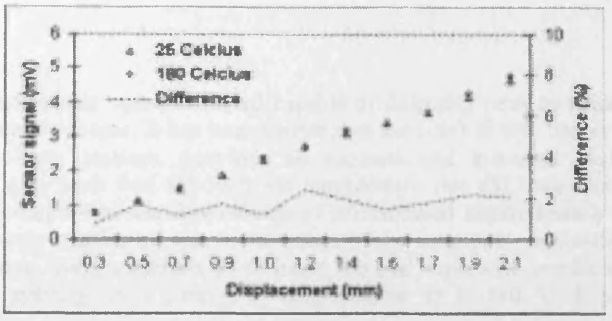

Fig. 9. The sensor signal at 25 ^{0}C and at 180 ^{0}C plotted together with the absolute value of their percentage difference.

The sensor signal at 180 ^{0}C shows average absolute values of 1.7 % deviation, and a 2.3 % maximum deviation, compared to the signal taken at 25 ^{0}C (Fig. 9). These values are within the repeatability percentage of the FM system. In Fig. 10 the inductance value reached 163 % change in inductance, ΔL, at 180 ^{0}C rising sharply and approximately linear.

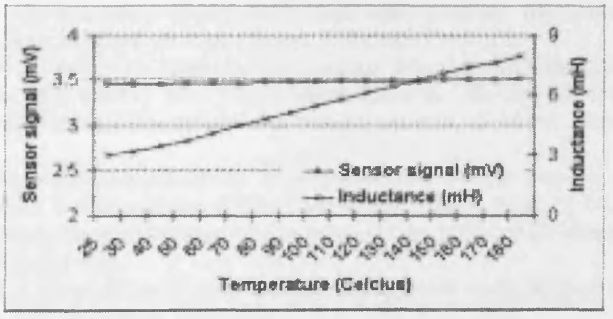

Fig. 10. The rise of inductance due to temperature increase has minute effect to the peak to peak sensor signal taken at ~1.6 mm peak to peak displacement.

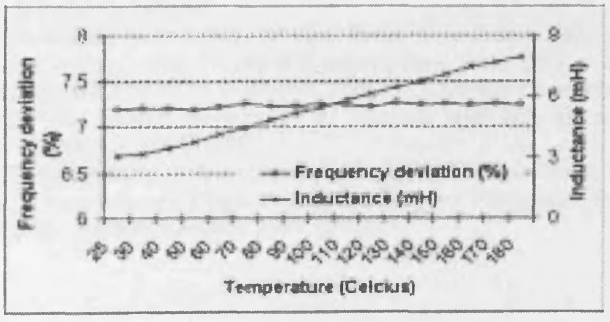

Fig. 11. The frequency dependence on temperature remains relatively uninfluenced from the rise of inductance due to temperature increase (displacement was set at ~1.6 mm peak to peak).

The notable different thermal expansion coefficients of the two materials of the bi-layer strip (α_1 = 5.9·10-6 K^{-1} for the amorphous magnetic film and α_2 = 17·10-6 K^{-1} for the CuBe layer) explains the high ΔL increase. In contrast the increase of temperature does not influences the peak to peak sensor

signal. As inductance increases with temperature the reference frequency, f_R, is also increasing but the percentage change ΔL remains approximately constant, thus Δf follows proportionally at 7.2 % Fig. 11. The sensor signal is relatively uninfluenced by the increase of temperature as the frequency deviation showed to be not very susceptible to the increase of the inductance value under these system settings. These findings allow the design and construction of temperature independent sensor families (in the range up to 180 ^{0}C) as required by industry.

4. Conclusions

The LabVIEW® based system was developed capable of detecting peak to peak displacements using the frequency modulation scheme. It has been shown that the LabVIEW® based measurement system, together with the bi-layer sensors, provides an accurate and low-cost method for determining displacement. It was also seen that although the temperature rise did cause inductance change, and hence frequency increase, the percentage change of Δf remained approximately constant. The sensor signal remained relatively unaffected due to the nature of the frequency modulation method. Thus, the bi-layer thin film sensor, using materials of different thermal expansion coefficients, can be used and have a good thermal stability over a range of temperatures up to 180 ^{0}C. It is considered that this temperature independent sensor system has the prospect of being used for applications such as airflow measurements in engine exhaust pipe where the operating temperatures are high and variable especially for application in car engines for measuring exhaust fume flow.

References

1. J. Kosel et al. *Non-contact signal detection of multifunctional bilayer sensor*, Proc. of Eurosensors XVIII, Rome, Italy, Sep. 13 15, 2004.
2. L. Mehnen et al. Optimisation of sensitivity and time constant of thermal sensors based on magnetoelastic amorphous bilayers, *J. Alloys Comp. 369* (2004) 198 201.
3. T. Meydan, *Amorphous materials in sensor applications, Magnetic Materials for Sensors and Actuators,* Tech. Digest, IEE Colloq. New Magn. Mater. London, UK, Oct. 11, 1994.
4. L. Mehnen et al. Magnetostrictive amorphous bimetal sensors, *J. Magn. Magn. Mater. 215* (2000) 779 781.
5. E. Kaniusas et al. *Biomedical applicability of magnetoelastic bilayer sensors*, Proc. Inter. Symp. on Applied Electromagnetics and Mechanics (ISEM), Versailles, France, May. 12 14, 2003.
6. E. Kaniusas et al. Magnetostrictive amorphous bilayers and trilayers for thermal sensors, *J. Magn. Magn Mater. 254* (2003) 624 626.
7. G. S. Katranas et al. *A novel frequency modulation based system using bilayer thin film displacement sensors*, Tech. Digest, IEEE Intermag San Diego, USA, May. 8 12, 2006.
8. DAQ PCI-6115/6120 User Manual, S-Series Simultaneous-Sampling Multifunction Device for PCI, National Instruments (2004)
9. G. S. Katranas et al. Simulation and measurement of bilayer sensor characteristics, *Sensors and Actuators A: Physical 129* (2006) 243 246.
10. J. D. Gibson, *The communications handbook*, CRC Press, Boca Raton, 2002, p. 68.1.
11. H. S. Black, *Modulation theory*, Van Nostrand Reinhold, New York, 1953, p. 27.
12. B. P. Lathi, *Signal processing and linear systems*, Oxford University Press, New York, 1998, p. 289.
13. S. R. Long et al, "The Hilbert techniques: an alternate approach for non-steady time series analysis," *IEEE GRSS Newsletter* (1995) 6 11.
14. F. Froehlich et al, *Encyclopaedia of Telecommunications*, Dekker, New York, 1995, p. 427.
15. OFV-303/OFV-3001, User Manual, Single Point Laser Doppler Vibrometer, Polytec GmbH (2002).
16. W. M. Harper, *Statistics*, Pitman, London, 1991, p. 172.

Bi-Layer Thin Film Sensor System for Medical Applications

G.S. Katranas, T. Meydan*, F. Borza

Wolfson Centre for Magnetics, School of Engineering, Cardiff University CF24 3AA

Abstract

A novel method has been proposed for accurately measuring physiological parameters associated with body movements, such as cardiac and respiratory activities, using bi-layer thin-film sensors. A bi-layer curvature sensor system was used the first time not only to monitor but also to map the five characteristic waves of the normal heartbeat rate (P, Q, R, S and T wave), hence providing additional medical information about the cardiac activity of the patient. Also during monitoring of lung ventilation, various parameters such as normal respiration, deep inhalation/exhalation and apnoea were easily distinguishable in the output signal. The bi-layer thin films used are the building blocks for a new generation of multi-functional sensor families. They consist of a magnetic layer and a non magnetic counter layer that is used to enhance the changes in the relative permeability of the material caused by tensile or compressive stresses during bending. The measuring system utilizes a personal computer based system using the LabVIEW® graphical programming package. This allows a high degree of software modularity and provides the features necessary for acquiring the sensor signal, analysing it and displaying the results. The results demonstrate that this system provides a robust, cost effective solution to monitoring cardio-respiratory activity with minimum inconvenience to the patient, which is necessary for prolonged, undisturbed monitoring.

Introduction

The non-disturbing monitoring of the cardio-respiratory activity of the human body is an important parameter during biometrical tests, such as polysomnography. This is a comprehensive recording of the physiological changes that occur during sleep. This diagnostic test monitors many medical techniques including electroencephalography (EEG), rapid eye movement (REM), electromyography (EMG), electrocardiogram (ECG), and respiratory activity while the patient is sleeping. During the sleep study the breathing; oxygen levels, heart tracing, and the different levels of sleep are recorded. A qualified sleep technician performs the test and monitors the patient's sleep through the night. The sleep technician will place electrodes on the head and face to monitor levels of sleep, apply ECG (electrocardiogram) patches to the chest to monitor the heartbeat, and place a flow sensor under the nose to monitor airflow. In addition, soft straps are placed around the chest and abdomen to monitor the rise and fall of the chest to determine whether the patient is breathing appropriately during sleep. These sensors, electrodes and straps can potentially disturb the patients sleep.

This paper describes the application of a novel system using bilayer thin film sensors, originally used for the detection of bending[1]. The system can also be used to measure, with minimum disturbance, various physiological activities that involve the dynamic deformations of the curvature of the skin.

Experimental

Measurement System

Bi-layer sensors are constructed from a ferromagnetic magnetostrictive layer that can be crystalline, nano crystalline or amorphous magnetic materials on a non-magnetic layer. Bi-layer sensors are cost effective and easy to operate and they have been developed to detect various parameters such as displacement, temperature, curvature, stress etc[2]. In this paper, a bi-layer with amorphous magnetostrictive layer is used because of its lack of magneto-crystalline anisotropy and high mechanical strength[3, 4]. Soft magnetic amorphous ribbons and thin films may exhibit high magnetostriction and therefore strong magneto-elastic effects. When a bi-layer thin film sensor is physically bent, stress develops along its length that is dependant by the geometry of the cantilever and its curvature, c. The changes in stress result in changes in the relative permeability of the material. These changes are detected by a pick-up coil, wound around one end of the bi-layer sensor, which produces the sensor signal, s, as a result of changes in the inductance, ΔL, and hence its reactance X_L[5, 6]. Thus, the change in ΔL corresponds to the change of skin curvature, Δc, where the sensor is applied. The bending sensor used is a bi-layer strip, which consists of a magnetostrictive layer on a non-magnetic layer (Copper Beryllium - CuBe). The magnetostrictive layer is an amorphous magnetic film, 2.9μm thick, was deposited from a $Fe_{81}B_{13.5}Si_{3.5}C_2$ target using the RF magnetron sputtering technique onto a 25μm CuBe layer. The measuring system consists of a personal computer (PC) based acquisition set-up and a circuit that modulates the sensor displacement signal with a reference signal, using the frequency modulation (FM) principle (Figure 1)[1].

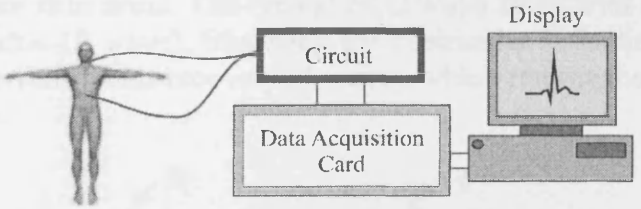

Fig. 1. Bi-layer sensor system for registering cardio-respiratory activity.

Signal detection was achieved through the use of LabVIEW® software and a NI-6120 data acquisition card with a maximum sampling rate of 800kS/s per channel and 16-bit resolution[7].

Sensor Application

Various internal physiological activities are mirrored on the human body in the form of active variations of the skin curvature, c. Depending on the body region these signals consist of three main components, cardiac activity, s_C, lung ventilation, s_R and various body movements, s_M[8]. For the detection of the heartbeat rate, f_C, the sensor was attached on the neck over the carotid artery with the aid of double sided adhesive tape (Fig. 2). Cardiac activity transmits blood pressure waves through the arterial system which result in the cyclic alteration of the vessel's radius, r. This deformation is transmitted to the skin, through the surrounding tissue, resulting in change of curvature, Δc, proportional to Δr[9]. The respiratory activity, f_R, was measured by fixing the sensor on the chest using double sided adhesive tape. As in the case of cardiac activity measurements, the deformation of the chest due to changes in respiration volume produces a sensor signal, s_R, which characterizes the lung ventilation.

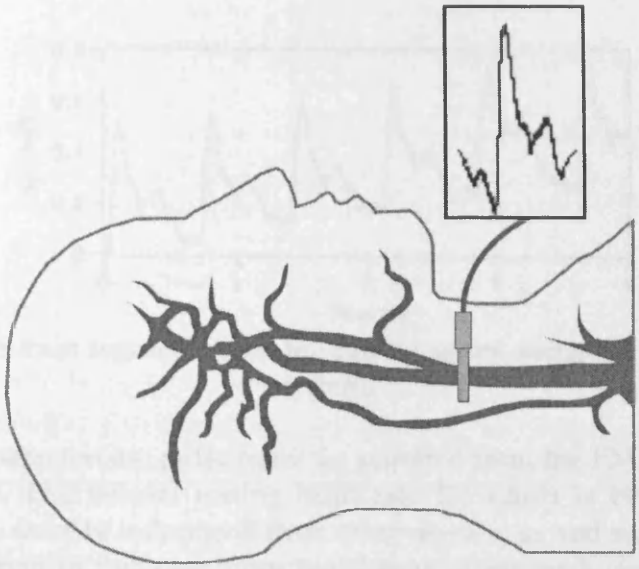

Fig. 2. Application of the bi-layer thin film sensor over the carotid artery

Results

An Electrocardiogram (ECG) is an illustration produced by an Electrocardiograph, which measures the electrical potential between various points of the body in order to show the electrical activity in the heart. Up to 12 contacts (electrodes) are usually affixed to the arms, legs and chest on clean, shaven skin areas. The typical ECG wave starts with the spread of the heart stimulation through the atria (P wave), triggering the ventricular activation (Q, R and S wave), and then ending up to the ventricular recovery (T wave), which returns the stimulated ventricular muscle to its resting state.

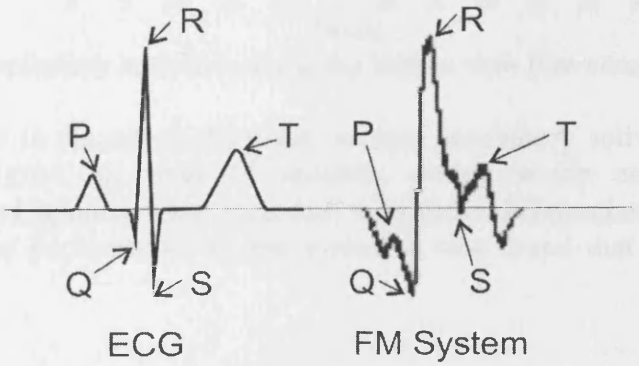

Fig. 3. Comparison between the basic ECG output and the acquired heartbeat from the FM system.

Figure 3 shows the hemo-dynamic activity at the carotid artery caused by the pumping of the heart. A bilayer curvature sensor system was used for the first time not only to monitor but also to map the five characteristic waves of the normal heartbeat rate (P, Q, R, S and T wave), hence providing additional medical information about the cardiac activity of the patient. Compared to the ECG, the bi-layer sensor system only needs one contact to the body (the bi-layer sensor) and there is no need for the preparation of the skin area.

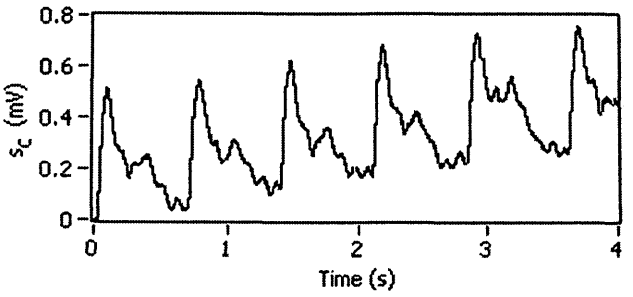

Fig. 4. A detected pulse train segment, from the carotid artery, using the bilayer thin film sensor system.

Fig. 4 demonstrates a characteristic pulse train, f_C, acquired from the FM system that corresponds to 81 beats per minute. The normal resting heart rate for adults is between 60-100 beats per minute. The signal s_C is usually influenced from other signals, s_R and s_M, that arise from various body movements including in this case from the change of the neck circumference during slow intake of air in the lungs. When the patient is holding his breath and immobile, only the signal from the cardiac activity, s_C, is detected.

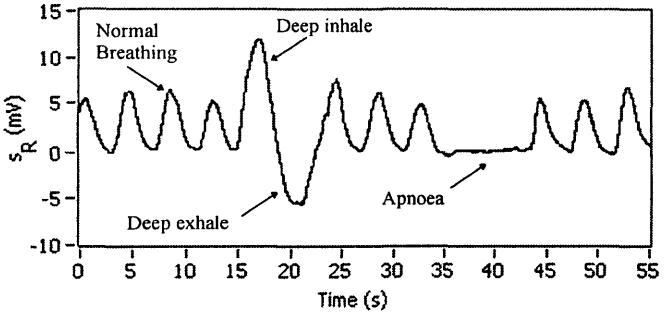

Fig. 5. Respiratory activities using the bilayer thin film sensor system.

When the bilayer sensor is placed on the chest, various respiratory activities can be monitored. Fig. 5 displays the signal, s_R, over 55 seconds, during which normal respiration, deep inhalation/exhalation and apnoea were recorded with clear differentiation between respiratory activities. Also from the performance of the system it was found that the repeatability of the results is 2.4%.

Conclusion

A new system incorporating bi-layer thin film curvature sensors has been developed. The system is capable of detecting cardio-respiratory activities using the frequency modulation principle. It has been shown that the LabVIEW® based measurement system, together with the bi-layer thin film sensors, provides an accurate, robust and low-cost method for monitoring various physiological parameters that arise from the change of skin curvature. This sensor system also provides minimum inconvenience to the patient, which is essential for prolonged, undisturbed monitoring.

References

1. G. S. Katranas, T. Meydan, S. Zurek, T. A. Ovari, F. Borza, presented in Intermag 2006, San Diego, USA.
2. J. Kosel, H. Pfutzner, L. Mehnen, E. Kaniusas, T. Meydan, M. Vázquez, M. Rohn, A. M. Merlo, B. Marquardt, Proc. of Eurosensors XVIII, Italy, Rome (2004)
3. L. Mehnen, E. Kaniusas, J. Kosel, J.C. Téllez-Blanco, H. Pfützner, T. Meydan, M. Vázquez, M. Rohn, C. Malvicino, B. Marquardt, J. Alloys Comp. 369 (2004)
4. T. Meydan, IEE Colloq. on New Magn. Mater. 183 (1994)
5. L. Mehnen, H. Pfützner and E. Kaniusas, J. Magn. Magn. Mater. 215-216 (2000)
6. E. Kaniusas, H. Pfützner, L. Mehnen, J. Kosel, J.C. Téllez-Blanco, G. Varoneckas, A. Alonderis, T. Meydan, M. Vázquez, M. Rohn, R. Seccardini, B. Marquardt, Proc. Inter. Symp. on Applied Electromagnetics and Mechanics (ISEM), Versailles (2003)
7. DAQ PCI-6115/6120 User Manual, S-Series Simultaneous-Sampling Multifunction Device for PCI, National Instruments (2004)
8. E. Kaniusas, L. Mehnen, C. Krell, H. Pfutzner, J. Magn. Magn. Mater. 215-216 (2000)
9. E. Kaniusas, H. Pfützner, L. Mehnen, J. Kosel, G. Varoneckas, A. Alonderis, T. Meydan, M. Vázquez, M. Rohn, A.M. Merlo, B. Marquardt, J. Ultragarsas (Ultrasound), 3 52 (2004)

ELSEVIER

Journal of Magnetism and Magnetic Materials 00 (2007) 000–000

Journal of magnetism and magnetic materials

www.elsevier.com/locate/jmmm

Parameter optimisation for the bi-layer sensor used in the frequency modulation based system

G. S. Katranas[a]*, T. Meydan[a]

[a]*Wolfson Centre for Magnetics, Cardiff University, Queens Buildings,Newport Road, Cardiff CF24 3AA,UK*

Elsevier use only: Received date here; revised date here; accepted date here

Abstract

Bi-layer sensors been used to detect a range of parameters such as displacement, temperature, curvature and stress. This is possible by accurately measuring low voltage signals ($\sim 10^{-4}$ V) associated with inductance changes of bi-layer thin-film sensors under bending stress. Bi-layer sensors consist of a magnetic layer and a non magnetic counter layer that is used to enhance the changes in the relative permeability of the material, caused by tensile or compressive stresses. The sensor sensitivity is governed by the bending stresses on the bi-layer and the coil parameters. These parameters are the coil's physical dimensions, number of turns and of course the cross sectional area and properties of the magnetic material (*ie* magnetostriction, relative permeability). Taking in consideration the modulating circuit component values and the desired frequency range, the combination of coil parameters and excitation current were optimized to provide the largest change of inductance and hence the largest change of relative permeability.

PACS: 07.07.D; 75.70; 75.70.K; 85.70.K

Keywords: Data acquisition; Frequency modulation; Magnetostriction; Thin films; Transducer

1. Introduction

When a bi-layer sensor is physically bent at its free end, stresses, σ, develop along its length. This results in changes in the relative permeability, μ_r, of the material. These changes are detected by a pick-up coil, wound around one end of the bi-layer sensor, which produces the sensor signal as a result of changes in the inductance, ΔL, and hence its reactance X_L. Thus, the change in ΔL corresponds to the displacement of the free end of the bi-layer sensor. As part of an electronic circuit the bi-layer sensor, acts as an inductor, L. Any changes ΔL may influence the alternating current (AC) that is used to excite the magnetic material, hence the properties of the output voltage signal [1].

2. Experimental

A. Measurement System

The measuring system consists of a personal computer (PC) based acquisition set up and a circuit that modulates the sensor displacement signal with a reference signal, using the frequency modulation principle. Signal detection and processing was achieved through the use of LabVIEW® software and a NI-6120 data acquisition card with a maximum sampling rate of 800 kS/s per channel and 16-bit resolution [2].

B. Frequency Modulation

The FM is achieved using a Colpitts oscillator. This circuit utilizes an LC tank with an inductor connected in parallel to two series capacitors [3]. The output is a sine wave at a frequency, which is defined by the values of L and C:

$$f = \frac{1}{2\pi \cdot \sqrt{\frac{L \cdot C_1 \cdot C_2}{C_1 + C_2}}} \tag{2}$$

The FM signal is demodulated in software via a differentiator followed by an envelope detector based on the Hilbert

* Corresponding author. Tel.: +44-2920-875923; fax: +44-2920-879538.
E-mail address: KatranasG@cf.ac.uk.

transform [3]. The bilayer sensor used in the measurement system was designed according to the principles of the frequency modulation method (*FM*). When placed in the modulation circuit (Colpitts oscillator), the bilayer sensor acts as its inductive component. Any change ΔL in the inductance L of the pickup coil (sensor) will shift the operating/oscillating frequency from f to $f + \Delta f$. Hence, frequency modulation is achieved. The capacitors where chosen to be $C_1 = C_2 = 1$ μF, in order to keep the circuit frequency between 1 kHz to 10 kHz. For signal quality purposes (to avoid signal aliasing) the sampling rate must be 20 samples per Hertz which means that at 10 kHz there will be a need to acquire 200,000 samples per second (200 kS/s). Even though the data acquisition card can accept up to 800 kS/s, the processing time needed is increased rapidly. Taking in consideration the capacitor value and the desired frequency range, the combination of coil parameters and excitation current were optimised, to provide the largest change of inductance and hence the largest change of relative permeability.

3. Results

A. Coil Parameter Optimisation

Using as a reference magnetic material a 28 μm thick Metglas® 2605SC [4] ($\ell = 40$ mm, $w = 5$ mm) agglutinated on a 75 μm Aluminium substrate, the effect of coil parameters on inductance, were examined. By keeping the coil cross sectional area constant and varying the length (5 mm – 20 mm) at steps of 5 mm and the number of turns (100 – 1000) at steps of 100, 40 coils were manufactured using a 60 μm diameter enamel copper wire.

Five consecutive readings were taken for each set of data and the average was plotted in Fig. 1 to Fig. 5. The non-repeatability error in the sensor optimisation data set was found to be ~1 %. The coils were placed in the Colpitts oscillator circuit and the resulting operating frequency and current through the coil were measured. An approximation of the relative permeability value was calculated from the measured frequency and current and through the use of Eq. 2 and Eq. 3:

$$L = \mu_o \mu_r \cdot \frac{N^2 A}{\ell} \tag{3}$$

It is these values, illustrated in Fig. 1 - Fig. 4, that give an indication of the optimum coil parameters for the magnetic material in question. By looking at Fig. 1 it can be seen that high values of relative permeability are recoded on longer coils at low numbers of turns, following Eq. 3. Fig. 1 also confirms that low turn coils ($N = 200$ - 400) are more suitable for sensors, since they display high values of current (compared with coils of high N), but it also shows that I increases as ℓ decreases as is expected from Eq. 4.

$$H = N\frac{I}{\ell} \tag{4}$$

It is apparent that low number of turns is a desired parameter for the design of the sensor coil (using the 2605SC - 28 μm sample) as current reaches a peak using coils of 200 - 400 turns, regardless of coil length. Current and relative permeability need to be high as to ensure high levels of sensor sensitivity as expected in Eq. 3 and Eq. 5:

$$v = -\mu_o \mu_r \cdot \frac{N^2 A}{\ell} \cdot \frac{dI}{dt} \tag{5}$$

The data points on Fig. 1 represent the number of turns which increases from right ($N = 100$) to left ($N = 1000$).

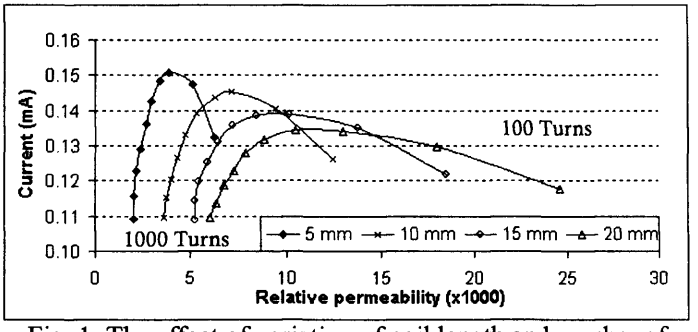

Fig. 1: The effect of variation of coil length and number of turns on relative permeability and excitation current (Sample 2605SC - 28 μm).

The next parameter to be decided was the length of the coil. Plotting I against μ_r (Fig. 1) shows that, at 300 turns, longer coils may have lower current values (9 %) than the shorter but they present much higher amounts of μ_r (72 %). If the relative permeability is high then the $\Delta\mu_r$ will be high (high ΔL) and hence the sensor sensitivity will increase. Thus, a coil of $N = 300$ and $\ell = 20$ mm would have the optimum dimensions needed for a sensor.

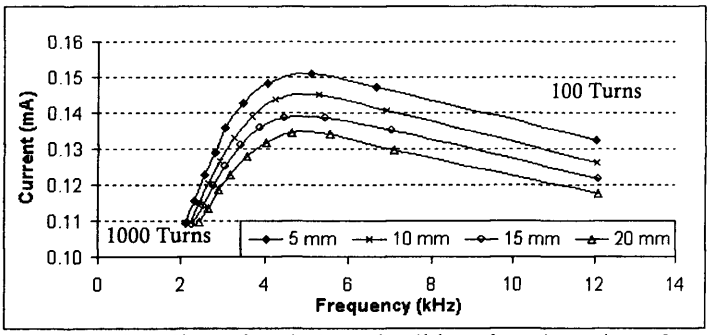

Fig. 2: The effect of variation of coil length and number of turns on excitation current and operating frequency (Sample 2605SC - 28 μm).

From Fig. 2 it can be seen that the operating frequency does change (decrease) with the increase of N, as expected from Eq. 1 and Eq. 2. It is also evident that using a 300 – 400 turn coil the current peaks at 5 kHz. The data points on Fig. 2 represent the number of turns which increases from right ($N = 100$) to

left (N = 1000). At this operating frequency the sampling rate will be 100 kS/s which will approximately take 1 - 2 seconds for the software to display the information signal ensuring continuous real-time acquisition and process of the data. The data shown on Fig. 1 and Fig. 2 show the optimum parameter selection only for the 2605SC – 28 μm sample.

B. Magnetic Material Selection and Thickness

The measurement system can be used not only for the detection of stress/displacement but also for the evaluation of bilayer magnetic material for sensor applications. Hence, a comparison was made between two materials of different saturation magnetostriction at a range of thicknesses (*th*) to conclude to an optimum coil dimension and magnetic material for the sensor. The materials used for this comparison were Metglas® 2605SC ($\lambda_s \approx 30{\cdot}10^{-6}$) and Metglas® 2705M ($\lambda_s \approx 0$) (Table 1) [4, 5]. The magnetic materials (ℓ = 40 mm, w = 5 mm) were either agglutinated (*Adh*) or deposited (*RF*) on the substrate using the *RF* sputtering method. The substrates used were Aluminium (Al), Copper-Beryllium (Cube) and Aluminium-Magnesium (AlMg).

Metglas® Material	2605SC ($\lambda_s \approx 30{\cdot}10^{-6}$)			2705M ($\lambda_s \approx 0$)		
Metglas® Thickness (μm)	28	12	2.9	24	5	2.9
Substrate	*Al*	*Al*	*CuBe*	*Al*	*CuBe*	*AlMg*
Substrate Thickness (μm)	75	75	25	75	25	30
Bilayer Fabrication	Adh	Adh	*RF*	Adh	*RF*	*RF*

Table 1: Bilayer strip fabrication method and layer thickness.

The 28 μm thick 2605SC was reduced in thickness down to 12 μm by means of mechanical polishing. As expected from Eq. 2 the reduction in cross sectional area of the sensor due to the decrease of magnetic material thickness increases the values of relative permeability (Fig. 3). The exponential decrease of relative permeability with the increase of number of turns is mainly due to the N^2 term in Eq. 2. The highest values of relative permeability are recorded between N = 100 – 300. An indication of the effect of thickness on relative permeability can be seen by comparing the 2605SC – 28 μm and the 2605SC - 2.9 μm. For this material the ~10 times reduction in thickness showed a ~3 times (averaged from N = 100 – 1000) increase in μ_r. This difference is non-linear and depends on the materials properties, operating frequency and the current induced in the coil. A comparison between strips that have similar dimensions and are of different magnetic material (2705M – 2.9 μm and 2605SC - 2.9 μm) can also be made. On average the 2705M displayed a ~ 2.4 % higher than 2605SC due to its greater as cast *DC* permeability [4, 5]. It can be seen that the drop in thickness effects in the opposite manner the excitation current. The current increases with thickness and peaks between N = 300 – 400 among the three thickest materials (2605SC – 28 μm, 2705M – 24 μm and 2605SC – 12 μm) and between N = 100 – 300 among the three thinnest materials (2705M – 5 μm, 2605SC – 2.9 μm and 2705M – 2.9 μm). Comparing the 2605SC materials, the 43 % reduction in thickness between the 28 μm and the 12 μm had a 23 % reduction in I whereas the 90 % decrease in *th* among the 28 μm and the 2.9 μm produced about 50 % less current. From the examination of the 2507M materials the reduction of thickness by 79 % (from 24 μm and the 5 μm) leads to a 43 % current fall and the decrease of *th* by 88 % (from 24 μm and the 2.9 μm) shows a 44 % drop in I. The effect of thickness reduction to current between the 2605SC and the 2705M can be performed by comparing both the 2.9 μm samples. The difference between these is below the 1 % repeatability of the data, hence the 2605SC – 28 μm and 2705M – 24 μm were examined instead. Even though there is a 4 μm difference between the two materials, the thickness reduction from 28 μm and 24 μm to 2.9 μm is of similar level 89 ± 1 %. It can be seen that even though the 2705M displays less current loss, the 2605SC does display higher values of λ which gives an advantage for selection as the magnetic material for the bilayer sensors. The highest amounts of I and μ_r occur as expected with low turn coils. By plotting the excitation current against the relative permeability, the effects of thickness and number of turns are made evident.

The data points on Fig. 3 represent the number of turns which increases from right (N = 100) to left (N = 1000). The first thing that is made apparent from the I versus μ_r relationship is that thinner materials (2705M – 5 μm, 2605SC – 2.9 μm and 2705M – 2.9 μm) display large amounts of relative permeability and smaller quantity of current compared to the thicker samples (2605SC – 28 μm, 2705M – 24 μm and 2705M – 12 μm).

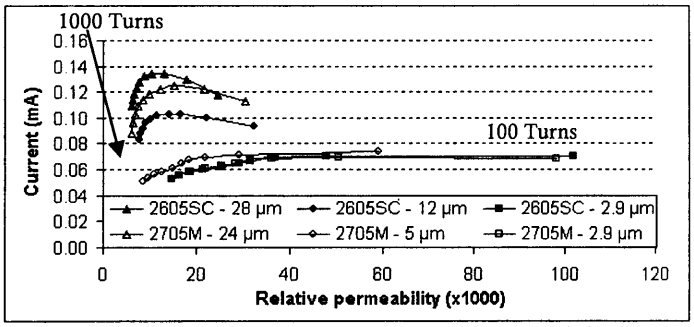

Fig. 3: The effect of variation of magnetic material thickness and number of turns on I and μr for samples with different λ_s.

The behaviour of the system shows that the current is reversely proportional to the relative permeability (Eq. 5). Therefore a "balance" between current and relative permeability will define the optimum coil dimensions and material for the bilayer sensor system. From the results it is estimated that low turn coils (N = 100 - 400) are more suitable for sensors, since they display high values of I and μ_r (compared with coils of high N).

By examining Fig. 4 it can be seen that the low turn coils (N = 100 – 300) do produce high μ_r but they also generate operating frequencies above 10 kHz depending on the thickness of the sample. An operating frequency above 10 kHz reduces significantly the data processing of the software and continuous real-time acquisition and process of the data is no longer possible. This upper frequency limit of the system shows that a sensor using magnetic material under ~5 μm in

hickness can have as a minimum 300 turns; less turns will ave $f > 10$ kHz.

The examination of Fig. 4 shows that the samples with less hickness, and hence less cross sectional area of magnetic naterial in the coil, produce higher operating frequencies as is expected from Eq. 1 and Eq. 2. Taking in consideration the imit of the system that prevents the use of coils that generate > 10 kHz it can be seen that the maximum current occurs at 300 turns for all samples. The operating frequency with $= 300$ for the 2605SC – 28 μm, 2705M – 24 μm and 2705M - 12 μm samples will be around 5.5 kHz whereas for the 2705M – 5 μm, 2605SC – 2.9 μm and 2705M – 2.9 μm it will e approximately at the 10 kHz limit.

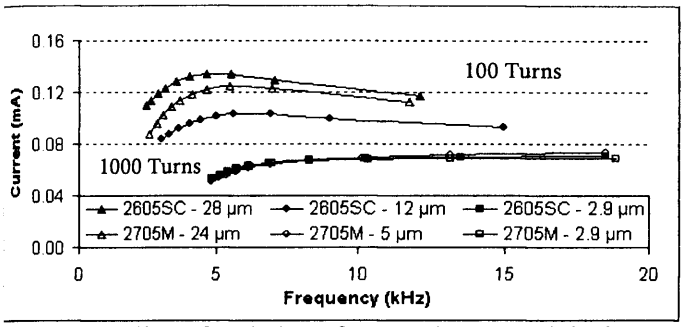

Fig. 4: The effect of variation of magnetic material thickness and number of turns on current and frequency for samples with different λ_s.

In the investigation of the data illustrated from Fig. 1 to Fig. 4 he coil's length, thickness, number of turns and magnetic naterial were varied and the performance behaviour (current, elative permeability and frequency) was examined in order to ptimise the design of bilayer sensor. From the parameters sed in the measurement system and the materials and sample hickness tested (Table 2), the optimum coil number of turns nd length were $N = 300$ and $\ell = 20$ mm. To further verify that hese are the optimum coil parameters, four sensor onfigurations were selected to be tested using the neasurement system and a controlled displacement (Fig. 5).

	(*i*)	(*ii*)	(*iii*)	(*iv*)	(*v*)
Metglas® Material	2605SC				2705M
Metglas® Thickness (μm)	28	2.9	28	28	2.9
Turns	300	300	300	1000	300
Length (mm)	20	20	5	20	20

Table 2: The four coils used in the measurement system to verify the selected optimum coil parameters.

As expected from Eq. 3, sensor (*i*) displays increased voltage utput (average increase of ~10 times) than (*ii*) since the hickness and hence the cross sectional area of the magnetic naterial in the coil is ~10 times higher. The thicker material nay have higher sensitivity but a thin strip has lower stiffness nd hence will bend to smaller displacements (low forces). his is useful in applications such as detecting the hemo-ynamic changes of the heart beat where the skin curvature hanges are dependant on the blood pressure in the vessel. If a material of high stiffness is used, the bending force exerted on the bilayer from the skin curvature changes will be too small and unable to bend the strip.

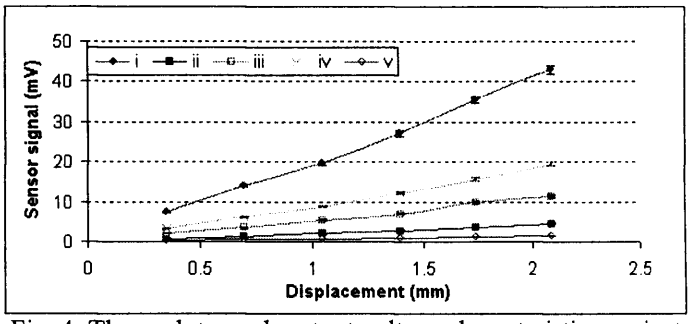

Fig. 4: The peak to peak output voltage characteristics against peak to peak displacement of bilayer sensors, using the configurations seen in Table 2.

Comparing sensor (*i*) and (*iii*) the effect of coil length reduction does produce lower output voltage (average ~26 %) which is explained by Eq. 4 and the results from Fig. 1. Increasing the number of turns on a coil will decrease the output voltage (average ~47 %) as seen from sensor (*i*) and (*iv*), which verifies the results of Fig. 3. Also from Fig. 5 it was seen that sensor (*ii*) with the 2605SC ($\lambda \approx 30{\cdot}10^{-6}$) outperformed by ~65 % the (*v*) with the 2705M ($\lambda \approx 0$). Thus, the effect of materials with high saturation magnetostriction was noted, and the 2605SC was chosen for use in bilayer sensors. The selected optimum coil parameters seem to give the highest output voltage compared with other configurations.

4. Conclusions

Industry today needs sensors that are cost effective and easy to operate and are able to detect multiple parameters such as displacement, temperature, curvature and stress; this is the reason why bi-layer sensors were developed. By optimising the bi-layer sensor parameters greater sensitivity can be achieved. It is considered that this system will lend itself to a number of automotive and biomedical applications.

References

[1] L. Mehnen, E. Kaniusas, J. Kosel, J.C. Téllez-Blanco, H. Pfützner, T. Meydan, M. Vázquez, M. Rohn, C. Malvicino, B. Marquardt, *J. Alloys Comp.* **369** (2004), p. 202.

[2] DAQ PCI-6115/6120 User Manual, S-Series Simultaneous-Sampling Multifunction Device for PCI, National Instruments (2004).

[3] G. S. Katranas, T. Meydan, T. A. Ovari, F. Borza, *IEEE Trans. Magn*, **43-3** (2006), p. 1035.

[4] 2605SC Magnetic Alloy Data Sheet, Metglas Inc., Conway, USA, 2004.

[5] 2705M Magnetic Alloy Data Sheet, Metglas Inc., Conway, USA, 2004.

Appendix E: Datasheets

- **Metglas 2605SC (Iron Based)**
- **Metglas 2705M (Cobalt Based)**
- **CuBe - Copper Beryllium ($Cu_{98}Be_2$)**
- **AlMg – Aluminium Magnesium ($Al_{95}Mg_5$)**
- **Cardiff University Thin Film Magnetron Sputtering System**
- **OPA37 Ultra-Low Noise Precision Operational Amplifier**
- **Kapton Polyimide Film**
- **LDV V450/1 Shaker System**

Metglas®

www.metglas.com

Magnetic Alloy 2605SC (Iron-based)

Technical Bulletin

Applications

- Pulse transformers
- Power transformers
- Current transducers
- Devices requiring a square-loop high saturation material

Benefits

- High saturation induction
- Extremely low core loss
- High B-H squareness

Typical DC Hysteresis Loop

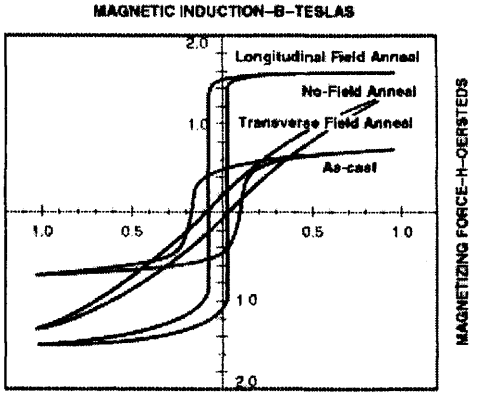

Typical Impedance Permeability Curves, Longitudinal Field Anneal

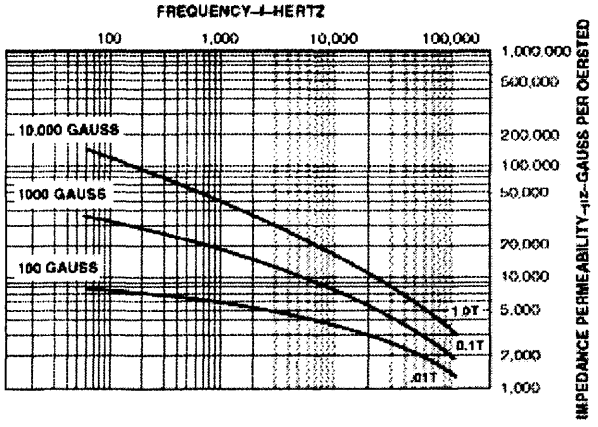

Physical Properties

Density (g/cc)	7.32
Vicker's Hardness (50g load)	880
Tensil Strength (GPa)	1-2
Elastic Modulus (GPa)	100-110
Lamination Factor (%)	>75
Thermal Expansion (ppm/°C)	5.9
Crystallization Temperature (°C)	480
Continuous Service Temp. (°C)	125

Magnetic Properties

Saturation Induction (Tesla)	1.61
Maximum D.C. Permeability (μ):	
Annealed	300,000
As Cast	>40,000
Saturation Magnetostriction (ppm)	30
Electrical Resistivity (μ--cm)	135
Curie Temperature (°C)	370

Typical Core Loss Curves, Longitudinal Field Anneal
METGLAS Alloy 2605SC

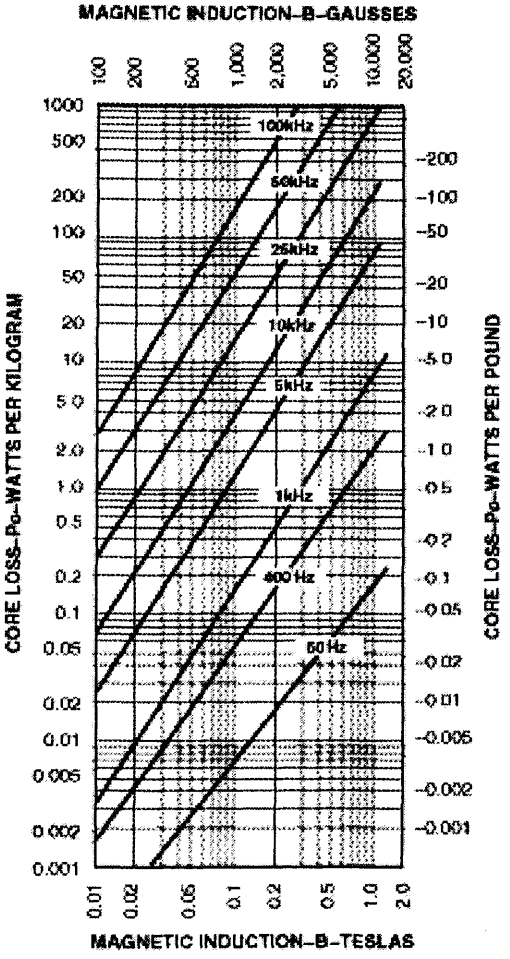

Contact Information:

USA

Metglas® ,Inc
140 Allied Drive
Conway, SC 29526

Tel: (800) 581-7654
Tel: (843) 349-7363
Fax: (843) 349-6815
E-mail: metglas@metglas.com

ASIA

Hitachi Metals Hong Kong

Room 1007, West Wing,
Tsim Sha Tsui Centre,
66 Mody Road, TST East,
Hong Kong.
Tel: (852) 27227680
Fax: (852) 27227660

EUROPE

Hitachi Metals Europe
Immermannstrasse 14-16
D- 40210 Düsseldorf
Germany
Tel : 49(0)211-16009-23
Fax: 49(0)211-16009-30

Metglas®

ww.metglas.com

Magnetic Alloy 2705M (Cobalt-based)

Technical Bulletin

plications

lexible electromagnetic shielding
lagnetic sensors
ligh frequency cores

nefits

ear-zero magnetostriction
ligh DC permeability at low fields
hout annealing
ligh tensile strength

Typical DC Hysteresis Loop

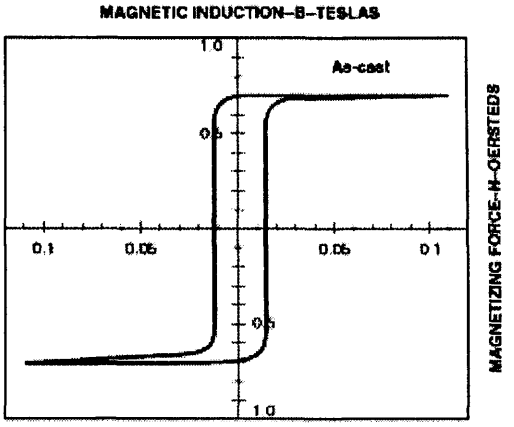

ical Impedance Permeability Curves, gitudinal Field Anneal

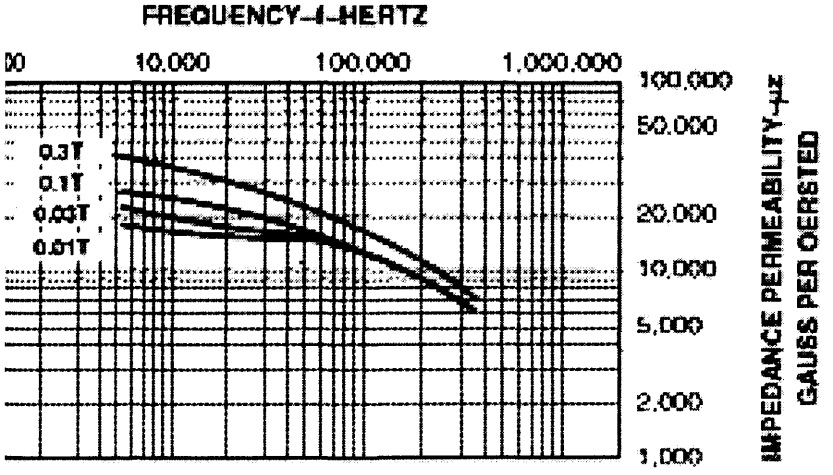

ysical Properties

nsity (g/cc)	7.80
ker's Hardness (50g load)	900
nsil Strength (GPa)	1-1.7
stic Modulus (GPa)	100-110
nination Factor (%)	>75
rmal Expansion (ppm/°C)	12.1
stallization Temperature (°C)	520
ntinuous Service Temp. (°C)	90

Magnetic Properties

Saturation Induction (Tesla)	0.77
Maximum D.C. Permeability (μ):	
Annealed	600,000
As Cast	290,000
Saturation Magnetostriction (ppm)	<<1
Electrical Resistivity (μ--cm)	136
Curie Temperature (°C)	365

Typical Core Loss Curves
METGLAS Alloy 2705M

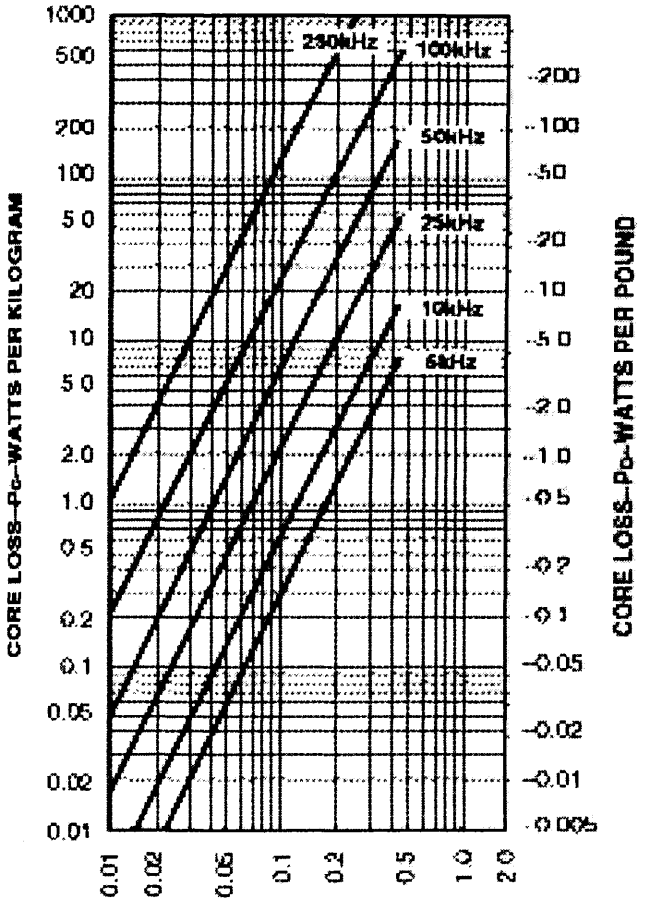

Typical Initial Magnetization Curves, As-cast
METGLAS Alloy 2705M

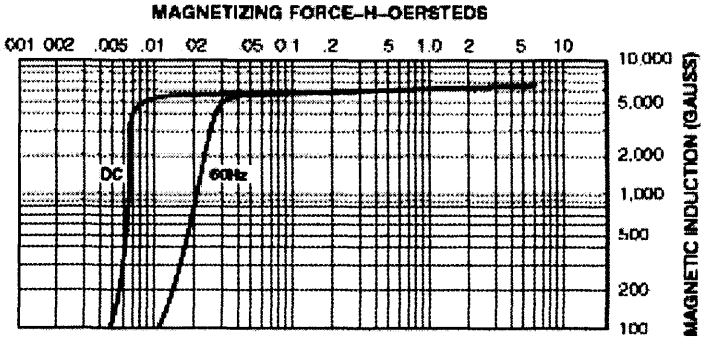

ntact Information:

iA

tglas® ,Inc
0 Allied Drive
nway, SC 29526

l: (800) 581-7654
l: (843) 349-7363
x: (843) 349-6815
nail: metglas@metglas.com

ASIA

Hitachi Metals Hong Kong

Room 1007, West Wing,
Tsim Sha Tsui Centre,
66 Mody Road, TST East,
Hong Kong.
Tel: (852) 27227680
Fax: (852) 27227660

EUROPE

Hitachi Metals Europe
Immermannstrasse 14-16
D- 40210 Düsseldorf
Germany
Tel : 49(0)211-16009-23
Fax: 49(0)211-16009-30

GoodFellow

Copper/Beryllium - Material Information

Cu98/Be 2

Buy Copper/Beryllium online

Buy small quantities online of Copper/Beryllium for research and/or development

Click to see Standard Catalogue items from one of the forms

Foil Insulated Wire Rod Wire

General Description:

Common Brand names : Ampcoloy 84® Berylco® Brush 190® Mallory®

Best mechanical properties of any Copper alloy which improve at sub-zero temperatures as low as -200C. Hardened by heat treatment this alloy machines best in the quarter hard cold work condition. Uses include springs of all kinds where high strength and corrosion resistance are important, resistance welding electrodes, dies and high strength, corrosion resistant tubing.

Electrical Properties

Temperature coefficient (K^{-1})	0.0010-0.0018
Electrical resistivity (µOhmcm)	5.4-11.5

Mechanical Properties

Elongation at break (%)	<50
Hardness - Brinell	100-360
Modulus of elasticity (GPa)	120-160
Tensile strength (MPa)	500-1300

Physical Properties

Density (g cm^{-3})	8.25
Melting point (C)	860-1000

Thermal Properties

Coefficient of thermal expansion @25-300C ($x10^{-6}$ K^{-1})	17.0
Thermal conductivity @23C (W m^{-1} K^{-1})	60-120

Click to see Standard Catalogue items from one of the forms

GoodFellow

Aluminium/Magnesium - Material Information

Al95/Mg 5

Buy Aluminium/Magnesium online

Buy small quantities online of Aluminium/Magnesium for research and/or development

Click to see Standard Catalogue items from one of the forms

Foil Tube

General Description:

Electrical Properties

Temperature coefficient (K^{-1})	0.0020
Electrical resistivity (µOhmcm)	5.6-6.1

Mechanical Properties

Elongation at break (%)	<20
Hardness - Brinell	60-120
Shear strength (MPa)	150-230
Tensile strength (MPa)	300-450

Physical Properties

Density (g cm^{-3})	2.65

Thermal Properties

Coefficient of thermal expansion @20-100C (x10^{-6} K^{-1})	23.0-23.5
Thermal conductivity @23C (W m^{-1} K^{-1})	125-130

Click to see Standard Catalogue items from one of the forms

Foil Tube

Thin Film Magnetron Sputtering System

Purpose

The Thin Film deposition system comprises a TORUS® source, which is both RF- and DC-compatible, and can deposit many classes of materials: conductors, semiconductors, insulators, and refractory materials. It is also capable of reactive sputtering.

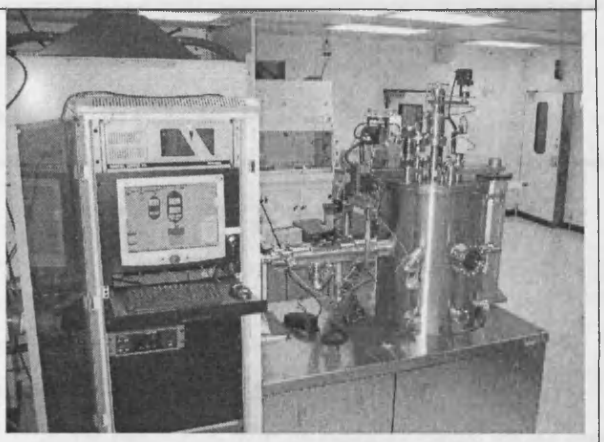

The main task for this system is to produce a varied range of advanced magnetic thin films, such as single and multi-layered amorphous and crystalline magnetic thin films, GMR (Giant Magneto-Resistance), AMR (Anisotropiclly Biased Magneto-Resistance) and GMI (Giant Magneto-Impedance) configurations for magnetic sensor applications.

Specification

Up to 10-9 Torr vacuum

RF and DC- flexible magnetron sputtering sources

Substrate semi-automatic front loading

Rotatable substrate platen for 3" diameter substrate with motor and controller

2" target conversion kit for a 3" source (useful to deposit both 2" and 3" targets)

Substrate cooling (water and liquid nitrogen)

Film thickness monitor

Plasma cleaning/milling for substrates and RF/DC-biasing of substrate

User Manual: Contact Dr. Firuta Borza

Operator: F. Borza, T. A. Óvári

Location: Clean Room, N3.07

Burr-Brown Products
from Texas Instruments

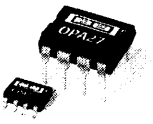

OPA27
OPA37

SBOS135A – JANUARY 1984 – REVISED OCTOBER 2003

Ultra-Low Noise, Precision OPERATIONAL AMPLIFIERS

FEATURES

- LOW NOISE: 4.5nV/√Hz max at 1kHz
- LOW OFFSET: 100μV max
- LOW DRIFT: 0.4μV/°C
- HIGH OPEN-LOOP GAIN: 117dB min
- HIGH COMMON-MODE REJECTION: 100dB min
- HIGH POWER-SUPPLY REJECTION: 94dB min
- FITS OP-07, OP-05, AD510, AND AD517 SOCKETS

APPLICATIONS

- PRECISION INSTRUMENTATION
- DATA ACQUISITION
- TEST EQUIPMENT
- PROFESSIONAL AUDIO EQUIPMENT
- TRANSDUCER AMPLIFIERS
- RADIATION HARD EQUIPMENT

DESCRIPTION

The OPA27 and OPA37 are ultra-low noise, high-precision monolithic operational amplifiers.

Laser-trimmed thin-film resistors provide excellent long-term voltage offset stability and allow superior voltage offset compared to common zener-zap techniques.

A unique bias current cancellation circuit allows bias and offset current specifications to be met over the full –55°C to +125°C temperature range.

The OPA27 is internally compensated for unity-gain stability. The decompensated OPA37 requires a closed-loop gain ≥ 5.

The Burr-Brown OPA27 and OPA37 are improved replacements for the industry-standard OP-27 and OP-37.

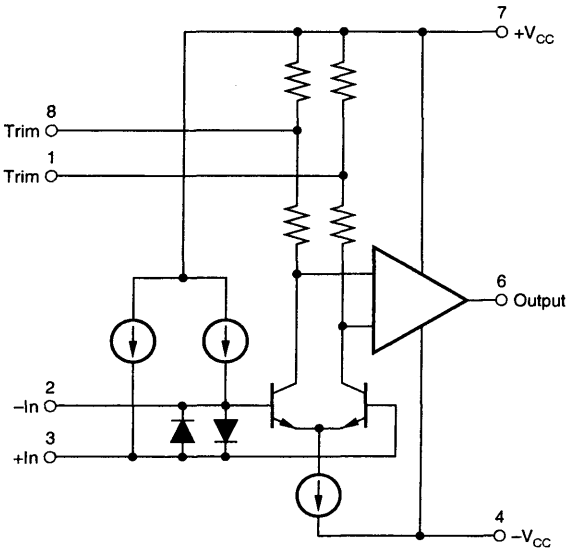

SPECIFICATIONS

At V_{CC} = ±15V and T_A = +25°C, unless otherwise noted.

PARAMETER	CONDITIONS	OPA27G OPA37G MIN	TYP	MAX	UNITS
INPUT NOISE[6]					
Voltage, f_O = 10Hz			3.8	8.0	nV/√Hz
f_O = 30Hz			3.3	5.6	nV/√Hz
f_O = 1kHz			3.2	4.5	nV/√Hz
f_B = 0.1Hz to 10Hz			0.09	0.25	µVp-p
Current,[1] f_O = 10Hz			1.7		pA/√Hz
f_O = 30Hz			1.0		pA/√Hz
f_O = 1kHz			0.4	0.6	pA/√Hz
OFFSET VOLTAGE[2]					
Input Offset Voltage			±25	±100	µV
Average Drift[3]	$T_{A\,MIN}$ to $T_{A\,MAX}$		±0.4	±1.8[6]	µV/°C
Long Term Stability[4]			0.4	2.0	µV/mo
Supply Rejection	±V_{CC} = 4 to 18V	94	120		dB
	±V_{CC} = 4 to 18V		±1	±20	µV/V
BIAS CURRENT					
Input Bias Current			±15	±80	nA
OFFSET CURRENT					
Input Offset Current			10	75	nA
IMPEDANCE					
Common-Mode			2 || 2.5		GΩ || pF
VOLTAGE RANGE					
Common-Mode Input Range		±11	±12.3		V
Common-Mode Rejection	V_{IN} = ±11VDC	100	122		dB
OPEN-LOOP VOLTAGE GAIN, DC	R_L ≥ 2kΩ	117	124		dB
	R_L ≥ 1kΩ		124		dB
FREQUENCY RESPONSE					
Gain-Bandwidth Product[5]	OPA27	5[6]	8		MHz
	OPA37	45[6]	63		MHz
Slew Rate[5]	V_O = ±10V, R_L = 2kΩ				
	OPA27, G = +1	1.7[6]	1.9		V/µs
	OPA37, G = +5	11[6]	11.9		V/µs
Settling Time, 0.01%	OPA27, G = +1		25		µs
	OPA37, G = +5		25		µs
RATED OUTPUT					
Voltage Output	R_L ≥ 2kΩ	±12	±13.8		V
	R_L ≥ 600Ω	±10	±12.8		V
Output Resistance	DC, Open Loop		70		Ω
Short Circuit Current	R_L = 0Ω		25	60[6]	mA
POWER SUPPLY					
Rated Voltage			±15		VDC
Voltage Range, Derated Performance		±4		±22	VDC
Current, Quiescent	I_O = 0mADC		3.3	5.7	mA
TEMPERATURE RANGE					
Specification		–40		+85	°C
Operating		–40		+85	°C

NOTES: (1) Measured with industry-standard noise test circuit (Figures 1 and 2). Due to errors introduced by this method, these current noise specifications should be used for comparison purposes only. (2) Offset voltage specification are measured with automatic test equipment after approximately 0.5 seconds from power turn-on. (3) Unnulled or nulled with 8kΩ to 20kΩ potentiometer. (4) Long-term voltage offset vs time trend line does not include warm-up drift. (5) Typical specification only on plastic package units. Slew rate varies on all units due to differing test methods. Minimum specification applies to open-loop test. (6) This parameter guaranteed by design.

SPECIFICATIONS

At V_{CC} = ±15V and –40°C ≤ T_A ≤ +25°C, unless otherwise noted.

PARAMETER	CONDITIONS	OPA27G OPA37G MIN	TYP	MAX	UNITS
INPUT VOLTAGE[1]					
Input Offset Voltage			±48	±220[3]	µV
Average Drift[2]	$T_{A\,MIN}$ to $T_{A\,MAX}$		±0.4	±1.8[3]	µV/°C
Supply Rejection	±V_{CC} = 4.5 to 18V				
	±V_{CC} = 4.5 to 18V	90 [3]	122		dB
BIAS CURRENT					
Input Bias Current			±21	±150[3]	nA
OFFSET CURRENT					
Input Offset Current					
E, F, G			20	135[3]	nA
VOLTAGE RANGE					
Common-Mode Input Range		±10.5[3]	±11.8		V
Common-Mode Rejection	V_{IN} = ±11VDC	96[3]	122		dB
OPEN-LOOP GAIN, DC					
Open-Loop Voltage Gain	R_L ≥ 2kΩ	113[3]	120		dB
RATED OUTPUT					
Voltage Output	R_L = 2kΩ	±11.0[3]	±13.4		V
Short Circuit Current	V_O = 0VDC		25		mA
TEMPERATURE RANGE					
Specification		–40		+85	°C

NOTES: (1) Offset voltage specification are measured with automatic test equipment after approximately 0.5s from power turn-on. (2) Unnulled or nulled with 8kΩ to 20kΩ potentiometer. (3) This parameter guaranteed by design.

CONNECTION DIAGRAMS

Top View

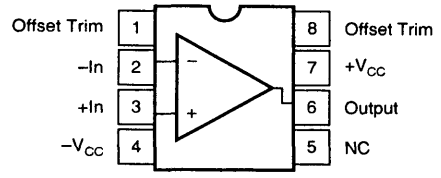

ABSOLUTE MAXIMUM RATINGS

Supply Voltage	±22V
Internal Power Dissipation [1]	500mW
Input Voltage	$\pm V_{CC}$
Output Short-Circuit Duration [2]	Indefinite
Differential Input Voltage [3]	±0.7V
Differential Input Current [3]	±25mA
Storage Temperature Range	–55°C to +125°C
Operating Temperature Range	–40°C to +85°C
Lead Temperature:	
P (soldering, 10s)	+300°C
U (soldering, 3s)	+260°C

NOTES: (1) Maximum package power dissipation versus ambient temperature. (2) To common with $\pm V_{CC}$ = 15V. (3) The inputs are protected by back-to-back diodes. Current limiting resistors are not used in order to achieve low noise. If differential input voltage exceeds ±0.7V, the input current should be limited to 25mA.

ELECTROSTATIC DISCHARGE SENSITIVITY

This integrated circuit can be damaged by ESD. Texas Instruments recommends that all integrated circuits be handled with appropriate precautions. Failure to observe proper handling and installation procedures can cause damage.

ESD damage can range from subtle performance degradation to complete device failure. Precision integrated circuits may be more susceptible to damage because very small parametric changes could cause the device not to meet its published specifications.

PACKAGE/ORDERING INFORMATION

PRODUCT	PACKAGE	PACKAGE DRAWING[1]	SPECIFIED TEMPERATURE RANGE	PACKAGE MARKING	ORDERING NUMBER	TRANSPORT MEDIA, QUANTITY
OPA27	DIP-8	P	–40°C to +85°C	OPA27GP	OPA27GP	Rail, 50
OPA27	SO-8	D	–40°C to +85°C	OPA27U	OPA27GU	Rail, 100
"	"	"	"	"	OPA27GU/2K5	Tape and Reel, 2500
OPA37	DIP-8	P	–40°C to +85°C	OPA37GP	OPA37GP	Rail, 50
OPA37	SO-8	D	–40°C to +85°C	OPA37U	OPA37GU	Rail, 100
"	"	"	"	"	OPA37GU/2K5	Tape and Reel, 2500

NOTE: (1) For the most current package and ordering information, see the Package Option Addendum located at the end of this data sheet.

Bulletin GS-96-7

General Specifications

DUPONT

Kapton®

polyimide film

General Specifications

Introduction

DuPont High Performance Materials manufactures and sells a variety of high-quality plastic film products in conformance with ISO 9002 certification.

These specifications describe the values and tolerances for Kapton® film properties. Where necessary for thorough understanding, test methods and procedures have been included.

Any aspects of the specifications that require further interpretation or clarification should be discussed with representatives of DuPont High Performance Materials.

Types of Kapton® Polyimide Film

DuPont makes several types of Kapton® film. Types HN, FN, and VN are used most commonly.

Types H, F, and V are alternative, special versions of these standard types. The specifications in this bulletin apply to them as well. In addition to these three types of Kapton®, films are available with the following attributes:

- antistat
- thermally conductive
- polyimides for fine line circuitry
- cryogenic insulation
- corona resistant
- pigmented for color
- conformable
- other films tailored to meet customers' needs

Data for these films are covered in separate product bulletins, which can be obtained from your DuPont Kapton® representative.

Type HN Film

Kapton® Type HN is a tough, aromatic polyimide film, exhibiting an excellent balance of physical, chemical, and electrical properties over a wide temperature range, particularly at unusually high temperatures. Chemically, its polyimide polymer makeup is the result of a polycondensation reaction between pyromellitic dianhydride and 4,4′diaminodiphenyl ether. Kapton® HN is available in the following gauges: 30 (7.5 µm), 50 (12.7 µm), 100 (25.4 µm), 200 (50.8 µm), 300 (76.2 µm), and 500 (127 µm). Other gauges, such as 75 (19.1 µm) and 400 (102 µm), are available by special request.

Type FN Film

Kapton® Type FN film is a heat sealable grade that retains the unique balance of properties of Kapton® Type HN over a wide temperature range. This is achieved by combining Type HN with DuPont Teflon® FEP fluorocarbon resin in a composite structure. **Table 1** lists the common types of FN film available. Other combinations are available. Consult your DuPont Kapton® marketing representative for further information.

Table 1
Kapton® FN Polyimide Film Types

	Construction, mil (μm)		
Designation	FEP	HN	FEP
120FN616	0.10 (2.5)	1.00 (25.4)	0.10 (2.5)
120FN616B	0.15 (3.8)	1.00 (25.4)	0.15 (3.8)
150FN019		1.00 (25.4)	0.50 (12.7)
200FN919	0.50 (12.7)	1.00 (25.4)	0.50 (12.7)
200FN011		1.00 (25.4)	1.00 (25.4)
250FN029		2.00 (50.8)	0.50 (12.7)
300FN021		2.00 (50.8)	1.00 (25.4)
300FN929	0.50 (12.7)	2.00 (50.8)	0.50 (12.7)
400FN022		2.00 (50.8)	2.00 (50.8)
500FN131	1.00 (25.4)	3.00 (76.2)	1.00 (25.4)

Type VN Film

Kapton® Type VN is the same tough polyimide film as Type HN Film, exhibiting an excellent balance of physical, chemical, and electrical properties over a wide temperature range, with superior dimensional stability at elevated temperatures. This product is available in 50 (12.7 μm), 75 (19.1 μm), 100 (25.4 μm), 200 (50.8 μm), 300 (76.2 μm), and 500 (127 μm) gauges.

Certification

Kapton® is certified to meet the requirements of the military specification ASTMD-5213-95 in addition to the items covered by this specifications bulletin. Written confirmation is availalbe with each delivery upon request.

Thermal Durability

The thermal durability of Kapton® film depends on the environmental conditions under which it is aged and tested. Its lifetime depends on the criterion of failure. Kapton® is routinely tested at the manufacturing site in the following manner:

Sheets of film 8.5″ × 11″ (216 mm × 279 mm) are freely suspended in an oven at a temperature of 400°C ±2°C (752°F ±3.6°F), monitored with a thermocouple to ensure accuracy. Sheets are removed after 2 hr (1 hr for 30 [7.6 μm] and 50 [12.7 μm] gauge film) and tested on an Instron Tensile Tester as described in **Table 2**. The elongation of the film at 23.5°C (74.3°F) should not be less than 10% after this aging at 400°C (752°F).

In addition, Kapton® conforms to ASTM D-5213-95, Standard Specification for Polymeric Resin Film for Electrical Insulation and Dielectric Applications.

Underwriters Laboratories, Inc. lists a thermal index of 200 to 220°C (392 to 428°F) (depending on gauge and type) for mechanical properties and 220 to 240°C (428 to 464°F) (depending on gauge and type) for electrical properties, under their file number E39505 for Kapton® polyimide film.

Properties of Type FN Film

Heat Seal Strength

Film-to-Film Seals

The peel strength of heat seals between the coated and uncoated sides of one-side coated Kapton® or between the coated sides of both one- and two-side coated Kapton® is determined as follows.

Seals are made in a jaw sealer at 350°C (662°F), 20 psi (1.4 bar), with a 20-sec dwell time. After cooling, the seals are cut into 1″ (25.4-mm) wide strips using a Thwing-Albert JDC sample cutter or its equivalent. The seal strength is measured with an Instron-type tensile tester. Seal strength is defined as the peak instantaneous strength occurring in each seal. Five specimen values are averaged.

The minimum peel strength between the coated sides of one- or two-side coated Kapton® film will be 700 g/in (2.7 N/cm), except for 120FN616 and 120FN616B, which will be 450 g/in (1.7 N/cm). The minimum peel strength between the coated and uncoated side of one-side coated Kapton® will be 450 g/in (1.7 N/cm).

Film-to-Copper Seals

The ability of FEP film to adhere to copper is measured using the same heat seal peel strength technique as described in "Film-to-Film Seals."

The peel strength is measured with the FEP side sealed to the untreated side of 1 mil (25.4 μm), ¾ oz GT copper foil; it will be a minimum of 300 g/in (1.2 N/cm).

As-Received Strength (Cold Peel) of Bonds Between Kapton® Type HN and Teflon® Layers

The bond between the Kapton® Type HN and Teflon® fluorocarbon resin layers on all Type FN products except 120FN616 and 120FN616B will have a minimum peel strength of 225 g/in (0.87 N/cm), measured using an Instron-type tensile tester and a 180° peel.

Table 2
Mechanical Properties of Kapton® Type HN Polyimide Film

Property	Property Value—Film Thickness, mil (μm) 0.30 (7.6)	0.50 (12.7)*	1.00 (25.4)*	2.00 (50.8)*	3.00 (76.2)*	5.00 (127)*	Method
Tensile Strength, psi (MPa) at 23°C (73°F). Machine Direction (MD) and Transverse Direction (TD), min.	16,000 (110)	20,000 (138)	24,000 (165)	24,000 (165)	24,000 (165)	24,000 (165)	ASTM D-882-91, Method A, using an Instron Tensile Tester (specimen size: ½" × 6" [12.7 mm × 152 mm]; jaw separation: 4" [102 mm]; jaw speed: 2"/min [51 mm/min]). Calculate the average of five specimens based on original measured thickness.
Elongation, %, MD and TD, min.	25	35	40	45	50	50	Same as above.
Shrinkage, %, MD and TD at 400°C (752°F), max.	4.0	4.0	2.5	2.5	2.5	2.5	I The percent shrinkage is obtained for either the MD or TD using the average of three measurements in either direction before and after conditioning. Prior to measurement, the 8½" × 11" (216 mm × 279 mm) specimen is conditioned by freely suspending it for 2 hr** in an oven controlled to 400°C (752°F).
Moisture Absorption, %, max.	4.0	4.0	4.0	4.0	4.0	4.0	ASTM D-570-92, using 24-hr immersion at 23°C (73°F). Average of three specimens.

*Also applies to Type VN, except shrinkage, which is shown in **Table 5**.

**1 hr for 30 and 50 gauge film

Table 3
Electrical Properties of HN Film

Property	Property Value—Film Thickness, mil (μm) 0.30 (7.6)	0.50 (12.7)*	1.00 (25.4)*	2.00 (50.8)*	3.00 (76.2)*	5.00 (127)*	Method
Dielectric Strength, AC V/mil (kV/mm), min.	3,000 (118)	3,000 (118)	6,000 (236)	5,000 (197)	4,500 (177)	3,000 (118)	ASTM D-149-94. (Average of ten specimens.) Flat sheets in air placed between ¼" (6 mm) diameter brass electrodes with 1/32" (0.8 mm) edge radius subjected to 60 cycles AC voltage at 500 V/sec rate of rise to the breakdown voltage.
Volume Resistivity, ohm-cm at 200°C (392°F), min.	10^{12}	10^{12}	10^{12}	10^{12}	10^{12}	10^{12}	ASTM D-257-93
Dielectric Constant at 1 kHz, max.	4.0	4.0	3.9	3.9	3.9	3.9	ASTM D-150-94. Use conducting silver paint electrodes, two-terminal system of measurement at standard conditions. Results are based on an average of five tests using measured thickness of specimens.
Dissipation Factor at 1 kHz, max.	0.0070	0.0050	0.0036	0.0036	0.0036	0.0036	Same as above.

*Also applies to Type VN

Table 4
Dielectric Strength of Kapton® Type FN Polyimide Films

Gauge Construction	Minimum Breakdown V/mil (kV/mm)
120FN616	4,200 (165)
120FN616B	4,200 (165)
150FN019	3,700 (146)
200FN919	3,200 (126)
200FN011	3,200 (126)
250FN029	2,750 (108)
300FN021	2,700 (106)
300FN929	2,700 (106)
400FN022	2,200 (87)
500FN131	2,200 (87)

Test Method
Average of ten specimens tested per ASTM D-149-92. Flat sheets in air placed between ¼" (6 mm) diameter brass electrodes with 1/32" (0.8 mm) edge radius subjected to 60 cycles AC voltage. Rise is 500 V/sec to the breakdown voltage.

General

Materials

Kapton® Type HN and Type VN films are polyimide polymers in the form of a film.

Kapton® Type FN film is a combination of Type HN film with Teflon® FEP fluorocarbon resin on one or both sides.

Uniformity

Material shall be uniform in composition and free from defects that impair serviceability and/or appearance in proven applications.

U.S. Cores

Cores shall be of sufficient strength to prevent collapsing from handling. Standard core internal diameters (I.D.) are nominally 3" and 6" (76 mm and 152 mm) with the following specifications:

Paper

3" (76 mm) I.D.	3.032" ± 0.008" (77.01 mm ± 0.2 mm)
6" (152 mm) I.D.	6.028" ± 0.010" (153.11 mm ± 0.25 mm)

Plastic

3" (76 mm) I.D.	3.024" ± 0.005" (76.81 mm ± 0.1 mm)
6" (152 mm) I.D.	6.041" ± 0.010" (153.44 mm ± 0.25 mm)

Core material will be plastic for 3" (76 mm) I.D. cores less than 5/8" (16 mm) wide.

Core material will be fiber for 3" (76 mm) I.D. cores wider than 5/8" (16 mm) and for 6" (152 mm) I.D. cores. A split 3" (76 mm) I.D. fiber core is standard for all universal and Step-Pac™ rolls.

If these cores are not suitable, further information on other options may be obtained from your DuPont Kapton® representative.

Table 5
Shrinkage of Kapton® Type VN Polyimide Film

	Property Value Film Thickness, mil (μm)				
Property	**0.50 (12.7)**	**1.00 (25.4)**	**2.00 (50.8)**	**3.00 (76.2)**	**5.00 (127)**
Shrinkage, %, MD and TD at 200°C (392°F), max.	0.10	0.10	0.10	0.10	0.10

Test Method
The percent shrinkage obtained for either the MD or TD by using the average of three measurements in either direction before and after conditioning. Temperature exposure 200°C ±2°C (392°F ±3.6°F) for 1 hr. Measurements must be made at the same temperature and humidity conditions before and after conditioning. To ensure sample/ambient equilibrium before and after conditioning, specimens should be exposed for 3 hr.

Width Tolerance
The maximum variation in film width from that specified on the order shall be as follows:

Slit Width Range	Tolerance
1½″ (38 mm) or less	±0.005″ (0.13 mm)
1½″ to 4″ (38 mm to 102 mm)	±0.030″ (0.76 mm)
>4″ (>102 mm)	±0.060″ (1.5 mm)

Luxembourg Supply

Cores shall be of sufficient strength to prevent collapsing from handling. Luxembourg supplies pad rolls in widths below 9½″ (240 mm) and universal wound rolls.

Standard core internal diameter for Luxembourg is 3″ (76 mm) (nominal 3″ ±0.008″ [76 mm ±0.2 mm]).

Standard cores for pad rolls are paper cores, except for widths below ½″ (13 mm), where it will be plastic.

Standard universal: core length

2.8″ ±0.08″ (70 mm ±2 mm) (split core)

Wide universal: core length

4.3″ ±0.08″ (110 mm ±2 mm) (non-split core)

A different put-up called Step-Pac™ is available from the U.S. Contact your DuPont Kapton® representative for more information.

Width Tolerance
The maximum variation in film width from that specified on the order shall be as follows:

Slit Width Range	Tolerance
0.9″ (22 mm) or less Universal	0.008″ (0.20 mm)
6″ (152 mm) or less Pad rolls	0.016″ (0.40 mm)
6″ to 9½″ (153 mm to 240 mm) Pad rolls	0.04″ (1.00 mm)

Outside diameter tolerance: ±0.4″ (10 mm)

Table 6
Kapton® Polyimide Film Specifications and Tolerances

Film Type	Thickness Nominal mil (μm)*	Thickness Tolerance Min. mil (μm)	Thickness Tolerance Max. mil (μm)	Width Range Min. in (mm)	Width Range Max. in (mm)	Unit Weight Min. g/m²	Unit Weight Max. g/m²	Area Factor ft²/lb	Area Factor (m²/kg)
30HN	0.30 (7.6)	0.24 (6.1)	0.36 (9.1)	3/16 (4.8)	52 (1320)	7.6	14.0	453	92.8
50HN	0.50 (12.7)	0.35 (8.9)	0.65 (16.5)	3/16 (4.8)	52 (1320)	14.0	26.0	272	55.7
100HN	1.00 (25.4)	0.85 (21.6)	1.15 (29.2)	3/16 (4.8)	52 (1320)	32.7	39.7	136	27.9
200HN	2.00 (50.8)	1.75 (44.5)	2.25 (57.2)	3/16 (4.8)	52 (1320)	66.9	77.9	68	13.9
300HN	3.00 (76.2)	2.72 (69.1)	3.28 (83.3)	3/16 (4.8)	52 (1320)	101.9	115.4	45	9.2
500HN	5.00 (127)	4.65 (118)	5.35 (136)	3/16 (4.8)	52 (1320)	169.5	192.5	27	5.5
50VN	0.50 (12.7)	0.35 (8.9)	0.65 (16.5)	3/16 (4.8)	52 (1320)	14.0	26.0	272	55.7
100VN	1.00 (25.4)	0.85 (21.6)	1.15 (29.2)	3/16 (4.8)	52 (1320)	32.7	39.7	136	27.9
200VN	2.00 (50.8)	1.75 (44.5)	2.25 (57.2)	3/16 (4.8)	52 (1320)	66.9	77.9	68	13.9
300VN	3.00 (76.2)	2.72 (69.1)	3.28 (83.3)	3/16 (4.8)	50 (1270)	101.9	115.4	45	9.2
500VN	5.00 (127)	4.65 (118)	5.35 (136)	3/16 (4.8)	50 (1270)	169.5	192.5	27	5.5
120FN616	1.20 (30.5)	1.10 (27.9)	1.40 (35.6)	3/16 (4.8)	44 (1118)	41.0	58.0	104	21.3
120FN616B	1.30 (33.0)	1.20 (30.5)	1.50 (38.1)	3/16 (4.8)	44 (1118)	47.0	54.0	92	18.8
150FN019	1.50 (38.1)	1.25 (31.8)	1.75 (44.5)	3/16 (4.8)	44 (1118)	53.0	74.0	77	15.8
200FN011	2.00 (50.8)	1.70 (43.2)	2.30 (58.4)	3/16 (4.8)	44 (1118)	77.0	104.0	54	11.1
200FN919	2.00 (50.8)	1.70 (43.2)	2.30 (58.4)	3/16 (4.8)	44 (1118)	77.0	104.0	54	11.1
250FN029	2.50 (63.5)	2.25 (57.2)	2.75 (69.9)	3/16 (4.8)	44 (1118)	87.0	113.0	49	10.0
300FN021	3.00 (76.2)	2.60 (66.0)	3.40 (86.4)	3/16 (4.8)	44 (1118)	111.0	142.0	39	8.0
300FN929	3.00 (76.2)	2.60 (66.0)	3.40 (86.4)	3/16 (4.8)	44 (1118)	111.0	142.0	39	8.0
400FN022	4.00 (102)	3.50 (88.9)	4.50 (114)	3/16 (4.8)	44 (1118)	163.0	200.0	27	5.5
500FN131	5.00 (127)	4.50 (114)	5.50 (140)	3/16 (4.8)	44 (1118)	195.0	239.0	23	4.7

*Reference: ASTM D-374-94, Method A, C, or D.

The usual dimensions of pad rolls are 3″ (76 mm) I.D. × 6″ (152 mm) or 9″ (230 mm) outside diameter (O.D.) for widths up to 4″ (102 mm). In Luxembourg, 152 mm, 180 mm, 203 mm, and 240 mm O.D. rolls are available. For wider rolls, the usual dimensions are 6″ (152 mm) I.D. × 9½″ (240 mm) or 11″ (280 mm) O.D. For Universal and Step-Pac™ rolls, the dimensions are 3″ (76 mm) I.D. × 6″ (152 mm), 8″ (203 mm), or 12″ (305 mm) O.D. If these dimensions are not suitable, information on other options is available from your DuPont High Performance Films technical or customer service representative.

Roll Types

Kapton® polyimide film is supplied in three types of rolls: pad, universal, and Step-Pac™ wind.

Pad Roll Specifications

- Core width will be the film width +⅛″ (+3.2 mm), –0.
- Core edges shall not project more than 1/16″ (1.6 mm) beyond the roll face on either side.
- Core shall not be recessed on either side.
- The outside and starting ends of the film shall be fastened in a manner to prevent unwinding.
- "Dishing" or "cupping" may not exceed 1/16″ (1.6 mm), measured with a straightedge across the diameter of the roll.

Universal and Step-Pac™ Roll Specifications

- The difference between the lengths of the projecting core on each side shall not exceed 3/16″ (4.8 mm).
- Film shall not project from the main body of the roll more than ⅛″ (3.2 mm).
- The outside and starting ends of the film shall be fastened in a manner to prevent unwinding.
- Roll face depression, the difference between the highest and lowest points of the roll, unstressed, shall not exceed 3/16″ (4.8 mm).

Table 7
Reference Guide: Standard Length versus Roll O.D. (U.S. Supply)

Type	Standard Length Roll	Roll O.D. 3″ Core I.D.	Roll O.D. 6″ Core I.D.
100HN	5,000 ft (1,525 m)	9½″ (241 mm)	11″ (279 mm)
	10,000 ft (3,050 m)	11″ (279 mm)	14″ (356 mm)
200HN	2,500 ft (763 m)	9½″ (241 mm)	11″ (279 mm)
300HN	1,670 ft (509 m)	9½″ (241 mm)	11″ (279 mm)
500HN	1,000 ft (305 m)	9½″ (241 mm)	11″ (279 mm)

Splices

Description

Three types of splice are available.

- Mylar® polyester film-based yellow tape (standard).
- Kapton® polyimide film-based tape (special requirements only).
- Heat seal splice, 12″ (305 mm) or less in width (Type FN).

Splices will be centered on the joint to ±¼″ (±6 mm). They will be smooth and wrinkle-free to avoid distortion of the adjacent film layers in the roll.

Tape Splices

Tape splices are standard on all gauges of HN and VN film and on all gauges of FN film more than 12″ (305 mm) wide.

Tape splices are made with the butt edges of the film covered on both sides with pressure-sensitive adhesive tape. Two-inch (50 mm) wide splicing tape is used.

Heat Seal Splices

Overlap heat seal splices are made on all FN films, except 250FN029, with an overlap that is a minimum of ⅜″ (9.5 mm) wide.

On 250FN029, a butt splice is made using 120FN616 as the joining tape applied on the FEP surface. The butt splice is oriented with the 120FN616 tape on the top of the film as it unwinds from a universal put-up and on the bottom as it unwinds from a pad.

Overlap heat seal splices for one-side and two-side FEP composites are oriented with the leading edge of the new film on the bottom for universal and Step-Pac™ put-ups. Pad put-ups of one- or two-side FEP composites have the leading edge of the new film on the top.

Packaging and Marking

Packaging

Kapton® polyimide film shall be adequately packed to prevent loss of contents or damage during shipment.

All film will be wrapped with a non-fibrous material.

Marking

Kapton® is identified, as shown in **Table 8**, to allow complete traceability back to the raw materials and processing conditions.

Arrangements for special markings can be made (such as part or specification number). Consult with your DuPont Kapton® technical or customer service representative for details.

All package marking information is available with bar code labels.

Table 8
Package Marking

	Shipping Container	Package	Core Label*
Scheduled Date	X	X	X
Customer Order Number	X	X	
DuPont Order Number	X	X	X
Gauge	X	X	X
Type	X	X	X
Width	X	X	X
Number of Rolls per Container	X	X	
Net Weight	X	X	
Actual Footage			X
Mill Roll Number	X	X	X
I.D. and O.D.**	X	X	

* Affixed to the core on all cores. 2.25" (57 mm) wide and over. Included with the package on all cores less than 2.25" (57 mm) wide

** Inside diameter of core and nominal outside diameter of roll

Permanent magnet vibration testing systems

9 to 489 N (2 - 110 lbf)

V101/2, V201/3, V406/8, V450/1 and V455/6 Shakers

PA Amplifiers

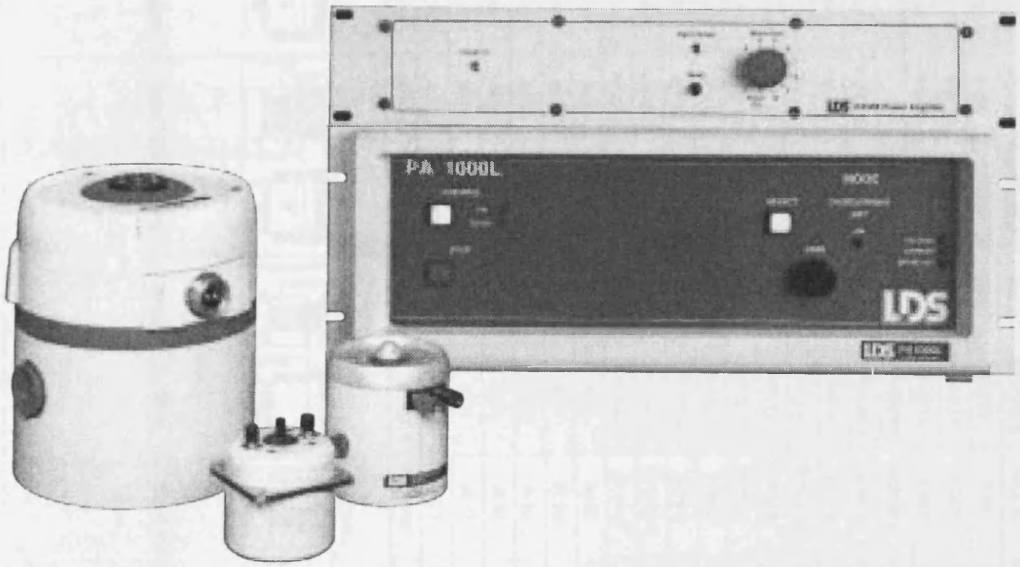

Typical system applications

- laboratory experiments
- modal studies
- electronic assemblies
- physiological research
- high speed actuators
- velocity transducers

A range of vibration testing systems designed to minimise operational costs whilst providing the maximum flexibility to the scientist or test engineer. Featuring:-

- Permanent magnet construction
- Low mass, high performance armature construction
- Wide frequency band operation - dc to 13 kHz
- Well proven armature suspension system
- Mounted on base or support trunnion
- Option of auxiliary suspension
- Ultra-compact energy efficient amplifiers

Total system solutions

With the addition of an LDS sine, random and shock controller we can provide total testing solutions. Alternatively our systems are designed to interface with any standard third party controller. Whichever route you choose, you have the assurance that all LDS products are supported by a world-wide sales and service organisation. From application engineering, installation and training through to maintenance, spares and repairs LDS offers a total service approach to keep your system operating efficiently and reliably.

LDS
LING DYNAMIC SYSTEMS

V101/2, V201/3, V406/8, V450/1, V455/6

Shaker system
configuration & performance parameters

Model	V101/2 – PA 25E		V201/3 – PA 25E		V406/8 – PA 100E		V406/8 – PA 500L		V450/1 – PA 500L		V455/6 – PA 1000L	
	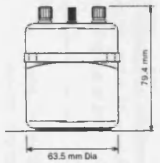		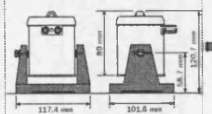		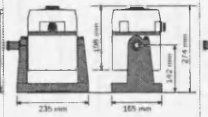		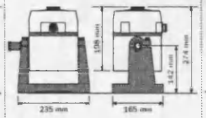		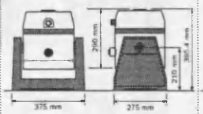		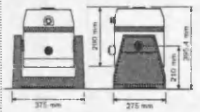	
	Metric	American	Metric	American	Metric	American	Metric	American	Metric	American	Metric	American
Armature diameter	-	-	-	-	38 mm	1.5 in	38 mm	1.5 in	63.5 mm	2.5 in	63.5 mm	2.5 in
System sine force peak - naturally cooled	8.9 N	2 lbf	17.8 N	4 lbf	98 N	22 lbf	98 N	22 lbf	178 N	40 lbf	178 N	40 lbf
System sine force peak - forced air cooled	-	-	17.8 N	4 lbf	98 N	22 lbf	196 N	44 lbf	311 N	70 lbf	489 N	110 lbf
Shaker sine force peak* - forced air cooled	-	-	26.7 N	6 lbf	196 N	44 lbf	196 N	44 lbf	311 N	70 lbf	489 N	110 lbf
System random force rms (IS05344)	-	-	-	-	38 N	8.5 lbf	89 N	20 lbf	214 N	48 lbf	302 N	68 lbf
Shaker max random force rms*	-	-	-	-	89 N	20 lbf	89 N	20 lbf	214 N	48 lbf	334 N	75 lbf
Armature resonance frequency	12000 Hz	12000 Hz	13000 Hz	13000 Hz	9000 Hz	9000 Hz	9000 Hz	9000 Hz	6000 Hz	6000 Hz	6000 Hz	6000 Hz
Useful frequency range	5-12000 Hz	5-12000 Hz	5-13000 Hz	5-13000 Hz	5-9000 Hz	5-9000 Hz	5-9000 Hz	5-9000 Hz	5-7500 Hz	5-7500 Hz	5-7500 Hz	5-7500 Hz
Effective mass of moving element	0.0065 kg	0.0143 lb	0.020 kg	0.044 lb	0.200 kg	0.44 lb	0.200 kg	0.44 lb	0.426 kg	0.94 lb	0.426 kg	0.94 lb
System velocity sine peak	1.31 m/s	51.6 in/s	1.49 m/s	58.7 in/s	1.52 m/s	60 in/s	1.78 m/s	70 in/s	1.78 m/s	70 in/s	2.5 m/s	98.4 in/s
Shaker velocity sine peak*	1.31 m/s	51.6 in/s	1.83 m/s	72 in/s	1.78 m/s	70 in/s	1.78 m/s	70 in/s	2.0 m/s	78.7 in/s	2.5 m/s	98.4 in/s
Max acceleration sine peak	1373 m/s²	140 gn	1334 m/s²	136 gn	981 m/s²	100 gn	981 m/s²	100 gn	730 m/s²	74.5 gn	1147 m/s²	117 gn
Amplifier rating	0.048 kVA	0.048 kVA	0.048 kVA	0.048 kVA	0.147 kVA	0.147 kVA	0.7 kVA	0.7 kVA	0.7 kVA	0.7 kVA	1.4 kVA	1.4 kVA
LDS amplifier	PA 25E	PA 25E	PA 25E	PA 25E	PA 100E	PA 100E	PA 500L	PA 500L	PA 500L	PA 500L	PA 1000L	PA 1000L
Suspension axial stiffness	3.15 N/mm	18 lbf/in	3.5 N/mm	20 lbf/in	12.3 N/mm	70 lbf/in	12.3 N/mm	70 lbf/in	17.5 N/mm	100 lbf/in	17.5 N/mm	100 lbf/in
Aux. suspension axial stiffness	-	-	8.76 N/mm	50 lbf/in	22.8 N/mm	130 lbf/in	22.8 N/mm	130 lbf/in	-	-	-	-
System displacement (continuous) pk-pk	2.5 mm	0.1 in	5 mm	0.2 in	14.0 mm	0.55 in	17.6 mm	0.69 in	19 mm	0.75 in	19 mm	0.75 in
Shaker displacement (continuous) pk-pk*	2.5 mm	0.1 in	5 mm	0.2 in	17.6 mm	0.69 in	17.6 mm	0.69 in	19 mm	0.75 in	19 mm	0.75 in
Vibrator mass-optional trunnion mounted	-	-	3.17 Kg	7 lb	22.7 kg	50 lb	22.7 kg	50lb	82 kg	180 lb	82 kg	180 lb
Cooling air flow rate	-	-	0.0012 m³/s	2.5 ft³/m	0.014 m³/s	30 ft³/m	0.014 m³/s	30 ft³/m	0.012 m³/s	25 ft³/m	0.012 m³/s	25 ft³/m
Shaker mass base mounted	0.91 kg	2 lb	1.81 kg	4 lb	14.1 kg	31 lb	14.1 kg	31 lb	64 kg	141 lb	64 kg	141 lb
Max. working ambient temperature Shaker: Amplifier:	 30°C 35°C	 86°F 95°F	 30°C 35°C	 86°F 95°F	 30°C 35°C	 86°F 95°F	 30°C 30°C	 86°F 86°F	 30°C 30°C	 86°F 86°F	 30°C 30°C	 86°F 86°F
Heat rejected to air Shaker cooling fan: Amplifier:	 - 0.067 kW	 - 0.067 kW	 - 0.067 kW	 - 0.067 kW	 - 0.15 kW	 - 0.15 kW	 0.46 kW 0.40 kW	 0.46 kW 0.40 kW	 0.29 kW 0.37 kW	 0.29 kW 0.37 kW	 0.75 kW 0.87 kW	 0.75 kW 0.87 kW
Electrical requirement Amplifier:	 0.09 kVA	 0.09 kVA	 0.09 kVA	 0.09 kVA	 0.27 kVA	 0.27 kVA	 1.5 kVA†	 1.5 kVA†	 1.4 kVA†	 1.4 kVA†	 2.9 kVA†	 2.9 kVA†
Acoustic noise at 2m** Shaker: Amplifier:	 - silent	 - silent	 - silent	 - silent	 105 dBA silent	 105 dBA silent	 105 dBA 47 dBA	 105 dBA 47 dBA	 105 dBA 47 dBA	 105 dBA 47 dBA	 105 dBA 47 dBA	 105 dBA 47 dBA

* Shaker ratings are those which can be achieved with a larger amplifier than that supplied as standard
** Maximum noise level during operation at full thrust, measured at 2m distance
† Includes cooling fan

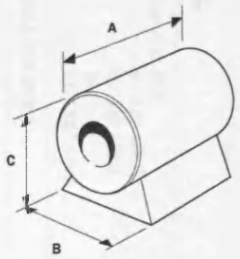

Cooling blowers

Blower	Wt Kg	A mm	B mm	C mm
V406/8 50 Hz	17	241	389	249
V406/8 60 Hz	15	241	365	249
V450/1 50/60 Hz	5.4	241	186	249
V455/6 50/60 Hz	5.4	241	186	249

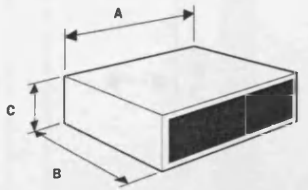

PA amplifiers

Amplifier	Wt Kg	A mm	B mm	C mm
PA 25E	9	488	337	92
PA 100E	15	488	337	92
PA 500L	20	448	412	188
PA 1000L	35	482	505	188

Armature insert patterns

Shaker	V101/2	V201/3	V406/8	V450/1	V455/6
Armature dia. mm	-	-	38	63.5	63.5
Centre insert	1	1	1	1	1
25.4 mm	-	-	6	-	-
50 mm	-	-	-	5	5

PCD inserts equi-spaced

Options

Shaker model	V101/2	V201/3	V406/8	V450/1	V455/6
Alternative inserts: M4	●	●	●	-	-
6/32" UNC	●	-	-	-	-
8/32" UNC	-	●	●	-	-
M5	-	-	-	●	●
10/32" UNF	-	-	○	●	●
Rubber isolation mounting	-	-	-	○	○
Base mounting	●	●	●	●	●
Support trunnion	-	○	○	○	○
Auxilliary suspension	-	○	○	-	-
Cooling fan	-	-	●	●	●

KEY ● standard ○ standard option - not available

PA series power amplifier characteristics

Amplifier model	PA 25E	PA 100E	PA 500L	PA 1000L
Rated sinusoidal power output (Matched resistive load)	48 W (5R3)	147 W (2R9)	500 W	1000 W
Maximum continuous sinusoidal VA output, 0.5pf	48 VA	147 VA	700 VA	1400 VA
Frequency range at rated power	10Hz - 10 kHz	10Hz - 10 kHz	10Hz - 14 kHz	10Hz - 14 kHz
Total harmonic distortion at rated output 20 Hz - 10 kHz	Typically 0.3 %	Typically 0.5 %	Typically 0.2 %	Typically 0.2 %
Maximum output voltage	16V rms	20V rms	40V rms	80V rms
Maximum no load voltage	24V rms	32V rms	45V rms	86V rms
Voltage regulation	1%	3%	2%	2%
Output current at rated VA	2.7A rms	7A rms	18A rms	18A rms
Maximum output current	3A rms	7A rms	18A rms	18A rms
Random output current	5.9A pk	14A pk	54A pk	54A pk
Overcurrent trip level	4.2A rms	10A rms	20A rms	20A rms
Input sensitivity for maximum output (400 Hz)	1.0V rms	1.0V rms	1.0V rms	1.0V rms
Signal to noise ratio	> 75 dB	> 75 dB	> 75 dB	> 80 dB
Amplifier efficiency	59 %	58 %	59 %	59 %
Protection	Fast acting current limit	Fast acting current limit	Output device protection	Output device protection

Some of the features listed are available as standard, others as options.
Please contact LDS for advice on the optimum specification to meet your system needs.
Specifications are correct at time of going to print. LDS reserves the right to amend specifications without prior notice.

LDS
LING DYNAMIC SYSTEMS

World leaders in vibration and environmental test systems

A United Dominion Company

Ling Dynamic Systems Limited
Heath Works, Baldock Road, Royston,
Hertfordshire SG8 5BQ, England.
Tel (UK) 01763 242424
International + 44 1763 242424
Fax (UK) 01763 249715
International + 44 1763 249715
Email sales@lds-group.com
www.lds-group.com

Ling Dynamic Systems Inc
60 Church Street, Yalesville,
Connecticut 06492, USA.
Tel (203) 265 7966
Toll Free # 1- 800 - GO TO LDS
Fax (203) 284 9399
Email sales@lds-usa.com

LDS SARL
Z.I. l'Eglantier - 17, rue des Cerisiers,
CE 1528 Lisses - 91015 Evry Cedex,
France.
Tel (1) 69 11 21 30
Fax (1) 69 11 21 31
Email lds@lds-france.com

Ling Dynamic Systems GmbH
Freisinger Straße 32,
D-85737 Ismaning, Germany.
Tel (+49) 89 96 98 9180
Fax (+49) 89 96 98 9189
Email mayer-lds@t-online.de

CE

All LDS equipment complies with current European and USA safety and EMC regulations

BSI REGISTERED FIRM

ISO 9001
Cert No. FM 26616

DATA-1/ISS2.2

Appendix F: List of Tables and Figures

Tables

Figures